High-resolution EM-CCD scintillation gamma cameras

Proefschrift

ter verkrijging van de graad van doctor
aan de Technische Universiteit Delft,
op gezag van Rector Magnificus Prof. ir. K.C.A.M. Luyben,
voorzitter van het College van Promoties
in het openbaar te verdedigen op dinsdag 29 januari 2013 om 15:00 uur

door Marc Albert Nijs KOREVAAR
doctorandus in de natuurkunde
geboren te Amsterdam.

Dit proefschrift is goedgekeurd door de promotor:
Prof. dr. F.J. Beekman

Copromotor:
Dr. ir. M.C. Goorden

Samenstelling promotiecommissie:

Rector Magnificus,	voorzitter
Prof. dr. F.J. Beekman,	Technische Universiteit Delft, promotor
Dr. ir. M.C. Goorden,	Technische Universiteit Delft, copromotor
Prof. dr. R. Boellaard,	Vrije Universiteit Amsterdam
Prof. dr. R. Verdaasdonk,	Vrije Universiteit Amsterdam
Prof. ir. A.J.M. van Tuijl,	Universiteit Twente
Prof. dr. P. Dorenbos,	Technische Universiteit Delft
Dr. F.W.B. van Leeuwen,	Universiteit Leiden
Prof. Dr. H.T. Wolterbeek,	Technische Universiteit Delft, reservelid

The research presented in this thesis was carried out at the Radiation Detection & Medical imaging (RD&M) section of the department of Radiation Radionuclides & Reactors (R^3), faculty of Applied Sciences, Delft University of Technology, The Netherlands.

This research has been financially supported by the Netherlands Ministry of Economic Affairs, IOP photonics grant IPD067766.

Printed by: Proefschriftmaken.nl || Uitgeverij BOXPress

ISBN: 978-90-8891-571-0

To the memory of Pia Korevaar-Pfluger

Contents

Chapter 1

Introduction

1.1 Medical imaging

The development of medical imaging techniques has dramatically changed clinical practice and biomedical science in the 20th century. It has provided medical doctors with a palette of excellent in vivo techniques to diagnose disease, where previously no or only limited methods were available. Its applications range from diagnosing bone fractures, identification of tumour locations and characteristics, imaging of the foetus in pregnant women to detecting cardiac disease. Furthermore, medical imaging has helped medical scientists to develop new therapeutics and better understand mechanisms of disease and human physiology.

A milestone in this development was the advent of biomedical tomography which enabled recording 3D images of living subjects. In tomography, derived from the Greek word *tomos* (slice) and *graphein* (to write), information from projections of properties (such as X-ray attenuation or molecule concentration) are obtained at multiple angles and are subsequently combined to reconstruct a stack of cross-sectional images (slices), that together result in a 3D image.

Biomedical imaging encompasses many different imaging modalities, which can roughly be divided into anatomical and functional modalities. Anatomical imaging modalities mainly reveal the structure and shape of human organs and tissues. In contrast, functional modalities mainly visualize the physiology and function of tissue in the human body. Some examples of human brain images obtained with different anatomical and functional modalities are shown in figure 1.1. Recently, it has become increasingly popular to combine anatomical and functional imaging modalities; this facilitates overlaying functional and anatomical images to better localize the functional information (e.g. the precise location of a tumour in the body).

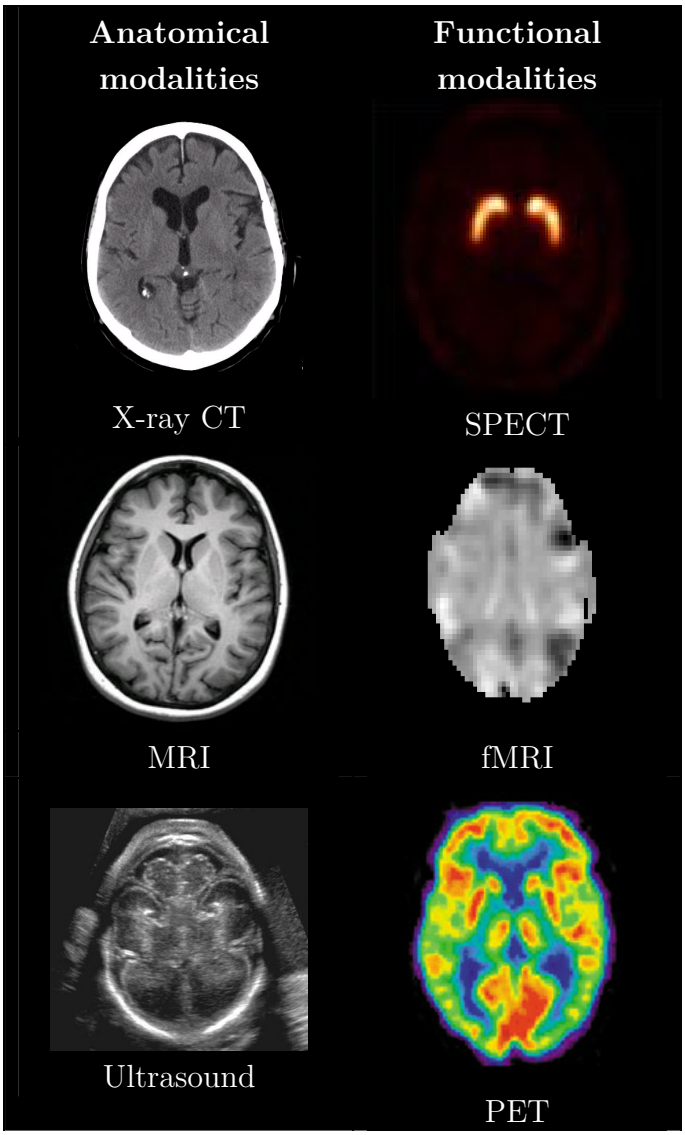

Figure 1.1: Different tomographic imaging modalities revealing the anatomy (left column) and function (right column) of the brain.

1.1.1 Overview of imaging modalities

1.1.1.1 Anatomical imaging modalities Well-known anatomical modalities include X-ray Computed Tomography (CT), medical ultrasound imaging and Magnetic Resonance Imaging (MRI). Both traditional X-ray imaging and CT are based on the property that the amount of X-ray attenuation in a certain tissue strongly depends on its density. X-rays were discovered more than 100 years ago by Röntgen[1] and used by him to make the first medical X-ray image of a human hand[2]. X-ray CT was pioneered by G. Hounsfield and A. Cormack who won a Nobel Prize for developing the first CT scanner[3]. Medical ultrasound uses sound waves that are sent into the human body. At locations where the density of tissue in the human body changes, the sound waves are partly reflected. Based on the information contained in these reflected waves, an image of the tissue density is made. MRI, an imaging modality that uses magnetic properties of tissues in the human body[4], was pioneered by F. Bloch and E. Purcell. They won the 1952 Nobel Prize for recognizing that certain nuclei, if placed in a strong magnetic field and irradiated with radio waves, resonate and emit a radio signal.

1.1.1.2 Functional imaging modalities Functional modalities include MRI, Doppler ultrasound, and nuclear medicine imaging modalities that use radioactively labelled molecules. Functional MRI (fMRI) is a technique that measures the functional activation in the brain by detecting changes in blood flow[5,6] and MRI is also used for functional imaging of the heart[7,8,9]. For cardiac imaging, Doppler ultrasound is used to measure the speed and direction of blood flow in the heart[10].
Nuclear medicine imaging investigations are very commonly performed procedures, accounting for more than 10 million scans per year in Europe[11] and the USA[12] each. These imaging investigations constitute planar gamma camera imaging, Single Photon Emission Computed Tomography (SPECT) and Position Emission Tomography (PET). Besides their clinical application, SPECT and PET imaging of small animals for pre-clinical research is getting more and more popular. Since the gamma detectors investigated in this thesis were developed for small-animal SPECT applications, nuclear medicine imaging techniques including small-animal SPECT are described in more detail in the next sections.

1.1.2 Nuclear medicine imaging

Imaging function of organs and tissues *in vivo* can be done with the aid of radioactively labelled tracer molecules. Prior to a scan, the tracer is injected and it subsequently distributes throughout the organism depending on the tracer chemical properties and the organism's physiology. For example, some tracers accumulate in specific tumour cells; others in the heart muscle e.g. proportionally to local blood flow, others mark certain receptors in the brain, and some mark bone growth. As the radionuclide in the tracer molecules decays, gamma radiation is emitted. By detecting this radiation with one or more gamma cameras (figure 1.2 (a)), the tracer distribution inside the organism can be visualized.

The concept of a tracer as a marker of biological function was first documented early in the 20th century by G. Hevesy together with F. Paneth[14] and a proof of principle was provided by tests in a plant[15]. The earliest research application of these tracers in humans was the study of the blood flow velocity with radium as tracer by H. Blumgart and O. Yens[16]. Since their first application to fundamental research into the physiology of plants, animals and humans, it would not be long before these techniques found their way into the clinical setting.

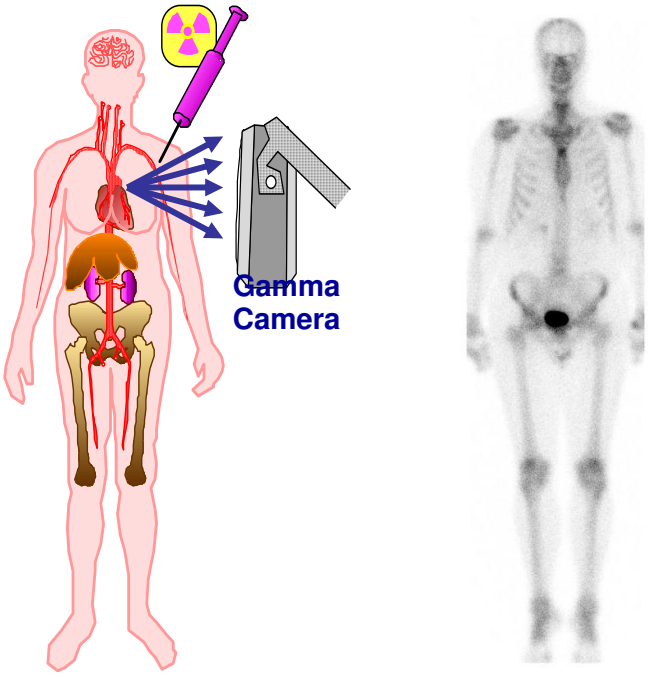

Figure 1.2: Nuclear medicine scan **(a)** The tracer, consisting of a chemical with a radioactive isotope is injected, localizes in certain tissues according to their function, and the emitted gamma photons are detected by a gamma camera. **(b)** Bone scan using the tracer methylene diphosphonate labelled with ^{99m}Technetium showing no abnormalities.[13]

One of the first clinical tracer molecule applications was the use of radiation detection probes. These probes were initially used in humans to quantify the uptake of iodine by the thyroid[17] and to locate tumours during surgery[18,19,20,21], an application for which probes are still in use today[22].

Following the introduction of probes in nuclear medicine, a next step was the development of a scanner which could make 2D (planar) images. The pioneer in this field was Benedict Cassen who developed the rectilinear scanner, an automated system for imaging patient organs[23]. Today, planar imaging is used for identifying bone metastases (an example of a bone scan is shown in figure 1.2 (b)), functional thyroid imaging, as well as for imaging the function of different organs.

Emission tomography was pioneered by D. Kuhl[24,25]. The two emission tomography modalities, PET and SPECT, differ in the tracer molecules that are imaged. In PET, the tracer has a positron emitting radionuclide as its label. When the emitted positron recombines with an electron, two gamma photons are emitted in approximately opposite

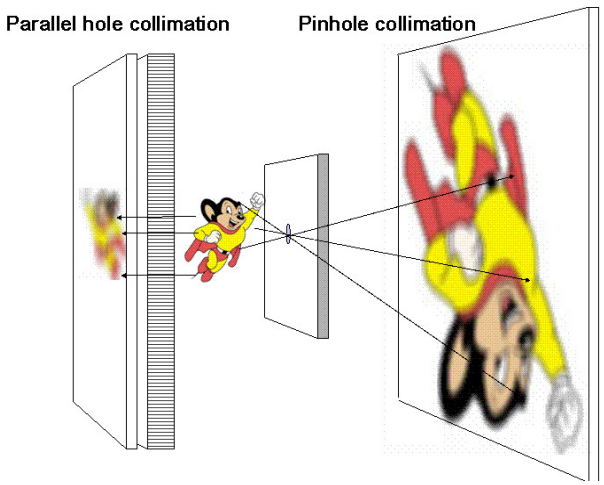

Figure 1.3: Parallel hole collimation versus pinhole collimation.[26]

directions. By detecting both gamma photons in coincidence, the recombination position can be located on a line of response. After many of these lines of response have been measured, a reconstruction of the 3D distribution of the radionuclide can be made. In SPECT, radionuclides emit a single gamma photon after decay. Via collimators[12] (with a function similar to lenses in optics) images of the object are formed on a gamma detector that is placed behind the collimator (figure 1.3). From these 2D detector images measured at different angles, a reconstruction of the 3D tracer distribution can be made. In the clinic, SPECT and PET are used for diagnosis of e.g. cardiac disease[27,28], bone disease[29], various types of cancer[30,31] and brain diseases[32,33] but also for image guided therapy[34,35].

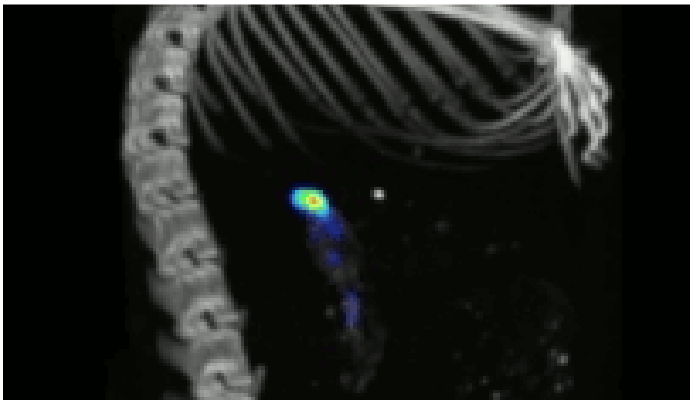

Figure 1.4: Combined SPECT-CT image of the mouse abdomen with radio-active holmium in a kidney tumour obtained with the U-SPECT-II/CT system (courtesy MILabs)

1.1.3 Small animal SPECT

Like many other imaging modalities such as CT, MRI, ultrasound and optical imaging[36,37], SPECT and PET are also applied to image small laboratory animals like mice and rats[38]. Small animal SPECT -as well as PET- facilitates *in vivo* quantitative assessments of molecular mechanisms and the development of new pharmaceuticals and diagnostic tracers[39,40]. The small size of mice and rats requires special collimation techniques different from those used in the clinic. While clinical SPECT uses parallel hole collimators which transmit only those photons that fall approximately perpendicular on them (figure 1.3, left), preclinical SPECT achieves high resolution by the use of pinhole collimation[41,42 ,43,44,45].

The principle is illustrated in figure 1.3, right; pinholes allow for magnification of the imaged object onto the gamma detectors and as a result the spatial resolution of the scanner can be much better than that of the gamma detector.

In recent years, many multi-pinhole high resolution SPECT systems have been developed[46,47,48]; some with resolutions below half a millimetre[49,50]. These high image resolutions are obtained with conventional gamma cameras (Anger Camera[51], described below) with a spatial resolution of 3 to 4 mm. A SPECT image of holmium in a kidney tumour (colour) obtained in

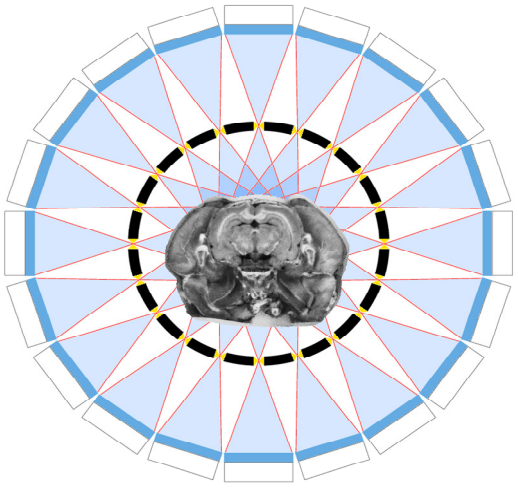

Figure 1.5: Design of multi-pinhole SPECT scanner with a small animal surrounded by a ring of pinholes and on the outside a ring of high resolution detectors.[55]

this way is shown in Fig 1.4. In this case anatomical information is provided by an X-ray CT scanner integrated with the SPECT system.

For small animal SPECT there is a large desire to improve the spatial resolution of the gamma detectors[52]. Recent theoretical analysis of pinhole SPECT scanners shows that when using very high resolution detectors a significant improvement in scanner performance is expected, while at the same time much more compact systems are possible because a high magnification factor is no longer required[53,54].

A possible design of such a high resolution scanner containing many pinhole gamma cameras is shown in figure 1.5.

1.2 Gamma detectors for SPECT

A gamma detector converts a gamma photon into a useful electrical signal that provides information on the gamma photon interaction position and its energy.

For gamma detectors in pinhole SPECT, three important figures of merit are the spatial resolution, energy resolution and detection efficiency[52]. A high spatial resolution allows for either a high image resolution or a more compact scanner. The energy resolution is important to discern scattered gamma photons from direct gamma photons. Finally, a high detection efficiency allows for shorter measurement times or a reduced dose of radioactive tracer.

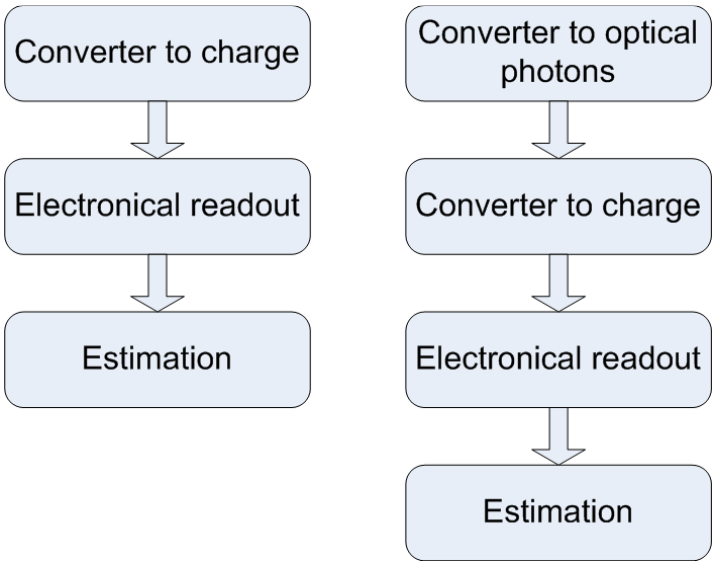

Direct conversion detection **Indirect conversion scintillation detection**

Figure 1.6: Block diagram depicting the different components of a direct conversion and indirect conversion (scintillation) detectors.

Gamma detectors can be divided into two classes; direct conversion and indirect conversion detectors[52]. The building blocks of both types of detectors are displayed in figure 1.6. In the case of direct conversion, the detector contains a material that directly converts the gamma photon energy into charge. Most prominent examples of direct conversion detectors are semiconductor gamma detectors; these are essentially photodiodes of sufficient thickness to efficiently absorb gammas[56,57]. These detectors can be made of Germanium[58], Cadmium Zinc Telluride (CZT)[59,60,61], Cadmium Telluride (CT) or Mercuric Iodide (HgI)[62] and are used in SPECT scanners[63,64,65,66]. The advantages of semiconductor diode detectors, compared to traditional Anger camera detectors, are that they have a better spatial and energy resolution.[52] However, they usually have a lower detection efficiency and for some materials manufacturing problems exist[52]. In

gas filled detectors, gamma photons interact with the gas and create ionizations, which are subsequently detected. A well know gas detector and the first detector used in nuclear medicine is the Geiger Muller tube[67,68], which gives off a maximal signal when either one or many photons interact with the gas. Other gas detectors such as multi wire proportional counters (MWPC) are used for X-ray and gamma detection[69,70,71,72] and PET imaging[73,74], despite poor energy resolution and low detection efficiency. Bolometers, that detect the absorption of (an) incident photon(s) by measuring the corresponding temperature increase[75,76], were improved significantly with the use of superconductive thermometers[77,78]. Arrays of these detectors can be used as gamma imagers with an excellent energy resolution, although they require cryogenic cooling[79].

In contrast, indirect conversion detectors do not directly convert the gamma energy into electrical charge but use an intermediate process. The most widely applied indirect conversion detectors are scintillator detectors, where the scintillator converts the gamma energy into optical photons. These optical photons are then converted to charge by a photo sensor. For both types of detectors, the charge is read out through an electronic system and the electrical signal is used to estimate the gamma photon's energy and interaction position. This thesis focuses on scintillation detectors, the most common detector type in nuclear medicine. The performance of a scintillation gamma detector depends on the scintillator used, the type of photo sensor, the electronical readout as well as the detection algorithm that estimates the position and energy of the scintillation. These elements are described in more detail below.

1.2.1 Scintillators

The scintillator converts the energy of the incoming gamma photons into light[72]. The emitted light due to an individual particle or photon is usually called a scintillation. The first scintillator for detection of photons was used in the discovery of X-rays by Röntgen[1]. Nowadays the most commonly used scintillator for gamma photon detection is NaI[80] which allows for large area scintillators to be used (typically 60 × 40 cm). Besides NaI, many other scintillators are available and some of them are used in medical imaging[81].

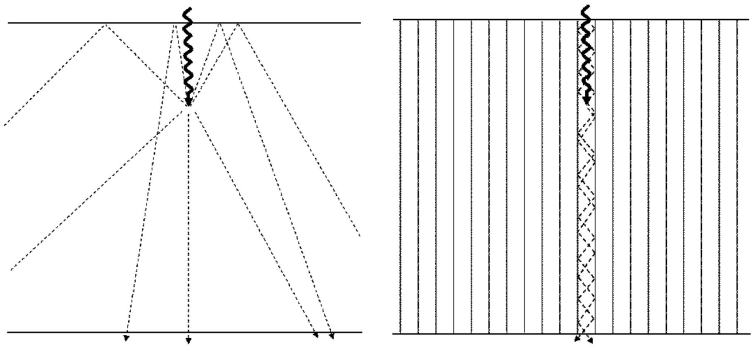

(a) **(b)**

Figure 1.7: Diagram of a gamma photon that interacts and creates optical photons (dashed) in **(a)** a continuous scintillator where light spreads out and **(b)** a pixellated scintillator where light is focused (e.g. to a pixel of a sensor).[82]

Scintillators can be used as continuous crystals or they can be subdivided in smaller pixels to restrict light spread (shown in figure 1.7). With continuous scintillators more light can reach the photo sensor, albeit spread over a larger area, whereas pixellated scintillators focus the light in a smaller area at the cost of light loss due to absorption at the interfaces.

1.2.2 Photo sensors

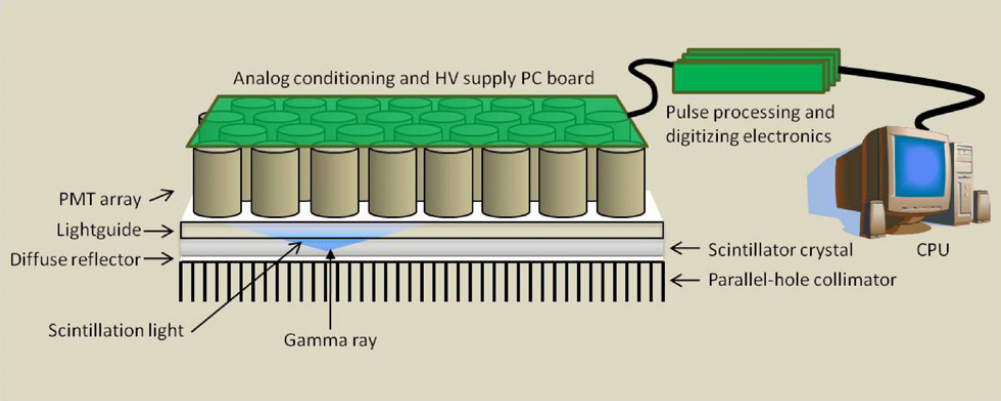

Figure. 1.8: Anger camera, consisting of a parallel hole collimator in front of a NaI scintillator read out with an array of PMTs (courtesy [49]).

1.2.2.1 Photomultiplier tubes The photo multiplier tube (PMT), developed early in the 20th century[83], contains a photocathode where the photon, by means of the photo electric effect, generates an electron. This single electron signal is amplified by accelerating it over a large voltage. Thus, the output signal of a PMT is a measure for the amount of light falling onto it. PMTs were combined with scintillators in nuclear detectors[84,85,86], but the first real gamma camera, consisting of a NaI scintillator coupled to an array of PMTs was developed by Anger[51,87] (figure 1.8). The invention of this gamma camera allowed the advent of SPECT imaging and the Anger camera still sets the standard in SPECT. Although the Anger camera is an established technology, research to improve its design and estimation process is ongoing[88,89,90]. Besides solid scintillators coupled to PMTs also liquid Xenon (LXe) can be used for gamma detection[91,92,93].

Position sensitive PMTs (PSPMT) were devised in 1985 by Hamamatsu[94]. In contrast to traditional PMTs which measure the amount of light, these can also provide position information due to a division of the PMT anode into multiple parts and are used in gamma camera prototypes[95,96,97,98,99,100].

(PS)PMTs have low noise but have a mediocre quantum efficiency (QE). PMTs have detector elements that are rather large (which is not beneficial for the spatial resolution) while those of PSPMTs are smaller.

1.2.2.2 Semiconductor photo sensors Different semiconductor sensors have been used for scintillation detection. In many studies, photodiodes[56] have been used in gamma detectors[101,102,103], but the achievable signal to noise ratio is limited[52].

Silicon drift detectors (SDD) are a special kind of photodiode with improved noise properties[104,105,52]; arrays of these detectors[106] have been used in scintillation gamma detection[107].

Avalanche photo diodes (APDs) use a large amplification of the signal, due to a high bias voltage, resulting in a more favourable signal to noise ratio compared to photodiodes[56] and were used for gamma detection[108]. Position sensitive APDs[109] (PSAPDs), which are read out at the corners, have also been applied in scintillation gamma detectors[110,111,112,113,114].

Finally, a type of semiconductor photo sensor that has recently become popular, the Silicon photon multiplier (SiPM), consists of a very large array of small avalanche photo diodes in Geiger mode. These diodes are biased at such a large voltage that each diode give off the maximum signal when one or more optical photons are absorbed, similar to a Geiger Muller tube[115,116,117]. When the total number of photons incident on the SiPM is small compared to the number of diodes, the summed output is proportional to the number of photons[118]. Given the good timing resolution of these devices they are mainly investigated for use in PET[119], but they can also be of value in SPECT gamma cameras[120,121]. SiPMs have low noise but mediocre QE and up to now medium sized detector elements.

1.2.2.3 (EM-)CCDs Charge coupled devices (CCDs) were devised in 1969 at AT&T Bell labs by W. Boyle and G. Smith who received the 2009 Nobel Prize for this invention that is now in use in thousands of applications, ranging from scientific, military and medical applications to many consumer products like cameras integrated in cell phones and video systems. A CCD consists of an area with capacitors which allow charge to be shifted between them. When photons are absorbed in the image area of a CCD, electron hole pairs are generated. These charges are shifted to a readout capacitance where they are converted to a voltage[122].

Because of their small pixel size and high quantum efficiency for optical photons, CCDs are popular imaging sensors and have been used as gamma detectors when coated with a scintillator[123]. Normal CCDs often can only detect the sum signal of a large number of scintillations, but detection of individual scintillations is hindered by the high read-out noise. A method to reduce this noise is to use an intensified CCD (ICCD), where an image intensifier amplifies the signal before it arrives at the CCD[124].
Alternatively, the new Electron Multiplying CCD (EM-CCD)[125,126,127] reduces this noise by using electron multiplication[128] to amplify the signal in the CCD. EM-CCDs are used in astronomy[129,130,131], spectroscopy[132,133] and biological imaging techniques[134,135]. They have been used as the photo sensor in beta probes[136] and high resolution gamma cameras[137,138] in combination with pixellated scintillators[139,140]. In these set-ups they allow for individual scintillation detection[82] and significantly enhance performance compared to CCDs.
EM-CCDs have high QE and a very small pixel size, allowing high resolution imaging. In this thesis a gamma detector set-up based on an EM-CCD (figure 1.9) is investigated.

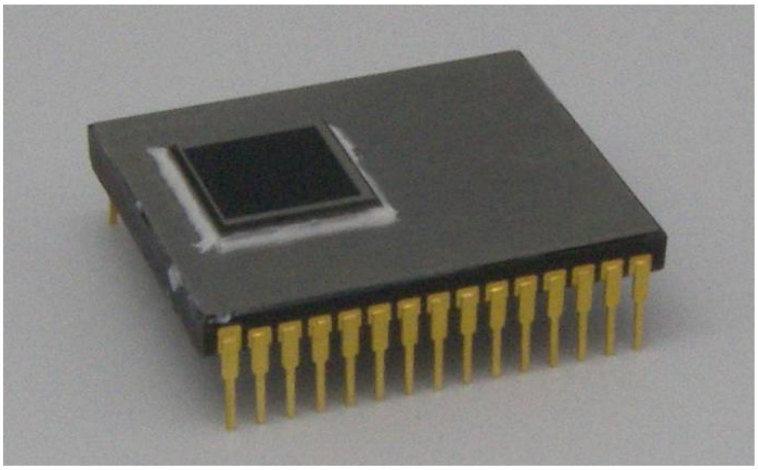

Figure 1.9: E2V CCD97, the EM-CCD used in the experimental set-up investigated in this thesis.

1.2.3. Estimation

Finally, the electrical signal produced by the photo sensor has to be analysed to estimate the gamma energy and the interaction position. Besides estimating the gamma energy and interaction position, one may also wish to estimate the depth-of-interaction (DOI). This is of special importance for gamma photons that enter the scintillator at an angle, which is common in pinhole gamma cameras. In this case, gamma photons that interact at variable depths in the scintillator are detected at different positions introducing position uncertainty for these photons (DOI-effect, illustrated in figure 1.10).

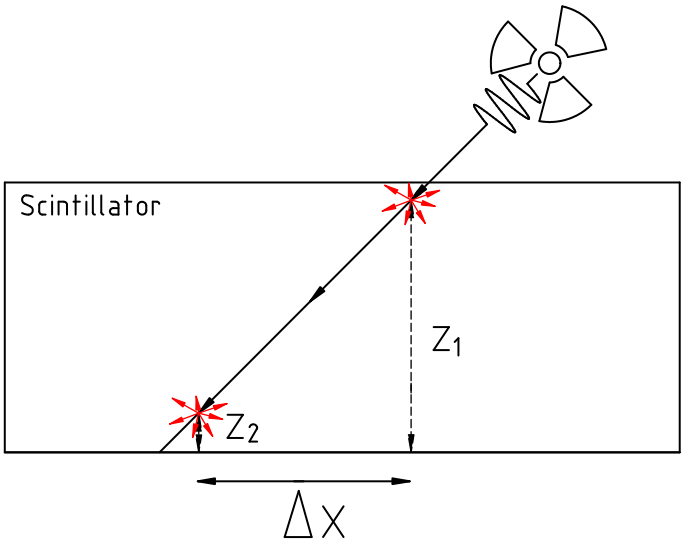

Figure 1.10: Depth-of-interaction (DOI) effect for gamma photons at an angle. The gamma photons can interact at variable depths (e.g. depth z_1 or z_2) resulting in a position uncertainty Δx, degrading the spatial resolution.

The algorithm used for scintillation detection in the Anger Camera is a centre of gravity method, called Anger Logic[51], sometimes combined with DOI detection[98]. Statistical estimation methods have, partially due to increasing computing power, become more popular recently. The most widely used method is the maximum-likelihood method[141,142], although other methods such as the nearest neighbour method[143] are also used.

1.2.4. High resolution gamma detectors

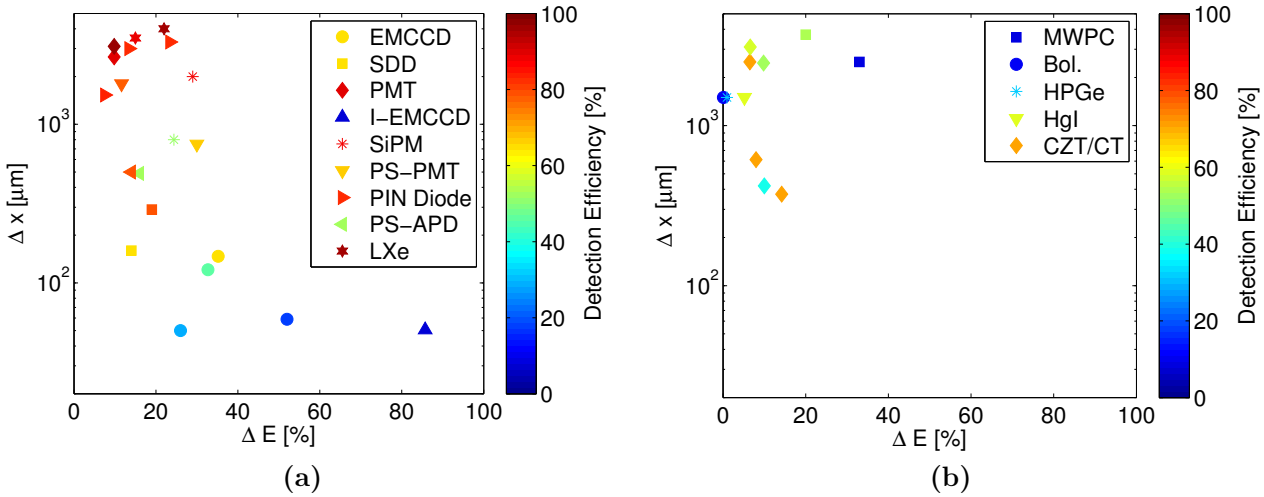

Figure 1.11: The spatial (y axis) and energy (x-axis) resolution for (a) different scintillation detectors: EM-CCD[144,145,146] (chapter 2 and 3), SDD[106,107], PMT[147], I-EMCCD[148], SiPM[120,121], PS-PMT[97,149], PIN Diode[102,103,150], PS-APD[112,114] and LXe[91,92,93]. and (b) different non scintillation detectors: MWPC[69,70,71], Bolometer[151], HPGe[58], HgI[62], and CZT/CT[59,60,61,66] as a function of the detection efficiency. The colour of the markers is a measure for the gamma detection efficiency.

A large number of gamma detectors, suitable for gamma imaging, have been reported in literature. Figure 1.11 shows a rough comparison of spatial resolution, energy resolution and efficiency of many of these detectors (references are provided in the caption). The values provided in the figure are for detecting the most common SPECT isotope ^{99m}Tc (141 keV gamma photon energy) or isotopes of similar energy. The comparison shows that EM-CCD based scintillation detectors exhibit the highest spatial resolution albeit often at poorer energy resolution compared to the other gamma detectors.

1.6 Thesis Outline

In this thesis, several ways to improve the performance of an EM-CCD-based high resolution scintillation gamma camera for SPECT are presented. First, different approaches for estimating the gamma photon's scintillation position and energy from the electrical output signal of the EM-CCD are investigated. In **chapter 2** we present a fast analytical algorithm that uses a multi-scale approach to estimate the energy and position -including the depth- of the scintillation. We show that the multi-scale algorithm can improve the performance of the gamma camera significantly over an algorithm that ignores the depth-dependence of the scintillation. **Chapter 3** describes a statistical detection algorithm that does not only incorporate a depth-dependent light spread model but also takes the statistical nature of the EM-CCDs response into account. The statistical maximum-likelihood estimation method used improves the accuracy of the energy estimate compared to the previous analytical approach.

In **chapter 4** we present a specially shaped scintillator combined with a new designed optical collimation. This special geometry allows to eliminate the deterioration of the spatial resolution due to the Depth-of-Interaction effect.

Both the properties of the scintillator and the EM-CCD parameters determine the performance of the gamma camera. In **chapter 5** we investigate experimentally how the use of different scintillator materials with different densities and light outputs influences spatial resolution, energy resolution and signal-to-background ratio. In addition, **chapter 6** reports on how the different EM-CCD parameters (e.g. noise) affect spatial and energy resolution of the gamma camera. For this we use a theoretical Cramer Rao lower bound approach, which is validated by experiments.

Chapter 7 investigates if improved collection of optical photons in the scintillator by means of a retro reflector that is placed on top of the scintillator improves the performance. In **chapter 8** we study the effect of a different readout approach to the EM-CCD based on combining the charge in adjacent pixels (so called binning) on the gamma camera performance.

Finally, the last two chapters of this thesis focus on a hybrid gamma detector that we constructed and that combines two types of sensors, the EM-CCD (below the scintillator) and SiPMs (attached to the sides of the scintillator.) In **chapter 9** we use a summed signal of the SiPMs to provide a priori knowledge on the number of scintillations detected in an EM-CCD frame and we investigate the effect of this on the signal-to-background ratio. A more advanced use of the SiPM signals is presented in **chapter 10** where we investigate the

use of different scintillation detection methods for our combined EM-CCD and SiPM gamma camera. Due to individual SiPM pixel readout we can also include position information from the SiPMs in the gamma detection algorithm.

Chapter 2

Multi-scale algorithm for improved scintillation detection in a CCD based gamma camera

Marc A N Korevaar[1,2], Jan W T Heemskerk[1,2], Marlies C Goorden[1,2], and Freek J Beekman[1,2,3]

[1] Department of Nuclear Medicine, Image Sciences Institute, University Medical Center Utrecht, Heidelberglaan 100, 3584 CG, Utrecht, the Netherlands
[2] Section of Radiation Detection and Matter, Department of R[3], Applied Sciences, Delft University of Technology, Mekelweg 15, 2629 JB, Delft, The Netherlands
[3] Molecular Imaging Labs (MILabs), Universiteitsweg 100, 3584 CG, Utrecht, the Netherlands

Phys. Med. Biol., 54, 4, pp.831-842, 2009

Abstract

Gamma cameras based on Charge Coupled Devices (CCDs) and micro-columnar CsI:Tl scintillators can reach high spatial resolutions. However, the gamma interaction probability of these scintillators is low (typically <30% at 141 keV) due to the limited thickness of presently available micro-columnar scintillators. Continuous scintillators can improve the interaction probability but suffer from increased light spread compared to columnar scintillators. In addition, for both types of scintillators gamma photons incident at an oblique angle reduce the spatial resolution due to the variable depth-of-interaction (DOI). To improve spatial resolution and spectral characteristics of these detectors, we have developed a fast analytic scintillation detection algorithm that makes use of a depth-dependent light spread model and as a result is able to estimate the DOI in the scintillator. This algorithm, performing multi-scale frame analysis, was tested for an Electron Multiplying CCD (EM-CCD) optically coupled to CsI:Tl scintillators of different thicknesses.

For the thickest scintillator (2.6 mm) a spatial resolution of 148 μm Full Width Half Maximum (FWHM) was obtained with an energy resolution of 46% FWHM for perpendicularly incident gamma photons (interaction probability 61% at 141 keV). The multi-scale algorithm improves the spatial resolution up to 11 %, the energy resolution up to 36 % and the Signal to Background counts ratio up to 46% compared to a previously implemented algorithm that did not model the depth-dependent light spread. In addition, the multi-scale algorithm can accurately estimate DOI. As a result, degradation of the spatial resolution due to the variable DOI for gamma photons incident at a 45 degree angle was improved from 2000 μm to 448 μm FWHM. We conclude that the multi-scale algorithm significantly improves CCD based gamma cameras as can be applied in future SPECT systems.

2.1. Introduction

Today, small animal Single Photon Emission Tomography (SPECT) pinhole imaging[44,45] can yield excellent image resolutions[46,47,151] down to the sub-half-mm scale[49,50]. At present these ultra-high resolutions are obtained using traditional gamma cameras, by employing the principle of pinhole magnification. For future improvements of small animal SPECT imaging, gamma cameras with better spatial resolution and significant energy discrimination are essential[54,153,154,155]. Compact, high-resolution gamma cameras using EM-CCDs in combination with micro-columnar CsI:Tl scintillators[139] are being developed by many research groups[137,138,140,146,165]. In such CCD-based detectors individual scintillation events can be detected in "photon counting" mode, enabled by readout at high frame rates. This detection method greatly improves the spatial resolution compared to integration of scintillation light signal[82]. However, the presently applied micro-columnar scintillators suffer from low interaction probability for gamma photons (< 30% at 141 keV) due to the limited thickness of commercially available scintillators (typically < 1mm).
A solution to the latter problem is the use of continuous scintillators, which are available in larger thicknesses and are also more cost effective. Furthermore continuous scintillators can be obtained for scintillator materials with higher atomic number Z and density than CsI:Tl, offering potential for a further improvement in sensitivity. However these scintillators have increased scintillation light spread and increased dependence of the light spread on the

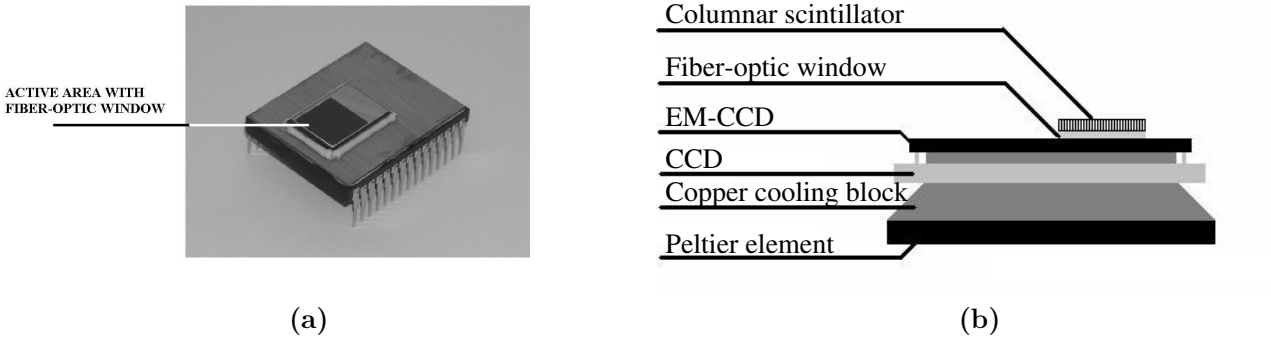

Figure 2.1: (a) EM-CCD with fiber-optic window. **(b)** Schematic of the gamma camera consisting of a continuous scintillator optically coupled through a fiber optic window to the EM-CCD, cooled by a Peltier element.

depth-of-interaction (DOI). This severely complicates accurate scintillation detection.
Gamma cameras equipped with both columnar and continuous scintillators suffer from degradation of spatial resolution due to the variable DOI for gamma photons incident at an oblique angle (figure 2.2(a)). Elsewhere a statistical scintillation detection algorithm, that uses information of the depth-dependent light spread, is applied to an EM-CCD based gamma camera with a micro-columnar scintillator[165]. However, long computation times of statistical algorithms can be prohibitive in many applications. To overcome this problem, a fast analytical scintillation detection algorithm, employing an analytical model for the depth-dependent light spread, is presented and applied to a gamma camera with continuous scintillators. This analytical multi-scale algorithm (MSA) enables an accurate estimate of the DOI and is compared with a previously proposed detection algorithm based on a simple

Gaussian filter (GFA)[138]. The spatial resolution, energy resolution and the signal to background counts ratio (SBR) are evaluated for both algorithms using CsI:Tl continuous scintillators of different thicknesses.

2.2. Methods

2.2.1 EM-CCD, optical coupling and scintillator

An electron multiplying CCD (EM-CCD) is a CCD with an internal gain in the charge domain (before read-out). Because of the internal gain the relative contribution of the read-out noise is reduced significantly, even at high frame rates. The internal gain is achieved by electron multiplication (avalanche multiplication or impact ionization) in the gain register. Details of the EM-CCD technology can be found in literature[126,127,166,167]. The EM-CCD used is the back-illuminated CCD 97 from E2V Technologies (Figure 2.1 (a)), with 512×512 active pixels, an active area of 8.192×8.192 mm^2 (16×16 μm^2 pixel size), and a Quantum Efficiency above 90% for light in the range of 500 to 650 nm. In order to exchange scintillators easily the EM-CCD is equipped with a 3 mm straight fiber-optic window. Shown in figure 2.1 (b) is a schematic of the gamma camera. To suppress the thermal dark current noise the EM-CCD is cooled to -40 ℃ using a Peltier element. The hot side of the Peltier is cooled using a RS44LT cooler purchased from FTS Systems. The cold side of the Peltier element is connected to a copper block, which is in thermal contact with the EM-CCD. For conversion of gamma photons into visible light continuous CsI:Tl scintillators from SCIONIX with a Tl concentration of 0.11 ± 0.01 mole percent are used. The detector face of the scintillators is polished using Buehler Micropolish II powder of 1 micron particle size. The top and sides of the scintillators were not treated.

The scintillators are optically coupled to the fiber optic window using Bicron BC-630 silicon optical grease. Due to the critical angle of the fiber optic window and the scintillator – window interface, there is a limited acceptance angle for light on the EM-CCD. The CsI:Tl scintillators tested have approximately the same area as the EM-CCD active area, the 600 μm thick scintillator area is 8.9 × 10 mm^2 and the 1.3 and 2.6 mm thick scintillator size is 9.2 × 10 mm^2. The scintillator thicknesses are 600 μm, 1.3 mm and 2.6 mm, resulting in an interaction probability for 141 keV gamma photons of 19%, 37% and 61% respectively.

2.2.2 Depth-of-interaction

A lack of knowledge about the depth (z-coordinate) within the scintillator at which a scintillation event has occurred (depth-of-interaction or DOI) causes serious degradation of the detector performance. In pinhole gamma cameras photons can enter the scintillator at an oblique angle causing the detected image to be blurred due to the varying DOI in the scintillator (figure 2.2 (a)). This effect in pinhole gamma cameras is called the "DOI effect"[168]. This DOI effect will limit the spatial resolution in EM-CCD pinhole cameras, given

the scintillator thicknesses required for sufficient interaction probability and the currently attained spatial resolutions.

Apart from the degrading effect on the spatial resolution, the varying DOI can also affect the energy resolution. The scintillation light spread on the EM-CCD depends on the DOI; events further away from the EM-CCD result in a wider light distribution than events occurring closer (figure 2.2 (b)). Therefore, the amplitude of the light spot on the EM-CCD does not provide the full information on the energy of the gamma photon; one must also consider the depth-dependent width of the light distribution. Disregarding the depth-dependence will degrade the energy resolution.

A detection algorithm that can detect the DOI and considers the depth-dependent width can improve spatial resolution and energy resolution of a gamma camera and is necessary for high-resolution gamma cameras with sufficient sensitivity.

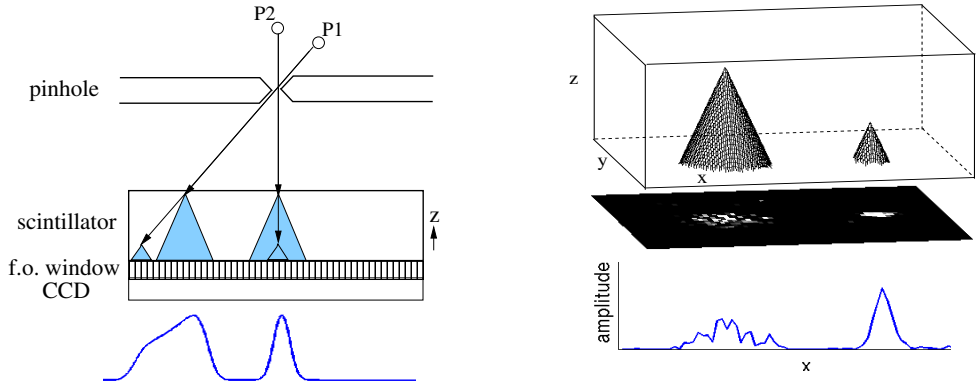

(a) **(b)**

Figure 2.2: **(a)** Diagram of a single pinhole gamma camera with point sources P1 and P2. The gamma photons interact at different depths resulting in a degradation of the spatial resolution (bottom) for photons incident at an oblique angle (DOI effect). Scintillation photons are incident on the entire fiber optic (f.o.) window, however the limited acceptance angle reduces the number of scintillation photons reaching the EM-CCD, resulting in a cone of acceptance. **(b)** Top: a scintillator with a scintillation with a large light spread (σ_{DOI}) (left) and a small σ_{DOI} (right). Shown are the cones of scintillation light reaching the EM-CCD. Middle: an EM-CCD frame corresponding to the two scintillations. Bottom: a profile of the frame, illustrating that the total number of photons (the integrated signal of the scintillation) is independent of σ_{DOI} (or interaction depth).

2.2.3 Scintillation detection algorithms

2.2.3.1 Gaussian filter algorithm The GFA is a fast scintillation detection algorithm that can be used for real-time frame analysis[138]. The CCD frame image I_{CCD} is corrected for the average dark background by subtracting the average background image A (additionally a threshold can be applied to I_{CCD}),

$$I_{bg.corr.} = I_{CCD} - A. \tag{2.1}$$

The corrected image ($I_{bg.corr}$) is then blurred with a 2-D Gaussian kernel ($g(x,y,\sigma)$) with fixed width σ resulting in a smoothed image

$$I_{smoothed} = I_{bg.corr.} * g(x,y,\sigma), \tag{2.2}$$

where * denotes a 2-D convolution. To increase speed, this convolution can be implemented as two orthogonal one-dimensional Gaussian convolutions, mathematically identical to a single 2-D convolution because of the separability of the Gaussian convolution operation. In this filtered image ($I_{smoothed}$) the scintillations appear as bright regions. Local maxima with amplitudes above a threshold are attributed to scintillation flashes and their amplitude and position (x,y) are recorded. The GFA does not estimate the DOI or z-coordinate of the scintillation and the spatial profile is not corrected for the DOI effect. It is assumed that the energy is proportional to the amplitude, ignoring the depth-dependent light spread.
The width σ of $g(x,y,\sigma)$ influences the GFA performance[146]. In this paper, the σ of the GFA has been optimized in order to obtain the best possible spatial resolution for each scintillation crystal.

2.2.3.2 Multi-scale algorithm The new scintillation detection algorithm presented in this paper, the multi-scale algorithm (MSA), is partly inspired by work in computer vision[169,170]. The MSA acts as a matched filter that takes the depth-dependent light spread in the continuous scintillator into account and can therefore accurately estimate the depth-of-interaction (DOI).
A single scintillation event will result in a light distribution $I(x,y,\sigma_{DOI})$ on the EM-CCD with a width σ_{DOI} that depends on the DOI (figure 2.2 (b)). The essential step in the MSA is the application of a convolution with a *set* of Gaussian kernels $g(x,y;\sigma)$ of increasing width (standard deviation σ) and a subsequent multiplication by the respective standard deviation σ. This results in the representation of the EM-CCD frame in multiple slices (see figure 2.3 (a)), each slice being characterized by σ. Scintillation events present in the acquired frame will have a distribution function $P(x,y;\sigma)=I(x,y,\sigma_{DOI})*g(x,y;\sigma)\cdot\sigma$ after the convolution step. The global maximum of $P(x,y;\sigma)$ is in the slice where the width of the Gaussian kernel matches the width of the light distribution on the EM-CCD, i.e. for $\sigma=\sigma_{DOI}$. Thus σ_{DOI} can be estimated by searching each slice for local maxima and selecting the slice with the global maximum. Once σ_{DOI} is determined, the energy and z-coordinate of the scintillation are estimated.

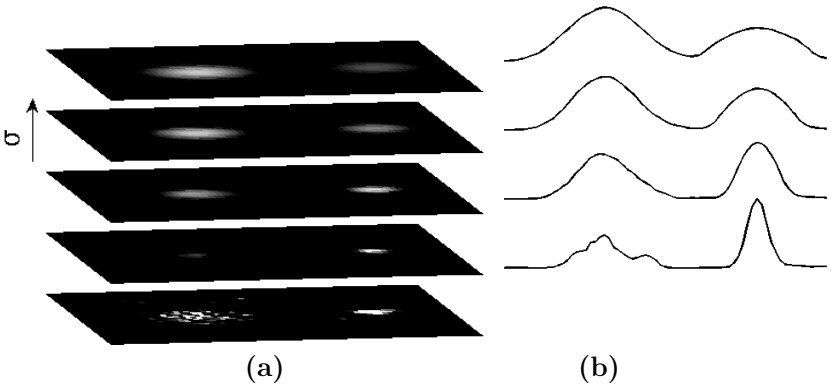

Figure 2.3: (a) Four slices of a multi-scale representation of the EM-CCD frame of figure 2.2(b) (bottom slice), representing 2 scintillations at different depths. The slices are calculated by convolution of the EM-CCD frame with a Gaussian and multiplication by σ. **(b)** Profiles of the multi-scale representation slices. The global maximum of each scintillation in the multi-scale representation (bottom slice for right scintillation, top slice for left scintillation) is found for $\sigma=\sigma_{DOI}$.

To relate the energy to σ_{DOI} we have to assume a specific light distribution function on the EM-CCD for a single scintillation event. Here it is assumed that all the energy of the gamma photon is deposited at a single interaction position. This assumption is substantiated by the high photoelectric absorption in CsI:Tl (at 141 keV this amounts to 87% of all inelastic photon interactions)[171] and the short average range and small energy of fluorescent X-rays (0.1mm and 35keV respectively)[172]. Assuming an isotropic light spread and neglecting optical photon interactions in the scintillator and with the scintillator surface the light spread can be approximated by a Gaussian,

$$I(x,y,\sigma_{DOI}) = \frac{\varepsilon E}{2\pi\sigma_{DOI}^2} e^{-\left(\frac{x^2+y^2}{2\sigma_{DOI}^2}\right)}, \tag{2.3}$$

where E is the energy of the scintillation, is an efficiency factor and the interaction position is at (x,y)=(0,0). The total number of photons on the CCD is proportional to the energy and does not depend on the DOI (illustrated in figure 2.2 (b)), in contrast to the width of the distribution. An explicit evaluation of the convolution results in

$$P(x,y;\sigma) = \frac{\varepsilon E\sigma}{2\pi\left(\sigma_{DOI}^2+\sigma^2\right)} exp\left(-\frac{\left(x^2+y^2\right)}{2\left(\sigma_{DOI}^2+\sigma^2\right)}\right). \tag{2.4}$$

The maximum in the slice characterized by σ is given by $P(x=0,y=0;\sigma)=\varepsilon E\sigma/2\pi(\sigma^2_{DOI}+\sigma^2)$. The global maximum (the largest of these maxima) occurs when the width of the Gaussian kernel and the light spread function match, i.e. for $\sigma=\sigma_{DOI}$. The energy is related to the maximum of $P(x,y;\sigma)$ by

$$E = \frac{4\pi}{\varepsilon}\sigma Max[P(x,y;\sigma)]. \tag{2.5}$$

The z-coordinate of the scintillation can be related to σ_{DOI} with an analytical light spread model or by using experimental data. We have chosen to determine the relation between σ_{DOI} and z by using calibration data of gamma photons incident at a known angle onto the scintillator surface. The calibrated relation between σ_{DOI} and z is used to determine z from the estimated σ_{DOI}. During a measurement the position (x,y,z) and the energy are recorded for every scintillation flash. The knowledge of the z-coordinate is used to correct the two-dimensional spatial profile for the DOI effect.

Depending on the desired accuracy and speed the number of slices can be varied. The range of σ depends on the scintillator thickness and has to be such that also scintillations at the top of the scintillator (having the largest light spread σ_{DOI}) can be detected. To increase speed, the convolutions are implemented as two orthogonal one-dimensional Gaussian convolutions, and the Gaussian kernels are truncated at 2σ.

2.2.4 Measurements

As a measure of performance of the MSA, its spatial resolution, energy resolution and signal to background ratio are compared with the values obtained by the GFA for CsI:Tl scintillators 0.6, 1.3 and 2.6 mm in thickness. The number of slices used in the MSA to

analyze these measurements is 10. To determine the spatial resolution a line pattern from a Tc-99m source (141 keV), projecting through a slit onto the scintillator, is acquired (figure 2.4 (b)). The spatial resolution is defined as the Full Width Half Maximum (FWHM) of the line spread function of the radioactive source, corrected for the width of the gamma photon beam. In our experiments we have investigated both perpendicular incidence (figure 2.4 (a)) and incidence at an angle of 45 ° (figure 2.5). The FWHM energy resolution is obtained by determining the full width at half maximum of the Tc-99m photopeak.

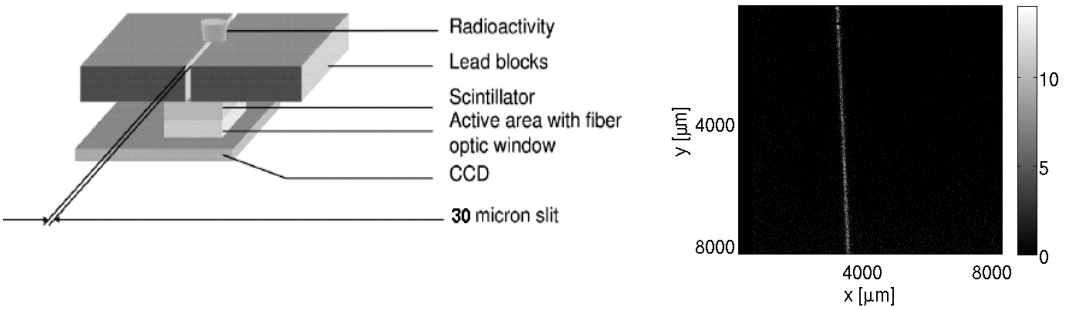

(a) **(b)**

Figure 2.4: (a) Measurement setup for acquiring line pattern images. **(b)** Image acquired using the GFA of the line pattern of a radioactive Tc-99m source through a 30 µm slit for the 600 µm CsI:Tl scintillator.

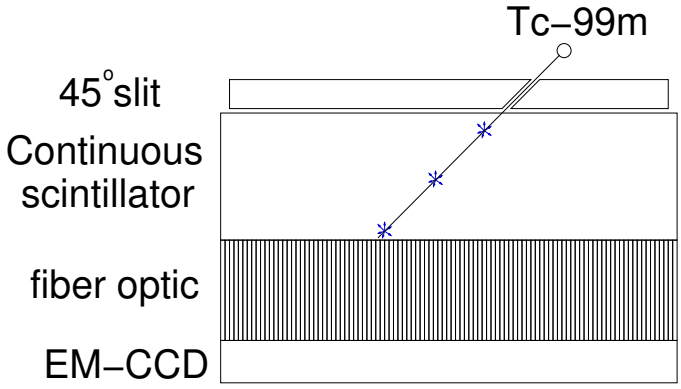

Figure 2.5: Measurement setup with the 45 ° slit

The Signal to Background Ratio (SBR) is defined as the ratio of the number of net signal counts in an irradiated area of the EM-CCD to the number of noise-induced background counts in a non-irradiated area of the same size. The number of net signal counts is obtained by subtracting the number of background counts from the counts in an irradiated area of the same size.

Comparison of the spatial resolution and SBR of the two algorithms is always done for an equal number of net signal counts. This is accomplished by setting an energy window for the MSA and then tuning the detection threshold for the GFA .

2.3. Results

2.3.1 Sigma optimization for GFA

As mentioned in section 2.2.3.1, the width σ of the Gaussian kernel of the GFA is optimized in order to get the best possible GFA performance. The spatial resolutions for perpendicularly incident gamma photons at different widths σ are shown in figure 2.6 for the 2.6 mm thick scintillator. For the other thicknesses similar results were obtained. The width σ yielding the best spatial resolution is chosen as the optimal σ for the comparison with the MSA. This optimal σ increases with scintillator thickness.

2.3.2 Spatial resolution

A line pattern image of a Tc-99m source projected perpendicularly through the 30 µm slit and analyzed by the GFA is shown in figure 2.4 (b). For perpendicular incidence, no DOI-correction needs to be applied to the spatial profile. Nevertheless use of the MSA instead of the GFA still slightly improves the spatial resolution by 11%, 10% and 5% for scintillator thicknesses of 0.6 mm, 1.3 mm and 2.6 mm, respectively. We believe that this improvement is due to the better match between the kernel width σ used to detect the scintillation, and the light spread σ_{DOI}, which results in more γ photons being detected with a higher accuracy. The slight improvement in the spatial resolution of the line pattern profile for the 1.3 mm thick scintillator is shown in figure 2.7. All results are summarized in table 2.1. The FWHM spatial resolution for both algorithms deteriorates with scintillator thickness.

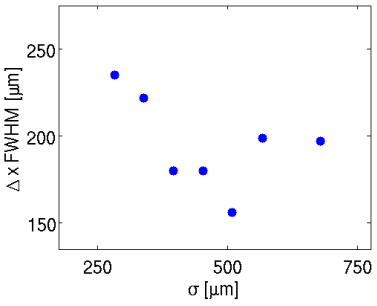

Figure 2.6: GFA FWHM spatial resolution along the x-direction for the 2.6 mm thick CsI:Tl scintillator for different widths σ of the Gaussian kernel.

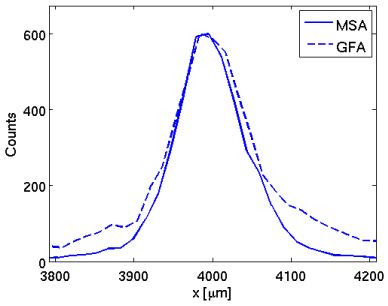

Figure 2.7: Profiles of the line pattern images for the GFA (dashed line) and MSA (solid line) for a 1.3 mm thick continuous CsI:Tl scintillator.

When the beam is incident at an oblique angle, an estimation of the z-coordinate is necessary to correct the spatial profile for the resolution degrading DOI effect. Figure 2.8 illustrates the capability of our algorithm to estimate the z-coordinate of the interaction for the 1.3 mm and 2.6 mm thick scintillators. Density plots are shown in figure 2.8 (a) (1.3 mm) and (c) (2.6 mm) with the gray scale representing the number of detected scintillation events as a function of x- and z-position, when the gamma photons of the Tc-99m source are incident under an angle of 45 ° . As expected, the scintillation events are distributed along a

line having a slope of approximately 45 ° with respect to the scintillator surface plane. Few scintillation events seem present at the top of the scintillator. This small discrepancy is most likely due to mechanical inaccuracies in the setup. The corresponding profiles obtained by the GFA and the MSA with DOI correction are shown in figure 2.8 (b) and (d) and the spatial resolution is listed in table 2.1. The MSA improves the DOI degraded spatial resolution by almost a factor of 5 (from 2.0 mm to 448 µm FWHM) for the 2.6 mm thick scintillator and by a factor of 3.3 (from 1.1 mm to 330 µm FWHM) for the 1.3 mm thick scintillator.

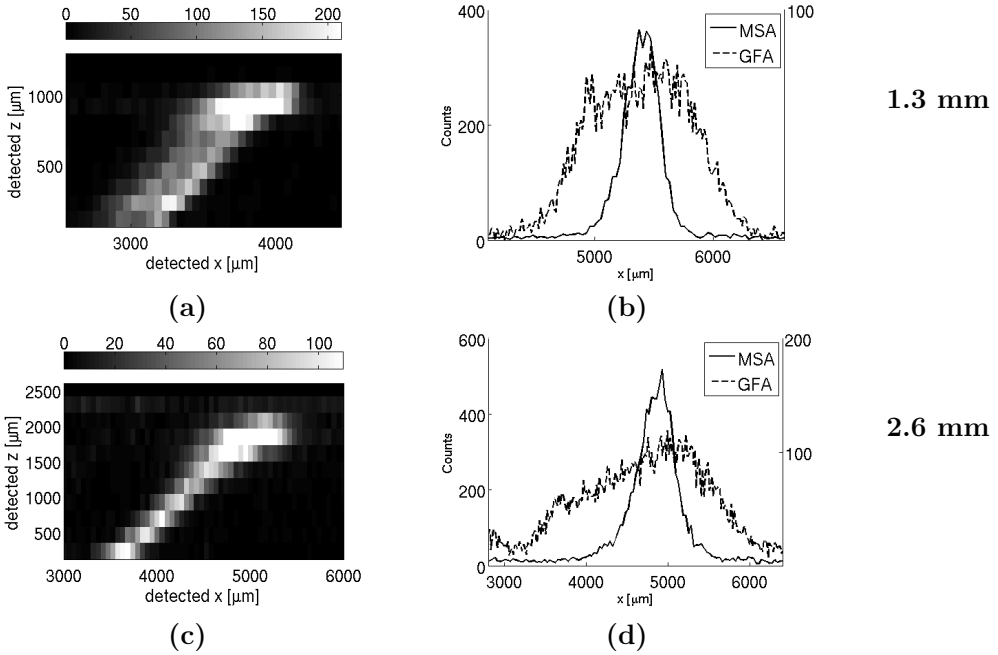

Figure 2.8: Density plots of the DOI, z, versus position x detected by the MSA are shown on the left. **Top:** 1.3 mm thick scintillator **bottom:** 2.6 mm thick scintillator. Image profiles for GFA (dashed line, left y-axis) and DOI-corrected MSA (solid line, right y-axis) are shown on the right.

2.3.3 Energy resolution and SBR

To investigate the capability of the MSA for improving the energy resolution we compare the energy spectra obtained with both algorithms for scintillator thicknesses of 0.6, 1.3 and 2.6 mm in figure 2.9. For all scintillator thicknesses the MSA outperforms the GFA. For the scintillator of 0.6 mm, the GFA does not even show a photopeak, whereas it is clearly visible when the MSA is used. For the 1.3 mm and 2.6 mm thick scintillators the photopeak acquired by the MSA is more narrow than the photopeak obtained by the GFA; respective improvements in FWHM energy resolution of 34% and 36% are obtained. Furthermore the MSA compared with the GFA results in an energy spectrum with significantly more counts present in the photopeak and less outside the photopeak. As already stated the results for the MSA were obtained for 10 slices (figure 2.3 (a)). The effect of the number of slices on the energy resolution in the MSA has also been investigated, and was found to be small.
Compared with the GFA, the MSA improves the SBR by 32%, 47% and 21% for scintillators of 0.6 mm, 1.3 mm and 2.6 mm respectively.

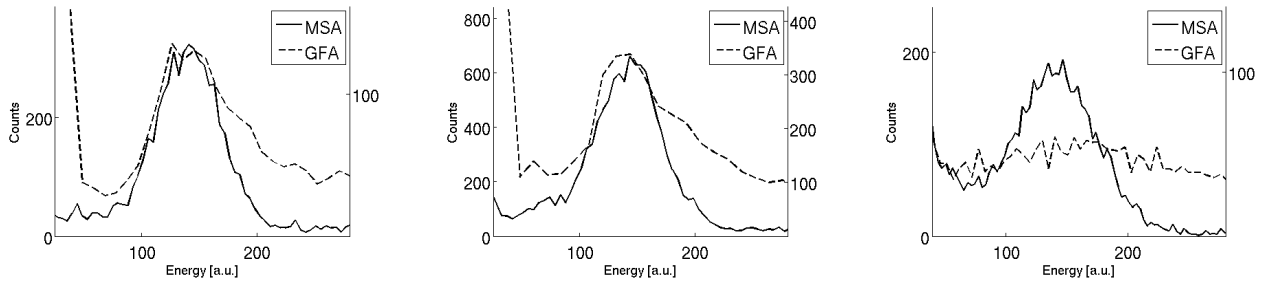

Figure 2.9: Energy spectra of a Tc-99m source for GFA (dotted line, right axis) and MSA (solid line, left axis) for scintillator thicknesses of 2.6mm (**a**), 1.3 mm (**b**) and 600 m (**c**).

Table 2.1: Spatial, energy resolution (FWHM) and SBR for the GFA and MSA

	Thickness	GFA	MSA	Improvement
Spatial resolution	0.6 [mm]	0.45 [mm]	201 [μm]	2.2 ×
(oblique angle)	1.3 [mm]	1.1 [mm]	330 [μm]	3.3 ×
	2.6 [mm]	2.0 [mm]	448 [μm]	4.5 ×
energy resolution	0.6 [mm]	n.a.	52 %	n.a.
	1.3 [mm]	70 %	46 %	34 %
	2.6 [mm]	75 %	48 %	36 %
SBR	0.6 [mm]	53	70	32 %
	1.3 [mm]	150	220	47 %
	2.6 [mm]	195	236	21 %
Spatial resolution	0.6 [mm]	66 [μm]	59 [μm]	11 %
(perpendicular)	1.3 [mm]	100 [μm]	90 [μm]	10 %
	2.6 [mm]	156 [μm]	148 [μm]	5 %

2.4. Discussion

In the present work we have shown that the use of a new analytical scintillation detection algorithm, the multi-scale algorithm, improves the spatial resolution, the energy spectrum and the SBR compared to the optimized Gaussian filter algorithm proposed previously[137]. The fast multi-scale algorithm uses information contained in the width of the light spread distribution, allowing an accurate estimation of the energy and a correction to the spatial profile for the DOI effect. The MSA is expected to be significantly faster than a statistical algorithm as this new algorithm does not require the calculation of many iterations.

In this work we have used a relatively simple model for light spread to facilitate fast blurring operations. More accurate modelling of the light spread function including effects such as inelastic scatter, fluorescent X-rays and reflections on the top and edges of the scintillator can further improve algorithm performance, possibly at the expense of computation time.

In this paper we did not focus on effects close to the edges of the camera. Like in almost any scintillation camera, the spatial resolution is expected to be less good at the edges and could be improved by more advanced modelling. Alternatively, a relative reduction of the number of event detections that suffer from edge effects can be achieved by choosing a larger active area of the gamma camera. A larger active area can be obtained using demagnifying optical

tapers[82] and larger CCDs, which are currently in development in our department.
We have investigated CsI:Tl scintillators of different thicknesses. For the thickest scintillator the improvement in spatial resolution at an oblique angle by the MSA compared with the GFA is most pronounced; an improvement of almost a factor of 5 is reached.
Using the MSA our gamma camera reaches a spatial resolution of 148 μm FWHM with an energy resolution of 46% FWHM for the 2.6 mm scintillator (interaction probability 61% at 141 keV). While the spatial resolution is much better than the spatial resolution of clinical gamma cameras (typically 3-4mm), the energy resolution is not yet as good. This is not so important for animal imaging as scatter rejection is often not required due to the lower scatter in animals compared to humans. However, we expect that the use of dense high light output scintillators that are currently under development in our group can improve the energy resolution as well as the spatial resolution and interaction probability.

2.5. Conclusions

In the present work we have developed a new analytical scintillation detection algorithm, the multi-scale algorithm, and compared it with the Gaussian filter algorithm[138]. The MSA improves the spatial resolution, the energy spectrum and the SBR compared to the optimized GFA. The multi-scale algorithm can accurately estimate the energy and correct the spatial profile for the DOI effect, improving the resolution up to almost a factor of 5.
The FWHM spatial resolution (both for gamma photons incident perpendicularly and at an oblique angle) obtained by both algorithms deteriorates with scintillator thickness, due to the increased light spread in thicker scintillators.
Statistical scintillation detection in EM-CCD cameras[165] may improve the detector performance further, however long computation times compared to analytical algorithms can be prohibitive in many applications. Besides new scintillators and statistical algorithms, further improvements in spatial resolution, energy resolution and SBR may be obtained by reduction of noise in the EM-CCD and read-out electronics.

2.6. Acknowledgements

We would like to thank Paul Schotanus of SCIONIX for providing us with CsI:Tl scintillators.

Chapter 3

Maximum-likelihood scintillation detection for EM-CCD based gamma cameras

Marc A N Korevaar[1,2], Marlies C Goorden[1,2], Jan W T Heemskerk[1,2] and Freek J Beekman[1,2,3]

[1]Section of Radiation Detection and Medical Imaging, Department of Radiation, Radionuclides and Reactors, Applied Sciences, Delft University of Technology, Mekelweg 15, 2629 JB Delft, the Netherlands

[2]Department of Nuclear Medicine, Image Sciences Institute, University Medical Center Utrecht, Heidelberglaan 100, 3584 CG, Utrecht, the Netherlands

[3]MILabs Molecular Imaging Laboratories, Universiteitsweg 100, 3584 CG, Utrecht, the Netherlands

Phys. Med. Biol., 56, pp.4785-4801, 2011.

Abstract

Gamma cameras based on charge-coupled devices (CCDs) coupled to continuous scintillation crystals can combine a good detection efficiency with high spatial resolutions with the aid of advanced scintillation detection algorithms. A previously developed analytical multi-scale algorithm (MSA) models the depth-dependent light distribution but does not take statistics into account. Here we present and validate a novel statistical maximum-likelihood algorithm (MLA) that combines a realistic light distribution model with an experimentally validated statistical model. The MLA was tested for an electron multiplying CCD (EM-CCD) optically coupled to CsI:Tl scintillators of different thicknesses. For ^{99m}Tc imaging, the spatial resolution (for perpendicular and oblique incidence), energy resolution and signal-to-background counts ratio (SBR) obtained with the MLA were compared with those of the MSA. Compared to the MSA, the MLA improves the energy resolution by more than a factor of 1.6 and the SBR is enhanced by more than a factor of 1.3. For oblique incidence (approximately 45°), the depth-of-interaction (DOI) corrected spatial resolution is improved by a factor of at least 1.1, while for perpendicular incidence the MLA resolution does not consistently differ significantly from the MSA result for all tested scintillator thicknesses. For the thickest scintillator (3 mm, interaction probability 66% at 141 keV) a spatial resolution (perpendicular incidence) of 147 μm full width at half maximum (FWHM) was obtained with an energy resolution of 35.2% FWHM. These results of the MLA were achieved without prior calibration of scintillations as is needed for many statistical scintillation detection algorithms. We conclude that the MLA significantly improves the gamma camera performance compared to the MSA.

3.1. Introduction

The use of multi-pinhole small-animal single photon emission tomography (SPECT) imaging[44,45] can yield excellent image resolutions[46,47,48,159]. Image resolutions better than half a mm are no longer proof-of-principle[49,50,173]. At present, these ultra-high resolutions are obtained using traditional gamma cameras, by employing the principle of pinhole magnification. For future improvements of small animal SPECT imaging, gamma cameras with better spatial resolution and significant energy discrimination capabilities are essential[53,140,153,154,155].

Compact, high-resolution gamma imaging cameras are being developed by many research groups[123,156,157,158,159,160,161,162,163,164]. A subset of these gamma cameras use micro-columnar CsI:Tl scintillators[138] in combination with EM-CCDs[137,138,140,146,148,165]. In such CCD based detectors individual scintillation events can be detected in photon counting mode, enabled by readout at high frame rates. This detection method greatly improves the spatial resolution compared to integration of the scintillation light signal[82]. The sensitivity of these detectors can be improved by using continuous instead of micro-columnar scintillators which are available in larger thicknesses[144,174] (chapter 2 and 7). A problem of pinhole gamma cameras with continuous crystals is the degradation of spatial resolution due to the variable depth-of-interaction (DOI) for gamma photons incident at oblique angles[168,175] (chapter 4). This degradation of spatial resolution can be reduced by using a detection algorithm that can detect the DOI. We have previously developed such a scintillation detection algorithm, the multi-scale algorithm (MSA), that uses an analytical model for the depth-dependent light distribution[144] (chapter 2). While this algorithm already improves significantly upon an algorithm that does not use a depth-dependent light distribution model, further improvements in performance are expected by using a statistical scintillation detection algorithm.

Previously, a statistical scintillation detection algorithm using a calibration based approach was applied to an EM-CCD based gamma camera with a micro-columnar scintillator[165] and to a simulation of a multi-anode photomultiplier tube based gamma camera with a thick continuous scintillator[99]. Furthermore an excellent overview article about maximum-likelihood scintillation detection is available[141]. Detection algorithms that rely on the calibration of individual scintillations have their disadvantages; given the large number of pixels of a CCD these calibrations are often time consuming and lead to a data storage challenge.

In this paper we present a novel statistical scintillation detection algorithm for EM-CCD based gamma cameras with continuous scintillators. This algorithm does not require calibration of gamma photon scintillations but instead uses analytical models for the light distribution and EM-CCD statistics. The statistical model derived in this paper is based on research into EM-CCD characteristics performed by many authors[167,176,177]. Maximum-likelihood estimation is used to determine the scintillation position and energy of the incoming gamma photon. The performance of this maximum-likelihood algorithm (MLA) is evaluated by comparison with the MSA in terms of spatial resolution, DOI corrected spatial resolution for oblique incidence, energy resolution and signal-to-background counts ratio (SBR).

3.2. Methods

3.2.1. EM-CCD, optical coupling and scintillator

The gamma camera consists of a CsI:Tl SCIONIX scintillator optically coupled, by a fiber optic plate (FOP), to the E2V CCD97 EM-CCD[126,127,166]. A schematic of the gamma camera is shown in

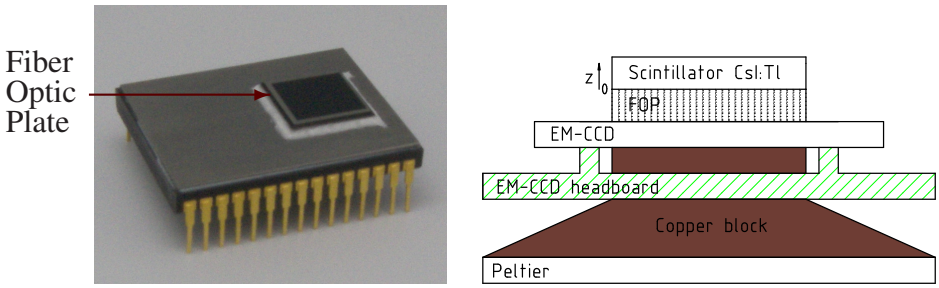

(a) **(b)**

Figure 3.1: (a) EM-CCD with a FOP. **(b)** Schematic of the gamma camera consisting of a continuous scintillator optically coupled through a FOP to the EM-CCD, cooled by a Peltier element.

figure 3.1 and is described in detail in[144] (chapter 2). The pixels here are binned[178] (chapter 8) on chip to a size of 16×32 μm^2. The FOP reduces the number of optical photons that reach the EM-CCD at large oblique angles (see appendix). The scintillator thicknesses used in this paper are 0.7 mm, 1.5 mm, 1.8 mm and 3 mm with interaction probabilities for ^{99m}Tc gamma photons (141 keV) of 20%, 42%, 47% and 66%, respectively.

3.2.2. Multi-scale algorithm

The MSA acts as a matched filter that takes the depth-dependent light distribution in the continuous scintillator into account and can therefore accurately estimate the DOI[144] (chapter 2). Implicitly, the MSA uses a Gaussian light distribution model. Here we employ the MSA with a threshold on the CCD data which is at a level of 3 times the σ (standard deviation) above the mean dark level of the individual pixel. The pixel σ and mean dark level is determined from dark CCD frames.

3.2.3. Maximum-likelihood algorithm

The maximum-likelihood algorithm (MLA) estimates the position and energy of scintillations by calculating the response of the detector for a given estimated position and energy and iteratively updating the estimate after comparison of the calculated response to the actual measurement (i.e. CCD frame). In order to accurately calculate the detector response and thus accurately determine the position and energy of scintillation events, the MLA requires advanced modeling of the detector in terms of mean scintillation photon distribution and detector statistics. The mean light distribution (figure 3.2 (a)) and statistical model (figure 3.3) and their validations are discussed below.

3.2.3.1. Light distribution In our gamma detector a gamma photon is absorbed in the scintillator and optical photons are generated (shown in figure 3.2 (a)). The first step in calculating the detector response consists of estimating the mean number of scintillation photons λ_i incident on each pixel i of the detector for a given scintillation position and energy. Assuming a single interaction position and neglecting interactions of optical photons with the scintillator but taking into account Fresnel reflections and the optical properties of the FOP, the mean light distribution can be modeled by

$$\lambda_i\left(\vec{\theta}\right) = \frac{\varepsilon\theta_N A}{4\pi}\frac{\theta_z}{\left|\vec{\rho}_i - \vec{\theta}_\rho\right|^3} f\left(\phi_i\right) + \theta_{bg}, \tag{3.1}$$
$$\vec{\theta} = \left(\vec{\theta}_\rho, \theta_N, \theta_{bg}\right) = \left(\vec{\theta}_r, \theta_z, \theta_N, \theta_{bg}\right) = \left(\theta_x, \theta_y, \theta_z, \theta_N, \theta_{bg}\right).$$

Here $\vec{\theta}$ is the parameter vector describing the scintillation event, it contains the scintillation position $\vec{\theta}_\rho$, consisting of $\vec{\theta}_r = (\theta_x,\theta_y)$ and θ_z representing the x, y and z coordinate of the scintillation, the number of generated optical photons θ_N and the background signal θ_{bg}. Furthermore, $\vec{\rho}_i$ is the pixel position, consisting of the lateral pixel position $\vec{r}_i = (x_i, y_i)$ and z position z_i, A is the area of an EM-CCD pixel, ε is an efficiency factor and the function $f(\phi_i)$ describes the Fresnel reflections and transmission of the FOP as a function of the angle (ϕ_i) of the photon with the fiber axis for pixel i (see appendix). The z axis is chosen perpendicular to the scintillator plane starting at the scintillator bottom (see figure 3.1 (b)). To obtain a simple expression for the mean light distribution, we have approximated (3.1) by a Gaussian with a cutoff at an angle ϕ_{cutoff}:

$$\lambda_i\left(\vec{\theta}\right) = H\left[\phi_{cutoff} - \arctan\left(\frac{\left|\vec{r}_i - \vec{\theta}_r\right|}{\theta_z}\right)\right]\frac{\varepsilon\theta_N A}{2\pi\sigma^2_{DOI}\left(\theta_z\right)}\exp\left[-\frac{\left|\vec{r}_i - \vec{\theta}_r\right|^2}{2\sigma^2_{DOI}\left(\theta_z\right)}\right] + \theta_{bg}. \tag{3.2}$$

Here H is the Heaviside step function and $\sigma_{DOI}(\theta_z)$ describes the width of the light distribution which depends on the scintillation z position (θ_z).

3.2.3.2. Statistical model The role of the statistical model (figure 3.3) is to provide a complete distribution of the detector output for a mean photon distribution described by the light distribution model. The number of optical photons generated is not a Poisson random variable[179,180], however, through rarity, the optical photons incident on one pixel of the EM-CCD are Poisson distributed[181,182]. An optical photon incident on the EM-CCD can reflect at different boundaries (scintillator-optical coupling, optical coupling-FOP, etc.) before reaching the EM-CCD and an optical photon reaching the EM-CCD can generate an electron-hole pair or not. Both these processes are Binomial selections whereby the Poisson distribution is retained and only its mean changes[183]. Besides these electrons generated by photons, also noise induced electrons can be present in a pixel of the EM-CCD. The main noise sources for electrons are dark current noise and CIC noise[167,176,177], shown in figure 3.3. These noise induced electrons are Poisson distributed. The sum of the photon generated electrons and noise induced electrons in one pixel is again a Poisson random variable

$$pr_{\text{el.}}\left(n|\bar{n}\right) = \frac{\bar{n}^n \exp\left(-\bar{n}\right)}{n!} \tag{3.3}$$
$$\bar{n} = \bar{n}_p + \bar{n}_n,$$

where n is the number of electrons in the pixel and $\bar{n}$ the mean number of electrons in the pixel consisting of the mean number of photon generated electrons $\bar{n}_p$ and the mean number of noise induced electrons $\bar{n}_n$. The electrons are amplified in the electron multiplication (EM) register and the conditional probability $pr_{EM}(g|n)$ for g electrons at the EM register output given n electrons in a pixel is, similar to [176], given by:

$$pr_{EM}\left(g|n\right) = H(g)\frac{g^{n-1}\exp\left(-\frac{g}{gain}\right)}{gain^n\left(n-1\right)!} + \delta_{0n}\delta(g). \tag{3.4}$$

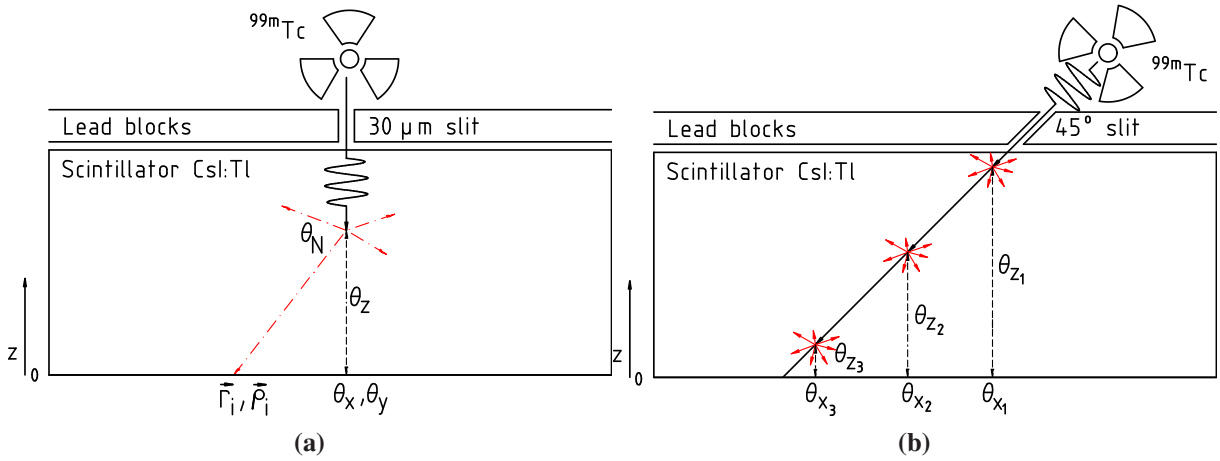

Figure 3.2: **(a)** Measurement setup for acquiring line pattern images showing parameters from equation (3.1). The gamma photon is absorbed in the scintillator and θ_N optical photons denoted by the dash dot lines are emitted. **(b)** Measurement setup with the 45° slit showing γ interactions at x coordinates θ_x and corresponding depths θ_z in the top of the scintillator (1), the middle (2) and the bottom (3).

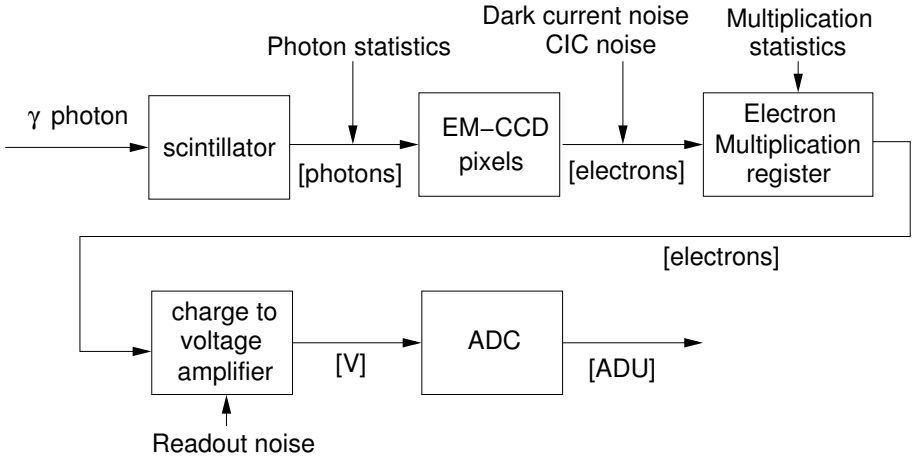

Figure 3.3: Schematic illustration of the statistical model with all modeled noise sources.

Here $H(g)$ is the Heaviside step function, δ_{0n} is the Kronecker delta and $\delta(g)$ is the Dirac delta function. We describe the number of electrons at the EM register output by a continuous variable g, which is allowed because $gain \gg 1$. The distribution pr_{EM} is normalized for integration over g for any given n. Combining distributions (3.3) and (3.4) yields the conditional probability $pr_{\mathrm{outputEM}}(g|\bar{n})$ of the number of electrons at the EM register output given a mean number of electrons in a pixel,

$$pr_{\mathrm{outputEM}}(g|\bar{n}) = \sum_{n=0}^{\infty} pr_{\mathrm{EM}}(g|n)\, pr_{\mathrm{el.}}(n|\bar{n}) =$$
$$H(g)\exp\left(-\bar{n}-\frac{g}{gain}\right)\sqrt{\frac{\bar{n}}{g\cdot gain}}I_1\left(2\sqrt{\frac{\bar{n}g}{gain}}\right)+\exp(-\bar{n})\delta(g). \tag{3.5}$$

Here I_1 is the modified Bessel function of the first kind and the Dirac delta function $\delta(g)$ describes the case of zero electrons at the input of the EM register.

Subsequently, the electrons at the output of the EM register are converted to a voltage in the charge-to-voltage amplifier. This conversion and other electronic noise in the analog electronics adds readout noise which has a Gaussian distribution. The output is a convolution of a Gaussian with the output signal[177], but can be approximated by a convolution with the Dirac delta function in (3.5)

only[167]. Applying this to the distribution in (3.5) results in

$$pr_{\text{output}}(g|\bar{n}) = H(g)\exp\left(-\bar{n}-\frac{g}{gain}\right)\sqrt{\frac{\bar{n}}{g\cdot gain}}I_1\left(2\sqrt{\frac{\bar{n}g}{gain}}\right) + \exp(-\bar{n})\frac{1}{\sqrt{2\pi}\sigma}\exp\left(-\frac{g^2}{2\sigma^2}\right), \tag{3.6}$$

where σ is the standard deviation of the Gaussian readout noise. The distribution is normalized for integration over g from -∞ to +∞. Equation (3.6) is the conditional probability to measure g electrons at the output given $\bar{n}$. Since we want to estimate $\bar{n}$ given a certain output g, we need the conditional probability $pr_{\text{output}}(\bar{n}|g)$. We have no prior knowledge of $\bar{n}$ and therefore assume that $pr(\bar{n})$ is constant for nonnegative $\bar{n}$ and zero for negative $\bar{n}$ as is typical in ML[182]. In that case Bayes rule[184] reduces to

$$pr_{\text{output}}(\bar{n}|g) = \frac{pr_{\text{output}}(g|\bar{n})}{\int_0^\infty pr_{\text{output}}(g|\bar{n})\,\mathrm{d}\bar{n}}. \tag{3.7}$$

Applying this to the approximation above results in a normalization of (3.6) for $\bar{n}$:

$$pr_{\text{output}}(\bar{n}|g) = \left[H(g)gain^{-1} + \exp\left(-\frac{g^2}{2\sigma^2}\right)\left(\sqrt{2\pi}\sigma\right)^{-1}\right]^{-1} pr_{\text{output}}(g|\bar{n}). \tag{3.8}$$

3.2.3.3. Maximum-likelihood estimation Combining the light distribution model (3.1) and the noise $\bar{n}_{\text{n}}$ with the normalized conditional probability (3.8) and multiplying over all pixels i the conditional probability for a scintillation described by vector $\vec{\theta}$ given the measured pixel values $\vec{g}$ is

$$pr_{\text{output}}\left(\vec{\theta}|\vec{g}\right) = \prod_i pr_{\text{output}}\left(\lambda_i\left(\vec{\theta}\right) + (\bar{n}_{\text{n}})_i|g_i\right), \tag{3.9}$$

where $\vec{\theta}$ is the vector describing the scintillation position, the number of generated optical photons and the background signal defined in (3.1). The maximum-likelihood estimate is obtained by maximizing (3.9) or its logarithm.

3.2.3.4. Implementation of MLA For the ML algorithm, the CCD frame is thresholded at a level of 3 times the Gaussian readout noise and the data are binned from 16 × 32 μm to 64 × 64 μm pixels by digital summation. The threshold on the data was necessary due to low amplitude drift in the CCD frame data. To obtain starting values for the vector $\vec{\theta}$ (see equation (3.1)) the CCD frame is initially searched with the MSA algorithm and the outcome is used as a first estimate. The starting value for θ_{bg} is set at $\bar{n}_{\text{n}}$, obtained from a measurement of the noise. Subsequently, a taxi cab type search algorithm maximizes the log of the likelihood equation (3.9). This search algorithm, which is a simple version of the Powell method[185] and similar to previously published work[186,187], evaluates $log[pr_{\text{output}}(\vec{\theta},\vec{g})]$ by varying only one of the elements of vector $\vec{\theta}$ at a time. The value that maximizes an arithmetic mean of the likelihood equation (3.9) is chosen as the new estimate of $\vec{\theta}$. This taxi cab type algorithm performs the same search for all elements in the vector $\vec{\theta}$ and this five-element search is repeated for 40 iterations.

3.2.4. Validation methods

3.2.4.1. Validation of the statistical model To validate the probability distribution equation (3.6) that was derived in this paper and that forms the basis of the MLA, a series of measurements was performed. The pixel values $\vec{g}$ of the EM-CCD were measured as a function of the mean number of incident photons. To this end we irradiated the EM-CCD with a light source with varying intensities

and measured its response. The measurements were fitted with equation (3.6) with *gain*, $\bar{n}$ and σ as fit parameters.

3.2.4.2. Scintillation light distribution on the detector The mean light distribution of optical photons on the EM-CCD as a function of the depth of the scintillation events (θ_z) was measured. The setup for this measurement consisted of a slit at an angle of approximately 45° as shown in figure 3.2 (b). The scintillations at a certain depth (θ_z) can be selected by combination of the detected position (θ_x,θ_y) with the known thickness of the scintillator. Scintillations detected at the same depth (θ_z) were summed to obtain mean scintillation light distributions as a function of depth. These mean light distributions at 15 different depths were fitted with equation (3.1) where the fit parameters were θ_x, θ_N, θ_{bg} and the reflectivity (see appendix). θ_z was set to the value of the known depth. The light distributions were fitted again with equation (3.1) with constant reflectivity (obtained from the previous fit) and with the Gaussian given by equation (3.2) with fit parameters θ_z, θ_x, θ_N and θ_{bg}. The value of ϕ_{cutoff} in equation (3.2) was chosen at 37°. The linear relation between σ_{DOI} and (θ_z) was determined from the latter fit.

3.2.5. Algorithm comparison

As a measure of performance of the statistical algorithm, its spatial resolution, energy resolution, SBR and linearity of response with energy are compared with the values obtained by the MSA. In the MSA the slices are selected in such a way that every slice corresponds to a depth in the scintillator of approximately 300 μm. However, in the case of oblique incidence more slices were chosen (approximately 70 μm per slice) to rule out any spatial resolution degradation due to a limited number of slices. To determine the spatial resolution, a line pattern from a ^{99m}Tc source (141 keV), projecting through a slit onto the scintillator, is acquired (illustrated in figure 3.2 (a)). The spatial resolution is defined as the full width at half maximum (FWHM) of the line spread function of the radioactive source without correction for the width of the gamma photon beam. In our experiments we have investigated both perpendicular incidence (figure 3.2 (a)) and incidence at an angle of approximately 45° (figure 3.2 (b)). The FWHM energy resolution is obtained by determining the FWHM of the ^{99m}Tc photo-peak for the scintillations in an area around the slit (with a width of 260 pixels). The energy in the energy spectra is calibrated by using the photo-peak of ^{99m}Tc at 141 keV. The SBR is defined as in previous research[144] (chpater 2). The uncertainties in the SBR, spatial and energy resolution measurement were determined using the bootstrap method[188] and are expressed as a standard deviation. Comparison of the spatial resolution and SBR of the two algorithms is always done for an equal number of net signal counts. This is accomplished by setting an energy window for the MSA and the MLA. The linearity of response with energy of the MLA is investigated using a ^{99m}Tc, ^{241}Am and ^{125}I source after which the measured relative photo-peak energy is compared with the known relative photo-peak energies of these isotopes.

3.3. Results

3.3.1. Validation of the statistical model

The output distribution of a single pixel was measured as a function of the mean number of detected photons per pixel and fitted using equation (3.6). The plots, shown in figure 3.4, show a fairly good

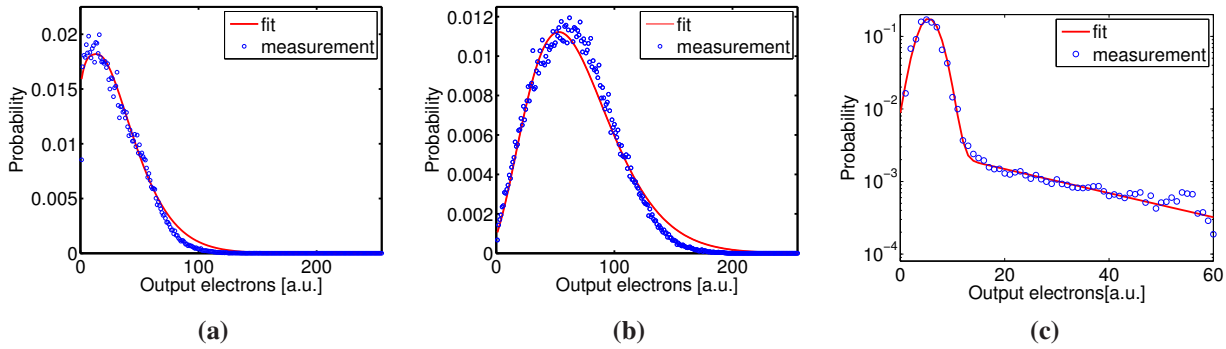

Figure 3.4: Measured distribution for a signal level and a fit with equation (3.6) for **(a)** 3.2 detected photons per pixel, **(b)** 6.6 detected photons per pixel and **(c)** no photons incident on the CCD ($\bar{n} = 0.1$ due to noise).

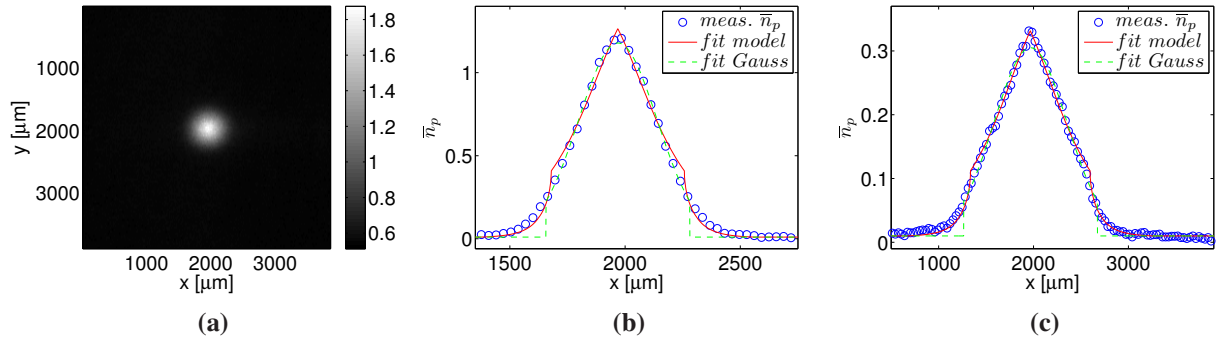

Figure 3.5: **(a)** Measured mean light distribution of scintillations at a depth of approximately 0.4 mm and a profile **(b)** at the same depth with a fit with the model (3.1) and a Gaussian (3.2). Profile and light distribution fits are also shown for a depth of approximately 1.3 mm **(c)**.

fit indicating that the statistical model gives an adequate description of the large noise and signal components.

3.3.2. Scintillation light distribution on the detector

The measured mean light distribution of scintillations on the detector pixels is shown in figure 3.5(a). The mean reflectivity obtained from the fit was 0.9976 ± 0.0004. The profiles and the fit results are shown in figure 3.5 (b) and (c) for depths of approximately 0.4 and 1.3 mm. The measurements and fits show that both the model (equation (3.1)) and the Gaussian (equation (3.2)) can describe the mean light distribution accurately.

3.3.3. Spatial resolution for perpendicular incidence

The influence of the algorithm on the spatial resolution is investigated using the line pattern measurement of ^{99m}Tc (as shown in figure 3.2 (a)) consisting of 100 000 CCD frames for the 3 mm thick scintillator and 50 000 CCD frames for the 1.8 mm thick scintillator. For the 3 mm thick scintillator the profiles of the line patterns obtained with the MLA and the MSA are shown in figure 3.6. Both profiles are approximately the same. For the 1.8 mm thick scintillator the results are shown in table 3.1. The FWHM spatial resolution for the MLA is slightly smaller than for the

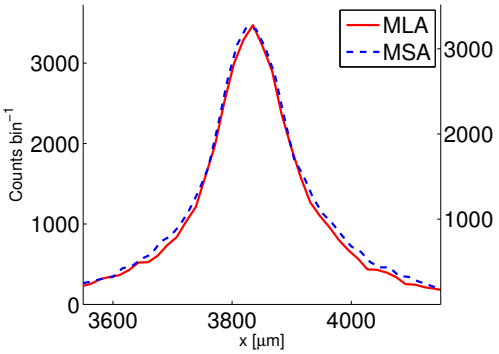

Figure 3.6: Profiles of line patterns of a ^{99m}Tc source for the MLA (solid, red, left y-axis) and the MSA (dashed, blue, right y-axis) for a 3 mm thick scintillator.

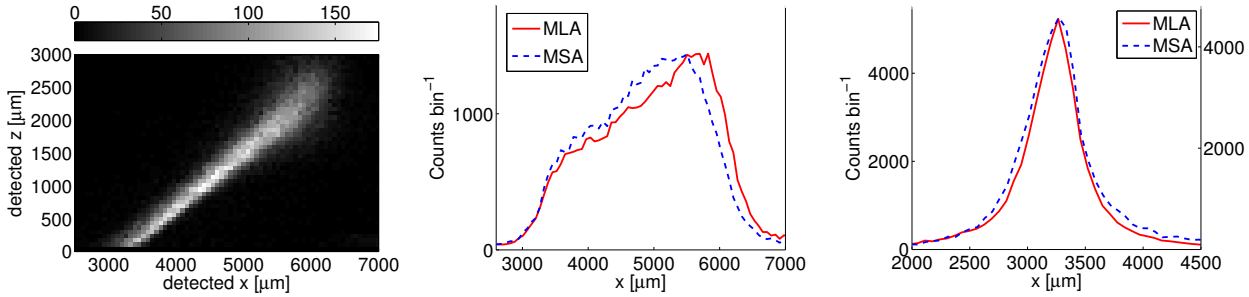

(a) **(b)** **(c)**

Figure 3.7: Shown for the 3 mm thick scintillator are **(a)** detected DOI for the MLA, **(b)** uncorrected profile for the MLA (solid, red) and MSA (dashed, blue) and **(c)** DOI corrected profile for the MLA (left y-axis) and MSA (right y-axis).

MSA, but only significantly for the 1.8 mm thick scintillator. The spatial resolution for the 3 mm scintillator was 150 µm for the MSA, a factor 1.02 ± 0.03 from the 147 µm for the MLA. The spatial resolution for the 1.8 mm scintillator was 125 µm for the MSA, a factor 1.10 ± 0.04 from the 114 µm for the MLA. All results and errors are summarized in table 3.1.

3.3.4. DOI detection and correction

Figure 3.7 illustrates the capability of our algorithm to estimate the z-coordinate of the interaction for the 3 mm thick scintillator. A density plot is shown in figure 3.7 (a) with the gray scale representing the number of detected scintillation events as a function of x- and z-position, when the gamma photons of the ^{99m}Tc source are incident under an angle of approximately 45°. As expected, the scintillation events are distributed along a line having a slope of approximately 45° with respect to the scintillator surface plane. Figure 3.7 (b) shows the spatial profile of the density plot in (a). It can be clearly seen that the intensity of the detected gamma beam is reduced by interactions of photons with the scintillator, as would be expected. For the 3 mm thick scintillator, the MLA is slightly more efficient at detecting scintillations far from the detector (at $z \approx 3$ mm or $x \approx 6$ mm) compared with the MSA (remember that the profiles are shown with an equal total number of counts). In figure 3.7 (c), the profile corrected for the DOI is plotted. Compared with the MSA the MLA improves the DOI corrected spatial resolution by a factor of 1.13 ± 0.04 (from 495 µm to 437 µm FWHM) for the 3

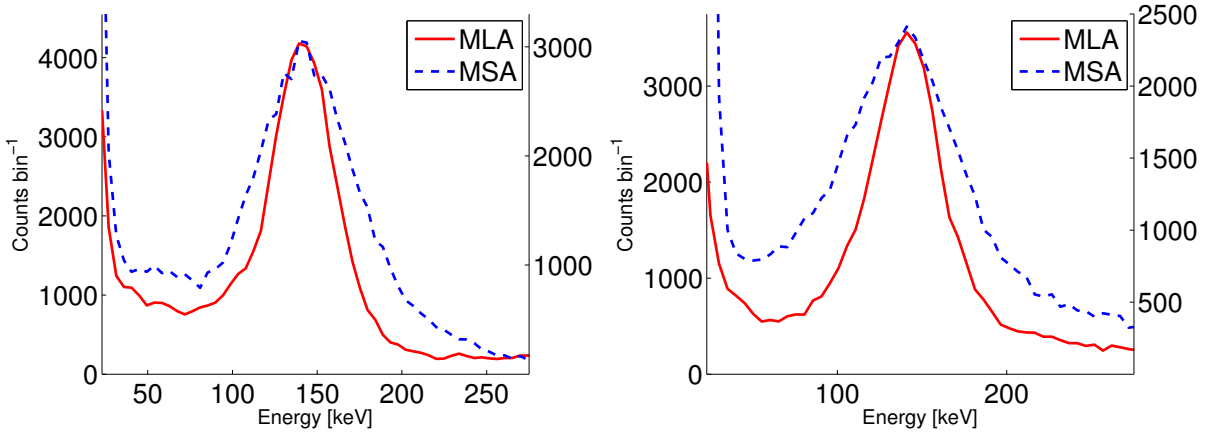

(a) **(b)**

Figure 3.8: Energy spectra of ^{99m}Tc for the MLA (solid, red, left y-axis) and the MSA (dashed, blue, right y-axis) for the scintillator with thickness of **(a)** 1.5 mm and **(b)** 3 mm.

mm thick scintillator and by a factor of 1.12 ± 0.02 (from 306 µm to 273 µm FWHM) for the 1.5 mm thick scintillator (see table 3.1). The measurements contain 100 000 (1.5 mm) and 75 000 (3 mm) CCD frames.

3.3.5. Energy resolution and SBR

The energy spectra for the MLA and MSA, shown in figure 3.8, consist of 100 000 CCD frames for the 1.5 mm scintillator and 95 000 frames for the 3 mm scintillator. For both scintillator thicknesses the MLA significantly improves upon the energy resolution obtained with the MSA. For the 1.5 mm thick scintillator the energy resolution improves from 53.3 % to 32.7 % by a factor of 1.63 ± 0.06, for the 3 mm thick scintillator the energy resolution improves from 65.3 % to 35.2 % by a factor 1.85 ± 0.09. Compared with the MSA, the MLA improves the SBR from 87 to 133 by a factor of 1.54 ± 0.10 (1.5 mm) and from 130 to 178 by a factor of 1.37 ± 0.11 (3 mm).

3.3.6. Linearity of response with energy

The energy spectra of ^{99m}Tc and ^{241}Am for the 1.5 mm thick scintillators are shown in figure 3.9 (a). The high energy tail of the ^{241}Am spectrum is probably due to the high count rate during the measurement which resulted in pile-up. The same measurement for ^{99m}Tc and ^{125}I was performed on a 0.7 mm thick scintillator. In figure 3.9 (b), the measured relative energy peak for ^{125}I, ^{241}Am and ^{99m}Tc (with respect to the ^{99m}Tc energy peak position) for the MLA and MSA are plotted versus the known isotope gamma energies. The responses with energy for the MLA and the MSA are approximately equal and linear.

3.4. Discussion

The MLA presented in this paper uses a validated statistical model of the EM-CCD, based on the work by various authors[167,176,177] and a Gaussian approximation to a realistic light distribution model. The results in this paper show that the use of a statistical model in a scintillation detection algorithm improves the performance. The MLA outperforms the previously developed MSA which, like the

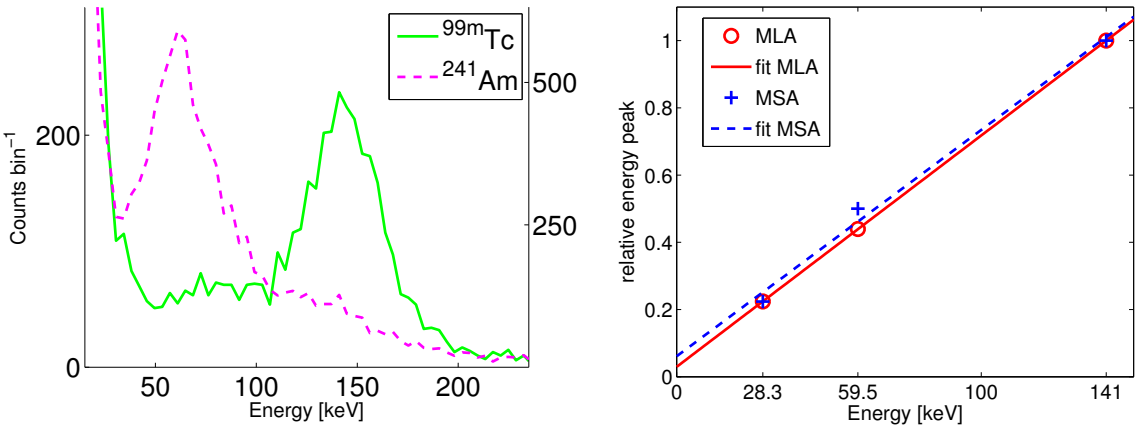

(a) **(b)**

Figure 3.9: Energy spectra of ^{99m}Tc (solid, green, left y-axis) and ^{241}Am (dashed, magenta, right y-axis) for the 1.5 mm scintillator in **(a)**. In **(b)** the relative energy peak positions are plotted as a function of energy for the MLA and MSA.

Table 3.1: Spatial resolution, energy resolution (FWHM) and SBR for the MLA and MSA.

	Thickness [mm]	MSA	MLA	Improvement factor
Energy resolution [%]	1.5	53.3 ± 1.4	32.7 ± 0.8	1.63 ± 0.06
	3	65.3 ± 2.9	35.2 ± 0.7	1.85 ± 0.09
Spatial resolution Δx [μm]	1.8	125 ± 2	114 ± 3	1.10 ± 0.04
	3	150 ± 3	147 ± 2	1.02 ± 0.03
Spatial resolution Δx [μm]	1.5	306 ± 4	273 ± 4	1.12 ± 0.02
at oblique incidence (45°)	3	495 ± 12	437 ± 9	1.13 ± 0.04
SBR	1.5	87 ± 4	133 ± 7	1.54 ± 0.10
	3	130 ± 7	178 ± 11	1.37 ± 0.11

MLA, uses a Gaussian depth-dependent light distribution model but no statistical model for detector response and noise. The aspect that benefits the most from the statistical approach is the energy resolution; a significant improvement of more than a factor 1.6 is found for scintillator thicknesses of 1.5 mm and 3 mm. Furthermore, the MLA improves the SBR by factors of 1.37 to 1.54, depending on the scintillator thickness, and the DOI corrected spatial resolution for oblique incidence by factors of 1.12 (1.5 mm thick scintillator) and 1.13 (3 mm). For the latter measurement, we chose to use many slices in the MSA (with a single slice corresponding to 70 µm instead of 300 µm in depth) to rule out any degradation of the MSA result due to too few slices. The spatial resolution for perpendicular incidence was, within uncertainty, the same with the 3 mm thick scintillator for both algorithms. However, for the 1.8 mm thick scintillator, the improvement for the MLA is small but significant. Furthermore, it was shown that the responses with energy for the MLA and MSA are approximately linear by a measurement for ^{99m}Tc and ^{241}Am with a 1.5 mm thick scintillator and for ^{99m}Tc and ^{125}I with a 0.7 mm scintillator. These measurements with ^{241}Am and ^{125}I were performed on rather thin scintillators because thick scintillators (3 mm) would make detection of these low energies very difficult.

The MLA, unlike many statistical scintillation detection algorithms, does not require calibration of individual scintillations for different scintillation positions and energies. Although calibration could improve performance close to the edges of the camera it requires a recurring large experimental effort to obtain the calibration data and it also requires a large amount of data storage for detectors with many pixels such as CCDs.

Using the MLA our gamma camera reaches a spatial resolution of 147 ± 2 μm FWHM with an energy resolution of 35.2 ± 0.8 % for ^{99m}Tc for the 3 mm thick scintillator (interaction probability 67 % at 141 keV). While the spatial resolution is much better than the spatial resolution of clinical gamma cameras (typically 3-4 mm), the energy resolution is not yet as good. However, this is not so important for animal imaging as scatter rejection is often not required due to the relatively low amount of scatter in animals compared to humans.

Furthermore, we expect to further improve the detector performance by combining the advantages of Silicon Photo Multipliers (SiPM) with those of EM-CCDs using SiPM side detection[189]. Moreover, we expect that further reduction of the noise in the EM-CCD, for instance by using an advanced CCD controller[190], can improve the energy resolution. To accurately determine how much a given reduction of noise will improve the performance of the EM-CCD based gamma camera a simulation study would be beneficial.

3.5. Conclusion

In this paper we have presented a statistical maximum-likelihood scintillation detection algorithm. The statistical model and light distribution model employed in the algorithm have been validated experimentally. We have compared the statistical scintillation detection algorithm with a previously presented analytical multi-scale algorithm and found that the use of a statistical instead of an analytical algorithm significantly improves the energy resolution, the spatial resolution for oblique incidence and the SBR.

3.6. Acknowledgments

This work was in part sponsored by the Netherlands Ministry of Economic Affairs, IOP photonics grant IPD067766. We thank Paul Schotanus of SCIONIX for providing us with CsI:Tl scintillators.

3.7. Appendix

The optical light distribution is determined by the various optical components of the detector (shown in figure 3.10). The optical system consists of the scintillator which absorbs gamma photons and emits optical photons. These optical photons can travel through the thin layer of optical grease (Bicron 630) to the fiber optic plate (FOP) with angle with the fiber axis ϕ_i. The FOP restricts lateral spreading of optical photons. An optical epoxy (Epotec 301-2 with refractive index $n_5 = 1.53$)[191] connects the FOP optically to the EM-CCD. To accurately model the light distribution of a scintillation as detected on an EM-CCD we use a model that describes the different optical components. The FOP is the most complicated part of the optical system. The Anteryon FOP core is made of FOC-1 glass ($n_3 = 1.805$) and the cladding is made of 8250 Scott glass ($n_4 = 1.487$). These refractive indices result in a critical angle ϕ_c of 34.5° with the fiber axis. The FOP is 3 mm thick and consists of fibers with a diameter of 5.4 μm. In order to take the transmission of skew rays[192] above the critical angle into account, the fibers are assumed to be cylindrical. The main causes of attenuation in a FOP are Fresnel

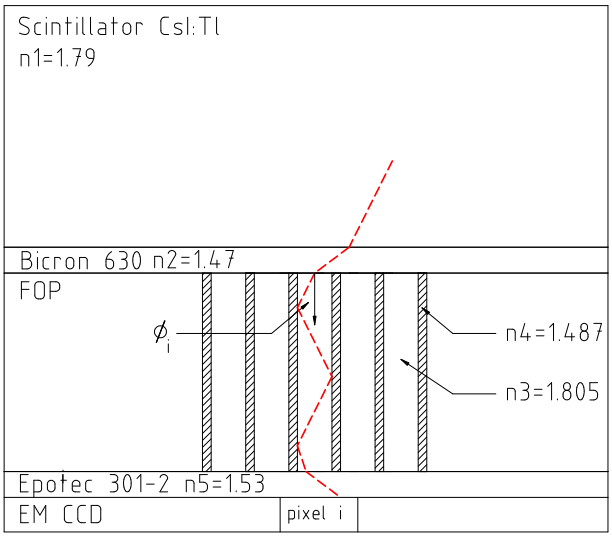

Figure 3.10: Diagram of the detector with the respective refractive indices indicated in the scintillator, FOP core and cladding and optical grease and epoxy. The actual width of a single core glass fiber is only 5.4 µm. The red dashed line shows a possible path of a photon from the scintillator to the EM-CCD detector.

reflections at the faces, an internal reflectivity less than 1 and absorption within the material of the fiber[193]. The Fresnel reflections at the faces of the FOP and at the CsI:Tl scintillator ($n_1 = 1.79$) [194] to optical grease (Bicron 630, $n_2 = 1.47$)[195] interface are taken into account. The internal reflectivity is assumed to be less than 1 and an equation from other research[196] is used. Given the relatively small thickness of the FOP, the absorption within the material is neglected. We neglect the small

Table 3.2: refractive indices

Material		Refractive index
CsI:Tl	n_1	1.79
Bicron 630	n_2	1.47
FOP core	n_3	1.487
FOP cladding	n_4	1.805
Epotec 301-2	n_5	1.53

difference in refractive indices between n_1 (1.79) and n_3 (1.805) and between n_2 (1.47) and n_5 (1.53) which simplifies the expression for the Fresnel transmission. Furthermore the angle of a photon with the scintillator surface is approximated by the angle with the fiber axis, denoted by ϕ_i. $f(\phi_i)$ from equation (3.1) can then be described by

$$f(\phi_i) = \left[\frac{1}{2}\left(T_s(\phi_i) + T_p(\phi_i)\right)\right]^3 \mathcal{R}^{n(\phi_i)l}\left\{1 - \frac{2}{\pi}\left[\arccos\left(\alpha(\phi_i)^{-1}\right) + \alpha(\phi_i)^{-1}\left(1-\alpha(\phi_i)^{-2}\right)^{\frac{1}{2}}\right]\right\}. \quad (3.10)$$

Here the first term with coefficients T_s and T_p describe the Fresnel transmission[197] of the scintillator to optical grease interface and the FOP top and bottom interfaces, $\mathcal{R}$ is the reflectivity, $n(\phi_i)$ is the number of reflections per unit length inside the FOP as a function of the angle with the fiber axis ϕ_i, l the length of the fibers and $\alpha(\phi_i)$ is defined as[192]

$$\alpha(\phi_i) = \frac{n_3 \sin(\phi_i)}{\sqrt{n_3^2 + n_4^2}}. \quad (3.11)$$

The angle with the fiber axis ϕ_i (in figure 3.10) can be approximated by

$$\phi_i = \arcsin\left(\frac{n_1}{n_3}\frac{\left|\vec{r}_i - \vec{\theta}_\mathrm{r}\right|}{\left|\vec{\rho}_i - \vec{\theta}_\rho\right|}\right) \approx \arcsin\left(\frac{\left|\vec{r}_i - \vec{\theta}_\mathrm{r}\right|}{\left|\vec{\rho}_i - \vec{\theta}_\rho\right|}\right). \tag{3.12}$$

The number of reflections $n(\phi_i)$ per unit length[196] is given by

$$n(\phi_i) = \frac{\phi_i}{R}\left[\left(1 - \frac{\phi_\mathrm{c}}{\phi_i}\right)\left(\frac{\phi_i^2}{\phi_\mathrm{c}^2} - 1\right)^{\frac{1}{2}}\right]\left[\operatorname{arccsc}\left(\frac{\phi_i}{\phi_\mathrm{c}}\right) - \frac{\phi_\mathrm{c}^2}{\phi_i^2}\left(\frac{\phi_i^2}{\phi_\mathrm{c}^2} - 1\right)^{\frac{1}{2}}\right] \qquad \phi_i > \phi_\mathrm{c} \tag{3.13}$$

$$n(\phi_i) = \frac{2\phi_i}{\pi R} \qquad \phi_i \leq \phi_\mathrm{c} \tag{3.14}$$

with R being the radius of the fiber.

Chapter 4

Pinhole Gamma-camera with Optical Depth-of-Interaction elimination

Marc A N Korevaar[1,2], Jan W T Heemskerk[1,2] and Freek J Beekman[1,2,3]

[1] Department of Nuclear Medicine, Image Sciences Institute, University Medical Center Utrecht, Heidelberglaan 100, 3584 CG, Utrecht, the Netherlands
[2] Section of Radiation Detection and Medical Imaging, Department of R[3], Applied Sciences, Delft University of Technology, Mekelweg 15, 2629 JB, Delft, The Netherlands
[3] Molecular Imaging Labs (MILABS), Universiteitsweg 100, 3584 CG, Utrecht, the Netherlands

Phys. Med. Biol., 54, 13, pp.N267-N272, 2009

Abstract

The performance of pinhole Single Photon Emission Computed Tomography (SPECT) depends on the spatial resolution of the gamma-ray detectors used. Pinhole cameras suffer from strong resolution loss due to varying depth-of-interaction (DOI) of gamma quanta that enter the detector material at an angle. We eliminate DOI effects in a scintillation gamma camera via a dedicated optic fiber bundle that acts as a focusing collimator for light generated in a scintillation crystal. A curved crystal is connected to a concavely shaped fiber-optic bundle such that the fibers connect perpendicular to the crystal's convex surface and point straight at the pinhole opening. Limiting the fiber numerical apertures can be used to suppress resolution losses due to light spread. Here we demonstrate experimentally that this prototype position-sensitive gamma sensor successfully eliminates DOI effects, has an intrinsic resolution of better than 280 µm Full Width at Half Maximum with an interaction probability 67% for 140 keV photons. Therefore the detector has great potential for increasing resolution of pinhole SPECT.

4.1 Introduction

Today, imaging of radio-labeled tracers with gamma-cameras, whether in planar or Single Photon Emission Computed Tomography (SPECT) mode, forms the most frequently used clinical molecular imaging procedure. SPECT imaging of small animals rapidly gains popularity as a key tool for the development of tracers, development of methods and (radio-labeled) agents for cancer therapy and to study animal models of human disease[44,45,46,48,49,198,199,200,201,202]. A key advantage of SPECT over optical molecular imaging is that the tracers can rapidly be translated to clinical application because gamma radiation has much lower attenuation and scatter in tissue than optical photons. Instrumental in these developments is the recent introduction of sub-mm and sub-half-mm resolution SPECT systems with high quantitative accuracy, mostly based on pinhole collimation technology. Pinholes cameras also have high potential for improving clinical SPECT devices. However, limited resolution and bulkiness of gamma-ray detectors can be perceived as the largest bottleneck to further improvement of SPECT device performance[54,153,155,203].

Commonly used scintillation detectors have an intrinsic resolution of a couple of mm. In these detectors the interaction position and energy of gamma quanta are extracted from the scintillation flashes via an array of photomultiplier tubes (PMTs). To improve detection accuracy a vast amount of research is directed at finding reliable alternatives to PMTs. In one class of novel detectors these PMTs are replaced by low-noise CCDs with fast read-out capabilities. In order to benefit from the high resolution light detection capabilities of CCDs novel structured scintillation crystals are being developed.

Recently investigated methods to obtain a much higher spatial resolution include sensors with scintillation crystals consisting of parallel bundles of tiny CsI needles ("columnar crystals") that are optically connected to CCDs. The CCDs are suitable for operating at high frame rates (e.g., 50 Hz)[138,146,148,162,163,204], which enables one to obtain images in which scintillation light flashes have a very high likelihood to be spatially separated; thus, it is possible to detect the photons individually (photon counting). The use of crystals consisting of columns with reflecting sides suppresses spatial resolution losses due to light spreading. At present however the gamma-ray interaction probability is low (typically <30% at 140 keV) due to the limited length of needles that can be manufactured. Moreover, when photons enter the crystal surface at an angle, varying depth-of-interaction (DOI) significantly reduces spatial resolution. The goal of the present work is to improve the interaction probability of a CCD based detector while simultaneously eliminating the associated resolution degrading DOI-effects of pinhole SPECT.

4.2 Methods

The principle of the camera with optical cone-beam collimation (OCC) is shown in figure 4.1. Parallax errors caused by gamma-rays entering the crystal at an angle (the DOI effect) and light spreading effects are eliminated using a 3-mm-thick curved monolithic CsI:Tl crystal which, together with a dedicated fiber-optic bundle, acts as a focusing collimator

(Optical cone beam collimator, OCC)[205,206,207]. The 3-mm-thick curved monolithic crystal with a diameter of 20 mm was machined from a larger crystal block. The dedicated fiber-optic bundle was machined from a 1:1.67 magnifying taper. The magnifying taper consists of many glass fibers, of 6 µm diameter, that propagate the light from one end to the other by means of total internal reflection[208]. The OCC is optically coupled to an Electron-Multiplying CCD (EM-CCD) using Bicron BC-630 silicone optical grease. Fibers with a limited numerical aperture (N.A.) suppress detection of photons whose angle of incidence is too large.

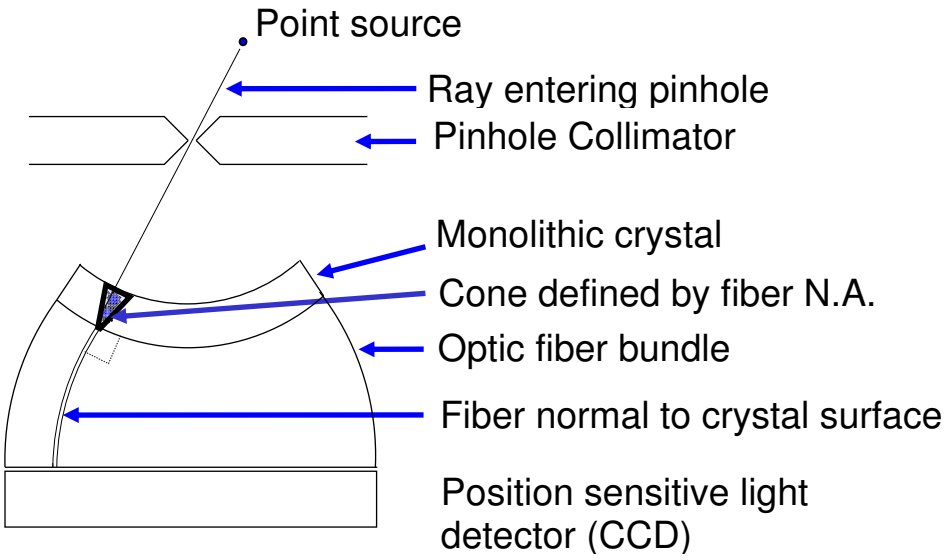

Figure 4.1: Principle of depth-of-interaction elimination through optical cone beam collimators (OCC). rays enter the crystal at an angle of 30°.

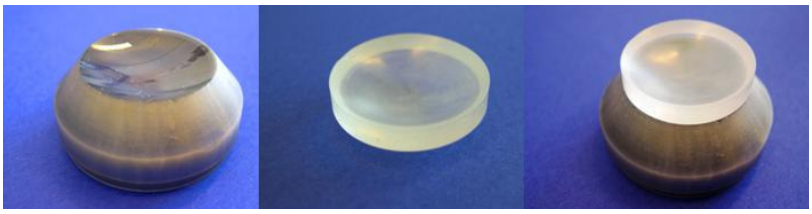

Figure 4.2: Left: optical cone beam collimator (OCC), center: curved crystal, right: OCC and crystal stacked.

The fibers are directed at the pinhole, which is also at the focal point of the convex side of the crystal. The fibers are normal to the crystal surface. The crystal and fiber-optics bundle are shown in figure 4.2. The pinhole diameter was 100 microns, the point source diameter was 300 microns, the source activity 100 MBq, the measurement time 4 minutes and the count rate approx. 50 counts per second. The pinhole to source distance was 20 mm, the pinhole to crystal distance was 21 mm and the opening angle of the gold pinhole was 62°. To calculate the FWHM of the radiation spot at the crystal surface the non-Gaussian pinhole response and point source shape were taken into account using the convolution method[209]. The pinhole transmission was calculated using the method described elsewhere[210]. Assuming a uniform and spherical point source this results in a radiation spot on the detector of 274

μm FWHM for the point source directly above the pinhole and 229 μm FWHM for the point source at an angle of 30°. The intrinsic spatial resolution was determined by correcting the measured resolution for the radiation spot.

The OCC is compared with the Optical Parallel Collimator (OPC) which consists of a flat CsI:Tl scintillator of the same thickness (3 mm) on top of a straight fiber optic taper.

We used an Electron Multiplying CCD (EM-CCD, type CCD97 from E2V Technologies). This CCD has an internal gain to reduce sensitivity to read-out noise, even at high read-out speeds (e.g. several Mpixels/second). The internal gain is achieved by electron multiplication (avalanche multiplication or impact ionization) in the gain register. To reduce the dark current, the EM-CCD was cooled to -50 ℃, using a Peltier element. The CCD was operated in photon-counting mode[82], in which the individual frames are analyzed by a scintillation detection algorithm[144] (chapter 2) to detect the individual gamma quanta. In order to cover the whole field of view the CCD was moved relative to the OCC in between measurements, but with the use of our future larger CCDs this will no longer be necessary.

4.3 Results

Initial results indicate that for the pre-eminent isotope in SPECT (^{99m}Tc, 141 keV) pinhole imaging can be performed with an intrinsic resolution of approx. 278 μm (Full Width at Half Maximum, corrected for the projected spot), an interaction probability of 67% and an energy resolution of 89% at 141 keV. Figure 4.3 shows the isolated effects of using the curved crystal with OCC, comparing it with a flat crystal CsI crystal (also 3 mm thick) combined with an optical parallel beam collimator (OPC). It shows that effects of DOI are adequately suppressed with OCC.

Table 4.1 shows the measured and intrinsic resolution (corrected for the projected spot size) of OPC versus OCC for the multi-scale algorithm[144] (chapter 2) that takes into account the varying light spread as a function of depth. As could be expected for gamma rays incident at normal angle, the differences between OPC and OCC are very small.
Figure 4.4 shows the energy spectrum of the OCC based detector for a ^{99m}Tc source with a 89% energy resolution at 141 keV.

Table 4.1: Spatial resolution measurements for OCC and OPC.

Angle	Type of Optical Collimation	FWHM measured	FWHM intrinsic (corrected for source size and pinhole size)
30°	Parallel-beam	1460 μm	1442 μm
30°	Cone-Beam	360 μm	278 μm
0°	Parallel-beam	386 μm	272 μm
0°	Cone-beam	389 μm	276 μm

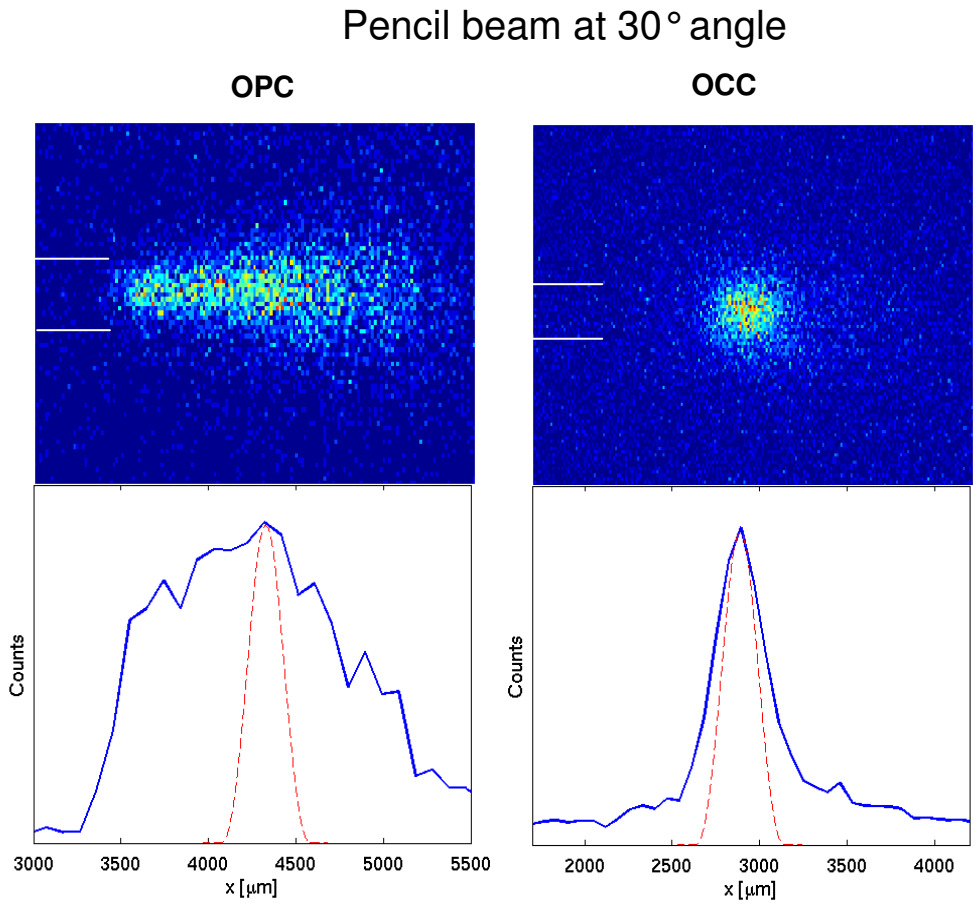

Figure 4.3: Left: optical parallel beam collimator (OPC), right: optical cone-beam collimator (OCC). OCC strongly suppresses depth-of-interaction- induced image degradation. The solid (blue) line is the measured profile and the dashed (red) line represents the spot on the detector when no detector blurring would be present (only blurring due to source and pinhole size). The x-axis of both figures has been scaled to the CsI:Tl crystal (i.e. multiplied by the demagnification factor of the taper).

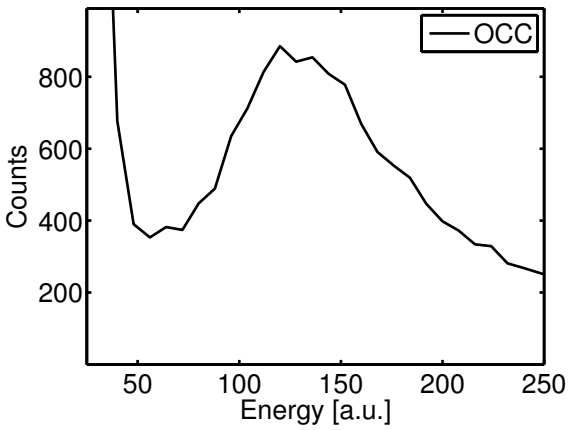

Figure 4.4: Energy spectrum of ^{99m}Tc measured with the optical cone-beam collimator (OCC).

4.4. Discussion and Conclusions

This paper presents the first pinhole gamma camera with intrinsic elimination of spatial resolution losses due to varying depth-of-interaction. In a first prototype the intrinsic

resolution of the camera is already below 280 microns. Energy and spatial resolution of future OCC-based detectors may be further improved by e.g. (i) using advanced statistical methods to characterize and localize scintillation events, (ii) fabricating crystals with higher density, better spectral matching or higher light yield, (iii) using light sensors with improved noise characteristics, and (iv) using new larger CCDs, currently under development for our group. Such larger CCDs will enable us to perform imaging using the full field of view. A point of further research is the effect of the numerical aperture of the optical fibers on the detector performance.

4.5. Acknowledgements

This work was sponsored in part by the Netherlands Organization for Scientific Research (NWO), grant 917.36.335 and by the Department of Economic Affairs IOP photonics grant IPD067766. Marc A. N. Korevaar thanks Frans van der Have, Marina Gaikhorst and Rene Nouse for support in production, radiation safety and transport of ^{99m}Tc point sources.

Chapter 5

Experimental comparison of high-density scintillators for EMCCD-based gamma ray imaging

Jan W T Heemskerk[1,2], Rob Kreuger[1], Marlies C Goorden[1,3], Marc A N Korevaar[1,3], Samuel Salvador[1], Zachary M Seeley[4], Nerine J Cherepy[4], Erik van der Kolk[1], Stephen A Payne[4], Pieter Dorenbos[1], Freek J Beekman[1,3,5]

[1] Radiation, Detection and Medical Imaging, Department of R[3], Applied Sciences, Delft University of Technology, Mekelweg 15, 2629 JB, Delft, the Netherlands
[2] Nuclear Medicine Department, University Hospital Vrije Universiteit Brussel, Laarbeeklaan 101, B-1090 Brussels, Belgium
[3] Rudolf Magnus Institute of Neurosciences, University Medical Center Utrecht, 3584 CG, Utrecht, the Netherlands
[4] Chemical Sciences Division, Lawrence Livermore National Laboratory, Livermore, CA 94550, USA
[5] MILABS, Universiteitsweg 100, Utrecht, the Netherlands

Phys. Med. Biol., 57, 14, pp.4545-4554, 2012

Abstract

Detection of X-rays and gamma rays with high spatial resolution can be achieved with scintillators that are optically coupled to electron-multiplying charge-coupled devices (EMCCDs). These can be operated at typical frame rates of 50 Hz with low noise. In such a set-up, scintillation light within each frame is integrated after which the frame is analyzed for the presence of scintillation events. This method allows for the use of scintillator materials with relatively long decay times of a few milliseconds, not previously considered for use in photon-counting gamma cameras, opening up an unexplored range of dense scintillators. In this paper we test $CdWO_4$ and transparent polycrystalline ceramics of Lu_2O_3:Eu and $(Gd,Lu)_2O_3$:Eu as alternatives to currently used CsI:Tl in order to improve performance of EMCCD-based gamma-cameras.

The tested scintillators were selected for their significantly larger cross-sections at 140 keV (^{99m}Tc) compared to CsI:Tl combined with a moderate to good light yield. A performance comparison based on gamma camera spatial and energy resolution was done with all tested scintillators having equal (66%) interaction probability at 140 keV.

$CdWO_4$, Lu_2O_3:Eu and $(Gd,Lu)_2O_3$:Eu all result in a significantly improved spatial resolution over CsI:Tl, albeit at the cost of reduced energy resolution. Lu_2O_3:Eu transparent ceramic gives the best spatial resolution: 65 μm full-width-at-half-maximum (FWHM) compared to 147 m FWHM for CsI:Tl. In conclusion, these 'slow' dense scintillators open up new possibilities for improving the spatial resolution of EMCCD-based scintillation cameras.

5.1 Introduction

High-resolution gamma detectors can play an important role in applications such as autoradiography[211,212,213], crystallography[161,164,214,215] and astrophysics[156,158]. Furthermore, it has been shown that for the improvement of future Single Photon Emission Computed Tomography (SPECT) devices, a high intrinsic detector resolution is essential[52,53,54,153,154,155,216]. Very high spatial resolution (below 60 microns) can be obtained with a detector consisting of micro-columnar scintillation crystals of CsI:Tl read out by an EM-CCD operating at high frame rates (~ 50 Hz)[137,138,140,146,204,217]. However, despite continuing progress in the field of micro-columnar crystals, the commercially available thickness of such crystals is currently limited to about 1.5 mm, resulting in interaction probabilities that are not sufficient for small-animal SPECT imaging or clinical application.

In contrast to micro-columnar scintillators, single crystal and transparent polycrystalline ceramic scintillators are available in a large variety of materials and thicknesses with a uniform response. However, compared to micro-columnar scintillation crystals, the resolution that can be obtained with optically transparent scintillators is limited because of the larger width of the light spread on the EM-CCD. This can be partly overcome by the use of a detection algorithm that takes into account the interaction-depth dependent light spread[144,145,165] (chapter 2 and 3) or by shaping the scintillators such that depth-of-interaction distortions are reduced[82,175] (chapter 4).

Traditionally, PMT-based gamma cameras are equipped with fast scintillators ($< 10^{-7}$ s decay time) to handle typical count rates of a few 10^5 cps. Using slow scintillators at these rates, the PMT signals would suffer from pulse pile–up, deteriorating the energy and spatial resolution of the camera. However, for a pre-clinical multi-pinhole setup with a large number of EMCCD-based gamma cameras[54,155] only a few events per frame will typically be present at a frame rate of 50 Hz (this frame rate is limited by the pixel readout rate of the CCD). Although the incident light is integrated for every frame, EMCCD-based gamma cameras can nevertheless detect and characterize multiple scintillation events simultaneously as long as their signals do not spatially overlap significantly.

The relatively long integration times create opportunities for using slow scintillators that have not been considered previously in PMT-based gamma cameras, but which may lead to high-resolution gamma images because of other favorable properties such as their high interaction probability or brightness. EM-CCD gamma cameras could then be used advantageously instead of traditional PMT gamma cameras for (e.g.) multi pinhole small-animal SPECT scanners. Despite the fact that temporal information within the frames is lost, CCD-based scanners can still be used for most fast dynamic scans. For some applications like gated (cardiac) murine scans, challenges with regard to temporal resolution may remain.

Several factors are important in the selection of a scintillator, int. al. light yield, photon emission spectrum, attenuation coefficient for the incoming gamma rays and (intrinsic) background radiation. Firstly, a high light yield is important because a larger amount of optical photons will allow a more precise estimation of the energy and position of the scintillation events; this also requires the emission spectrum of the scintillator to match the spectral response of the EM-CCD. Secondly, a higher attenuation coefficient is

advantageous because it allows a thinner scintillator to achieve the desired interaction probability with, on average, a reduced light spread on the detector as a consequence. A small light spread improves the accuracy of the position estimation[144] (chapter 2) Furthermore, a dense (hence thin) scintillator has the additional advantage that smaller light spreads on the CCD allow operation at a higher count rate. The balance between attenuation coefficient and light yield is crucial, since a scintillator with a high light output could compensate for a low attenuation coefficient (scintillation events can be accurately detected further from the CCD surface in the thicker scintillators required in that case) and vice versa. A low light yield can to some extent be compensated for by applying retro-reflectors to increase the number of light photons reaching the EM-CCD without increasing their spread on the EMCDD[174] (chapter 7).

In the present investigation we test different scintillators in our EMCCD-based gamma camera, in an effort to improve its performance. To this end, we have experimentally compared the spatial resolution, energy resolution and the dark count rate (no source present) of our gamma camera employing several optically transparent scintillators, all with equal (66%) interaction probability for ^{99m}Tc emitted gamma photons.

5.2 Materials and Methods

5.2.1 Scintillators

We have tested a number of candidate materials that appeared promising in terms of scintillation light yield and/or ^{99m}Tc 140 keV radiation attenuation length: CsI:Tl, Lu_2O_3:Eu, $(Gd,Lu)_2O_3$:Eu and $CdWO_4$. CsI:Tl is currently used because of its high light yield (~ 54-66 photons/keV[81,218]), in combination with a good correspondence of its emission spectrum to the sensitivity of the EM-CCD that we employ.

Lu_2O_3:Eu (5% doping) was selected for its large mass attenuation coefficient for 140 keV radiation (13.3 cm^{-1}, compared to 3.6 cm^{-1} for CsI:Tl). Furthermore, its measured light yield of 50-70 photons/keV is similar to that of CsI:Tl (see light yield setup described elsewhere[219]). The $(Gd,Lu)_2O_3$:Eu material is similar to Lu_2O_3:Eu but approximately half of the Lu has been replaced by Gd in order to reduce the intrinsic activity (due to ^{176}Lu-emission). Its density is approx. 10% lower than that of Lu_2O_3:Eu, but its light yield is comparable (70 photons/keV, [219]). The Lu_2O_3:Eu and $(Gd,Lu)_2O_3$:Eu scintillators are so-called ceramic scintillators; these materials are not monocrystalline but polycrystalline, with average grain size of ~100 microns, phase purity of >99.5% and with residual porosity of <0.6%. Further details on the fabrication and morphology of these materials can be found elsewhere[220]. In general, optical scatter can occur in transparent ceramics at grain boundaries, particularly if any residual porosity or secondary phase is present. However the samples used for these experiments exhibited low optical scatter; between 0.1 and 0.2 cm^{-1} for Lu_2O_3:Eu and between 0.03 and 0.08 cm^{-1} for $(Gd,Lu)_2O_3$:Eu (the setup is described elsewhere[220]). Therefore, optical scatter was not expected to degrade the scintillators' performance for thicknesses up to a few millimeters as considered in this work.

Finally, $CdWO_4$ was included because it has a gamma attenuation length (9.0 cm^{-1}) that is almost equal to $(Gd,Lu)_2O_3$:Eu while being monocrystalline. However, its light yield is only approx. 25-33% of that of CsI:Tl (20 photons/keV[81], ~15 photons/keV[221]).

The properties of the scintillators used in the experimental comparison are summarized in Table 5.1. Thicknesses for 66% interaction probability are also indicated, the figures are based on attenuations lengths from the NIST XCOM database[171]. The attenuation lengths include both photoelectric and Compton effects. The CsI:Tl and $CdWO_4$ crystals were approx. 1.2 × 1.2 cm^2 in size in order to fit properly onto the EM-CCD detector; the circular Lu_2O_3:Eu and $(Gd,Lu)_2O_3$:Eu samples measured 1.2 cm in diameter. All scintillators had been polished on top and bottom prior to detector mounting.

Table 5.1: Summary of the relevant properties of the scintillation crystals compared in this work.

Scintillator	CsI:Tl	Lu_2O_3:Eu	$(Gd,Lu)_2O_3$:Eu	$CdWO_4$
	Monolithic	Ceramic	Ceramic	Monolithic
Light output for 140 keV gamma [photons]	8400	7000-9800	7000-9800	2100-2800
Peak emission wavelength λpeak [nm]	560	610	610	475
Refractive index at λpeak	1.79	1.94	1.92	2.24
Thickness for 66% interaction probability at 140 keV [mm]	3.0	0.85	1.0	1.2
Scintillator decay time [s]	1	1-2 · 10^3	1-2 · 10^3	14

5.2.2 EMCCD-based gamma camera, read-out electronics and algorithm

The scintillation gamma camera that was used in the current investigation has been described in detail elsewhere[138,146], only a brief overview is presented here. Our setup employed a back-illuminated CCD97 from E2V technologies. This device has a sensitivity exceeding 90% for visible photons in the range of 500 to 650 nm, matching very well the emission wavelengths of the considered crystals. The EM-CCD has an internal gain mechanism based on electron multiplication that results in a sub-electron noise level per pixel when the device is cooled to -30 ℃. The photosensitive area consists of 512 lines of 512 pixels that are 16 × 16 μm^2 in size, resulting in a total area of 8.2 × 8.2 mm^2. The crystals were coupled with Scionix BC90/147 optical grease to a ~3 mm thick fiber optic interface on the EM-CCD. No reflectors have been applied.

Read-out of the EM-CCD was performed by an in-house developed electronics board that transfers the CCD frames to a PC via a Matrox Meteor II framegrabber. The camera was read out at a rate of 50 frames per second and was operated in (gamma) photon-counting mode through post-processing of the complete images.

The photon-count algorithm that analyzed the individual EM-CCD frames is capable of detecting the position (both in *x*-, *y*-coordinates and the depth-of-interaction) and relative

energy of the individual scintillation events through correction of electronic background and multi-scale filtering (for an extensive description of the multi-scale photon-count algorithm[144] see chapter 2). In said paper, 10 different filter widths (scales) have been included in the algorithm and it was found that including more scales has only a small effect on the performance. For the different tested scintillators we applied 10-12 scales and the range of the scales was verified for each crystal by line source measurements at oblique (~45 ˚) angles. This allowed us to estimate the filter width that corresponds to scintillation events in the top of the crystal; the maximum filter width for each crystal was set such that it exceeded the maximum light spread of the scintillation events for that crystal thickness, to ensure inclusion of all events.

5.2.3 Measurements

For the different scintillators we compared the energy and spatial resolution and the dark count rate. To this purpose, each scintillator was tested in our gamma camera set-up, shown in figure 5.1. A 30-μm-wide slit was placed on top of the camera, which was irradiated with a ^{99m}Tc source with an activity of around 40 MBq. Because of source strength regulations in our lab the average detector countrate was around or below one event per frame. For the electronic background correction a series of frames without radio-active source was registered; for the Lu_2O_3:Eu and $(Gd,Lu)_2O_3$:Eu measurements this necessitated removal of the scintillator, because of their intrinsic radio-activity.

Energy spectra were calculated as histograms of the energy values of the events detected in an area covering half of the CCD surface with the slit centered in the image. This was to prevent edge effects of the circular Lu_2O_3:Eu and $(Gd,Lu)_2O_3$:Eu samples in the corners of the EM-CCD to affect the comparison. The energy resolution is the ratio of the measured full-width-at-half-maximum (FWHM) of the photopeak and the photopeak position in the energy spectrum. Scintillation events within energy windows ranging from -50% to +50% of the energy peak value were included in the calculation of the spatial resolution and the dark count measurements.

The spatial resolution of the camera was determined as the measured full-width-at-half-maximum (FWHM) of the profile of the image of the slit, corrected for the width of the slit itself[138]. To show the effects of electronic noise and inherent (^{176}Lu) scintillator activity we have measured the number of background events (per frame *within the appropriate energy window*) for each scintillator when the camera was not irradiated (i.e. dark counts).

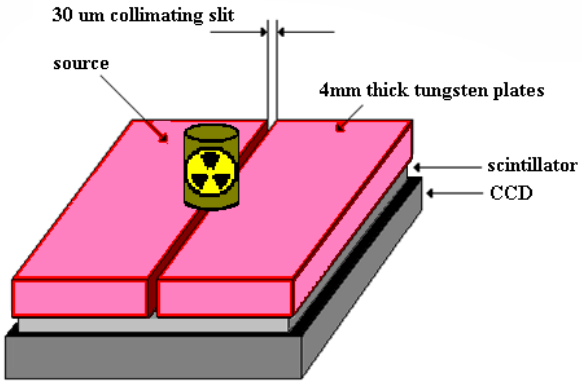

Figure 5.1: Experimental setup for determination of the spatial and energy resolution. A ^{99m}Tc source is placed in proximity to the gamma camera, which is irradiated through a 30-µm-wide slit.

5.3 Results

Figures 5.2 and 5.3 show the energy spectra and line profiles obtained with the different scintillators. The values for energy and spatial resolution derived from these figures, as well as the dark counts, are listed in table 5.2. In figure 5.4 we plot spatial (x-axis) vs. energy resolution (y-axis), indicating the relation between these quantities for the different scintillators. In such a plot, the scintillator with the best overall performance will be found in the lower left corner.

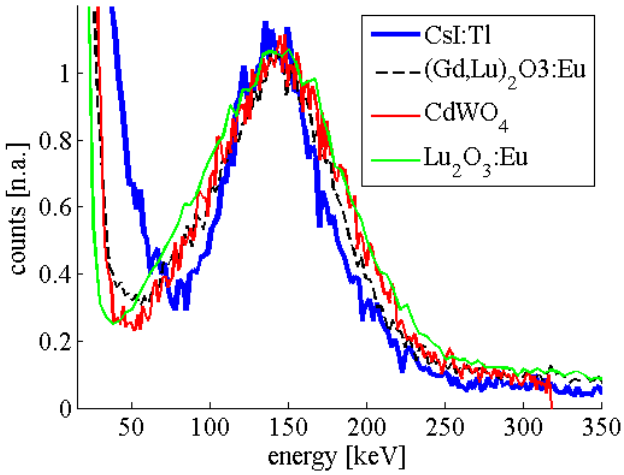

Figure 5.2: Energy spectra for different scintillation crystals, each with 66% interaction probability for 140 keV gammas.

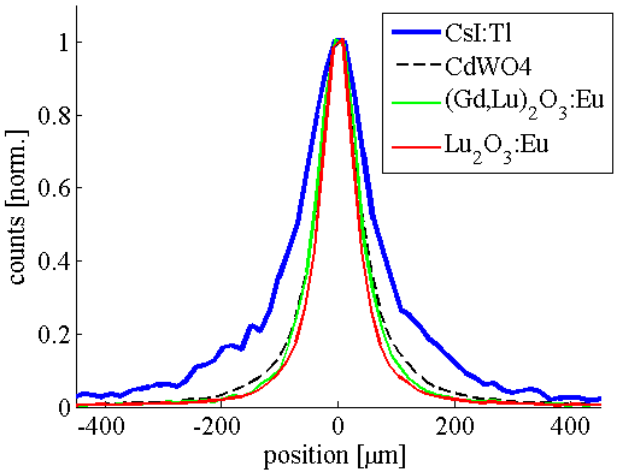

Figure 5.3: Profiles of the line source for different scintillation crystals, each with 66% interaction probability for 140 keV gammas.

Table 5.2: Results of the energy resolution, spatial resolution and dark count measurements.

Crystal	CsI:Tl	Lu_2O_3:Eu	$(Gd,Lu)_2O_3$:Eu	$CdWO_4$
Energy Resolution [%]	53	84	75	80
Spatial Resolution				
(FWHM) [µm]	147	65	75	87
(FWTM) [µm]	465	190	238	285
Dark counts [frame^{-1}]	$1.4 \cdot 10^{-3}$	$8.8 \cdot 10^{-2}$	$4.8 \cdot 10^{-2}$	$2.0 \cdot 10^{-3}$

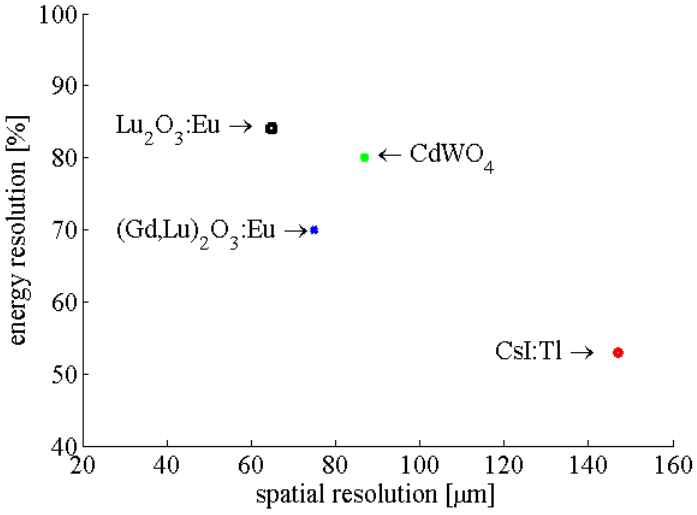

Figure 5.4: Comparison of the performance of the different scintillation crystals, by displaying measured spatial vs. energy resolution.

As can be inferred from table 5.2 and figure 5.4, there is no single scintillator in this study that has the best performance in terms of spatial *and* energy resolution. The energy resolution (figure 5.2) obtained with CsI:Tl (53%) is significantly better than that obtained with the $CdWO_4$, $(Gd,Lu)_2O_3$:Eu and Lu_2O_3:Eu scintillators (80%, 75% and 84%

respectively). However, the Lu_2O_3:Eu ceramic achieves the best spatial resolution, (closely) followed by the $(Gd,Lu)_2O_3$:Eu and $CdWO_4$ scintillators (FWHM: 65 μm, 75 μm and 87 μm respectively, FWTM: 190 μm, 238 μm and 285 μm resp.). The spatial resolution of the CsI:Tl crystal (147 μm FWHM, 465 μm FWTM) is considerably worse, by more than a factor of 2. One can see that the full-width-at-tenth-maximum (FWTM) values of the line source profiles scale roughly with the FWHM values.

From table 2 one notes that the numbers of dark counts for Lu_2O_3:Eu and $(Gd,Lu)_2O_3$:Eu are significantly higher than for $CdWO_4$ and CsI:Tl.

5.4 Discussion

The use of a denser scintillating material considerably improves the spatial resolution of our EMCCD-based gamma detector. This is because denser materials allow the use of thinner scintillators for a certain desired interaction probability which reduces, on average, the light spread on the EM-CCD. There is a clear correlation between the thickness of the scintillation crystal and the measured spatial resolution, with CsI:Tl having the worst (147 μm FWHM, 465 μm FWTM) and Lu_2O_3:Eu having the best (65 μm FWHM, 190 μm FWTM) performance in this respect.

The $(Gd,Lu)_2O_3$:Eu and Lu_2O_3:Eu scintillators have a dark count rate which is significantly higher than that of CsI:Tl and $CdWO_4$, by up to a factor of 60. We believe that this is caused by an intrinsic background level due to the natural radioactivity of ^{176}Lu present in these scintillators (about 50 Bq for our samples). The ^{176}Lu decay generates scintillation events with a continuous energy spectrum up to ~600 keV, overlapping with the spectrum of the 140 keV ^{99m}Tc (true) events. The background of $(Gd,Lu)_2O_3$:Eu is approx. 40% below that of Lu_2O_3:Eu, corresponding to the different quantities of Lu in these scintillators. These numbers show that for expected event rates in preclinical multi-pinhole SPECT (a few events per frame), dark counts (less than 0.1 per frame) constitute a small percentage of the total number of detected events.

The energy resolution is worse for the three newly tested scintillators compared to CsI:Tl. One would expect the thin scintillators Lu_2O_3:Eu and $(Gd,Lu)_2O_3$:Eu, with an expected light yield similar to that of CsI:Tl[I], to perform better than $CdWO_4$, but the results indicate differently. Measurements with a second $(Gd,Lu)_2O_3$:Eu scintillator have confirmed that the degraded energy resolution was not due to high optical scatter or a badly mounted sample as there was only a minor improvement of energy resolution from the reported 75% to 70%, which is just outside the statistical error of ±3%. The effect of the intrinsic ^{176}Lu activity on the energy resolution is also expected to be small. The emitted γs and βs give a wide but low background in the energy spectrum when the crystal is unirradiated.

[I] We would like to point out that the light yield of CsI:Tl is expected to degrade by ±10% at a temperature of -30 ° C; the light yields of Lu_2O_3:Eu and $(Gd,Lu)_2O_3$:Eu are not known exactly, but like $CdWO_4$ they are not expected to have a strong temperature dependence.

There are several possible explanations for the reduced energy resolution. Firstly, it is possible that the CCD detects less photons than expected, as the exact light yields of the scintillator samples in our gamma camera setup are unknown. Furthermore, the relatively high optical density (refractive index) of Lu_2O_3:Eu and $(Gd,Lu)_2O_3$:Eu results in a smaller critical angle of reflection, reducing the relative amount of scintillation photons reaching the CCD compared to a setup with CsI:Tl.

Another reason for the reduced energy resolution could be that, contrary to our initial assumption, the integration time of the CCD is not sufficient to collect all of the scintillation photons for Lu_2O_3:Eu and $(Gd,Lu)_2O_3$:Eu in a single frame, especially if the scintillation occurs just before the end of the integration period (20 ms). We have estimated this effect by simulating scintillation events detected by the EM-CCD with a 50% energy resolution and 1 or 2 ms decay time, arriving randomly in the integration time window (frame) and integrating these light signals till the frame is read out. We found that this partial integration does indeed degrade the energy resolution; about 10-20% (relatively) of the energy resolution of Lu_2O_3:Eu and $(Gd,Lu)_2O_3$:Eu is due to this effect. Experimentally, we have noticed (in particular for Lu_2O_3:Eu) that some events seem to be spread out over two CCD frames, supporting this hypothesis. A correction for this partial integration effect may improve the energy resolution of Lu_2O_3:Eu and $(Gd,Lu)_2O_3$:Eu to surpass the one of $CdWO_4$. We do not expect afterglow to play a role here because i) no afterglow was observed by us in decay time measurements and ii) the count rates are rather low, limiting afterglow buildup, if afterglow would nevertheless be present.

The tested $CdWO_4$ scintillator is a monocrystalline material that does not suffer from optical scatter, and has less than half the thickness of the CsI:Tl scintillator. Therefore, compared to CsI:Tl, the light spots on the detector are relatively small and well-defined. However, its energy resolution is worse than that of CsI:Tl; we believe that this is mainly caused by the fact that its light yield is expected to be only ~25-30% of that of CsI:Tl. Moreover, it has a higher optical refractive index than CsI:Tl, which further reduces the amount of scintillation photons to be detected by the EM-CCD. Note that energy resolution is less important for small animal imaging than for clinical applications, as scatter rejection is often not required due to the lower amount of scatter in animals compared to humans.

Given our results, we believe that for improving both the energy and spatial resolution of our gamma camera one should find a scintillator which has at least an attenuation coefficient and light yield as high as Lu_2O_3:Eu has, but without natural radioactive isotopes. Moreover, to obtain an energy resolution similar to CsI:Tl or better, its light yield should be considered in conjunction with the refractive index. For the presently used scintillation detection algorithm the energy resolution will be better when the scintillator has a decay time smaller than the CCD integration period (< 1 ms). The development of a novel detection algorithm may relax the latter requirement.

5.5 Conclusion

Dense, though 'slow', scintillators $CdWO_4$, $(Gd,Lu)_2O_3$:Eu and Lu_2O_3:Eu considerably improve the spatial resolution of our photon-counting gamma camera compared to CsI:Tl, however at the cost of degraded energy resolution. This can be attributed to the reduced light yield (in the case of $CdWO_4$), the refractive index of the scintillator (for $CdWO_4$, $(Gd,Lu)_2O_3$:Eu and Lu_2O_3:Eu) or the slow decay time of $(Gd,Lu)_2O_3$:Eu and Lu_2O_3:Eu). We conclude that the investigation of dense scintillators that were previously not considered in gamma detectors, because of their slow decay times, opens new possibilities for improving the spatial resolution of CCD-based scintillation cameras.

5.6 Acknowledgements

The authors would like to thank Paul Schotanus of Scionix Netherlands for valuable discussions and providing us with the CsI:Tl and $CdWO_4$ scintillators. This work was sponsored in part by the (Netherlands) Ministry of Economic Affairs, Agriculture and Innovation IOP photonics grant IPD067766. The lutetia-based materials development was supported by the U.S. Department of Energy (Enhanced Surveillance Subprogram), and conducted by Lawrence Livermore National Laboratory under Contract DE-AC52-07NA27

Chapter 6

Cramer Rao lower bound optimization of an EM-CCD based scintillation gamma camera

Marc A N Korevaar[1], Marlies C Goorden[1], and Freek J Beekman[1,2]

[1]Section of Radiation Detection and Medical Imaging, Department of Radiation, Radionuclides and Reactors, Applied Sciences, Delft University of Technology, Mekelweg 15, 2629 JB Delft, the Netherlands
[2]MILabs, Universiteitsweg 100, 3584 CG, Utrecht, the Netherlands

submitted to *Phys. Med. Biol.*

Abstract

Scintillation gamma cameras based on low noise Electron Multiplication (EM-)CCDs can reach high spatial resolutions. For further improvement of these gamma cameras, more insight is needed in how various parameters that characterize these devices influence their performance. Here we use the Cramer Rao lower bound (CRLB) to investigate the sensitivity of the energy and spatial resolution of an EM-CCD based gamma camera to several parameters. The gamma camera setup consists of a 3 mm thick CsI:Tl scintillator optically coupled by a fiber optic plate to the E2V CCD97 EM-CCD. For this setup, position and energy of incoming gamma photons are determined with a maximum-likelihood detection algorithm. To serve as basis for the CRLB calculations, accurate models for the depth-dependent scintillation light distribution are derived and combined with a previously validated statistical response model for the EM-CCD. Sensitivity of the lower bounds for energy and spatial resolution to the Electron Multiplication (EM) gain and the depth-of-interaction (DOI) are calculated and compared to experimentally obtained values. Furthermore, calculations of the influence of the number of detected optical photons and noise sources in the image area on the energy and spatial resolution are presented. Trends predicted by CRLB calculations agree with experiments, although experimental values for spatial and energy resolution are typically a factor 1.5 above the calculated lower bounds. Calculations and experiments both show that an intermediate EM gain setting results in the best possible spatial or energy resolution and that the spatial resolution of the gamma camera degrades rapidly as a function of the DOI. Furthermore, calculations suggest that a large improvement in gamma camera performance is achieved by an increase of the number of detected photons or a reduction of noise in the image area. A large noise reduction, as is possible with a new generation of EM-CCD electronics, may improve the energy and spatial resolution by a factor 1.5.

6.1. Introduction

Multi-pinhole small animal Single Photon Emission Computed Tomography (SPECT) imaging[44,45,47,48] can yield image resolutions below half a mm[49,50,124]. At present these ultra-high resolutions are obtained using traditional gamma cameras, by employing the principle of pinhole magnification. For future improvements of small animal SPECT imaging, gamma cameras with better spatial resolution and significant energy discrimination are essential[53,140,153,154,155].

Compact, high resolution gamma imaging cameras are being developed by many research groups[157,158,159,161]. In a subset of these gamma cameras micro-columnar CsI:Tl scintillators are being used in combination with EM-CCDs[137,138,140,146,165,222,223]. In such CCD based detectors individual scintillation events can be detected in photon counting mode, enabled by readout at high frame rates. This detection method greatly improves the spatial resolution compared to integration of the scintillation light signal[82]. The sensitivity of these detectors can be improved by using continuous instead of micro-columnar scintillators which are available in larger thicknesses[144,174] (chapter 2 and 7). When using such continuous scintillators, a detection algorithm that models the depth-of-interaction (DOI) dependent light distribution[144] (chapter 2) is essential to achieve good performance. A detection algorithm that also takes the EM-CCD statistics into account in the detection algorithm leads to further improvements[145,165] (chapter 3).

An important characteristic of a detector such as a gamma camera is the lower bound on its performance, i.e. the best performance that could theoretically be obtained. The most widely used method for calculating the lower bound is the Cramer-Rao lower bound (CRLB) method[224]. It has been used for determining the lower bound in source localization and wave direction measurement[225,226] and also for optimization of system parameters in MRI[227], localization[228], frequency estimation[229], X-ray imaging[230] and SPECT scanners[231]. For designing detectors with an optimal performance one would like to know the sensitivity of the lower bound to changes of detector parameters. Such an optimization method has been applied to an APD based and also a SiPM based scintillation PET detector[232,233], timing of PET detectors[234,289] and an Anger camera[235].

In this paper we present CRLB calculations on a gamma camera consisting of a 3 mm thick CsI:Tl scintillator optically coupled to a photodetector by a fiber optic plate (FOP). Lower bounds on the spatial and energy resolution of this gamma camera are calculated and the sensitivity of these lower bounds to several parameters of the gamma camera is investigated. Parameters considered here are EM gain, DOI, the number of detected scintilation photons and noise originating in the image area, such as dark current noise and clock induced charge (cic) noise. Investigating the effect of the number of detected photons and noise on the performance is relevant because of the ongoing search for scintillators[236] and recently developed new EM-CCD electronics that can reduce the noise by more than a factor 10.[189,237] Trends predicted for EM gain and DOI are validated by experiments.

6.2. Methods

In general, the Cramer Rao method can be used to estimate the lower bound on the spatial and energy resolution of a detector. Here we applied this method to our EM-CCD based scintillation gamma camera. Input to these CRLB calculations was a statistical model for the detector response to incoming gamma photons which is described in section 6.2.1. Subsequently, in section 6.2.2 equations for the CRLB are provided. Finally, the experimental detector setup, detector parameters and validation methods are described in sections 6.2.3, 6.2.4 and 6.2.5 respectively.

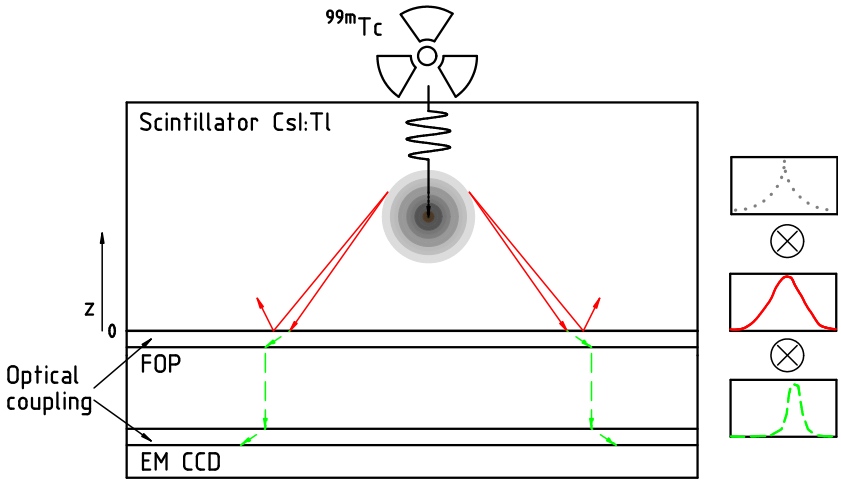

Figure 6.1: Diagram showing three different processes that determine the light distribution as detected by the EM-CCD; the distribution of the centroid of the energy deposition in the scintillator (gray, dotted), the light distribution in the scintillator including transmission through the optical coupling for a single optical point source (red, solid) and the minimum light spread in the optical components between scintillator and EM-CCD (green, dashed). It was assumed that a convolution of these three distributions accurately represents the mean light distribution on the EM-CCD.

6.2.1. Detector response model for incoming gamma photon

To arrive at an accurate description of the detector response we took into account the gamma energy deposition distribution due to multiple interactions, the light distribution in the scintillator, the optical coupling between scintillator and EM-CCD and a detailed statistical model for the EM-CCD response. Our approach is the following: we assume that the mean light distribution at the EM-CCD can be described as a convolution[238] of three probability distributions (figure 6.1), describing (i) the distribution pr_c of the centroid of the energy deposition in the scintillator, (ii) the light distribution λ_{ph} for a single optical point source in the scintillator including the transmission of the optical coupling between scintillator and EM-CCD, and (iii) the additional light spreading $\lambda_{o.c.}$ in the optical coupling. These three probability distribution are derived below in sections 6.2.1.1, 6.2.1.2 and 6.2.1.3. The total mean light distribution on the detector, λ_{tot} is then given by a convolution of these 3 distributions,

$$\lambda_{tot} = pr_c \otimes \lambda_{ph} \otimes \lambda_{o.c.} \tag{6.1}$$

The statistical EM-CCD model that uses the mean light distribution as its input was derived and validated in a previous paper and it is summarized in subsection 6.2.1.4.

6.2.1.1. Mean interaction position A gamma photon can interact with a scintillator via different mechanisms. For ^{99m}Tc, the most widely used SPECT isotope[239], the dominant mechanism in a CsI:Tl scintillator is the photoelectric effect. However scatter such as inelastic Compton scatter is also present. Furthermore, after initial energy deposition by the photo electric effect or Compton scatter, K_α X-rays play a significant role by depositing the energy further away from the initial interaction position. The relative occurrence of these different interaction mechanisms is determined by the type of scintillator and the gamma photon energy. These processes can cause the energy of a gamma photon to be absorbed in multiple interaction positions. In this paper we followed the strategy of approximating multiple interaction positions by a single interaction position at the centroid of the deposited energy[238,240] taking into account the probability distribution of these centroids over the

scintillator volume. This probability distribution was calculated using Monte Carlo software Geant4 version 9.4.[241] The Geant4 low energy Electromagnetic physics Lawrence Livermore model was used for detailed modelling of all relevant processes. The resulting centroid distribution was fitted with the following empirical exponential function, somewhat similar to previous research[238],

$$pr_c(\vec{r}) = a_1 \exp\left(-a_2 |\vec{r}|^{a_3}\right). \tag{6.2}$$

6.2.1.2. Scintillation light distribution including transmission through FOP When a gamma photon is absorbed in the scintillator, optical photons are generated (shown in figure 6.1). We did not take the fluctuation in the total number of optical photons generated in the scintillator into account as it is small in comparison to the other statistical random variables. Previously we modeled the mean number of scintillation photons $\lambda_{ph,i}$ incident on each pixel i of the detector, assuming a single interaction position and neglecting interactions of optical photons within the scintillator but taking into account Fresnel reflections and the optical properties of the FOP[145] (chapter 3). We validated that the resulting light distribution can be approximated well by a simple Gaussian with a cutoff at an angle ϕ_{cutoff}:

$$\lambda_{ph,i}\left(\vec{\theta}\right) = H\left[\phi_{\text{cutoff}} - \arctan\left(\frac{\left|\vec{r}_i - \vec{\theta}_{\text{r}}\right|}{\theta_{\text{z}}}\right)\right] \frac{\varepsilon\theta_{\text{N}} A}{2\pi\sigma^2_{\text{DOI}}(\theta_{\text{z}})} \exp\left[-\frac{\left|\vec{r}_i - \vec{\theta}_{\text{r}}\right|^2}{2\sigma^2_{\text{DOI}}(\theta_{\text{z}})}\right] + \theta_{\text{bg}}, \tag{6.3}$$

$$\vec{\theta} = \left(\vec{\theta}_{\rho}, \theta_{\text{N}}, \theta_{\text{bg}}\right) = \left(\vec{\theta}_{\text{r}}, \theta_{\text{z}}, \theta_{\text{N}}, \theta_{\text{bg}}\right) = \left(\theta_{\text{x}}, \theta_{\text{y}}, \theta_{\text{z}}, \theta_{\text{N}}, \theta_{\text{bg}}\right).$$

Here H is the Heaviside step function, $\vec{\theta}$ is the parameter vector describing the scintillation event; it contains the scintillation position $\vec{\theta}_{\rho}$, consisting of $\vec{\theta}_{\text{r}} = (\theta_{\text{x}},\theta_{\text{y}})$ and θ_{z} representing the x, y and z coordinate of the scintillation, the number of generated optical photons θ_{N} and the background signal θ_{bg}. Furthermore, $\vec{r}_i = (x_i, y_i)$ denotes the lateral pixel position, $\sigma_{DOI}(\theta_z)$ describes the width of the light distribution which depends on θ_{z}, A is the area of an EM-CCD pixel and ε is an efficiency factor. The z-axis was chosen perpendicular to the scintillator plane starting at the scintillator bottom (see figure 6.2). In this paper we chose ε and σ_{DOI} such that the light distribution agreed with the amplitude and the width of a measured scintillation (see section 6.2.5.1)

6.2.1.3. Optical coupling light distribution While in (6.3) the angle-dependent transmission coefficient of the optical coupling between scintillator and EM-CCD was taken into account, light spreading in the optical components was ignored. Ignoring this can lead to the unrealistic result that scintillations at the bottom of the scintillator can be detected with a resolution equivalent to the pixel size. It is therefore essential to include the light distribution due to the optical grease and the FOP. The shape and width of this light distribution were obtained from measurements of individual scintillations that occur at the bottom of the scintillator where it can be assumed that light spreading (nearly) only results from the optical components. These measured light distributions were fitted with a Gaussian.

$$\lambda_{o.c.}(r) = \frac{1}{2\pi s^2_{o.c.}} \exp\left(-\frac{r^2}{2s^2_{o.c.}}\right) \tag{6.4}$$

with r being the lateral distance from the primary interaction position and $s_{o.c.}$ the standard deviation of the light distribution width.

6.2.1.4. Statistical model For the statistical model of the EM-CCD we used the expressions derived previously in chapter 3.[145] In the derivation of these expressions the photon statistics, the statistics of the multiplication register and the pixel and readout noise were taken into account. The probability distribution $pr_{\text{output}}(g_i|\bar{n}_i)$ of detecting g_i electrons at the EM-CCD output for pixel i given a mean number of electrons $\bar{n}_i$ in the same pixel can be expressed as

$$pr_{\text{output}}(g_i|\bar{n}_i) = H(g_i)\exp\left(-\bar{n}_i - \frac{g_i}{gain}\right)\sqrt{\frac{\bar{n}_i}{g_i \cdot gain}}I_1\left(2\sqrt{\frac{\bar{n}_i g_i}{gain}}\right) + \exp(-\bar{n}_i)\frac{1}{\sqrt{2\pi}\sigma}\exp\left(-\frac{g_i^2}{2\sigma^2}\right), \tag{6.5}$$

where $H(x)$ is the Heaviside step function, *gain* the gain of the EM-register, I_1 the modified Bessel function of the first kind and σ the standard deviation of the Gaussian readout noise. The distribution was normalized to 1 for integration over g_i from -∞ to +∞.

The mean number of electrons $\bar{n}_i$ in the normalized conditional probability (6.5) was assumed to be the sum of the mean number of electrons due to noise in the image area $\bar{n}_{\text{n}}$ (noise per pixel which is assumed to be independent of the pixel index) and the mean number of photon generated electrons (the mean number of light photons in a pixel (6.1) multiplied by the EM-CCD Quantum Efficiency (QE)). Multiplying this distribution over all pixels i gives the conditional probability for the measured pixel values $\vec{g}$ given a scintillation described by parameter vector $\vec{\theta}$

$$pr_{\text{output}}\left(\vec{g}|\vec{\theta}\right) = \prod_i pr_{\text{output}}\left(g_i|\text{QE}\cdot\lambda_{tot,i}\left(\vec{\theta}\right) + \bar{n}_{\text{n}}\right). \tag{6.6}$$

6.2.2. Cramer Rao lower bound

Using the probability distribution from (6.6) we can calculate the CRLB for the n'th component of the parameter vector θ[224,242]:

$$var\left(\hat{\theta}_n - \theta_n\right) \leq \left\langle \left[\frac{\partial}{\partial\theta_n}\log\left[pr_{\text{output}}\left(\vec{g}|\vec{\theta}\right)\right]\right]^2\right\rangle^{-1}. \tag{6.7}$$

Here $\hat{\theta}_n$ denotes the estimated value of θ_n.

6.2.3. Detector setup: EM-CCD, optical coupling, scintillator and algorithm

The gamma camera consisted of a 3 mm thick CsI:Tl SCIONIX scintillator optically coupled, by a FOP, to the E2V CCD97 EM-CCD[126,127,166]. The FOP reduces the number of optical photons that reach the EM-CCD at large oblique angles (see appendix of chapter 3)[145]. The EM-CCD was cooled to -40° Celsius to reduce the thermal dark current noise, a component of the noise in the image area. The CsI:Tl thickness of 3 mm used in the simulations and experiments results in an interaction probability for ^{99m}Tc photons (141 keV) of 66%. The scintillation position and energy were determined using a maximum-likelihood scintillation detection algorithm[145] (chapter 3). A schematic of the gamma camera is shown in figure 6.1 and figure 6.2 and is described in detail in previous publications[144,145] (chapter 2 and 3).

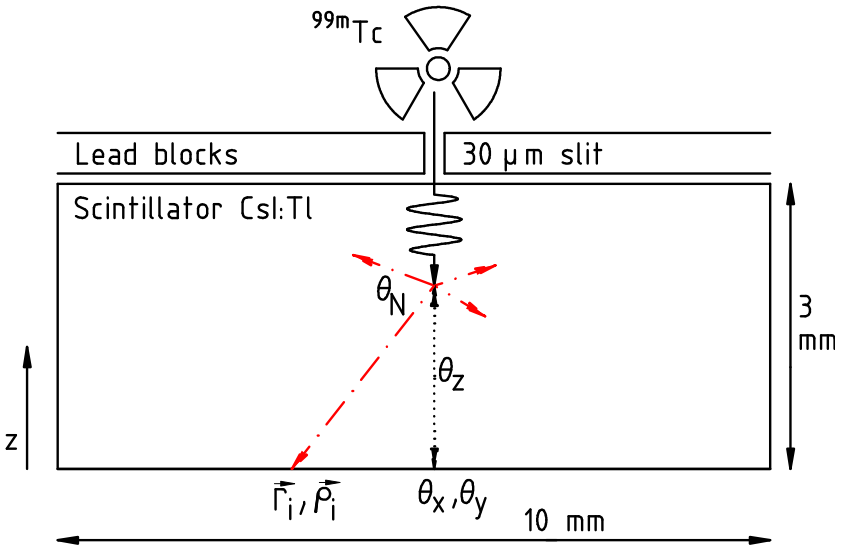

Figure 6.2: Measurement and simulation setup for the EM-CCD scintillation gamma camera. Shown is the ^{99m}Tc source, the lead blocks with a slit and the CsI:Tl scintillator with a single gamma photon interacting at position θ_x,θ_y,θ_z.

6.2.4. Parameters for simulated detector setup

For the CRLB calculation we modeled the EM-CCD based gamma camera with parameters chosen the same or similar to those in experiments (see section 6.2.3). The values of the different noise sources and the light distribution parameters are provided in table 6.1. The parameters, not treated before are the number of analog to digital converter (ADC) bins, the gain after the EM gain from electrons to digital units (DU) and the total detected photons per scintillation calculated with (6.3).

Table 6.1: Cramer Rao detector parameters, the first group of parameters is derived from datasheets and the measurement setup, the second group of parameters are chosen based on measurements of the EM-CCD output and the measured scintillation light distribution in 6.3

Parameter	Value
Scintillator thickness [mm]	3
QE [%]	$9 \cdot 10^1$
pixel size [µm]	16
ADC bins	2^8
θ_N [photons MeV$^-$1]	59600 [236]
σ_{DOI} [µm]	$0.577 \cdot \theta_z$
ε	0.54
ϕ_{cutoff} [°]	45
total detected photons per scintillation	$6 \cdot 10^2$
$s_{o.c.}$ [µm]	50
gain	5000
σ [electrons pixel^{-1}]	2000
$\bar{n}_n$ [electrons pixel^{-1}]	0.1
gain after EM [DU electrons^{-1}]†	0.005

6.2.5. Validation methods

6.2.5.1. Scintillation light distribution validation The mean light distribution of optical photons on the EM-CCD at a number of depths of the scintillation events (θ_z) was measured previously. The setup for this measurement is described in chapter 3.[145] Here we used these measurements to validate (6.1); the behaviour of the amplitude and width of the scintillation light distribution in the CsI:Tl scintillator as a function of depth. The absolute value of the efficiency factor ε and σ_{DOI} in 6.3 was obtained from a single scintillation such as shown in chapter 3.[145] At different depths the individual scintillation flashes (for depths < 850 μm) or the sum of many scintillation flashes (for larger depths) were fitted with a Gaussian function where the fit parameters were standard deviation (σ_{DOI}) and amplitude (ε). Fitting sums of individual scintillations for larger depths was necessary because these scintillations have a relatively small amount of photons per pixel compared to the noise.

6.2.5.2. Cramer Rao lower bound validation for gain and DOI We validated the calculated CRLB trend for the energy resolution and spatial resolution as a function of the *gain* experimentally. For the spatial resolution this was done for multiple depth ranges. Furthermore the calculated trend of the CRLB for the spatial resolution as a function of DOI was validated. While the *gain* setting can easily be changed in the experimental set-up, the DOI is not a parameter that can be set at will; it was estimated for each single scintillation event by the maximum-likelihood algorithm[145] (chapter 3) and this information was used.

To experimentally determine the spatial and energy resolution, a line pattern from a ^{99m}Tc source (141 keV), projecting through a slit onto the scintillator, was acquired (illustrated in figure 6.2). The spatial resolution was defined as the Full Width at Half Maximum (FWHM) of the line spread function of the radioactive source corrected for the width of the gamma photon beam due to the slit width of 30 μm. The FWHM energy resolution was obtained by determining the FWHM of the ^{99m}Tc photo-peak for the scintillations in an area around the slit (with a width of 260 pixels).

6.2.6. Cramer Rao lower bound sensitivity to noise in the image area and the number of detected photons

The CRLB sensitivity to noise in the image area and to the number of detected scintillation photons, parameters that can not be varied in our experiment but could in the future be adapted by using a novel EM-CCD, another electronical readout setup, a different scintillator or a scintillator equipped with a reflector, were also calculated and are presented in the results section. When varying one parameter the other parameters were held constant at the values provided in table 6.1.

6.3. Results

6.3.1. Mean light distribution

6.3.1.1. Energy deposition centroid distribution In figure 6.3 the distribution $pr_c(\vec{r})$of the centroid of the energy deposited in the CsI:Tl scintillator is plotted along the x direction (by summation over all y en z). This distribution was obtained from Monte Carlo simulations. The option of setting an energy window on the result and thus selecting only scintillations which deposit all their energy in the scintillator did not influence the outcome significantly. The result was fitted with the exponential function (6.2) with coefficients provided in table 6.2

† DU: digital units

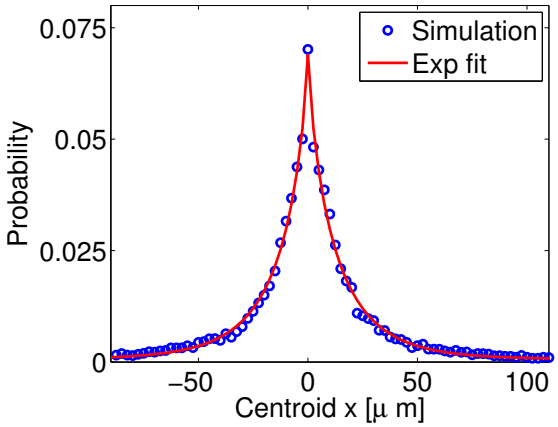

Figure 6.3: Simulated energy centroid distribution in the x direction (by summation over all y en z) with a 3 mm thick CsI:Tl scintillator for ^{99m}Tc (141 keV). The fit is with exponential function (6.2) providing the parameters in table 6.2.

Table 6.2: Exponential fit parameters in (6.2)

Parameter	Value
a_1	0.070
a_2	0.14 [μm^{-a_3}]
a_3	0.77

6.3.1.2. Optical coupling light distribution The minimal light distribution due to the light spreading in the optical coupling layer between scintillator and FOP and in the FOP itself is shown in figure 6.4. This figure represents a measurement of a single scintillation at the bottom of the scintillator. A profile with a fit of the corresponding scintillation with a Gaussian is also shown. Saturation of the measurement, which is due to the combination of a large *gain* and a large intensity on the EM-CCD directly below the scintillation, is clearly visible in this plot.

6.3.1.3. Total light distribution validation With the energy deposition centroid distribution 6.3.1.1, the optical coupling light spreading distribution 6.3.1.2 and the scintillator light distribution (6.3) as its ingredients, the model for the total light distribution is complete (6.1). In figure 6.5, the predictions of this model for the amplitude and width (expressed in standard deviation σ) of the mean scintillation light distribution as a function of depth are shown together with experiments.

To illustrate the importance of taking the minimal light distribution due to optical coupling into account, we have also plotted predictions of our model without considering this distribution. In this case the theoretical light spread and measured values disagree at lower depths. For large depths the measured light spread σ is somewhat above the value of the model, possibly due to reflections at the top of the scintillator or due to the limited accuracy of positioning when summing the scintillations at larger depths.

6.3.2. Validation of CRLB trends with experiments

Experimental results for the energy resolution as a function of *gain* were compared with CRLB calculations in figure 6.6. The CRLB calculations at different depths were combined taking Beer's

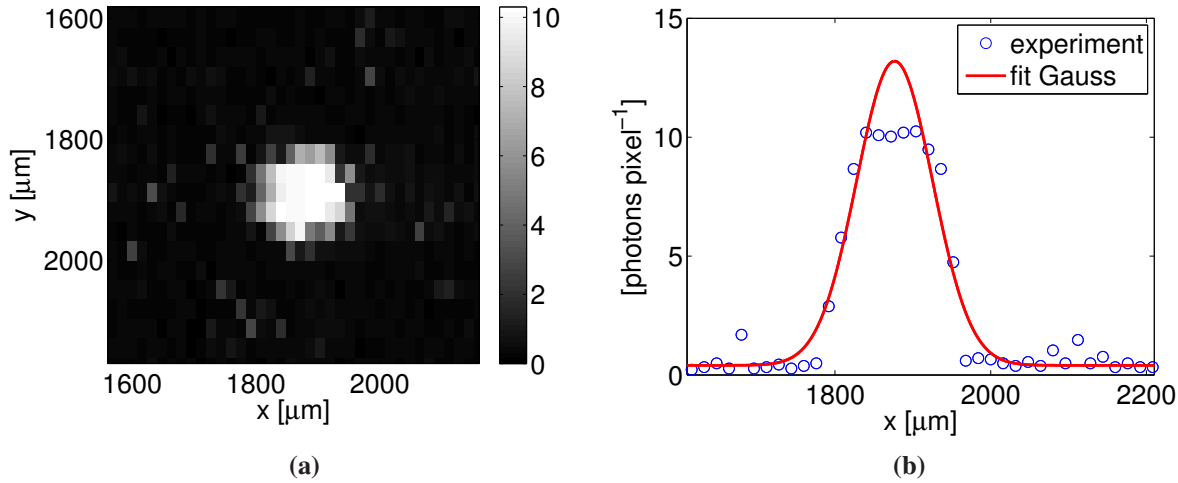

(a) **(b)**

Figure 6.4: **(a)** Example scintillation measured at the bottom of the scintillator resulting in a minimal light distribution on the detector and **(b)** a profile through this scintillation light spot with a corresponding Gaussian fit.

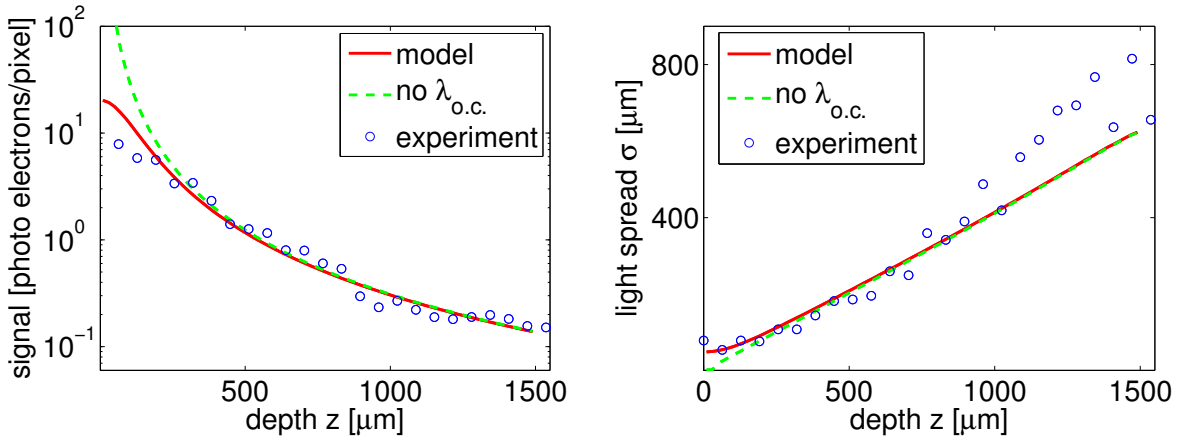

(a) **(b)**

Figure 6.5: **(a)** Mean fitted amplitude and **(b)** mean fitted light spread σ of the measured light distribution of scintillations as a function of the depth at which the gamma photon interacts. The data points at lower depth < 850 µm were obtained by fitting individual scintillations and those at higher depth by fitting the average of multiple scintillations. The amplitude and sigma according to the model (6.1) (red solid line) and the model without the optical coupling light distribution (6.4) (green dashed line) are shown as well.

law into account. For the spatial resolution these results are shown in figure 6.7 for different depth ranges. The CRLBs for spatial and energy resolution, in accordance with the experiments, show an unpronounced minimum for intermediate *gain*. The *gain* at this minimum is the optimal *gain* setting, which should not be too high nor too low. That the *gain* should neither be too high or too low is caused by the need to balance the conflicting requirements of a high *gain* to reduce the effect of the readout noise and a low *gain* to reduce the saturation in the detector.

Furthermore, the energy and spatial resolution as a function of DOI (averaged over the *gain*s plotted in figure 6.6 to reduce the statistical error) are shown in figure 6.8. Both the measurement and the CRLB calculations show that the energy resolution deteriorates slightly with DOI; for the measurement this effect is somewhat larger. For the spatial resolution we see that both the

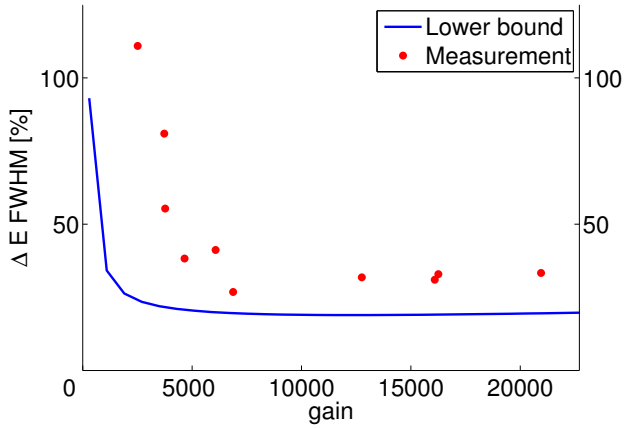

Figure 6.6: Calculated CRLB and measurement of energy resolution as a function of the *gain*.

measurement and the CRLB calculations deteriorate strongly for larger DOI. A scintillator with a larger attenuation coefficient than CsI:Tl which can be thinner and have the same interaction probability as 3 mm CsI:Tl , would be an advantage[236].

In all cases, the trend found in the measurements is similar to the calculated lower bound. However, the CRLB for the energy resolution is approximately a factor 1.5 better than the experimentally found energy resolution, except for low *gain* where the experimental resolution deteriorates earlier than the CRLB. For the spatial resolution the CRLB is typically a factor 1.5 better than the experimental resolution, with the exception of scintillations at small depths which have up to a factor 2.7 difference between CRLB and experiment.

6.3.3. Sensitivities of CRLB to noise in the image area and the detected photons

The sensitivity of the lower bounds to the noise in the image area for the energy resolution and the spatial resolution at different depth ranges is shown in figure 6.9. This type of noise influences the lower bound by a large amount. Lowering the noise from the present value of 0.1 to 0.01 [electrons pixel^{-1}] is predicted to improve the spatial and energy resolution by approximately a factor of 1.5. Such a reduced amount of noise in the image area is feasible by combining cooling, to reduce the thermal dark current noise, with advanced read out electronics, reducing the cic noise[189,237]. Should the noise in the image area be reduced to this level the CRLB for the energy resolution is 14 %.

Finally, the sensitivity of the lower bounds to the number of detected photons per scintillation is shown in figure 6.10. This number, approximately 600 in the current setup, is influenced by the scintillator light output, the light collection efficiency and the EM-CCD Quantum Efficiency (QE). Like noise in the image area, this number is of significant influence on the lower bound. This agrees with experimental findings which show that it is better to use back illuminated CCDs instead of front illuminated CCDs[146], the latter detecting approximately 3 times less photons because of the lower QE. This previously published experimental comparison did involve a micro columnar instead of a continuous scintillator as was used here. As the QE for the back illuminated EM-CCD is already as high as 90 %, little improvement in the number of detected photons is possible by a further increase of the QE. However an increase in the number of detected photons can also be achieved by using improved scintillation light collection efficiency[174] (chapter 7) or choosing a different scintillator material to increase the scintillator light output[236] (chapter 5). A resulting increase in detected

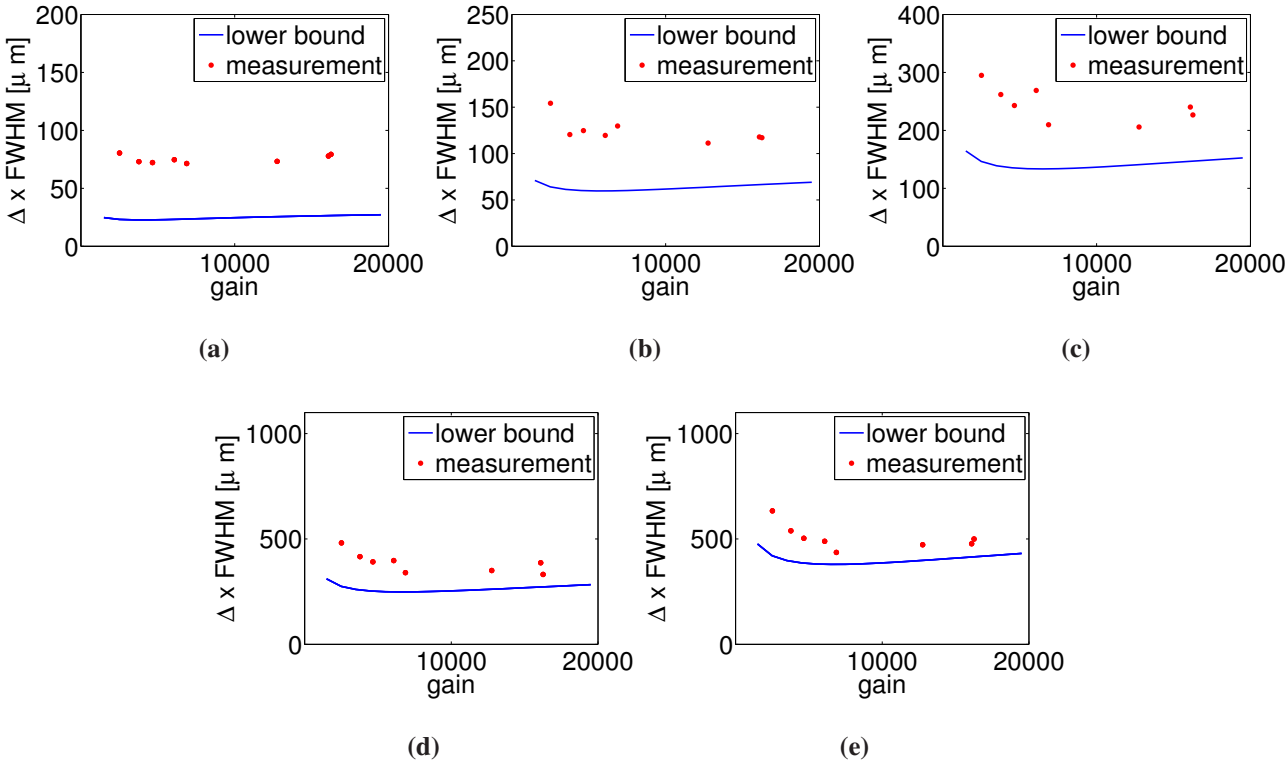

Figure 6.7: Calculated CRLB and measurement of the spatial resolution as a function of the *gain* for depth ranges: **(a)** 0 to 0.5 **(b)** 0.5 to 1, **(c)** 1 to 1.5, **(d)** 1.5 to 2 and **(e)** 2 to 2.5 mm.

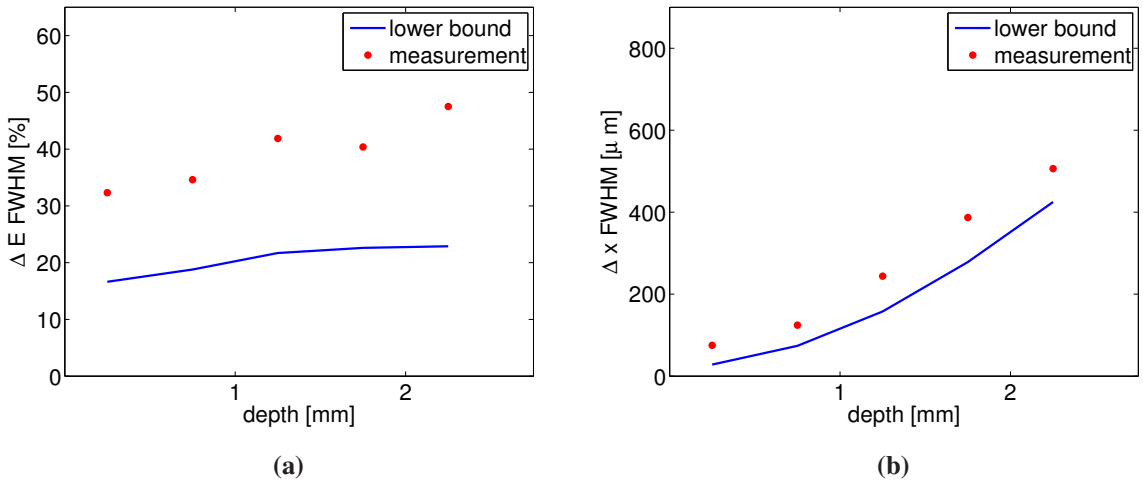

Figure 6.8: Calculated CRLB and measurements of **(a)** the energy resolution and **(b)** the spatial resolution averaged over the *gain* as a function of the depth.

photons of 50 % is predicted to improve the spatial resolution by 26 % and energy resolution by 33 %.

6.4. Discussion

CRLB calculations shown in this paper were based on a light distribution model that includes a model for the centroid of the deposited energy in the scintillator (determined with Geant4) and the

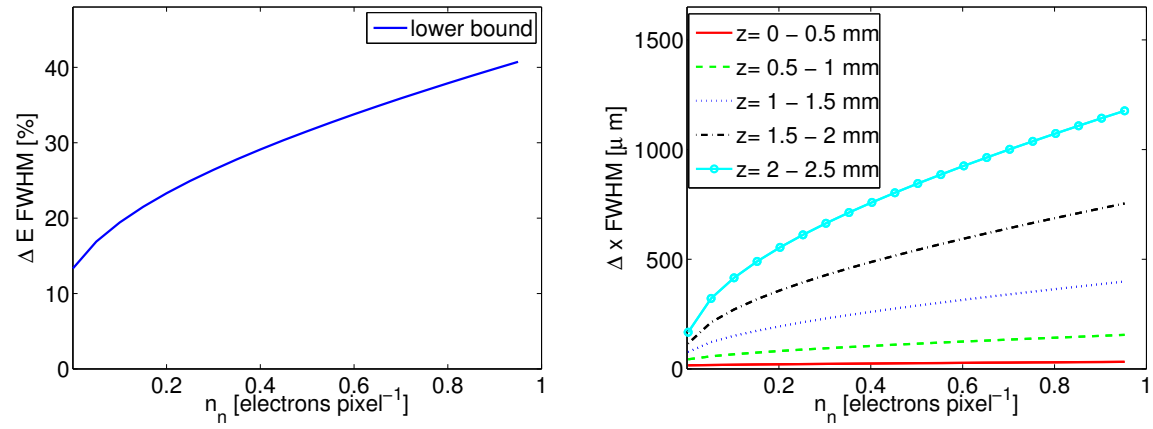

(a) **(b)**

Figure 6.9: Calculated CRLB for the **(a)** energy resolution and **(b)** spatial resolution for different depth ranges as a function of the noise in the image area. All other parameters were chosen as in table 6.1.

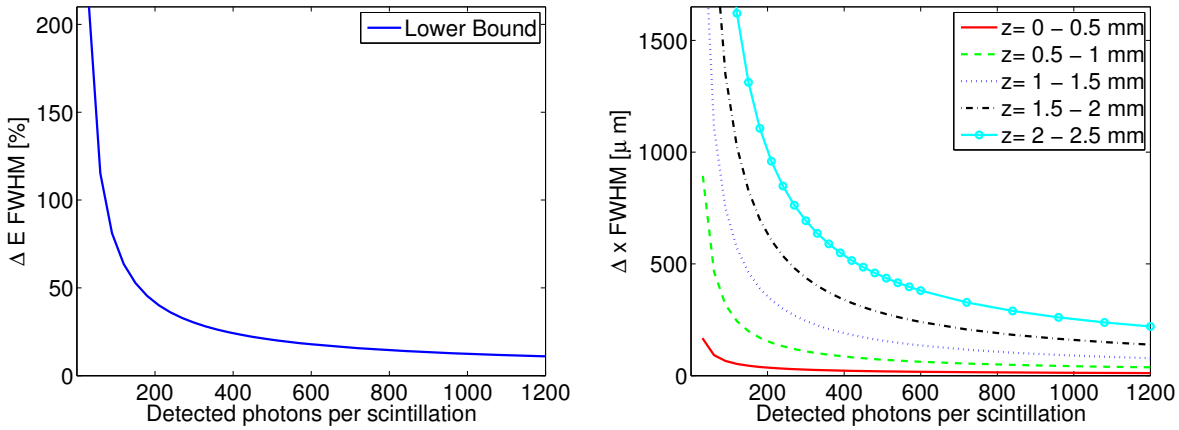

(a) **(b)**

Figure 6.10: Calculated CRLB for **(a)** the energy resolution and **(b)** spatial resolution for different depth ranges as a function of the number of detected photons. All other parameters were chosen as in table 6.1.

minimal light distribution due to the FOP and optical grease. This allowed us to construct a light distribution model that describes the measured data as a function of depth relatively well (figure 6.5). Furthermore, a statistical model for the EM-CCD was used that was validated in chapter 3.[145]

In general, we found that measured energy and spatial resolutions are typically a factor 1.5 above the calculated CRLB. We believe that this is mostly caused by the presence of drift in the output of the measurement system over time. Such a drift can result in a change of for instance the *gain* over time which changes the response of the detector and therefore the detected energy. Furthermore electrical instability of the measurement system can adversely affect the spatial and energy resolutions negatively. Specifically for scintillations close to the detector, the measured spatial resolution is much worse than the calculated CRLB. We believe this is caused by the difficulty to detect scintillations there because of saturation of the output signal (see figure 6.4) and possibly also because of divergence of the gamma photon beam and pixel binning (to 64 $\times$ 64 μm). However, in all cases, trends predicted by CRLB lower bound calculations are in accordance with experiments.

The lower bound as a function of *gain* shows that there is an optimal *gain* determined by the contradicting requirements to i) amplify the signal above the readout noise and ii) prevent saturation for large signals. Furthermore it is predicted that low noise in the image area and a large number of detected photons are essential for good performance. A significant reduction in noise in the image area by a factor 10 reduces the CRLB for the energy resolution to 14 % and could improve the gamma camera performance by a factor 1.5. Such a reduction in noise has been demonstrated by research on EM-CCDs[189,237]. The performance of the gamma camera depends strongly on the number of detected photons which is affected by the CCD QE; which is already as high as 90 % using back illuminated CCDs instead of front illuminated CCDs. An increase in the number of detected photons can be achieved by improving the scintillation light collection efficiency[174] (chapter 7) or choosing a scintillator material with a higher light output[236]. No effect on the gamma camera performance by a reduction of the readout noise is expected as a high enough *gain* renders the performance insensitive to the readout noise. Of interest would also be to investigate if the pixel size of the EM-CCD has a large influence on the energy and spatial resolution. The influence of these parameters, that cannot simply be changed in our current set-up, are essential to understand when considering a next generation EM-CCD based gamma camera. CRLB calculations such as presented in this paper can guide the decision making process in development of new EM-CCD based gamma cameras when benefits of e.g. improved noise in the image area can be judged with respect to costs.

6.5. Conclusion

In this paper we have investigated the CRLB of the energy resolution and spatial resolution of an EM-CCD based scintillation gamma camera and validated predicted trends with experiments. Such calculations can guide for the design of next-generation EM-CCD based gamma cameras. The CRLB results were shown to be very sensitive to the DOI in the scintillator, noise originating in the image area and the number of detected scintillation photons. The use of new EM-CCDs in combination with new low-noise readout electronics and scintillators with higher light output and better light collection efficiency are expected to improve the scintillation gamma camera performance significantly.

Acknowledgments

This work has been sponsored in part by the Netherlands Ministry of Economic Affairs, IOP photonics grant IPD067766. We would like to thank Paul Schotanus of SCIONIX for providing us with CsI:Tl scintillators and Dr. Bernd Rieger for the useful comments.

Chapter 7

Micro-machined retro-reflector for improving light yield in ultra-high resolution gamma cameras

Jan W.T. Heemskerk[1,2], Marc A.N. Korevaar[1,2], Rob Kreuger[2], C.M. Ligtvoet[3], Paul Schotanus[4], Freek J. Beekman[1,2,5]

[1] Image Sciences Institute, University Medical Center Utrecht, 3584 CG, Utrecht, the Netherlands
[2] Radiation, Detection and Medical Imaging, Department of R[3], Applied Sciences, Delft University of Technology, Mekelweg 15, 2629 JB, Delft, the Netherlands
[3] Department of Medical Technology and Clinical Physics, University Medical Center Utrecht, 3584 CG, Utrecht, the Netherlands
[4] Scionix Radiation Detectors and Crystals, PO Box 143, 3980 CC, Bunnik, the Netherlands
[5] MILABS, Universiteitsweg 100, Utrecht, the Netherlands

Phys. Med. Biol., 54, 10, pp.3003-3014, 2009.

Abstract

High-resolution imaging of X-ray and gamma-ray distributions can be achieved with cameras that use Charge Coupled Devices (CCDs) for detecting scintillation light flashes. The energy and interaction position of individual gamma photons can be determined by rapid processing of CCD images of individual flashes. Here we investigate the improvement of such a gamma camera when a micro-machined retro-reflector is used to increase the light output of a continuous scintillation crystal. At 122 keV we found that retro-reflectors improve the intrinsic energy resolution (Full Width at Half Maximum (FWHM)) with 32% (from 50% to 34%) and the signal-to-noise ratio by 18 %. The spatial resolution (FWHM) was improved by about 4%, allowing us to obtain a resolution of 159 µm. The Full Width at Tenth Maximum (FWTM) improvement was 13%. Therefore, this enhancement is a next step towards realizing compact high resolution devices for imaging gamma emitters.

CHAPTER 7

7.1. Introduction

Today, the majority of clinical procedures using tracers to visualize specific tissue binding sites are carried out with planar gamma camera imaging, Single-photon Emission Computed Tomography (SPECT) or Positron Emission Tomography (PET). Imaging of single-photon-emitting radiopharmaceuticals with gamma cameras, in planar or tomography mode, makes up the largest fraction of these molecular imaging procedures. In addition to these clinical applications, SPECT imaging of laboratory animals is currently a rapidly expanding field since resolutions better than 0.5 mm can readily be achieved. This allows for both the visualization and the accurate quantification of ligand concentrations in small animals such as rodents with resolutions down to subcompartments of mouse organs[49,50,112,173]. This affects most preclinical imaging procedures since rats and mice form the majority of the experimental animal population.

For a more beneficial resolution-sensitivity trade-off, most dedicated small-animal SPECT systems employ pinhole collimation as opposed to other types of collimation[46]. Introductions to the subject of pinhole SPECT can be found in different studies[44,45,243]. Stationary small-animal pinhole SPECT systems[48,49,112,173,244] provide the advantage that one can perform dynamic imaging with arbitrarily short frame lengths[48,50,180].

For further improvement of future SPECT devices, a high intrinsic detector resolution is essential[54,153,154,155,216]. It has been shown that very high spatial resolutions (below one hundred microns) can be obtained with a detector consisting of CsI:Tl micro-columnar scintillation crystals read out by a CCD operating at high frame rates[82,137,138,140,146,178,204,245] (chapter 8). However, due to the low capture efficiency of CsI:Tl and the limited thickness of available micro-columnar crystals, these crystals are not well-suited for small-animal imaging.

To increase the capture efficiency of our gamma camera, the micro-columnar crystal has been replaced by a thicker continuous (monolithic) CsI:Tl crystal in combination with an advanced multi-scale detection algorithm[144,175] (chapter 2 and 4). One drawback of continuous crystals is that the spread of scintillation light is not confined and therefore significantly larger than for micro-columnar crystals. Furthermore the light spread on the CCD will be dependent on the depth of the scintillation event in the crystal (depth-of-interaction, DOI). The multi-scale algorithm can incorporate information from the light spread in the estimation of scintillation position (which includes DOI) and energy, provided a sufficient amount of photons is detected[144] (chapter 2). With increased light output of the scintillation crystal, it is expected that the energy and position of the scintillation events can be estimated more accurately.

The light output of the scintillation crystal can be enhanced by using a reflective coating on the top of the crystal[217]; in some cases the amount of photons reaching the CCD surface will almost be doubled. However, the light spread will also increase (figure 7.1 (a)). More improvement can be expected from the application of a retro-reflector: the reflected photons appear to arrive from the scintillation location directly; additional light spread is avoided (figure 7.1 (b)).

Examples of the application of retro-reflectors in scintillation gamma cameras have so far been based on photo-multiplier tubes[198] and avalanche photodiodes[245]. However, the retro-

reflectors used in those experiments have relatively large reflective elements and are unsuited in combination with relatively thin crystals and ultra-high resolution light sensors such as CCDs. Therefore, the goal of the present paper is to develop a retro-reflector based on microscopic, high precision reflective elements and to test it in a CCD-based gamma camera for high resolution imaging tasks. To this end we have first conducted ray-tracing simulations of the (optical) photon trajectories to predict the efficiency of differently structured reflective coatings. Then, the most efficient of these coatings has been manufactured and tested experimentally by measuring the SNR and the energy and spatial resolution of a gamma camera with and without the reflector.

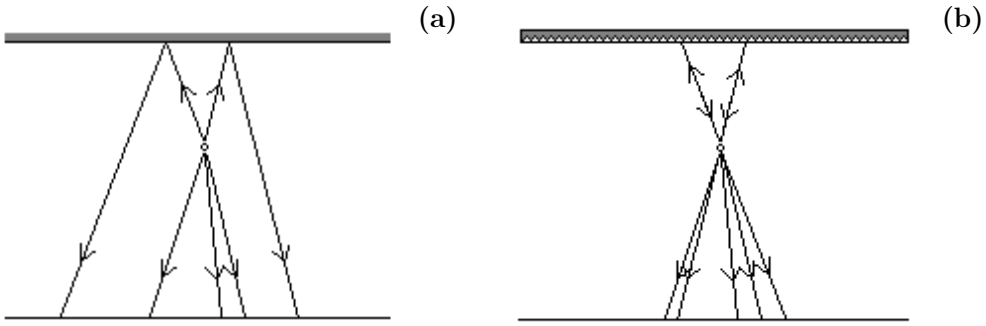

Figure 7.1: In case of the specularly reflective surface **(a)**, photons will be reflected back from the top of the scintillation crystal to the detector at the bottom. With an ideal retro-reflector **(b)**, the photons are reflected back through their point of origin (i.e. the location of the scintillation) onto the detector, thus maintaining the spatial resolution.

7.2. Materials and Methods

7.2.1 EM-CCD, read-out electronics and photon-counting algorithm

The scintillation gamma camera that is used in this experiment consists of a continuous scintillation crystal being read-out by an electron-multiplying (EM-)CCD[125]. Here we only summarize its characteristics; a comprehensive description of this gamma camera is provided elsewhere[138,146].

Gamma photons are captured in the scintillation crystal and the light flashes that are generated are detected by a back-illuminated EM-CCD. The EM-CCD that is used in these experiments is a CCD97 from E2V technologies. The quantum efficiency of the CCD97 exceeds 90% for the range of visible light from 500 to 650 nm. It has an active area of 512 lines of 512 pixels that are 16 × 16 μm^2 in size. To reduce the dark current to a level below 0.1 e/pixel/s the EM-CCD is cooled via a Peltier element and liquid cooler to a temperature of -50 ℃.

Read-out of the EM-CCD is performed by an in-house developed electronics board that transfers the signal to a PC. In order to improve the read-out frequency of our camera the lines are read out in pairs of two, which allows us to operate the camera at a rate of 50 frames per second. Through post-processing of the acquired images, the camera is operated

in photon-counting mode: each individual frame is analyzed for the presence of scintillations by a Multi-Scale gaussian filter Algorithm[144] (MSA, chapter 2). This algorithm estimates the center of gravity and the DOI for the separate scintillation events; the DOI is estimated through matching of the light spread with the scale of the filter. The energy of the scintillation is determined by the peak height of the signal after matched filtering.

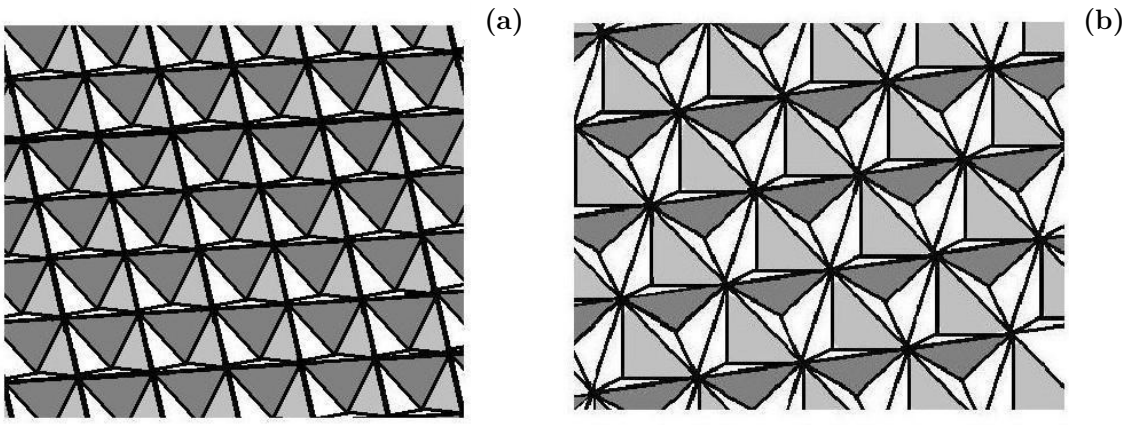

Figure 7.2: Different retro-reflective structures that were simulated: 75 μm square pyramids **(a)** and 75 μm tetrahedral retro-cubes **(b)**. Based on simulations the retro-reflector with tetrahedral retro-cubes was selected for physical experiments.

7.2.2 Scintillation Crystal

An (approx.) 1.5×1.5 cm^2, 2-mm-thick CsI:Tl crystal was used, courtesy of SCIONIX Netherlands, which has an interaction probability of >50% for 140 keV ^{99m}Tc gamma photons. The continuous CsI:Tl crystal is proximity coupled to a CCD via a fiber-optic window using optical grease (Bicron BC-630). As a result of the high Tl concentration of the material, the emission spectrum of the CsI:Tl crystal (ranging from approx. 450 to 650 nm) closely coincides with spectral response of the CCD97.

7.2.3 Ray-tracing simulations

The efficacy of different reflector designs was first characterized by simulating the number of reflected photons per scintillation event and their spread on the detector. These figures have been estimated for different types of reflectors with a ray-tracing code that calculates the paths of the optical photons. The reflectors that we have simulated are i) (specular) mirror-like, ii) a retro-reflector with square pyramids, iii) a retro-reflector consisting of regular tetrahedra (i.e. parts of regular cubes); the geometric and material properties of the simulated crystal are consistent with our laboratory set-up (i.e. 2 mm thick CsI:Tl). The square pyramid and tetrahedral retro-reflector are shown in figures 7.2 (a) and (b), resp.

For each type of reflector we have simulated many scintillations events taking place at random depths throughout the crystal, but with a scintillation depth distribution according to Beer's law. Approx. 7800 photons were simulated in each event which is typical

for a scintillation event of ^{99m}Tc in CsI:Tl[II]. We assume that the generated optical photons have random directions (with an isotropic distribution) and that ideal reflections occur at the boundaries of the reflectors with a probability of 95%. Between the crystal and the reflector we simulate an optical medium with the same optical density as the optical grease present in our experiment; at the boundary between scintillator and CCD we assume complete transmission of rays *within the critical angle of internal reflection*. Photons with trajectories leaving the sides of the crystal are considered to be lost.

Once the individual photon traces have been determined, it is straightforward to calculate the number of photons arriving on the CCD (either directly or after reflection) and their spread. The size of the scintillation light spread on the detector *of the directly detected photons* is uniquely determined by the distance of the scintillation event from the detector surface and the critical angle. The center-of-gravity of the light spot corresponds to the x- and y-coordinates of the scintillation event.

The 'gain' of each reflector is defined as the relative number of reflected photons vs. direct photons for a large number of scintillations (>5000). Only those reflected photons that arrive at the detector within the light spread of the directly detected photons are included in this gain, since we assume (based on our MSA algorithm) that the extra photons outside this light spot do not contribute to an improvement of the spatial and energy resolution. Whether or not the calculated number of detected light photons corresponds with the actual number of experimentally detected photons is debatable, since the simulation does not include any photons losses outside of the crystal or a noise model for our detector. However, as these loss factors will be equal for crystals both with and without reflector, the detected trends of the simulations should be accurate. Results of the simulations are presented in section 7.3.1.

7.2.4 Retro-reflector

To experimentally validate our retro-reflector we compare the gamma-ray detection capabilities of a camera with reflector to those with an uncoated crystal. The reflector is applied to the crystal side that is not read out by the CCD (i.e. the top of the crystal) with the same optical grease as used for coupling to the CCD. To remove possible air inclusions in the reflector cavities, the crystal with reflector was temporarily placed in vacuum.

The retro-reflector has been designed in-house and micro-machined for this experiment specifically. The outcome of the ray-tracing simulations indicated that for 75-μm tetrahedral cubes a large number of photons are reflected back onto the detector, within the original photon spread. Thus, the retro-reflector we have designed consists of tetrahedral retro-cubes with a baseline of 75 μm molded into a polymer resin, which has subsequently been hardened and on which a highly reflective aluminum film has been vapor deposited (figure 7.3). Aluminum films have a reflectivity of >90% for the range of wavelengths of the

[II] According to literature (scintillator.lbl.gov), CsI(Tl) generates approx. 59.000 photons per MeV of gamma radiation

CsI:Tl emission spectrum (450-650 nm)[III]. The reflective tetrahedral cavities will ensure that a large fraction of the incident photons is retro-reflected in the direction of their origin.

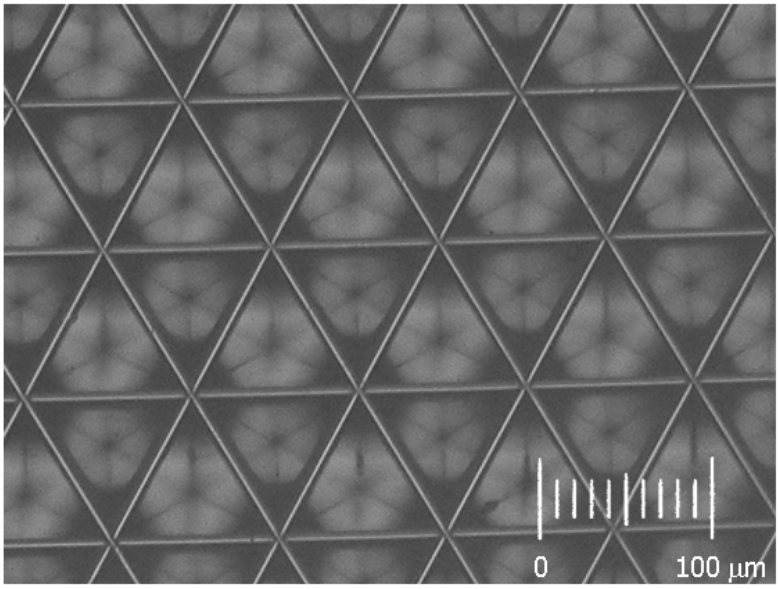

Figure 7.3: Photograph of a micro-machined retro-reflector, specially designed for this experiment. The baseline of the tetrahedral elements is 75 µm.

7.2.5 Measurements

The properties we investigate to evaluate the reflector are the spatial and energy resolution and SNR. The crystal is irradiated by a Co-57 (122 keV) source through a 30-µm-wide slit between two tungsten plates. From the MSA list-mode data energy spectra are constructed as histograms of the intensities of the detected scintillations. The energy resolution that is determined from these spectra provides a measure for the ability of the EM-CCD-based gamma camera to distinguish scintillations of different radioisotopes. It is derived as the full width at half maximum (FWHM) of the peak of the Co-57 signal in the energy spectrum.

The spectra are subsequently used to set the energy windows for event selection for the reconstruction of the projected image. For both the camera with and without the retro-reflector, this energy window ranges from 50% to 150% of the energy peak value (i.e. peak value ± 50%, roughly corresponding to twice the FWHM of the photopeak for the uncoated crystal). The spatial resolution is determined from the FWHM of the projection of the slit, corrected for the width of the slit itself[82].

The signal-to-noise ratio (SNR) is defined as the net number of counts within the area irradiated by the slit divided by the number of false positives counts detected on an equally sized non-irradiated area of the CCD. The irradiated area is taken to be 30 columns wide, which is slightly wider than the full width at tenth maximum (FWTM) of the profile of the slit.

[III] See, for instance, http://www.mellesgriot.com/products/optics/oc_5_1.htm or http://www.edmundoptics.com/TechSupport/DisplayArticle.cfm?articleid=259

Each of the measurements consists of a total number of 25.000 frames and the results are described in sections 7.3.2 and 7.3.3.

7.3. Results

7.3.1 Ray-tracing simulations

We present the numerical results for a CsI:Tl scintillation crystal of 2 mm thickness irradiated by 140 keV (^{99m}Tc) gamma radiation. Figure 7.4 shows the photon spread for a crystal without reflector ('directly detected photons'), covered with a specular reflector, a retro-reflector with 75-μm-side square pyramids and a retro-reflector with 75-μm-baseline tetrahedra (for the reflectors the total signal of reflected and direct photons is shown). For clarity, we show the results for simulated scintillations occurring at the average scintillation depth (~900 μm). We can see that, direct photons are exclusively detected with a deviation from the center of gravity smaller than ~1500 μm, as the 'detection cone' is cut off at the critical angle of total internal reflection at the scintillator-CCD interface. The photons that have been reflected by the reflectors, however, can have larger deviations.

For both retro-reflectors and specular reflectors, the gain was found to vary over the depth of the crystal. Figure 7.5 shows the variation of reflector gain with scintillation depth. This variation is the result of the fact that for a perfect retro-reflector, in general, each photon will have to reflect three times in order to reflect exactly into the direction of its origin. However, in the simulations we found that a significant number of photons will reflect only twice (or even once). For scintillations close to the top surface of the crystal, these imperfectly (retro-)reflected photons have a larger chance of arriving within the spread of the directly detected photons, than for scintillations close to the detector.

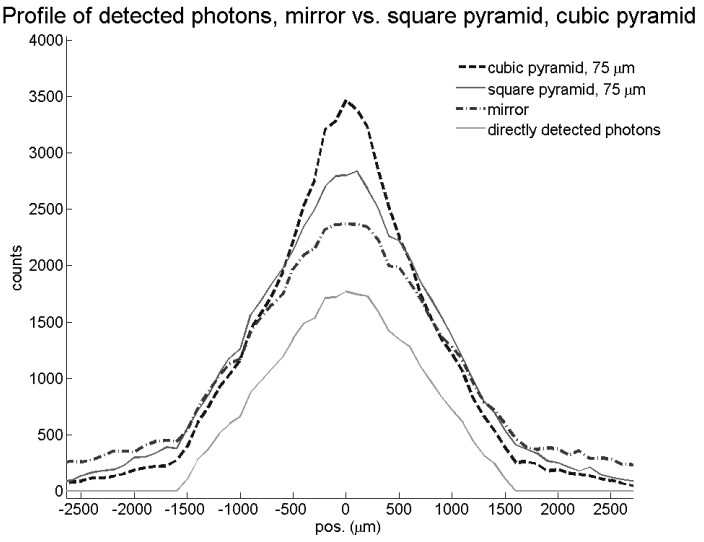

Figure 7.4: Comparison of the photon spread without any coating (light grey, solid), with a specular reflector (black, dash-dot), and with retro-reflectors with square pyramids of 75 μm (dark gray, solid) and tetrahedral retro-cubes of 75 μm (dark gray, dashed) at the average scintillation depth (900 μm).

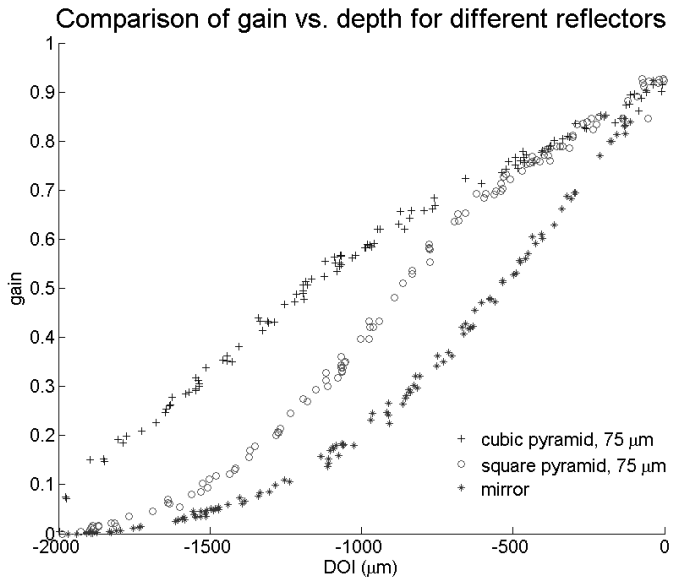

Figure. 7.5: Comparison of the numerically calculated gain of the three different reflectors vs. the depth-of-interaction (only 1 in every 50 data points is shown here). For scintillations close to the crystal surface (DOI is low) the gain is highest for all three reflectors. The cubic retro-reflector has a superior performance, in particular for scintillations occurring deeper in the crystal.

Therefore, the gain was found to be largest for scintillations with a small DOI. The overall gain is largest, and its variation is smallest, for the tetrahedral retro-reflector. Table 7.1 lists the overall gain for the 5000 simulated events for all reflector types.

Because the multi-scale photon-count algorithm provides an estimation of the DOI, we can correct for the variation of the gain in the determination of the energy values using the calculated gain factors from figure 7.5 (see 7.3.2).

Table 7.1: Simulated reflection gain for different coatings.

Retro-reflector	# of direct photons	# of reflected photons	Gain (%)
Mirror	9037066	3329131	36.8
Square 75 μm	9037534	4372173	48.4
Tetrahedral 25 μm	9039292	5382168	59.9
Tetrahedral 75 μm	9035540	5360889	59.3
Tetrahedral 125 μm	9036769	5328560	59.0

From our simulations we conclude that the tetrahedral retro-reflector (retro-cubes) has an efficiency that is $> 20\%$ higher than the retro-reflector constructed from square pyramids and >1.5 times as high as a normal mirror. Therefore, we expect that application of this new retro-reflector will lead to a significant improvement of the light output of our scintillator and a subsequent improvement of the spatial and energy resolution of our EM-CCD-based gamma camera.

In principle, smaller retro-cubes will enhance the ability to reflect light back into the original direction. In our simulations we have found that below a size of ~75 μm the

improvement is only small[IV], whereas for retro-cubes of 125 μm a large variation in gain values for scintillations with small DOI arises. This indicates the influence of the lateral position of the individual scintillations (with respect to the retro-reflector) on the gain. We have therefore decided to fabricate a retro-reflector with a baseline of 75 μm.

The experimental validation of the application of this retro-reflector in comparison with an uncoated crystal is presented in the next two sections.

7.3.2 Measured energy spectrum and SNR

Figure 7.6 (a) shows the experimentally obtained energy spectra for the crystal with and without retro-reflector, accumulated in the entire crystal thickness.

For the spectrum with the retro-reflector, the estimated energy values of the scintillation events have been corrected for the DOI-dependent gain due to the retro-reflector. According to the simulations (figure 7.5), for scintillations occurring close to the top of the scintillation crystal almost twice the amount of photons will be detected compared to scintillations close to the detector. The position of the photopeak is therefore dependent on the DOI. To correct for this, the DOI information of the individual scintillations from the MSA algorithm[144] (chapter 2) is used to scale the energy as a function of the DOI. The scaling factors have been derived directly from the calculated gain values of figure 7.5. With this correction a single narrow photopeak is obtained (figure 7.6 (a)), showing that there is good agreement between simulations and experiment.

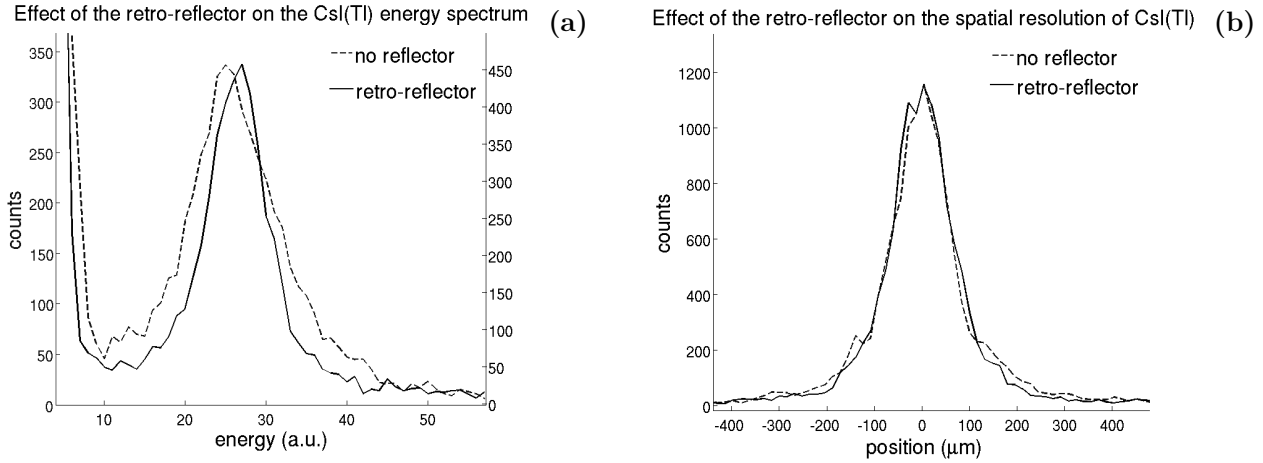

Figure 7.6: (a) Energy spectrum for the 2-mm-thick CsI:Tl crystal, for the case of no coating (dashed, left y-axis), and the specially designed retro-reflector (solid, right y-axis). The energy window for the SNR and spatial resolution measurements runs from 12.5 to 37.5 (a.u.) on the x-axis for both cameras. **(b)** Profiles of the images of the slit for the crystal with retro-reflector and without.

From these spectra the energy window for SNR and spatial resolution comparison of the different optical coatings was determined as explained before (i.e. ranging from 12.5 to 37.5 (a.u.)). Table 7.2 shows the overall energy resolution and SNR for the coated and uncoated

[IV] 25–μm tetrahedral structures could also have been constructed, but the limited advantage in gain would not compensate for the extra expense and expected mechanical difficulties in fabrication.

crystal, showing an improvement of the energy resolution as well as the SNR when the retro-reflector is applied. The improvement of the SNR is the result of the inclusion of more true positive counts as well as a reduced background level due to the better energy resolution.

7.3.3 Spatial resolution

Figure 7.6 (b) shows the accumulated profiles of the images of the slit for the camera with retro-reflector and without. Figure 7.7 shows the variation of the spatial resolution (in µm FWHM) for events at different DOIs. In figure 7.7 the improvement of the spatial resolution through the application of the retro-reflector is clearly visible, although limited to scintillations occurring in the top of the crystal (small DOI).

Table 7.2: Energy and spatial resolution and SNR for the CsI:Tl crystal with and without retro-reflector.

	without reflector	with retro-reflector	Improvement (%)
Energy Resolution (%)	50	34	32
Spatial Resolution			
FWHM (µm)	165	159	3.6
FWHM (µm)	424	370	12.6
Signal / false-pos. counts	4125/251	4444/230	
SNR	16.4	19.3	17.5

The spatial resolution is listed in table 7.2, for both Full Width at Half Maximum (FWHM) and Full Width at Tenth Maximum (FWTM), showing a significant improvement of the FWTM by using the retro-reflector. However, the improved spatial resolution (FWHM) for small DOIs shown in figure 7.7 does not directly translate into an improvement of the FWHM of the reconstructed profile of the line source (figure 7.6 (b)). This is because the width of the accumulated profile is dominated by the FWHM of the smallest profiles (for large DOIs) which show almost no improvement in figure 7.7. Nonetheless, for applications where the DOI-information is taken into account in the image reconstruction (e.g. pinhole gamma imaging) the retro-reflector will present a clear improvement as shown in figure 7.7.

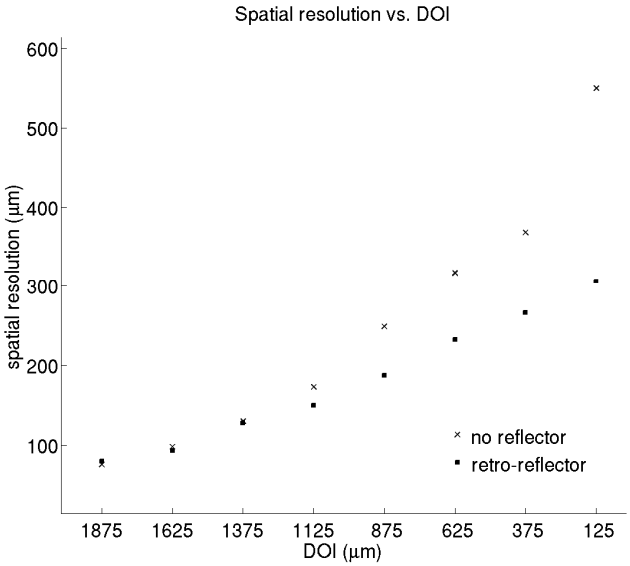

Figure 7.7: Variation of the spatial resolution (FWHM) of the continuous CsI:Tl crystal with the estimated depth-of-interaction, measured with and without retro-reflector.

7.4. Discussion and Conclusions

We have shown that the use of micro-machined retro-reflectors greatly improves both energy resolution and SNR of CCD-based gamma cameras, by 32% and 17.5%, resp. In agreement with the outcome of the ray-tracing simulations the retro-reflector significantly improves the light output, in particular for scintillations occurring close to the top of the scintillator. Furthermore, because the multi-scale algorithm allows for a depth-of-interaction separated analysis, we have found that the spatial resolution also significantly improves for scintillation events occurring further from the CCD surface, even up to 50% for scintillations in the top of the crystal; the overall FWTM resolution improved by 12.6%.

The application of the retro-reflector in our CCD-based gamma camera presents a further step in improving the camera's performance and bringing its energy resolution up to par with that of PMT-based gamma cameras. In SPECT, sufficient energy resolution is essential to discriminate scattered photons from primary photons. However, in small-animal SPECT, the amount of scattered photons is relatively low due to the small sizes of the objects under investigation. Furthermore the amount of scatter in pinhole apertures is quite low and does not give rise to strong contamination of projection data, even without energy discrimination[247]. The energy spectra presented in this work clearly indicate that the current prototype camera may be able to perform sufficient scatter rejection for applications such as small-animal SPECT.

For further development of EMCCD-based gamma cameras we are searching for scintillators giving an excellent energy and spatial resolution in combination with a high capture efficiency. All three factors will depend on the light yield and thickness of the scintillation crystal. The degrading effects of having a thick crystal (for high detection efficiency) on spatial and energy resolution might be alleviated by using a retro-reflector.

Retro-reflectors thus provide an important tool for combining good spatial and energy resolution with a high detection efficiency.

7.5 Acknowledgements

This work was sponsored in part by the Netherlands Organization for Scientific Research (NWO), grant 917.36.335.

Chapter 8

On-chip pixel binning in photon-counting EMCCD-based gamma camera: a powerful tool for noise reduction

Albert H. Westra[1], Jan W. T. Heemskerk[2,3], Marc A. N. Korevaar[2,3], Albert J. P. Theuwissen[4], Rob Kreuger[3], Kees M. Ligtvoet[1], Freek J. Beekman[2,3,5]

[1] Department of Medical Technology and Clinical Physics, University Medical Center Utrecht, 3584 CG, Utrecht, the Netherlands
[2] Image Sciences Institute, University Medical Center Utrecht, 3584 CG, Utrecht, the Netherlands
[3] Radiation, Detection and Medical Imaging, Department of R[3], Applied Sciences, Delft University of Technology, Mekelweg 15, 2629 JB, Delft, the Netherlands
[4] Electrical Engineering, Delft University of Technology, Delft, The Netherlands.
[5] MILABS, Universiteitsweg 100, Utrecht, the Netherlands

IEEE Trans. Nucl. Sci., 56, pp.2559-2565, 2009

Abstract

Charge Coupled Devices (CCDs) optically coupled to scintillation crystals can be used to construct high resolution gamma cameras. Previously, several groups have reported intrinsic detector spatial resolutions below 100 microns. When the CCD images can be read out fast enough, the energy and interaction position of individual gamma quanta can be estimated by a real-time image analysis of the scintillation light flashes. The Electron-Multiplying CCD (EM-CCD) is well-suited for fast read out, since even at high frame rates it has extremely low readout noise. However, due to the often very low light levels present in scintillation gamma cameras, further reduction of noise is desirable. Here, the EM-CCD is optically coupled to a 1000-μm-thick columnar CsI:Tl crystal for Tc-99m and I-125 imaging. We investigate noise reduction through summing of signals in pixels before the gain register and readout circuit of the EM-CCD ("pixel binning"). We compare the energy and spatial resolution, photopeak efficiency (PE) and signal-to-noise ratio (SNR) of an EMCCD-based gamma camera for the case of binning vs. non-binning. When pixels were read out simultaneously in groups of 4 the spatial resolution is slightly worse in the direction of binning, but the number of false-positive counts resulting from background noise for I-125 was reduced by 74% compared to the no binning case. We conclude that the use of charge binning when reading out EM-CCDs may significantly improve the energy spectra and noise properties of CCD-based high-resolution gamma cameras.

8.1 Introduction

High-resolution gamma and X-ray detectors are currently under development in a large number of laboratories[54,82,123,137,138,140,154,156,157,158,159,160,161,162,164]. Such detectors can be useful to improve small animal SPECT systems[45,49,54,82,248]. Very high spatial resolution, combined with energy discrimination capabilities can be obtained through the use of micro-columnar scintillation crystals that are read out by EM-CCDs (Figure 8.1).[82,138,140] These compact gamma cameras can determine the position and energy of individual scintillation events (photon-counting) and in some cases achieve spatial resolutions better than 60 μm.[82,137,138,140] The use of back-illuminated instead of front-illuminated EM-CCDs leads to significant improvements with respect to energy resolution and the number of false-positive counts[146].

Despite the continuous improvement of the spatial and energy resolution and noise properties of EM-CCD-based gamma cameras, additional noise reduction can widen the range of applications.

In low light level applications, the performance of an EM- CCD is limited by the thermally generated dark current and the clock-induced charge (CIC) that is the result of the charge transfer through the device[167,249]. The dark current can be suppressed by cooling the EM-CCD; CIC however is a temperature-independent noise source.

The amount of CIC noise is proportional to the number of transfers that the signal is subject to before readout. Here we reduce this number of transfers by summing the signal of multiple lines (binning) before it is transferred through the serial readout and gain register. Binning has been applied in other CCD-based gamma cameras[137,140] for increasing frame rates. The goal of the present paper is to deduce the efficacy of binning for reducing the CIC noise. To this end, we present energy spectra, SNR measurements as well as image profiles for spatial resolution measurements obtained with and without binning.

8.2 Materials and Methods

8.2.1 EM-CCD, scintillators and optic coupling

An Electron-Multiplying CCD (EM-CCD) is a CCD with an added feature: internal gain in the charge domain (i.e. before readout). Because of this internal gain an EM-CCD is less sensitive to readout noise, even at high readout speeds (e.g. several Mpixels/second). The internal gain is provided by electron multiplication (avalanche multiplication or impact ionization) in the gain register (see Figure. 8.2). Details of the EM-CCD technology are available in several papers[125,126,127,250].

The EM-CCD used in the present work is the back-illuminated CCD97 from E2V Technologies, which has 512 lines of 512 pixels, with a pixel size of 16 × 16 μm^2 and a quantum efficiency exceeding 90% for visible light in the range of 500 to 650 nm (figure 8.1 (a))[45,250]. It is cooled to -50 °C to reduce the dark current to levels below 2 10^{-2} e/pixel/frame (according to the manufacturer). The temperature-independent CIC noise, which is also called spurious charge or charge transfer noise, has a level of approx. 3.3 10^{-5} e/transfer for our read-out frequency of 50 frames per second at a pixel frequency of 11 MHz[249,250]. In the

worst case scenario, the charge has to pass through 512 lines of the image area, 520 lines of the storage area and 552 serial transfer columns before the gain stage, adding up to $5.2\ 10^{-2}$ e/pixel. It is therefore the dominant noise source in our application.

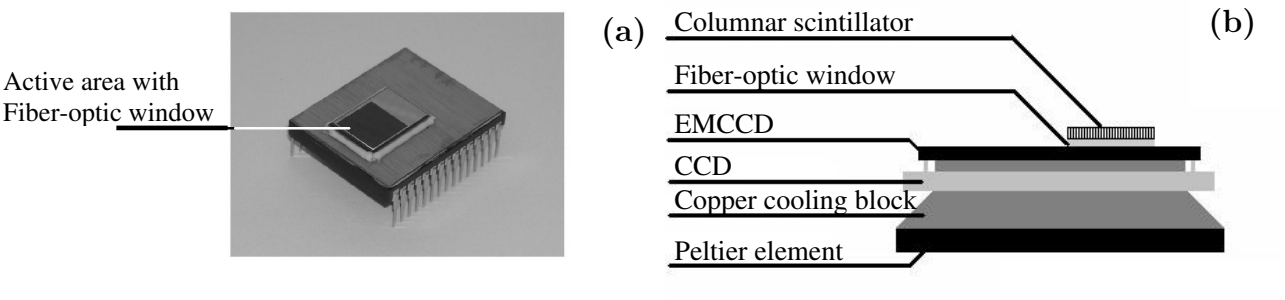

Figure 8.1: EM-CCD chip with fiber-optic window **(a)** and a compact EMCCD-based gamma camera (**b**)**.** A Peltier element cools the CCD chip, thereby reducing the dark current noise.

For the conversion of the incident gamma rays to visible photons, we used a 1000-μm-thick micro-columnar CsI:Tl scintillation crystal (Hamamatsu FOS, type J6671), which has a capture efficiency of almost 100% for I-125 and ~30% for Tc-99m. The peak wavelength of the emission spectrum lies at 550 nm, which is in the optimal range of our EM-CCD, while the columnar structure of CsI:Tl yields a high spatial resolution. A fiber-optic taper can be used to increase the effective detector area per CCD, but in our experiment a 3-mm-thick straight fiber optic window is present for protection of the CCD. The scintillation crystal was coupled to the fiber-optic window using Bicron BC-630 silicon optical grease.

8.2.2 Photon-counting algorithm

The electronics board that drives and reads out the EM-CCD is connected to a Digital Signal Processor (DSP), type TMS320C6416 from Texas Instruments. This DSP executes a photon-counting algorithm that performs a real-time analysis of each of the frames of the EM-CCD to detect and localize individual scintillation events.

Summarized, the algorithm proceeds as follows: first, before each measurement sequence an average (dark) background image is acquired. Then for each frame during acquisition, this background image is subtracted from the raw EM-CCD image. Next, a filtering step is performed by convolution of the background-corrected image with a 2D Gaussian filter. In this filtered image scintillation events will appear as bright regions and the peak position and intensity of each of these bright regions are transferred in list mode to a PC. The peak amplitude of the bright spots after filtering provides a measure for the energy that has been released in the scintillation event.

A more detailed description of the algorithm can be found elsewhere[162]; a description of the influence of the width of the 2D Gaussian kernel on the spatial and energy resolution of the gamma camera can be found in previous work[146]. The physical width of the Gaussian convolution (σ) in both the horizontal and vertical direction is set to the same value (i.e. σ is 64 μm), for both the case of binning and not binning.

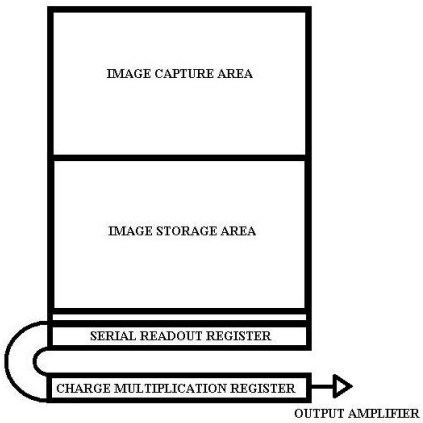

Figure. 8.2: Schematic lay-out of the EM-CCD. The internal electron multiplication gain is achieved in the charge multiplier that has been added before the readout capacitor. The binning of lines is performed by summing of the signal of multiple lines in the serial readout register. This is achieved through downward transfer of lines into the register, before the previous line(s) has been shifted serially through the register. The signal of any number of lines can thus be summed before it enters the charge multiplier[166].

8.2.3 On-chip binning

To improve the noise characteristics of our EM-CCD, we have binned the signal of multiple lines before their transfer through the serial readout and gain register. This effectively reduces the number of transfers that the signal is subject to, which in turn reduces the amount of CIC noise since it is linearly dependent on the number of transfers. Binning also reduces the susceptibility of the signal to the noise in the serial readout and gain register and readout circuit.

In normal operation EM-CCDs are read out the following way: after line-by-line (i.e. parallel) transfer of the signal from the storage area to the serial readout register, it is shifted pixel by pixel (i.e. serially) through the gain stage and the readout capacitor. Due to the fact that the readout electronics of our camera have been developed in-house, we have the ability to transfer multiple lines (rows) into the serial register before the serial transfer (binning). Effectively we thus sum the charge signal of multiple pixels in a column before it is transferred through the gain stage. Unfortunately, due to the structure of the device, binning of the charge in the direction of the rows can only be performed just before the read-out capacitor[V]. Though this can reduce the influence of the read-out noise it will have no effect on the CIC noise. Consequently, we only perform vertical binning in our comparison.

About half of the total number of transfers that the signal is subject to is in the serial readout and gain register; therefore binning could reduce the influence of the CIC by almost half. For instance, binning 4 lines would reduce the contribution of the CIC noise for the serial transfers through the readout and gain register, compared to the signal, by a factor of 4; instead of shifting 4 pixels through the registers, we are shifting only 1. Since the serial and gain register transfers amount to half the total number of transfers, this effectively

[V] Furthermore, in our particular setup horizontal binning can only be applied in conjunction with vertical binning, while vertical binning can also be applied independently.

reduces the total CIC noise by ~ 40%. Furthermore, summation of the signal of multiple pixels increases the signal in the serial register. The larger signal is less susceptible to the noise added in the readout circuit and to the standard deviation of the total noise[VI], thereby increasing the signal to noise ratio further. However, the contribution of the statistical noise generated in the gain register will not improve. The stochastic nature of the electron multiplication gain leads to a factor √2 increase of the variation of the noise over the gain register, independent of the amount of charge entering the gain stage.

Since binning occurs in the charge domain it is an essentially noiseless operation. It is often used in high-speed microscopy or fluoroscopy to either improve the readout rate of the camera or to reduce the influence of the noise in the readout capacitor[251]. However, binning will often lead to loss of spatial resolution as the pixel size is increased by the binning factor.

8.2.3 Measurements

To determine the spatial and energy resolution, photopeak efficiency (PE) and signal-to-noise ratio (SNR) of the camera, line pattern images were acquired using a setup with two (4 mm thick) tungsten blocks separated by a narrow slit (30 μm wide). Tc-99m (141 keV) and I-125 (27-35 keV) sources are placed behind the slit and a line pattern is projected through the slit onto the scintillator. The use of a slit to determine the line spread function is a standard method for measuring intrinsic resolution of clinical gamma cameras.

Energy spectra were recorded for the I-125 and Tc-99m sources consecutively for the irradiated area of the CCD (50 lines wide centered on the image of the slit). The energy resolution is determined from the FWHM of the peaks of the energy spectra after subtraction of the background level.

The spatial resolution is defined as the Full Width at Half Maximum (FWHM) of the line spread function corrected for the width of the gamma beam of 30 μm, on the assumption that both the beam itself and the response from an infinitely narrow beam are Gaussian. The scintillation events that are accepted for the determination of the spatial resolution are those with a light yield that fall within a 10% energy window (+/-14 keV) symmetrical around the photo-peak energy for Tc-99m and within a window ranging from 20 keV to 50 keV for I-125.

The photopeak efficiency (PE) was determined as the ratio of the signal counts within the photopeak compared to the background counts. For both the I-125 and Tc-99m photopeak (of the independently measured energy spectra), counts that lie below the baseline of the photopeak, were identified as background; counts above the baseline were identified as photopeak signal (Figure. 8.3). The signal-to-noise ratio (SNR) is defined as the total number of counts in the energy windows (I-125: 20 to 50 keV; Tc-99m: 126 to 155 keV) divided by the number of noise-induced false-positive counts detected in the appropriate energy windows of dark (unirradiated) images. The count rate of the experimental setup (several cps/mm^2 below the slit) is similar to what can be expected in practical small-animal

[VI] Note, however, that this latter effect could also be achieved by summing or averaging the signal after read-out.

pinhole SPECT imaging.

We compare measurements performed with binning of 2 and 4 lines with no binning. For this comparison the gain of the EM-CCD was adjusted such that the output signal of the camera was equal for all cases. The EM-CCD was irradiated with the slit oriented in both the horizontal and vertical direction (on the EM-CCD image) in order to determine resp. the spatial resolution both along the direction of binning (i.e. the vertical direction) and perpendicular to the direction of binning (horizontal). Each of the measurements described below consists of a total number of 25000 analyzed frames.

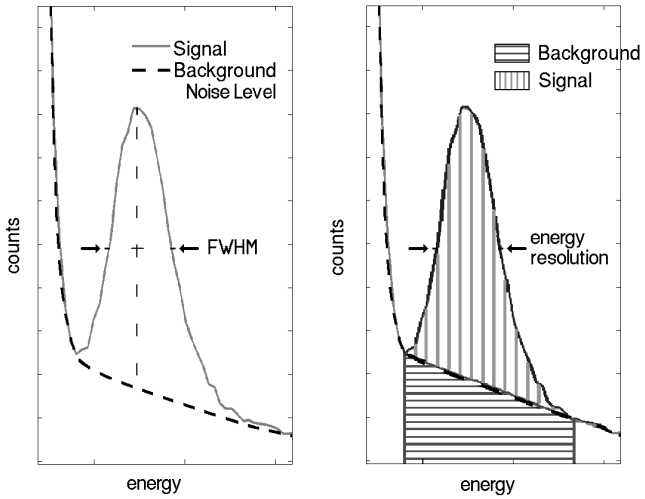

Figure 8.3: Definition of the energy resolution and photopeak efficiency (PE) deduced from the energy spectra. The energy resolution is determined as the FWHM of the photopeak after subtraction of the background noise level. For determination of the photopeak efficiency the number of counts above the background level is considered signal; the number of counts below this level is considered background (right).

8.3 Results

8.3.1 Energy resolution, PE and SNR

Figure 8.4 shows the energy spectra acquired with I-125 and Tc-99m for the case without binning and for binning of 2 and 4 lines. Furthermore, the background spectra measured without any radioactive sources present are also provided.

The scale of the energy axis is calibrated assuming that the peaks of I-125 and Tc-99m are situated at 30 keV and 141 keV respectively. The energy resolution is determined as the FWHM of the separate I-125 and Tc-99m peaks after subtraction of the background noise level. The I-125 peaks could be well fitted with Gaussians, the Tc-99m peaks less so.

The energy resolution was estimated to be 32% FWHM (45 keV) for Tc-99m and 59% (17.6 keV) for I-125 without binning. Binning of 4 lines resulted in an energy resolution of 28% (40 keV) for Tc-99m and 53 % (15.9 keV) for I-125, showing an improvement for both. The energy resolutions both with and without binning are listed in table 8.1.

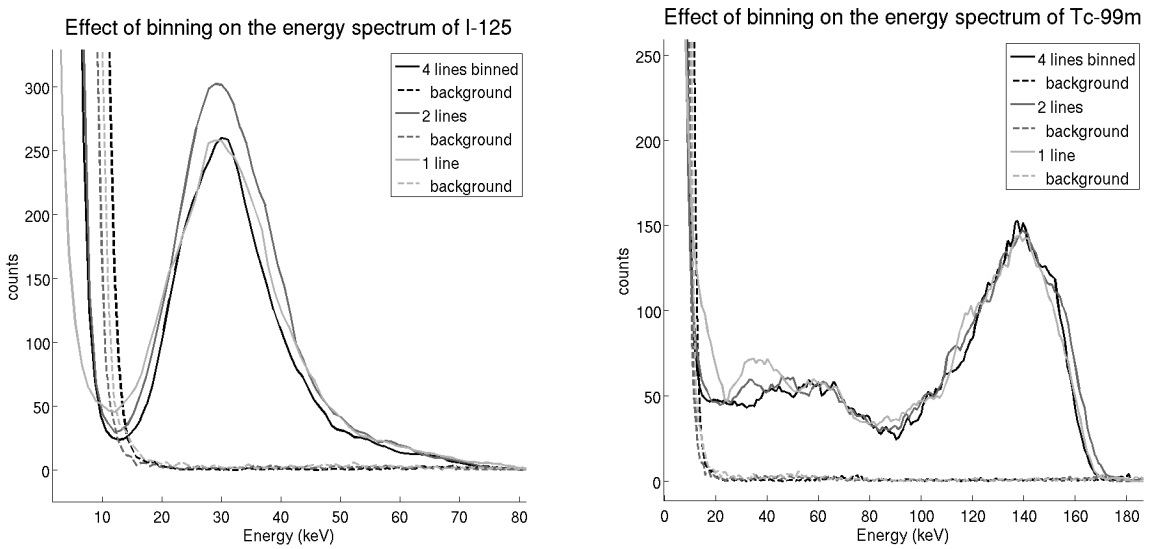

Figure 8.4: Comparison of the energy spectra, when imaging I-125 and Tc-99m separately, for the cases of binning of lines vs. no binning. The spectra have been measured for an area of 50 lines wide centered on the image of the slit; the non-irradiated background spectra have been measured for the entire CCD.

Table 8.1: Energy and Spatial Resolution for Tc-99m and I-125. Summary of the resolution measurement results, as measured from the energy spectra (figure 8.4) and the corresponding Tc-99m and I-125 image profiles (figure 8.7), for no binning and for binning 2 and 4 lines.

		Tc-99m		I-125	
	binning	horizontal	vertical	horizontal	vertical
Spatial	1	55.8	54.0	46.1	49.7
Resolution	2	50.9	60.0	42.4	48.0
(μm)	4	53.5	83.8	42.4	76.7
		[keV]	[%]	[keV]	[%]
Energy	1	45	32	17.6	58.7
resolution	2	46	32.6	17.5	58.3
	4	40	28.4	15.9	53.0

The PE measurements with and without binning, for both the I-125 and Tc-99m energy windows, are presented in figure 8.5 and tables 8.2 and 8.3.
The signal is determined from the energy plots (figure.8.5) as the vertically striped area under the peak: the background is determined from the horizontally striped background level. Binning improved the PE by 118 % for I-125 and by 58 % for Tc-99m. Tables 8.2 and 8.3 also include the ratio of the total signal of the photopeaks to the false positive counts in identical energy windows for completely dark (unirradiated images). For the I-125 energy window these numbers indicate a clear improvement of the SNR; for the Tc-99m window the SNR does not seem to improve. For I-125 an important parameter, the number of false counts in the energy windows for the unirradiated CCD, decreases significantly with binning.

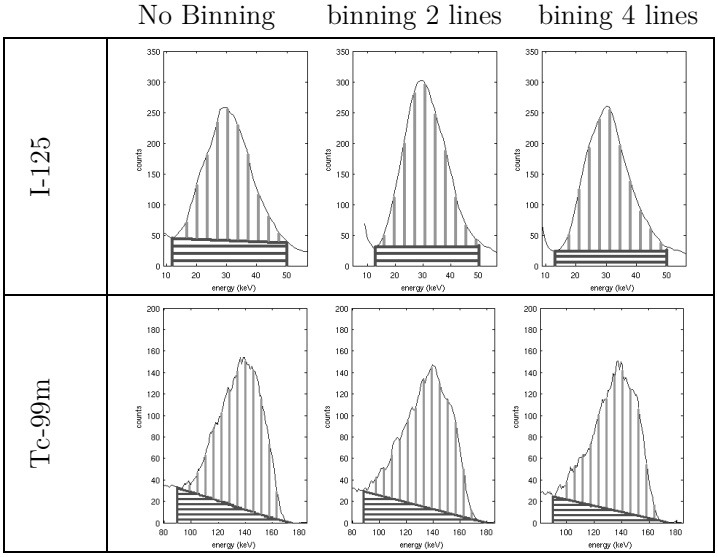

Figure 8.5: Comparison of the photopeak efficiency of I-125 (top) and Tc-99m (bottom) for the case of binning of lines vs. no binning. These are derived from the individual spectra of both sources. The horizontally delineated areas mark the background counts, the vertically delineated areas the signal counts.

Table 8.2 Summary of the PE and SNR measurements for Binning and without Binning for I-125. Summary of the Photopeak Efficiency (PE) and SNR results, as measured from the energy spectra (figure 8.5) and the corresponding energy windows of the dark images, for no binning and for binning 2 and 4 lines.

	binning	Energy window (keV)	Total peak area / background	Photopeak efficiency
50 lines only	no binning	12-50	4950 / 1540	2.2
	2 lines		5746 / 1110	4.2
	4 lines		5068 / 871	4.8
	binning	Energy window (keV)	Total counts/ Noise counts	SNR
Line signal	no binning	20-50	4332 / 357	12.1
compared to	2 lines		5352 / 294	18.2
dark image	4 lines		4636 / 92	50.4

Table 8.3: PE and SNR measurements for Binning and without Binning for Tc-99m. Summary of the Photopeak Efficiency (PE) and SNR results, as measured from the energy spectra (figure 8.5) and the corresponding energy windows of the dark images, for no binning and for binning 2 and 4 lines.

	binning	Energy window (keV)	Total peak area / background	Photopeak efficiency
50 lines only	no binning	90-180	6735 / 1492	3.5
	2 lines		6487 / 1218	4.3
	4 lines		6610 / 1007	5.6
	binning	Energy window (keV)	Total counts / Noise counts	SNR
Line signal	no binning	126-154	3722 / 75	49.6
compared to	2 lines		3515 / 74	47.5
dark image	4 lines		3909 / 80	48.9

8.3.2 Spatial resolution measurements

Figure.8.6 shows I-125 image profiles taken perpendicular to the line pattern without binning (single line readout) and for binning of 4 lines. Figure 8.6 left shows the profile when the line is projected vertically (in the EM-CCD image); figure 8.6 right shows the profile when the line is projected horizontally. In the first case the profile of the line lies perpendicular to the direction in which the binning takes place, and thus the effective pixel size does not change with binning. In the latter case, the binning of lines is along the profile of the projected line, and thus the effective pixel size for binning 4 lines is 64 μm in that direction.

The resolutions determined from Full Width at Half Maximum (FWHM) of the profiles for both Tc-99m and I-125 are listed in Table 8.1. The uncertainty on the spatial resolution measurements is of the order of 1.5 μm. Use of binning slightly improves the spatial resolution in the direction perpendicular to the binning of lines for Tc-99m from 55.8 μm to 53.5 μm and for I-125 from 46.1 μm to 42.4 μm.

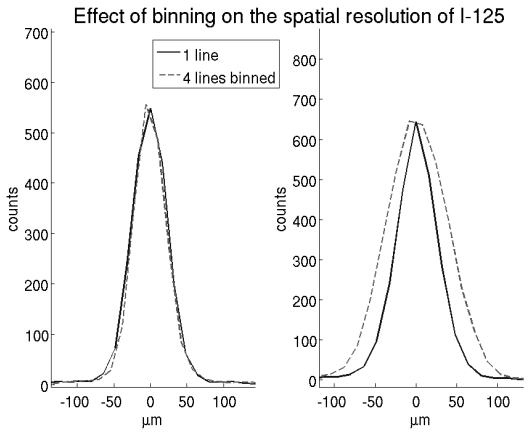

Figure 8.6: Image profiles of the projection of the slit in the I-125 energy window, not binned (1 line) and binned for 4 lines. The left figure shows the effect of binning on the resolution in the horizontal direction; the right figure shows the effect of binning on the resolution in the vertical direction. In the vertical direction binning increases the effective pixel size by a factor of 4 to 64 μm.

The loss of resolution in the parallel direction, along which binning occurs, is from 54.0 μm to 83.8 μm for Tc-99m and from 49.7 μm to 76.7 μm for I-125. This is far less than the effective increase in pixel size. The spatial resolution in the parallel direction is still better than 1.5 pixel lengths (96 μm).

8.4 Discussion

In the present paper we have shown that the use of binning increases the PE and SNR and reduces noise induced false-positive counts in CCD-based gamma camera for imaging of I-125. Furthermore we showed that binning results in some improvement of the energy resolution, even when this has been determined after the subtraction of the background noise. Without this background correction the energy resolution for not binning would be far worse. Unfortunately the improvements in spectral characteristics and energy resolution

come at the cost of some loss in spatial resolution in the direction of binning; increasing the effective pixel height by a factor of 4 degrades the resolution along the direction of binning by just over 50%. However, the resulting spatial resolution is in the range of the effective pixel size; we believe that for configurations where the spatial resolution is in the range of multiple times the pixel size or larger (e.g. in the case of thicker crystals) the loss of spatial resolution due to binning will be relatively small.

In the direction perpendicular to the binning, one would expect at least to see an improvement of the spatial resolution. For the I-125 signal indeed we see some improvement, for the Tc-99m signal an improvement cannot be detected, which can be explained by the strong signal in the case of 140 keV photons.

We expect that particularly in case of binning more pixels, further improvements in energy and spatial resolution are possible with the application of advanced centroiding algorithms. In the direction of binning, the current spatial resolution is less than 1.5 times the pixel size; this might very well be reduced by e.g. Anger logic or fitting algorithms that enable sub-pixel determination of the location of the individual scintillation events. Recently, a Maximum Likelihood Estimation Maximization (MLEM) algorithm has been developed for 3D position and energy estimation that can partly correct for depth-of-interaction (DOI) effects[165]. At this stage however, such algorithms are computationally intensive.

Even though sufficient energy resolution is essential in clinical SPECT in order to distinguish primary photons from scattered photons, small animal SPECT results in relatively small numbers of scattered photons. This is due to the small sizes of the objects being imaged. Furthermore, the amount of scatter in pinhole apertures is quite low, and does not give rise to strong contamination of projection data even without energy discrimination[247]. Therefore the energy discrimination capabilities of our prototype gamma camera should prove more than sufficient for application in small animal pinhole SPECT. The optimal tradeoff between spatial resolution and energy resolution and noise depends on the specific imaging task. For example for very small objects (e.g. mice) scatter rejection is of minor importance and spatial resolution can be maximized. For clinical applications a lower intrinsic resolution is required while energy resolution can be very important.

8.5 Conclusion

In the present work we have investigated energy and spatial resolution and spectral characteristics of an EMCCD-based gamma camera, when the signal of multiple pixels in a column is summed before entering the gain register of the EM-CCD. The use of this pixel binning leads to improvements in energy resolution, while maintaining sufficient spatial resolution. Further improvements might be possible if the signal could be binned for columns as well as for lines.

The signal-to-noise ratio has improved significantly for the low-energy I-125 γ-photons. Furthermore binning can facilitate the readout of the EM-CCD at higher frame rates. We conclude that binning in EM-CCDs is a promising technique, in particular for low light level detection, such as in gamma cameras used for SPECT imaging.

8.6 Acknowledgment

A. W. and J. H. share first authorship of this paper.

Chapter 9

Enhanced high-resolution EMCCD-based gamma camera using SiPM side detection

J.W.T. Heemskerk[1,2], M.A.N. Korevaar[1,2], J. Huizenga[2], R. Kreuger[2], D.R. Schaart[2], M.C. Goorden[1,2], F.J. Beekman[1,2,3]

[1] Department of Nuclear Medicine, Image Sciences Institute, University Medical Center Utrecht, Room STR 5.153, Universiteitsweg 100, 3584 CG, Utrecht, the Netherlands.
[2] Section Radiation Detection and Medical Imaging, Department of R[3], Applied Sciences, Delft University of Technology, Mekelweg 15, 2629 JB Delft, The Netherlands.
[3] MILabs Molecular Imaging Laboratories, Universiteitsweg 100, STR 5.203, 3584 CX Utrecht, The Netherlands.

Phys. Mes. Biol., 55, 22, pp.6773-6784, 2010

Abstract

Electron-multiplying charge coupled devices (EM-CCDs) coupled to scintillation crystals can be used for high-resolution imaging of gamma-rays in scintillation counting mode. However, the detection of false events as a result of EM-CCD noise deteriorates the spatial and energy resolution of these gamma cameras and creates a detrimental background in the reconstructed image. In order to improve the performance of an EMCCD-based gamma camera with a monolithic scintillation crystal, arrays of silicon photon-multipliers (SiPMs) can be mounted on the sides of the crystal to detect escaping scintillation photons, which are otherwise neglected. This will provide *a priori* knowledge about the correct number and energies of gamma interactions that are to be detected in each CCD frame. This information can be used as an additional detection criterion, e.g. for the rejection of otherwise falsely detected events.
The method was tested using a gamma camera based on a back-illuminated EM-CCD, coupled to a 3 mm thick continuous CsI:Tl crystal. Twelve SiPMs have been mounted on the sides of the CsI:Tl crystal. When the information of the SiPMs is used to select scintillation events in the EM-CCD image the background noise level for ^{99m}Tc is reduced by a factor of 2. Furthermore, the SiPMs enable detection of ^{125}I scintillations. A hybrid SiPM-/EMCCD-based gamma camera thus offers great potential for applications such as *in vivo* imaging of gamma emitters.

9.1 Introduction

Single-photon emission computed tomography (SPECT) is a prominent molecular imaging modality, both in clinical and in pre-clinical (e.g. small-animal) research. The application of pinhole geometries leads to unsurpassed imaging capabilities in small-animal SPECT[49,173,200] and is also applied for human SPECT imaging of specific regions-of-interest, e.g. brain[252], chest[112] and extremities[253]. Introductions to pinhole and small-animal SPECT imaging are provided by several authors[44,45,243].

Gamma detectors with high intrinsic spatial resolutions in combination with energy discrimination capabilities may be essential for the improvement of future multi-pinhole SPECT devices, as has been shown by simulations and modeling[53,54,153,155,216,254]; recent work[255] validates the efficacy of high-resolution detectors in small-animal SPECT applications. High-resolution gamma-ray detectors have been developed for applications ranging from astronomy and particle physics to biomedical imaging[82,123,140,148,154,156,157,158,159,160,161,162,164,165,245].

Very high spatial accuracy (below 60 microns) can be obtained with a detector consisting of an EM-CCD operating at high frame rates, that detects individual gamma photons in an optically coupled micro-columnar CsI:Tl scintillation crystal with the use of scintillation detection algorithms[138,140,146,148,165,178] (chapter 8). The application of continuous (or monolithic) crystals can improve the sensitivity for incoming ^{99m}Tc gamma photons (140 keV) at some cost in spatial and energy resolution[144,236] (chapter 2 and 5).

The spatial and energy resolution obtained with continuous crystals is, in principle, reduced because of the increased width of the light spread distribution compared to micro-columnar crystals. This can partly be overcome by the use of detection algorithms that take into account the depth-dependent light spread distribution[144,VII] (chapter 2). With such a depth-sensitive algorithm, EMCCD-based gamma cameras equipped with monolithic, 2.6 mm thick CsI:Tl crystals (corresponding to 60 % ^{99m}Tc absorption) have achieved a spatial resolution of ~150 μm, (intrinsic) depth-of-interaction correction and an energy resolution of 48 % for ^{99m}Tc imaging[144,175] (chapter 2 and 4); the application of micro-retroreflectors even improves the energy resolution to 34%[174] (chapter 7).

However, noise in the EM-CCD complicates the detection of scintillation events occurring at some distance from the EM-CCD surface (i.e. in the top of the scintillation crystal). In particular the detection of ~30 keV ^{125}I gamma photons (and characteristic X-rays) is significantly compromised, as these photons are absorbed at a greater distance from the detector surface (over 50% of ^{125}I gamma photons are absorbed in the top 200 μm of the CsI:Tl crystal) and generate far less scintillation photons than ^{99m}Tc (approx. 25%). As a result, true scintillation events can hardly be distinguished from the noise, which may lead to a background of falsely detected events in the reconstructed image or loss of sensitivity when thresholding is applied. Additional information on the true number of scintillation events therefore could assist the detection algorithm in separating true from false-positive detections.

[VII] The multi-scale algorithm actually uses information from the light spread to deduce the depth at which the scintillation occurred (the depth-of-interaction or DOI).

Since most light detectors (including EM-CCDs) read out only a single surface of the scintillation crystal, a considerable amount of scintillation photons is lost because they escape from the sides[217]; taking into account internal reflections within the crystal this could amount to 40-60% of the total number of scintillation photons. The information that these photons contain about the position and energy of the scintillation events has thus far not been exploited in CCD-based gamma imaging.

In this paper we introduce a novel method[256] to use the information from these photons; silicon photomultipliers (SiPMs)[116,257,258] attached to the sides of the crystal (see figure 9.1) are used to detect the previously neglected photons. The information that is extracted from the SiPM signals consists of the number of scintillation events in each measured frame; this number will serve as *a priori* information for the detection algorithm. To investigate the efficacy of our hybrid SiPM-enhanced EMCCD-based gamma camera, we compare its performance in terms of signal-to-noise ratio, spatial and energy resolution for ^{99m}Tc and ^{125}I imaging to the same setup without SiPMs.

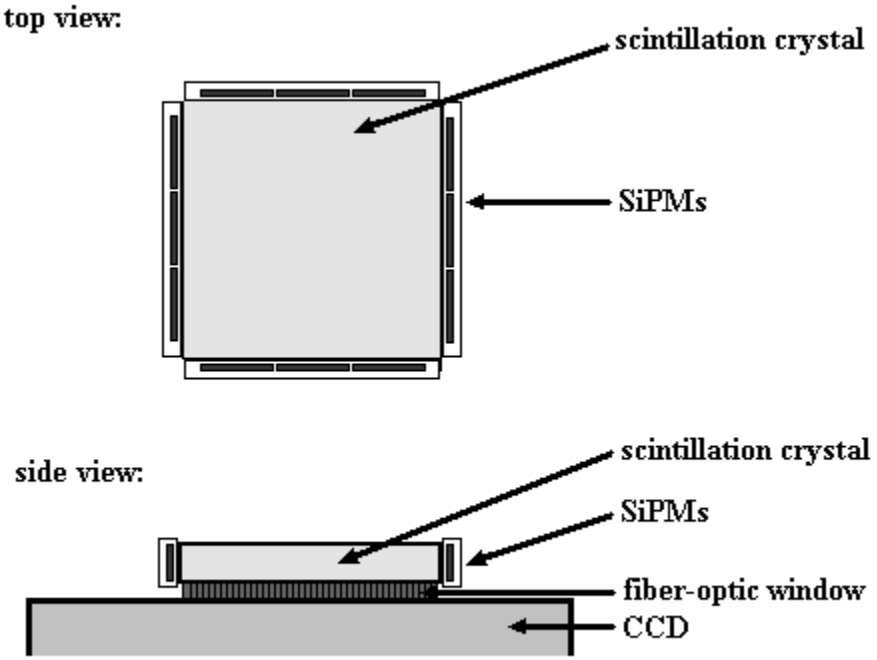

Figure 9.1: Experimental EMCCD-based gamma camera set-up with SiPM side detectors. A Peltier element cools the EM-CCD chip to reduce its dark current. Silicon photon-multipliers (SiPMs) are coupled to the sides of the scintillation crystal. The crystal and SiPMs are also cooled through thermal contact with the EM-CCD.

9.2. Materials and Methods

9.2.1 EM-CCD gamma camera

The scintillation gamma camera that is used in this research consists of a scintillation crystal coupled to an EM-CCD and is operated in gamma photon-counting mode, see figure 9.1. Gamma photons are converted in the crystal and the individual scintillation flashes are detected by the EM-CCD. A comprehensive description of this gamma camera is provided elsewhere[138,146].

We use a 3 mm thick continuous CsI:Tl crystal, which is proximity-coupled to the EM-CCD via a fiber-optic plate using optical grease. The crystal has an interaction probability of ~66% for 141 keV ^{99m}Tc gamma photons and ~100% for ~30 keV ^{125}I gamma photons and X-rays. The emission spectrum of the scintillation photons of the crystal has a maximum at 550 nm.

The EM-CCD used here is a back-illuminated CCD97 from E2V technologies. The quantum efficiency of the CCD97 surpasses 90% in the range of visible light between 500 and 650 nm, which matches nicely with the spectral emission of the crystal. It has an active area of 512 lines with 512 pixels, each 16 × 16 μm^2 in size. To reduce the dark current to a level below 0.1 e $pixel^{-1}$ s^{-1} the EM-CCD is cooled to a temperature of -50 ℃ using a Peltier element backed by a liquid cooler. The read-out of the EM-CCD is performed by an in-house developed electronics board; by reading out the EM-CCD lines in pairs of two we achieve a frame rate of 50 Hz.[259]

The frames are transferred to a Matrox Meteor-II framegrabber. The camera is operated in gamma photon-counting mode by off-line processing with an analytical scintillation detection algorithm[144] (chapter 2). This algorithm analyzes each separate frame for the presence of (possibly multiple) scintillations and determines the spatial coordinates and the intensity of each individually detected event, presenting the data in list-mode (indicating x, y, z-coordinates, intensity and frame number).

9.2.2 Silicon photo-multipliers

SiPMs are photon detectors that consist of a large number of avalanche photo-diodes (APDs) connected in parallel and operated in Geiger mode[116,257]. When a single APD (or: micro-cell) detects an optical photon, it will discharge, resulting in an output signal with fixed charge content. The presence of a large number of these APDs in a single SiPM basically presents a proportional photon counter, provided that the photon density is sufficiently low (i.e. when no more than a single photon is detected within the recovery time of the microcell)[119]. The accumulated signal of the cells in an SiPM is proportional to the number of cells discharging (i.e. increasing with the number of photons that is detected). SiPM readout of scintillator crystals currently enjoys increasing interest for medium energy gamma detectors, in particular for (time-of-flight) positron emission tomography (PET)[118,260,261], combined PET-MRI[262] and small-animal PET[263].

We have selected Hamamatsu S10931-100P(X) type SiPMs, which are 3x3 mm^2 in size and consist of 900 100×100 μm^2 cells. On all four sides of the crystal 3 SiPMs have been mounted using Bicron BC-630 optical grease. Through thermal contact with the EM-CCD, the SiPMs are cooled to a temperature of -27.4 (±0.2) ℃ and they are operated at a bias voltage of approx. 67.4 V. For each SiPM the bias voltage can be adjusted separately, to ensure relatively equal gain and noise levels. The spectral response of the SiPMs peaks at 400 nm, which lies somewhat lower than the peak emission of the CsI:Tl crystal; nevertheless the photon-detection efficiency should be around 20-25%.[258]

In this first proof-of-principle setup the SiPMs are applied as gamma photon counters. The signals of the 12 SiPMs are first preamplified by a 16-channel read out board (the design of which is described and characterized elsewhere[264]) and subsequently summed. The summed signal is shaped and amplified by an Ortec 572 spectroscopy amplifier. Spectra of the amplitudes of the sum pulses are recorded by an Ortec AD114 peak-sensitive ADC and these spectra are used to set an appropriate threshold on a Canberra SCA 2035 constant fraction discriminator (CFD). The CFD logic output pulses are counted with a National Instruments PCI-6034E card. A simplified electronics scheme for the SiPM-enhanced EMCCD-based gamma camera is shown in figure 9.2.

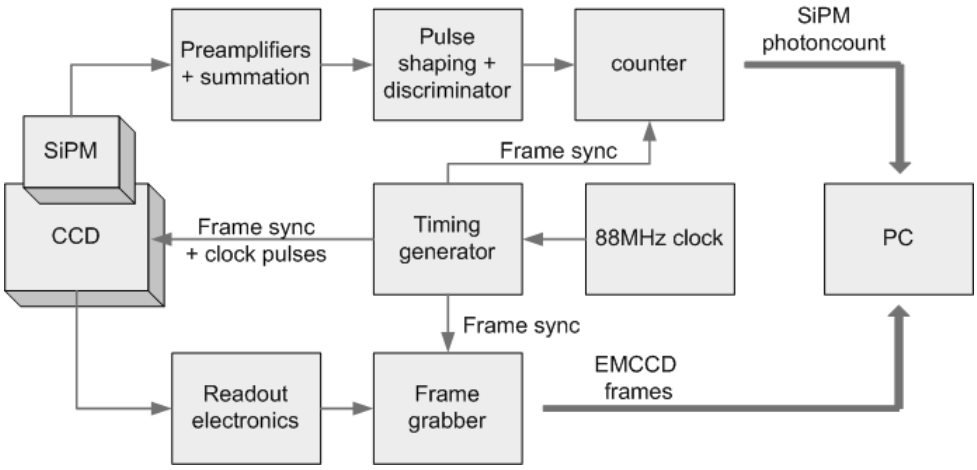

Figure 9.2: Simplified electronics scheme of the SiPM-enhanced EMCCD-based gamma camera. The gamma photon count of the SiPMs can be applied as *a priori* knowledge for the analytic scintillation detection algorithm. A timing circuit ensures synchronization between the EMCCD frames and the counter for the SiPM pulses.

9.2.3 Measurements

In order to verify the performance of the SiPMs and to set the appropriate thresholds for the CFD, the hybrid gamma camera has been irradiated by both ^{99m}Tc and ^{125}I flood and line sources. The line sources are created by collimation using a 30 μm wide slit in 4 mm thick tungsten plates.

For measurements of the spatial and energy resolution of the hybrid gamma camera the crystal is irradiated by ^{99m}Tc and ^{125}I line sources only. In order to determine the energy

resolution for the camera without SiPMs, energy spectra are constructed as histograms of the intensities of the detected events, such as determined by the scintillation detection algorithm[144] (chapter 2).

The energy spectra of the EM-CCD are used to determine the energy windows for reconstruction of the image of the slit and determination of the spatial resolution. For a fair comparison of the efficacy of the SiPMs, for both the camera with and without SiPMs, the energy windows are set to range from 50 % to 150 % of the position of the full-energy peak of the EM-CCD spectrum[174] (chapter 7). This is because in the current setup the SiPMs indicate how many events, detected by the scintillation detection algorithm, to include in the listmode; the SiPMs' information does not influence the location or energy of detected events.

The spatial resolution is determined by measuring the full-width-at-half-maximum (FWHM) of the projection of the slit, corrected for the width of the slit itself by deconvolution[82]. The SNR is defined as the *net* number of counts within the area irradiated by the slit (taken to be 50 lines for ^{99m}Tc and 200 lines for ^{125}I) divided by the number of false positives in an equally sized area of the EM-CCD covered by the tungsten plate (i.e. a non-irradiated area). The number of net signal counts is obtained by correcting the total signal for the false positives[144,174] (chapter 2 and 7).

To include almost all SiPM sum signals within the SiPM photopeak the CFD threshold has been set at (*photopeak position – FWHM* of the SiPM pulse-height spectra) for both the ^{99m}Tc and the ^{125}I measurements. The number of events above the threshold is counted per CCD frame. The effect of the inclusion of this *a priori* SiPM information on the performance of the gamma camera is investigated for a single measurement for each source (of 25.000 frames), by either ignoring or including the SiPM event count in the post-processing scintillation detection algorithm.

Because the number of incident gammas in a small-animal pinhole geometry is expected to be less than one per frame[54,155,173], in the simplest implementation, those frames for which the SiPMs detect no events have been discarded (*rejection* method); in a more advanced implementation the SiPMs' event count is used to select the number of most likely scintillation events (i.e. those with the highest detected energy) that the scintillation detection algorithm detects in each frame (*counting* method). Both the *rejection* and the *counting* method are compared to the case where the SiPM information is ignored.

9.3. Results

9.3.1 Characterization of SiPMs

In figure 9.3 we show the ^{125}I and ^{99m}Tc pulse-height spectra of the SiPMs measured for both line and flood sources. The good agreement between the spectra of the line sources and those of the flood sources indicates that the overall summed signal of the SiPMs (i.e. the total number of detected scintillation photons) is relatively independent of the location of the scintillation events in the crystal. The ratio of the peak positions of the ^{99m}Tc and ^{125}I spectra

indicates a good linearity of the SiPMs' response with the deposited gamma energy, in the range of energies investigated.

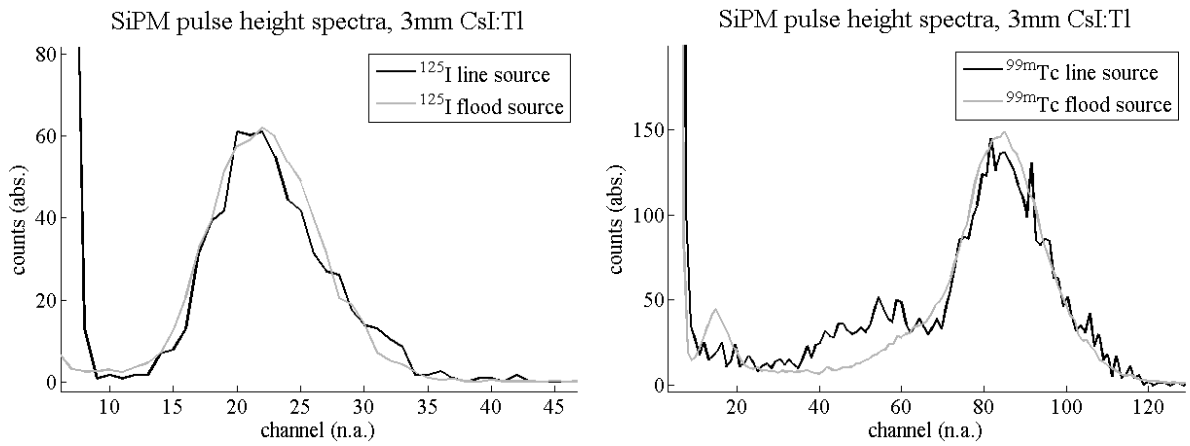

Figure 9.3: SiPM pulse-height spectra for ^{125}I and ^{99m}Tc sources. In both cases the SiPM pulses can be clearly distinguished from the background. For the ^{99m}Tc line source the spectrum seems to indicate a slight increase of scatter (to the left of the photopeak), presumably arising from the collimating slit.

9.3.2 EM-CCD Energy spectra

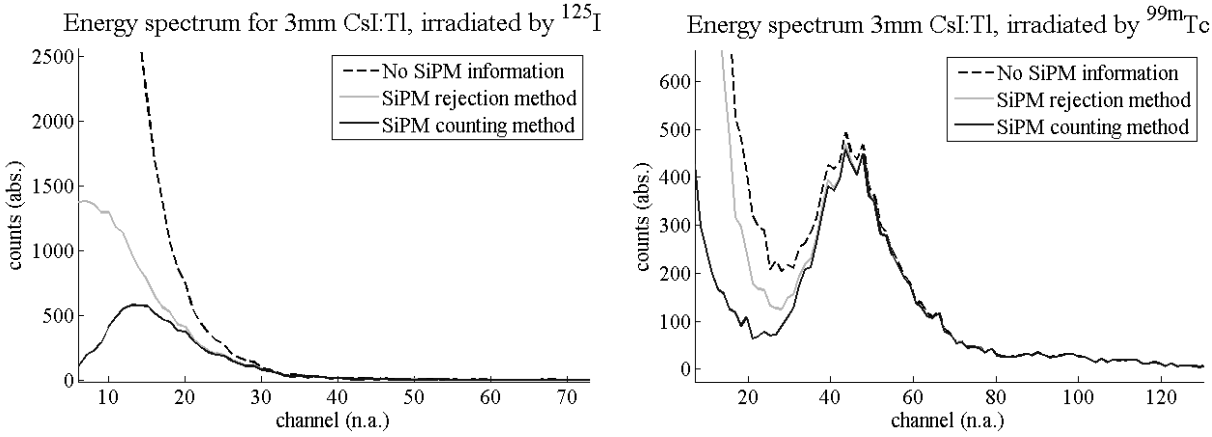

Figure 9.4: EM-CCD energy spectra of the ^{125}I and ^{99m}Tc signal for the camera with the SiPMs' event count ignored (dashed and dotted curves), with the *rejection* method (grey solid curves) and the more advanced *counting* method (black solid curves).

Figure 9.4 shows the energy spectra that have been acquired with the EM-CCD. It is clear that by including the SiPM information the energy spectra are improved dramatically by the rejection of false positive events. For ^{99m}Tc the background of low-energy counts (below the full-energy peak) is significantly suppressed. In the case of ^{125}I it is not even possible to separate true positives from the noise without applying the SiPMs. Compared to the *rejection* method, the *counting* method clearly leads to further reduction of the noise level.

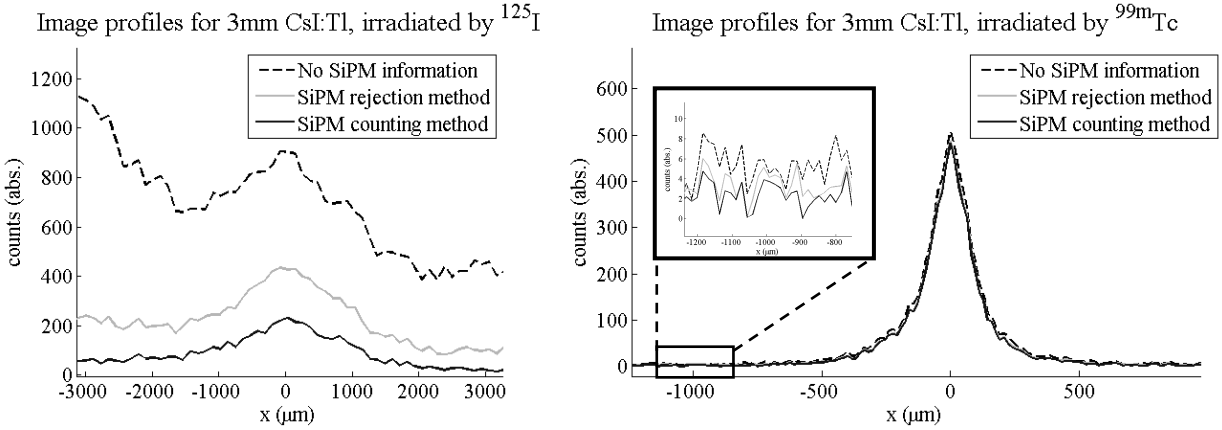

Figure 9.5: Profiles of the images of the slit for the gamma camera for the *rejection* and *counting* methods and without the application of the SiPMs.

9.3.3 Spatial resolution and SNR

Figure 9.5 shows the profiles of the images of the line sources, from which we have measured the FWHM spatial resolution values, for the camera employing the *rejection* and *counting* methods and without including the information of the SiPMs. The data are included in table 9.1.

For ^{99m}Tc one can see that the application of the SiPMs reduces the background without significantly reducing the signal itself. The spatial resolution is also somewhat improved. For ^{125}I, the improvement of the profile of the slit (i.e. the spatial resolution) and the reduction of the background are even more striking. In particular the *counting* method allows the ^{125}I scintillations to be distinguished from the background, although significant blurring occurs due to the relatively low number of scintillation photons generated at ~30 keV. However, without the information from the SiPMs, applying only the energy window, it is only barely possible to distinguish any ^{125}I signal from the background.

Table 9.1: Energy resolution (in FWHM (%)) measured from the EM-CCD energy spectra (figure.9.4) and spatial resolution values (FWHM and FWTM (μm)) and signal-to-noise ratio (SNR) as measured from the slit image profiles (figure 9.5). For ^{125}I the resolution has been determined after subtraction of a background level. The SNR is defined as the net number of counts within the image of the slit, divided by those in an equally sized area that is not irradiated.

	^{125}I			^{99m}Tc		
	SiPMs ignored	with SiPMs		SiPMs ignored	with SiPMs	
		rejection	*counting*		*rejection*	*counting*
EM-CCD Energy Resolution FWHM	no photopeak	-	~ 30 keV (~ 100 %)	75±2 keV (54 %)	68±3 keV (48 %)	69±2 keV (49 %)
Spatial Resolution FWHM	~1900 μm	~1700 μm	~1600 μm	164 (±4) μm	162 (±4) μm	160 (±3) μm
Spatial Resolution FWTM		-	-	551 (±16) μm	524 (±16) μm	519 (±23) μm
Signal/False-positive counts (SNR)	2092/18465 (0.11)	4029/4396 (0.92)	2585/1285 (2.0)	7071/205 (34.5)	6569/138 (47.5)	6493/100 (64.7)

9.4 Discussion

In the present investigation we have shown that the use of *a priori* knowledge of the SiPMs can significantly improve the performance of our EMCCD-based gamma camera. Two striking improvements can be noted: first, it is now possible to clearly detect ^{125}I scintillations, which, without use of the SiPMs, could barely be distinguished from the background at all; the SNR for ^{125}I has improved by a factor of almost 20. Secondly, for ^{99m}Tc the SNR has been improved by a factor of almost 2.

From the profiles of the line sources we can see that the rejection of frames without SiPM counts (i.e. most likely dark frames) already leads to reduction of the background level (false positive counts), viz. an improvement of 33 % in the case of ^{99m}Tc. Using the SiPM gamma photon count as an estimator of the number of most likely events from the scintillation detection algorithm leads to a further improvement (an additional 50%). Furthermore, the energy spectra show that applying the SiPMs information also significantly reduces the number of false counts in the EM-CCD images.

In this work we have used the information provided by the SiPMs only to indicate the number of scintillation events in each frame. In principle, more information can be extracted from the SiPMs and the use of this information might further improve gamma camera performance. In particular, the energy resolution of the SiPMs for ^{125}I and ^{99m}Tc (53 % and 29 %, respectively) is significantly better than that of the EM-CCD. In future work, we hope to use the signal of the SiPMs to further improve the energy resolution of the EMCCD-based gamma camera by combining pulse-height information from the SiPMs with the energy estimation from the scintillation detection algorithm. Other near-future investigations will include the extraction of spatial information from the pulse-heights of the individual SiPMs. This spatial information will allow us to exclude areas of the EM-CCD from the scintillation detection algorithm for further improvements of the noise performance of our gamma camera as well an acceleration of the algorithm[256]. Ultimately, for a very large area EM-CCD a high frame rate could be maintained by a partial read out, based on the information provided by the SiPM side detectors. Also, the SiPMs might improve the detection of (partially) overlapping scintillation flashes, which can cause problems with the analytical multi-scale algorithm used here. Finally, the method shown here could be combined with other methods such as micro-retroreflectors or optimized scintillation crystal materials[174,236] (chapter 5 and 7) for further improvement of the energy resolution.

9.5 Conclusion

In the present paper we have combined the benefits of the good signal-to-noise ratio of SiPMs with the unsurpassed spatial resolution of EMCCD-based gamma cameras. It has been shown that for ^{99m}Tc, SiPM side detectors improve the gamma camera SNR while the good detection efficiency and excellent spatial resolution are maintained. Moreover, the application of the SiPM allows detection of ^{125}I scintillations with a thick continuous scintillator, which could previously hardly be achieved. For future investigations we hope to

include energy and spatial information from the SiPMs in the detection algorithm to further improve the accuracy of our gamma camera.

We conclude that both SiPMs and EM-CCD are suitable devices for scintillation gamma detection, and that a hybrid SiPM/EM-CCD gamma camera can combine the advantages of both types of light sensor: high spatial resolution and excellent SNR. Thus, hybrid SiPM/EM-CCD gamma cameras are very promising and may enhance future SPECT and gamma autoradiography devices.

9.6 Acknowledgements

This work has been sponsored in part by the Netherlands Ministry of Economic Affairs, IOP photonics grant IPD067766. The authors would like to thank S. Seifert for valuable discussions and technical assistance.

Chapter 10

Improved EM-CCD gamma camera performance by SiPM pre-localization

S. Salvador[1,4], M.A.N. Korevaar[1, 2], J.W.T. Heemskerk[1, 2], R. Kreuger[1], J. Huizenga[1], S. Seifert[1], D.R. Schaart[1], and F.J. Beekman[1, 2, 3]

[1] Section of Radiation Detection and Medical Imaging, Department of R[3], Applied Sciences, Delft University of Technology, Mekelweg 15, 2629 JB Delft, The Netherlands
[2] Department of Nuclear Medicine, Image Sciences Institute, University Medical Center Utrecht, Heidelberglaan 100, 3584 CG, Utrecht, The Netherlands
[3] MILabs Molecular Imaging Laboratories, Universiteitsweg 100, 3584 CG, Utrecht, The Netherlands

Phys. Med. Biol., 57, 22, pp.7709-24, 2012

[4] Present Address: LPC Caen, ENSICAEN, Université de Caen, CNRS/IN2P3, 6 bd Maréchal Juin, 14050 Caen Cedex, France

Abstract

High spatial resolution gamma-imaging can be achieved with scintillators read out by low-noise, fast, electron-multiplying charge-coupled devices (EM-CCDs). Previously we have shown that false-positive events due to EM-CCD noise can be rejected by using the sum signal from silicon photomultipliers (SiPMs) mounted on the sides of the scintillator. Here we launch a next generation hybrid CCD-SiPM camera that utilizes the *individual* SiPM signals and Maximum-Likelihood Estimation (MLE) pre-localization of events to discriminate between true and false events in CCD frames. In addition SiPM signals are utilized for improved energy discrimination. The performance of this hybrid detector was tested for a continuous CsI:Tl crystal at 140 keV. With a pre-location accuracy of 1.06 mm (FWHM) attained with MLE the signal-to-background ratio (SBR) was improved by a factor of 5.9, 4.0, or 2.2 compared to EM-CCD-only readout, at the cost of rejecting respectively 47%, 9% or 4% of the events. Combining the *pre*-location and SiPM energy estimation improved the energy resolution from 50% to 19% while maintaining the spatial resolution at 180 µm.

10.1 Introduction

While clinical gamma cameras as used today in Nuclear Medicine typically have intrinsic resolutions for gamma-ray detection of a few mm[52], mathematical system analysis[53,155] and simulations[54,153] have shown that detectors with intrinsic resolutions approaching 100 µm can be useful to achieve high tomographic resolution with (very compact) SPECT devices. Several laboratories are developing cameras with spatial resolutions below a few hundred micrometers in the field of small-animal pinhole SPECT imaging[124,140,222,254,255,265,266,267,254]. Those ultra-high resolution gamma detectors can be based on direct or indirect gamma detection. Often, indirect gamma detectors based on a scintillating crystal coupled to position-sensitive photodetectors are used. For our future pre-clinical SPECT devices we are developing such a high resolution gamma detector based on Electron-Multiplying Charge-Coupled Devices (EM-CCDs)

EM-CCDs can be used to accurately detect the position of the scintillation light produced by each gamma interaction in the crystal. With columnar CsI:Tl crystals coupled to EM-CCDs, a spatial resolution of about 60 µm can be achieved[82,138,146,148]. However, the sensitivity of these configurations is low for 140 keV photons due to the limited thickness of currently available columnar crystals. To increase the detection efficiency, monolithic scintillators can be used[144,190,236] (chapter 2, 5 and 9). Because of the larger light spread onto the EM-CCD compared to using columnar crystals energy and spatial resolutions are degraded. This can be partly remedied by the use of an appropriate detection algorithm that takes into account the depth-of-interaction dependency of the light spread[144] (chapter 2). With this algorithm, an EM-CCD-based gamma camera coupled to a monolithic 3 mm thick CsI:Tl crystal achieves a spatial resolution of about 160 µm and an energy resolution of 54% for ^{99m}Tc imaging[190] (chapter 9). Still, the spatial and energy resolution as well as signal to noise ratio are degraded due to the small number of detected optical photons with respect to the EM-CCD noise. A better energy resolution would improve dual isotope imaging capabilities and reduce the number of background event for tomographic reconstruction. Less background improves the statistics of the detected events for the reconstruction, particularly when one works with small injected doses.

Silicon photomultipliers (SiPMs)[116,119,257,258,268,269] are currently being investigated by different research groups for use in PET detectors. An array of SiPMs mounted at the bottom of a continuous crystal achieves ~1.5 mm spatial resolution for 511 keV gamma radiation[270]. SiPMs mounted on top of a pixilated crystal do better: 0.8 mm.[271] Recently 0.8 mm resolution for an SiPM readout of a pixelated crystal for 122 keV gamma-rays was obtained.[112] Nevertheless, EM-CCD readout for SPECT detectors has still a much better spatial resolution.

Several groups have proposed additional sensors on the sides of continuous crystals for PET imaging[272] and SPECT imaging[256] to catch scintillation photons escaping through the sides of the crystal. Beekman proposed to add side detectors to use them for e.g. pre-localization or estimating the number of counts in order to improve the overall performance of a relative noisy high resolution position sensitive sensor at the bottom of the crystal. First results with an EM-CCD detector at the bottom have been published recently[190] (chapter 9),

(detector geometry shown in figure 10.1). In this first prototype device we simply summed the signals of the SiPMs and passed them to a discriminator to estimate the number of gamma interactions per CCD frame. Subsequently, CCD frames were rejected in the CCD event detection algorithm when no SiPM interactions had been detected in that frame, the so-called *rejection* method. In the same paper a more evolved method was proposed; i.e. the *counting* method in which the number of SiPM-detected interactions in each CCD frame was used in the detection algorithm to select the corresponding, most likely true-positive, CCD events by highest energy order within a certain energy window. These methods improved the signal-to-background ratio (SBR) by respectively a factor of 1.4 and 1.8 for ^{99m}Tc imaging, and strongly improved the detection of low energy gamma rays, such as ~27 keV photons from ^{125}I.

In this paper, we propose and validate the use of the *individual* SiPM detector signals in order to not only estimate the number of gamma-interactions, but also pre-locate them within the scintillator with the aim to further improve both the signal-to-background ratio and energy resolution of EM-CCD γ-images.

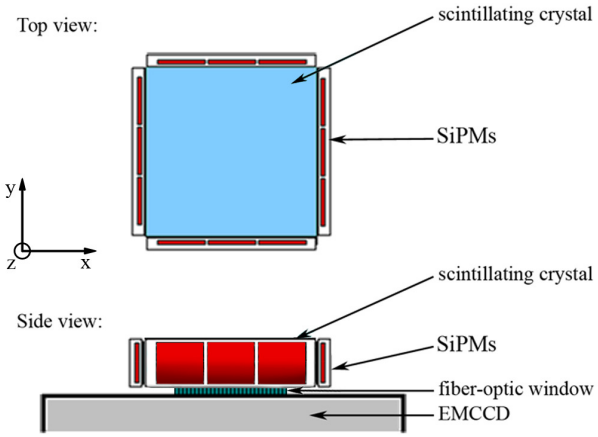

Figure 10.1: EMCCD-based gamma camera set-up with SiPM detectors on the scintillator sides.

10.2 Materials and Methods

10.2.1 EM-CCD with scintillator

The scintillation gamma camera used in this research consists of a 12 × 12 mm^2, 3 mm thick CsI:Tl scintillating crystal coupled to an EM-CCD operating in gamma photon-counting mode (figure 10.1). Gamma photons are converted in the crystal into scintillation photons detected by the EM-CCD. A detailed description of this gamma camera principle is provided elsewhere[82,146].

The scintillator material (SCIONIX corp.) has a light-yield of ~52 ph/keV[273], a decay time of 1 µs and a peak emission at a wavelength of 540 nm. The crystal is optically coupled to the EM-CCD via a Fiber Optic Plate (FOP) with Scionix BC90/147 optical

grease (n = 1.47). The 3 mm thickness of the crystal results in a 66% interaction probability for the 140 keV gamma-rays from ^{99m}Tc.

The EM-CCD is back-illuminated (CCD97, E2V technologies) with a quantum efficiency approaching 93% at 550 nm wavelength. The active area consists of 512 × 512 pixels, each 16 × 16 μm^2 in size. To reduce the dark current to a level below 0.1 e/pixel · s the EM-CCD is cooled to a temperature of (-30.5±0.1) ℃ using a Peltier element backed by a liquid cooler. The read-out of the EM-CCD is performed by an in-house developed electronic board[138]. By reading out the EM-CCD lines in pairs of two we achieve a frame rate of 50 Hz[259]. Frames are transferred to disc by means of a Matrox Meteor-II frame grabber PCI board. An analytical Multi-Scale Algorithm[144] (MSA, chapter 2) is used to retrieve the coordinates (x, y, z) and the energy of the scintillation(s) in each frame.

10.2.2 Silicon PhotoMultipliers

The silicon photomultipliers (SiPMs) are coupled with BC90/147 optical grease to the side surfaces of the scintillator (figure 10.1) in order to detect the light normally escaping from these surfaces. The SiPMs used here are MPPC-S10931-100P from Hamamatsu Corp. composed of 30 × 30 microcells with a 100 μm pitch and 78.5% fill factor. Three SiPMs are mounted on each of the four crystal sides. The photon-detection efficiency (PDE) of this device is approx. 15% for 550 nm wavelength according to photon counting measurements[274] for SiPMs with the same microcell structure. Through thermal conduction from the EM-CCD, the SiPMs are cooled down to (-12.2±0.1) ℃. Their temperature is monitored with a small NTC in contact with one of the SiPMs. Their bias voltages are set to -68.82 V. A common negative SiPM high voltage is used with our electronic pre-amplifier boards.

Figure 10.2 shows a simplified schematic view of the electronic set-up for the experiment. The signals of the 12 SiPMs are linearly pre-amplified by an in-house built 12-channel electronic board. The pre-amplifier circuit description can be found elsewhere[275,276]. The circuit includes an individual adjustment of the SiPM bias voltages to ensure equal gain and noise level of the SiPMs. The 12 output signals are sent to a 12-channel LeCroy 2249W charge integrating ADC unit (CAMAC). A sum signal from the 12 SiPMs is made on the main electronic board and sent to a LeCroy 623B octal discriminator to generate a 3 μs gate signal (sufficient to collect 95% of the signal charge) with a dual timer (SEN/TU 277). The gate signal is sent to the ADC unit for SiPM signal charge integration. The sum signal threshold of the discriminator is set well above the SiPM dark current level and corresponds to approx. 17 keV in the energy spectrum. The digitized values of the SiPM charges are assembled in data list-mode for each event and recorded by a PC: the SiPM event list.

The synchronization in the data analysis between the SiPM event list and the EM-CCD frame number is achieved by successively counting the number of SiPM gate pulses (registered events) for every EM-CCD frame of 20 ms. Therefore, a CAMAC scaler board is employed to count the number of SiPM gate pulses in between frame synchronization pulses. These pulses are extracted with the frame pulse generator from the video signal. The scaler counts are written to an SiPM counter list for every EM-CCD frame. The proper synchronization of the SiPM event list with the EM-CCD frames is then ensured by

referencing the SiPM event list and the EM-CCD frames to a common start signal: 6 LED light flashes sent to the crystal via an optical fiber at the start of each data acquisition just before a frame readout. These light flashes, separated by 200 ns, appear in one of the first recorded CCD frames and are detected as 6 consecutive "overflow events" in the SiPM event list and by 6 counts in the SiPM counter list. After this common starting point, the SiPM events belonging to a frame are obtained by taking the number of events from the SiPM event list as indicated by the SiPM counter list for that frame. It was checked for our 40 seconds lasting data acquisition files that the number of events in the SiPM counter list was equal to the number of events in the SiPM event list and that the last event in the SiPM counter list was found in the corresponding CCD frames

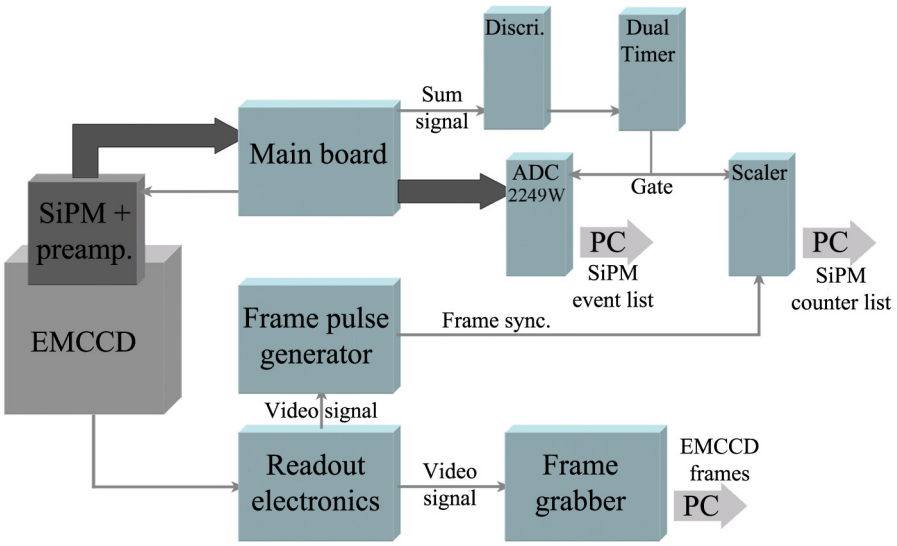

Figure 10.2: Electronic block diagram of SiPM-EMCCD gamma camera. A frame pulse generator ensures synchronization between the EM-CCD frames and the scaler for the SiPM pulses.

10.2.3 SiPM scintillation detection

The SiPM event information from the list-mode data file is processed in several steps. First, the SiPM energy estimate, Q_{tot}, is determined from the software-sum $Q_{tot} = \sum_{i=1}^{12} Q_i$ of the individual SiPM signals Q_i. Then the spatial coordinates are obtained by a maximum-likelihood algorithm using the Q_i and look-up-tables (LUTs) which are constructed from Monte Carlo simulations and calibration measurements.

10.2.3.1 Maximum-likelihood estimation with SiPMs (MLE-S) Since the spatial information of the event is contained in the relative amplitudes of the SiPM signals, we define the normalized SiPM signals $m_i = Q_i/Q_{tot}$, (i=1,…12) and use the following likelihood function to retrieve the event at position (x,y):

$$L\{m / x,y\} = \prod_{i=1}^{12} \frac{1}{\sigma_i(x,y)\sqrt{2\pi}} e^{-\frac{(m_i-\mu_i(x,y))^2}{2\sigma_i^2(x,y)}} \qquad (10.1)$$

Here the signals **m** (= $m_1,\ldots,m_{12}$) represent SiPM light signals with a Gaussian probability density function with parameters $\mu_i(x,y)$ and $\sigma_i(x,y)$ for a scintillation at position (x,y). The correlation between the signals **m** is neglected for simplicity. With look-up tables (LUTs) for $\mu_i(x,y)$ and $\sigma_i(x,y)$ we estimate the event position (x,y) by maximizing the log-likelihood function:

$$lnL\{m / x,y\} = -\left[\sum_{i=1}^{12}\left(ln\left(\sigma_i(x,y)\sqrt{2\pi}\right) + \frac{\left(m_i - \mu_i(x,y)\right)^2}{2\sigma_i^2(x,y)}\right)\right] \qquad (10.2)$$

The LUTs $\mu_i(x,y)$ and $\sigma_i(x,y)$ are obtained from simulations and calibrations for binned positions (x,y) over the entire field-of-view (FOV) of the scintillator (see section 10.2.3.2). The event position (x,y) is estimated by calculating the log-likelihood values (10.2) for the measured data set **m** at all LUT (x,y) grid points and subsequent determination of a weighted average over the (x,y) coordinates giving log-likelihood values within 8% of the maximum value. The 8% value was found to give the best results while measuring the MLE-S spatial resolution. Moreover, a threshold on the log-likelihood values is applied to remove multiple scattering events in the crystal for the interaction position estimation[187]. The threshold is set at -3 standard deviations from the mean value of the averaged likelihood value distribution.

10.2.3.2 SiPM LUTs generation The generation of the μ_i and σ_i LUTs is done by a Monte-Carlo (MC) simulation of the set-up using the GEANT4 V9.3 code[241] combined with experimentally determined response characteristics. The CsI:Tl crystal is modelled with its geometry and optical properties according to the literature (see table 10.1). The simulated SiPM detectors consist of epoxy layers on top of silicon with dimensions as given by the device specifications[277]. The 12 detectors are coupled to the scintillator by an optical grease of refractive index of 1.47. The fiber optic plate is modeled as a glass plate with refractive index 1.53 coupled to the crystal by the optical grease.

Table 10.1: Optical and geometric properties of the CsI:Tl crystal included in the GEANT4 simulations.

Light yield (ph/keV)	Wavelength at peak emission (nm)	Refractive index	Density (g/cm^3)	Decay time (ns)	Intrinsic energy resolution @140 keV (%)	Size (mm^3)	Finish
52 [273]	540 [273]	1.79 [278]	4.51 [278]	1000 [273]	5.9 [179]	12×12×3	Polished

All standard electromagnetic processes are included in the simulation. The GEANT cross section tables extend well below the 17 keV detection threshold of our hardware. The MC simulation generates $2 \cdot 10^6$ gamma-rays of 140 keV, incident perpendicularly on the scintillator over the entire FOV of 12 × 12 mm^2. Secondary particles, e.g. Compton scattered γs, are tracked for another interaction or escape from crystal. For each primary interaction, the x, y and total deposited energy values of the interaction are recorded as well as the number of collected optical photons per SiPM (N_{ph}). For each event in the post simulation process, the photo electron output signal (hereafter noted Q_i^{Sim}) of each SiPM is sampled from a Gaussian distribution. The mean value, $\mu_{\text{p.e.}}$, of this Gaussian distribution is

given by N_{ph} multiplied by the detector PDE (~15%) and added to a random number of electrons, $N_{d.c.}$(2.04 on average), which we derive from SiPM dark count rate measurements for our ADC integration time (3 μs) at their operating temperature of -12 ˚ C.

$$\mu_{p.e.} = N_{ph} \times PDE + N_{d.c.} \tag{10.3}$$

The sigma value $\sigma_{p.e.}$of the distribution is given by:

$$\sigma_{p.e.} = \alpha\sqrt{\mu_{p.e.}} \tag{10.4}$$

Here, α is a parameter matching the experimentally observed average energy resolution ($\sigma_{p.e.}/\mu_{p.e.} = \sigma_Q/\mu_Q$) of the SiPMs for 140 keV events in the centre of the crystal and found to be 1.6. This parameter accounts for all individual sources of variance (scintillator energy resolution, SiPM dark current, excess variance, electronics, acquisition etc.) and electronic gains in the experimental signals Q_i and is used in the simulations for any position (x,y).

Finally, the distribution of the normalized SiPM signals $m_i^{sim} = Q_i^{Sim}/Q_{tot}^{Sim}$ is constructed for each of the 12 SiPMs and every 125 × 125 μm² binned gamma interaction position over the whole FOV, resulting in 12 × 96 × 96 signal distributions. Figure 10.3(a) gives an example of such a distribution for SiPM #2 and for gamma interactions located at the centre of the crystal (0,0). The photoelectric peak of the distributions are then fitted by a Gaussian curve to retrieve the 96 × 96 grid $\mu_i(x,y)$ and $\sigma_i(x,y)$ LUTs. Figure 10.3(b) shows the μ_i and σ_i LUTs for the first three SiPMs versus the position of the interaction.

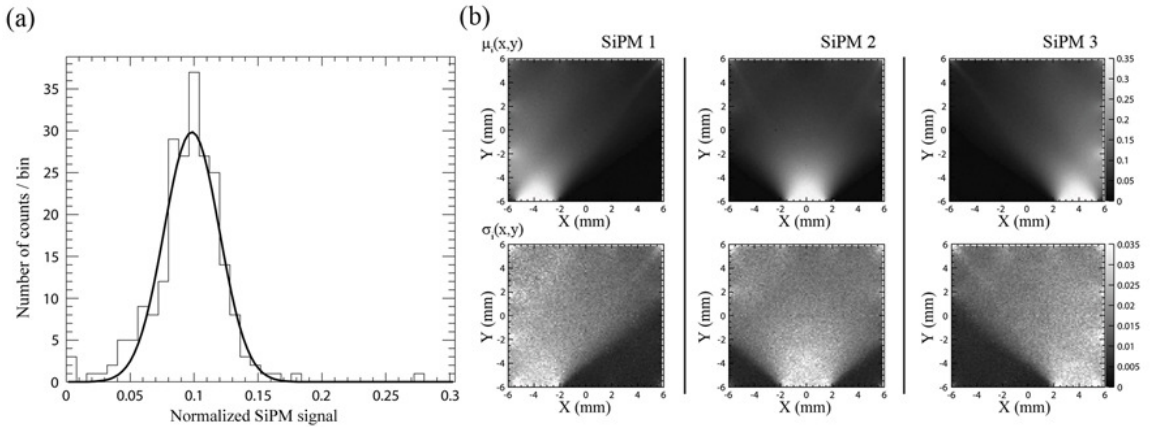

Figure 10.3: (a) Normalized charge distribution of SiPM #2 for gamma interactions located at the centre of the crystal and the applied Gaussian fit (solid black line). **(b)** $\mu_i(x,y)$ and $\sigma_i(x,y)$ LUTs for three SiPMs. Grey scales indicate values of the parameters for an (x,y) event position.

These simulated LUTs assume a linear response of the SiPMs. In order to improve the agreement of the LUTs with the experimental set-up, we apply a correction based on a calibration measurement similar to other researchers[277] with the linearity test phantom defined in section 10.2.5.1. With this phantom the SiPM signal distribution for 6 × 6 irradiated positions of the crystal can be recorded. In these 6 × 6 calibration positions the experimental $\mu_i(x,y)$ and $\sigma_i(x,y)$ LUT^{exp} are calculated. By dividing them by the simulated look-up-table (LUT^{sim}) values in the corresponding positions, 6 × 6 correction maps can be constructed for the SiPMs. These correction maps are then bilinearly interpolated to the 96 × 96 grid and applied to the simulated LUT^{sim} $\mu_i(x,y)$ and $\sigma_i(x,y)$ to obtain the LUTs for

equation (10.2). So, we combine a high resolution simulated LUT with a low resolution calibration measurement. All results provided in this article are obtained after this calibration correction has been applied to the LUTs.

10.2.4 Combining EM-CCD and SiPM data

The hybrid gamma camera can combine the information from the MSA event detection algorithm for the EM-CCD with the SiPM detector using different methods. Two of them only check if events have SiPM sum signals above a particular threshold. The first of these two methods, the *rejection* method, discards frames where no SiPM event has been detected. The second method, the *counting* method, uses the number of events from the SiPM event counter list to select the same number of EM-CCD MSA reconstructed events, in order of highest energy, in the corresponding frame. An elaborate description of both methods is given by a previous investigation of these methods[190] (chapter 9).

A third method launched here (the *pre-location* method), estimates the location of the events obtained from the MLE-S algorithm to select the MSA events. For each MLE-S reconstructed event a region of interest (ROI) with a radius, expressed as a number of SiPM spatial standard deviations (σ_{SiPM}, defined in section 10.2.5.1), is set around the MLE-S interaction location. Then the algorithm searches in the MSA event list of that frame an interaction position within this ROI. If an event is found in the ROI, the matching MSA (x,y,z) coordinates are taken for the scintillation position, while the SiPM software-sum signal (Q_{tot}) is used for its energy. Otherwise the MLE-S event is discarded. When all MLE-S events for a frame have been checked, the remaining MSA events not attributed to a ROI are discarded. Due to the low count rate in case of SPECT imaging[82], the probability that more than one event is detected within the same ROI in an EM-CCD frame is sufficiently low to assume that no degradation can be seen either in the energy spectrum or in the reconstructed image.

10.2.5 Measurements

In order to measure the performance of the SiPMs and EM-CCD individually and their combination in the hybrid gamma camera, the detector has been irradiated with a source consisting of a 0.5 ml Eppendorf cup partly filled with ^{99m}Tc (140 keV).

10.2.5.1 SiPM performance To show that the MLE-S algorithm for SiPM data works properly with corrected LUTs, we used a linearity test phantom consisting of 6 × 6 holes, 170 µm in diameter, made in a 12 × 12 mm^2, 5 mm thick lead plate. The hole pitch was 2 mm in x and y directions. The phantom was positioned 3 mm above the crystal and uniformly irradiated by the ^{99m}Tc source placed 6 cm above the centre of the phantom. The same setup has been used to obtain images for the LUT correction map calculation.

The energy resolution is measured as the FWHM (full-width-at-half-maximum) of a Gaussian fit to the photoelectric peak in the energy spectrum built from the SiPM Q_{tot} signal. The event positions are estimated with the MLE-S algorithm and corrected LUTs.

Then, projections in each direction are made over 2 mm wide areas centered on the holes and used to measure the spatial resolution in the other direction; See for example figure 10.4(b). The spatial resolution (FWHM) at the hole positions are determined as 2.35 times the standard deviation (σ_{SiPM}) obtained from Gaussian fits applied to the x and y projections of the holes. The error of the spatial resolution is calculated using the bootstrap method[187] and includes an estimated error for limiting the projections to 2 mm wide areas. The MLE-S spatial resolution is summarized as the average of x- and y- FWHM resolution of the holes in the EM-CCD FOV, i.e. 8×8 mm^2. To check if corrected LUTs give a good event position estimation, we measure the non-linearity in the CCD FOV as the average observed absolute x- and y- difference between the mean position of each hole projection and the corresponding known hole position in the phantom.

10.2.5.2 Hybrid gamma camera performance For evaluating resolutions of the different methods utilizing the EM-CCD SiPM combination, a line-shaped irradiation pattern in the middle of the CCD was made by collimation of the ^{99m}Tc source, using a 30 μm wide slit in a 4 mm thick tungsten plate. Data were acquired for 100,000 frames. The gamma camera was tested for the *rejection*, *counting* and *pre-location* event position estimation methods as well as the *CCD only* MSA method (discarding SiPM information) for comparison.

Energy spectra are acquired for events reconstructed in a CCD area of 128 rows of pixels on both sides of the slit and the energy resolutions are extracted as the Gaussian fitted FWHM of the photopeak[145,236] (chapter 3 and 5). An MSA energy window from 67% to 200% of the mean photopeak value is used to select events for the slit images, rejecting scattered events in the collimator. Line spread functions (LSF) of the slit are made by making image projections parallel to the slit direction. The spatial resolution is then obtained for each method by the FWHM of Gaussian fits to the slit LSFs and FWTM (Full-Width-Tenth-Maximum) of these LSFs. The uncertainties in energy and spatial resolutions have been calculated using the bootstrap method.

The number of true counts is defined as the total number of counts within an area irradiated by the slit corrected for the number of false positives (background), which are the events detected in an equally sized area of the EM-CCD covered by the tungsten plate (i.e. a non-irradiated area)[144,174] (chapter 2 and 7). The signal-to-background ratio (SBR) is then defined as the number of true counts in a 50 lines wide area below the slit divided by the number of false positives.

10.3 Results

10.3.1 SiPM performance

Figure 10.4(a) presents the 2D image of the linearity phantom obtained by the *SiPM only* MLE-S position estimation of events from the ^{99m}Tc source. Figure 10.4(b) shows the projections in the x and y directions for the areas indicated by the white lines in the 2D image. The different peak heights in figure 10.4(b) are caused by varying spatial resolution. The SiPM spatial resolution varies between 0.85 mm and 1.4 mm within the EM-CCD FOV. The average resolution within the CCD FOV is 1.11±0.35 mm FWHM (σ_{SiPM} =0.47 mm) and the average spatial non-linearity in that area is 175±130 μm. The energy spectrum for ^{99m}Tc is shown in figure 10.5 together with the Gaussian fit used to estimate the energy resolution (solid black curve). The measured energy resolution, the average spatial resolution as well as the average non-linearity are listed in table 10.2. The FWHM energy resolution is 21±2% for ^{99m}Tc over the CCD FOV.

Table 10.2: Energy, average spatial resolutions (FWHM in μm) and non-linearity for the *SiPM only* performances obtained with the linearity phantom and ^{99m}Tc gamma source.

FWHM energy	FWHM (μm)		Non-linearity (μm)	
resolution (%)	<x>	<y>	<x>	<y>
21±2	1110±350	1090±330	170±120	180±140

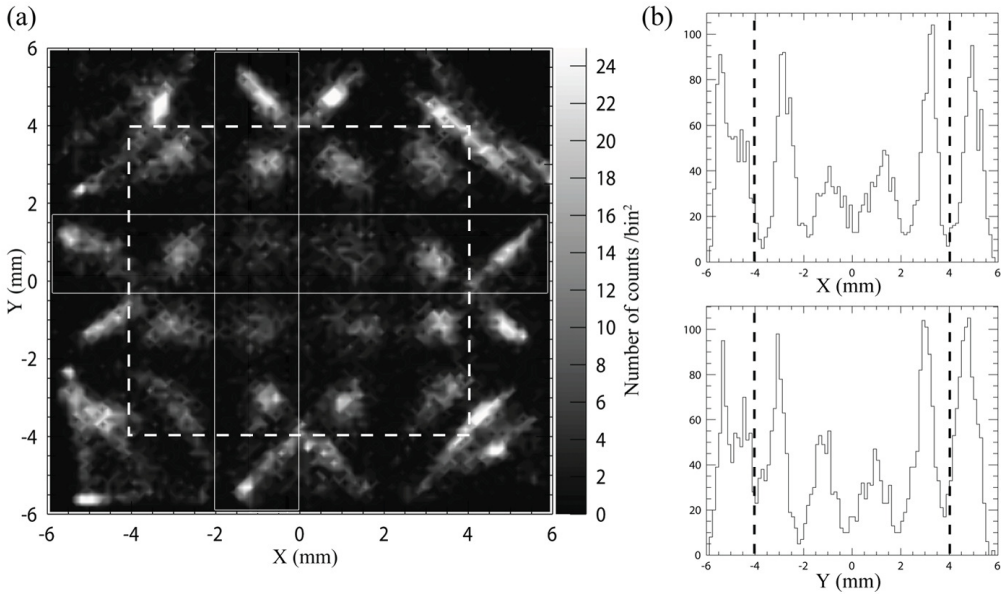

Figure 10.4: (a) Image based on *SiPM only* (MLE-S) of a linearity phantom irradiated with ^{99m}Tc. Dashed lines show boundaries of the EM-CCD FOV. **(b)** Image projections for positions enclosed by the white lines in **(a)**.

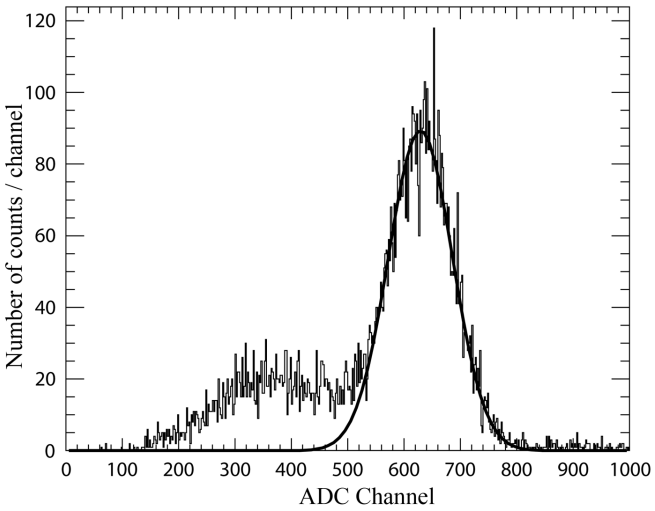

Figure 10.5: Energy spectrum of SiPM software-sum signal Q_{tot} with the linearity phantom irradiated by a ^{99m}Tc gamma source. Energy resolution is calculated as FWHM of the Gaussian fit (solid black curve).

10.3.2 Hybrid gamma camera performances

In figure 10.6 the energy spectra obtained with the different methods are shown. The energy resolution (also mentioned in table 10.3) is 78% for the *CCD only* MSA energy spectrum when the SiPM information is completely discarded. By accepting only matching events from the MLE-S algorithm in the *pre-location* method, the resolution is very similar: 75%. However, the resolution of the SiPM energy spectrum for these *pre-location* method events is much better: 19%.

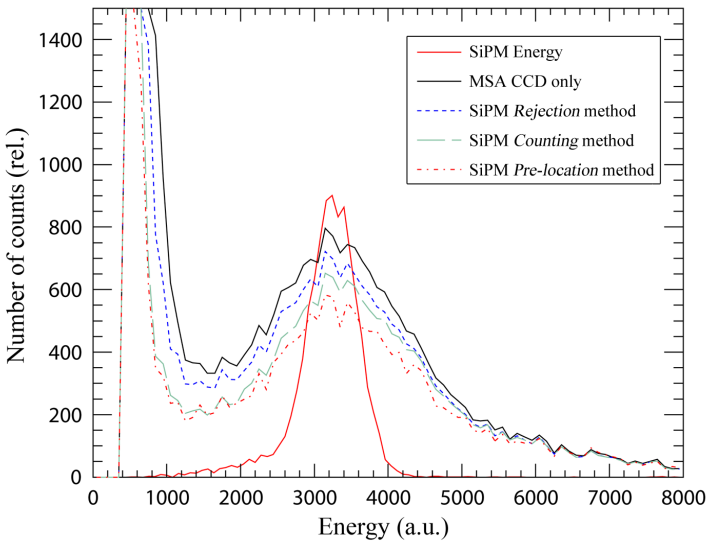

Figure 10.6: Energy spectra for 140 keV events (^{99m}Tc) obtained from the MSA algorithm using the different methods and energy spectrum obtained with SiPMs.

This is slightly better, although within the error bars, than the 21% obtained with the linearity phantom in table 10.2, because for the slit measurement only events within ±128 lines around the slit are included in the energy spectrum, while with the linearity phantom events over the whole scintillator area are included. This effectively reduces the amount of Compton scatter from the phantom included in the energy spectrum photopeak.

Line spread functions of the slit are plotted in figure 10.7 for the four different scintillation detection methods. These are used to obtain the FWHM and FWTM of the hybrid gamma camera.

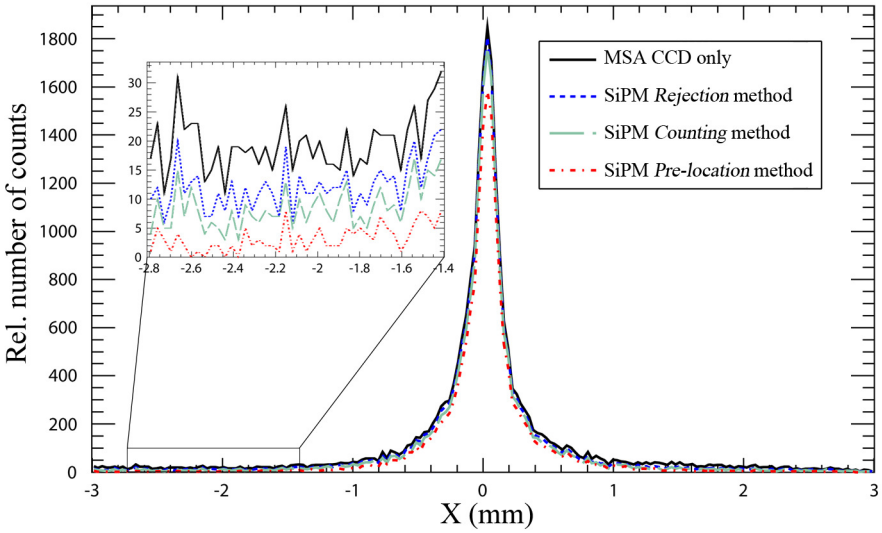

Figure 10.7: Line spread functions of the images of ^{99m}Tc line source for the different scintillation detection methods. For the *pre-location* method, ROI is $3 \times \sigma_{SiPM}$. The enlarged inset illustrates the differences in background events.

It is clear that the use of SiPM information reduces the background in the non-irradiated area, in particular with the *pre-location* method. However, this *pre-location* method rejects also more true events than the other methods depending on the ROI radius. This reduction is shown in figure 10.8(a) by the relative number of true counts within the slit profile given by the *pre-location* method compared to those from the *counting* method as function of the ROI radius expressed as number of σ_{SiPM} values (SiPM spatial standard deviation). Figure 10.8(b) presents how the SBR improves relatively to *CCD only* method as a function of the ROI radius. For a ROI radius of $3 \times \sigma_{SiPM}$ the loss of counts is found to be 9% for an SBR improvement of a factor 4.0. Above a ROI radius of $3 \times \sigma_{SiPM}$, the loss of counts reduces to 4%, while the SBR improvement drops down to 2.2. On the other hand, by rejecting 47% of the events the SBR improvement rises to a factor 5.9. Subsequent results are therefore evaluated with a standard ROI radius of $3 \times \sigma_{SiPM}$. Table 10.3 summarizes the results obtained with the different methods and also includes the SiPM results from the slit measurements.

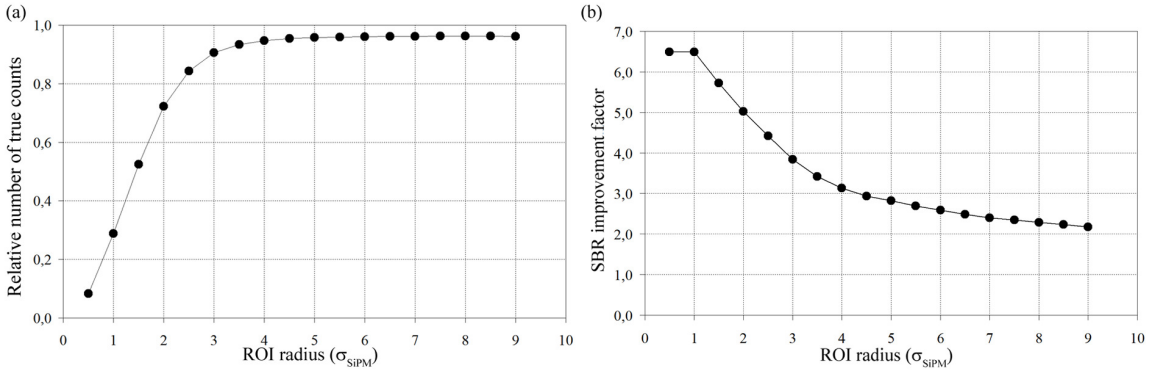

Figure 10.8: (a) Plot of the number of true counts for the *pre-location* method relative to the *counting* method as function of the ROI radius. **(b)** SBR improvement factor of the *pre-location* method relative to *CCD only* versus the ROI radius.

Table 10.3. Energy resolution measured from the energy spectra (figure 10.6), spatial resolution (FWHM and FWTM) and signal-to-background ratio (SBR) as measured from the slit LSFs (figure 10.7) for the different scintillation detection methods. The results of the EM-CCD event position estimation without the use of the SiPM (*CCD only*) and the (MLE-S) *SiPM only* event position estimation are also shown for comparison.

	CCD only (MSA)	SiPM only (MLE-S)	SiPM based Frame *Rejection*	SiPM based Event *Counting*	SiPM based *Pre-location*
Energy resolution FWHM (%)	78±2	19±3	77±4	75±3	19±3
Spatial resolution FWHM (µm)	178±14	923±15	177±15	175±14	181±24
Spatial resolution FWTM (µm)	813±43	1930±240	761±47	758±84	736±78
True/false-positive cts	18685/541	-	17941/352	17256/260	15632/114
SBR	34.5		60.0	66.4	137.0

10.4 Discussion

In this paper we show that utilizing SiPM side detectors with *individual* read-out improves the performance of an EM-CCD gamma camera. First, it is interesting to note that the SiPM energy resolution is improved to 19%, compared to 29% for a previous setup using SiPM sum signals[190] (chapter 9). Moreover, the individual readout of SiPMs combined with MLE-S results in a pre-location spatial resolution of approx. 1 mm. Thus a setup without CCD could be useful for low to medium resolution applications.

We also show that Look-Up-Tables for MLE-S can be constructed by Monte-Carlo simulations corrected with coarse calibration data, making the system calibration fast and practical. However, the 2D image from the linearity phantom measurement shows artifacts at the borders of the scintillator. These can be attributed to the fact that for these areas only a few of the 12 SiPMs have a significant signal. These artifacts can possibly be reduced

by the use of more, though smaller, SiPMs on the sides and calibrations at a finer grid and use of SiPMs with higher PDE and other improved properties currently being developed. Almost no events are found in the image for the holes in the corners of the linearity phantom. This is caused by rather poor calibration data for these holes. Nonetheless, in the CCD FOV (not at the very crystal edges) the MLE-S gives a good event position estimate for our pre-localization method. Therefore a long and difficult calibration process to improve the position estimate for crystal edge events could be avoided.

In table 10.3 is shown that the number of background counts in the *CCD only* image can be reduced by almost a factor of 2 when the SiPMs are used as a simple scintillation counter and by a factor of 4 when pre-localization is used. Then the signal-to-background ratio increases from 34.5 (*CCD only*) to 137 (*pre-location*). The improvement depends on the conditions for matching SiPM *pre-location* and MSA event location, as can be seen in figure 10.8: The smaller the ROI radius the more true events are rejected while the SBR is improved. For example at rejecting 47% of the true events (at ROI radius of 1.5 $\times$ σ_{SiPM}), the SBR is improved to 203. For a large ROI, the event rejection reduces to 4%. Then the *pre-location* method becomes almost equal to the *counting* method, because for a large ROI MLE-S events always match the MSA events. The remaining 4% rejection is caused by the fact that some of the matching MLE-S events are rejected because of the likelihood threshold test. Due to this test, the SBR improvement of 2.2 is just slightly better than the factor 1.9 for the *counting* method.

From table 10.3, one sees that the *pre-location* method maintains the FWHM spatial resolution at 180 µm, like CCD MSA.The FWTM values are slightly reduced from 813 µm to 736 µm by removing more of the false-positive counts in the tails of the line profiles than the *rejection* and *counting* methods as can be seen in the inset of figure 10.7. The energy resolution obtained with the MSA algorithm for EM-CCD frames is 78% for 140 keV gamma-rays while in previous measurements[190] (chapter 9) it was around 50%. This could be caused by aging of the EM-CCD or the fact that in the current set-up the SiPM bias voltages are set higher to improve the SiPM photon detection efficiency (PDE). With this higher bias voltage we could observe the cross-talk photons produced in the SiPM avalanches[280] via photon transport through the scintillator in the EM-CCD video frames. We believe that this extra noise is the cause of the degraded energy resolution given by the MSA event position estimation algorithm for the EM-CCD frames. But this degradation does not affect the results in the *pre-location* method, since the event energy is no longer estimated from the EM-CCD MSA information, but from the SiPM energy estimate with 19% energy resolution. Yet, the extra noise is probably the cause of the slightly degraded spatial resolution of 180 µm compared to 160 µm for the previous measurements[190] (chapter 9).

For lower energy photons (i.e. ~27 keV X-rays emission from ^{125}I), SiPM *rejection* and *counting* methods have been shown to be useful to improve energy resolution and to distinguish events from the background[190] (chapter 9). However, after careful investigation, the use of the *pre-location* method has shown no further improved results for these low energy photons. This can be explained by a degraded spatial and energy resolution of the SiPM set-up due to the lower number of photons emitted compared to ^{99m}Tc 140 keV scintillations events. With a degraded spatial resolution the ROI becomes almost as large as

the EM-CCD FOV and then the *pre-location* method does not help to reject false-positive counts. However, next generation SiPM are expected to change this outcome.

In future work, the use of the SiPM individual read-out combined with a statistical algorithm to retrieve the CCD event information[145] (chapter 3) may possibly lead to more improvements of the *hybrid* gamma camera performance. Ultimately, the development of a single statistical algorithm combining next generation SiPMs and EM-CCD data might significantly improve the performance of our *hybrid* gamma camera. Such a hybrid gamma camera may be successfully applied in our next SPECT systems: For example it was shown that with detector resolutions between 0.1 and 0.2 mm the system resolution can be halved compared to the current setup with clinical gamma detectors[155], as used in our commercialized U-SPECT-II system[173]. We have studied concept scanners that require a few tens of CCDs when installed around a dedicated multi-pinhole collimator[54] and optimized according to the model proposed previously[155]. We believe that this is technically and, soon, also economically feasible. Given the expected event rates for such a system, we expect about 400 cps per CCD. With the 50 Hz frame rate presently already available and with a proper detection algorithm these events can easily be identified in the CCD images. The current MSA algorithm runs at 2 seconds per frame on a Core2 Duo 3 GHz processor and is dominant compared the 10 ms processing time for MLE-S end pre-location method per SiPM event. With dedicated hardware (e.g. DSP, FPGA or GPU) or multiprocessor systems the event processing can eventually be done online[88,138,187,281].

Today many image reconstruction methods exist that inherently deal with gaps between detectors. However, when one wants to produce a SPECT system with almost full detector coverage, dead space around useful crystal area should be limited. When using the concept of side detectors a combination of smaller SiPMs, longer (almost) straight fiber optic tapers, larger CCDs and other geometries to read out the crystal sides[256,282] could be used to accomplish a high performance full ring pre-clinical SPECT system.

10.5 Conclusion

In this paper, we have presented a new hybrid gamma imaging detector combining an EM-CCD and silicon photomultipliers as side detectors for the scintillation readout. With a position detection algorithm using the additional information from the SiPM *pre-location* the FWHM energy resolution is considerably improved: from 50% (EM-CCD setup without SiPM side detectors) to 19%. This improved energy resolution comes together with a high intrinsic spatial resolution of 180 µm (FWHM). The signal-to-background ratio for commonly used ^{99m}Tc-based radiotracers in SPECT imaging is improved by a factor 4.0 compared to an *EMCCD-only* setup. Such a hybrid device might enhance future high-resolution small-animal SPECT scanners. Because a 19% energy resolution is not sufficient to perform dual isotope SPECT with isotopes that have their energy peaks close to each other (eg ^{99m}Tc and ^{123}I), it would be desirable to further improve the energy resolution by combining the method proposed in here with other improvements of the EM-CCD detectors, such as the use of special read out methods[178,290] (chapter 8), special reflectors[174] (chapter 7), better scintillators[236] (chapter 5) and improved detection algorithms[141,145] (chapter 3).

10.6 Acknowledgments

This work was sponsored by the Technology Foundation STW grant IPD067766 and by grant *PID06015* of the program Pieken in the Delta Zuidvleugel of the Ministry of Economic Affairs and Provincie Zuid-Holland

Chapter 11

Summary and outlook

The development of high resolution gamma detectors is an important step towards improvement of SPECT imaging. Currently, most SPECT imagers still use the traditional Anger camera consisting of a NaI scintillator read out by an array of photo multiplier tubes. To improve upon the Anger camera, different high spatial resolution gamma detectors are being considered. In this thesis we investigated a scintillation gamma detector based on a high sensitivity and high resolution light sensor -the EM-CCD- that has the potential to achieve a large improvement in resolution over the Anger camera. Such EM-CCD based gamma cameras may be particularly useful in pre-clinical SPECT.

This sensor, first announced more than a decade ago, is a special kind of CCD with on-chip signal amplification[115,116]. Because of this amplification, the readout noise, typically the dominant noise source in CCDs, is overcome in EM-CCDs.
In scintillation gamma detectors, EM-CCDs have initially been used in combination with CsI:Tl scintillators which were structured in micro columns, to prevent the light photons from spreading too much[114,120]. In this set-up, it was shown that, because of its low noise, the EM-CCD allows for individual gamma photon detection[123].

The research described in this thesis focuses on the use of EM-CCD based gamma detectors in combination with continuous instead of columnar scintillators. Because these continuous scintillators are available in much larger thicknesses than columnar scintillators, their use can improve gamma photon detection efficiency. Additionally, the choice of scintillating materials is very limited for columnar scintillators. However, the use of thicker continuous scintillators presents new challenges such as a larger spread of the scintillation photons before they reach the EM-CCD and larger variation of the depth-of-interaction in the scintillator. If gamma photons enter the detector at an oblique angle the variation of the depth-of-interaction causes a variation of the detected position, resulting in a degradation of the spatial resolution. This degradation is known as the depth-of-interaction effect, which is present in most SPECT pinhole cameras. It becomes more pronounced when thicker scintillators are being used and therefore plays a major role for the relatively thick continuous scintillators considered in this thesis.

One way to tackle the problems caused by the variable depth-of-interaction is to use a detection algorithm that models the light spread as a function of depth, thereby enabling the detection of the depth-of-interaction. In this thesis two new detection algorithms were presented and validated. The first of these detection algorithms, introduced in **chapter 2**, is a fast analytical scintillation detection algorithm based on analysis of a recorded scintillation at multiple scales and thus named the multi-scale algorithm. We showed that the multi-scale algorithm can detect the depth-of-interaction in an experiment where gamma photons are incident at an oblique angle and use this information to reduce the depth-of-interaction effect. This resulted in a 5-fold improvement of the spatial resolution for gamma photons incident at an angle of 45 degrees compared to an analytical Gaussian filter algorithm that did not use any depth-of-interaction information. Furthermore, the multi-scale algorithm also improved the energy resolution and signal-to-background ratio significantly compared to the Gaussian filter algorithm.

A second detection algorithms investigated in this thesis is a statistical Maximum-Likelihood algorithm that not only models the depth-dependent light distribution on the EM-CCD but also takes into account the statistical nature of the EM-CCD output. In **chapter 3**, we addressed the research question whether the use of such a statistical scintillation detection algorithm further improves upon the multi-scale algorithm. We found that the use of the statistical Maximum-Likelihood algorithm resulted in a substantial improvement in energy resolution by more than a factor 1.6, a significant improvement of the spatial resolution for gamma photons incident at an oblique angle and of the signal to background ratio. Regardless of the algorithm used we found that the thickness of the scintillator has a strong influence on the spatial resolution; for larger thicknesses the spatial resolution degrades continuously from a resolution of 59 μm for a 0.6 mm thick scintillator to a resolution of 147 μm for a 3 mm thick scintillator.

Another approach to resolve the depth-of-interaction effect, involving the use of a new detector design, was presented in **chapter 4**. This new detector geometry consisted of a curved scintillator fitted to a concavely shaped optical taper with all fibers pointing towards the pinhole. As a consequence, the centroid of the scintillation light distribution of a point source is independent of the depth-of-interaction. This new curved detector was compared to a regular flat detector with comparable taper thickness for gamma photons incident perpendicularly and at an oblique angle of 30 degrees. The flat detector reached a spatial resolution below 280 μm for perpendicular incidence but this was degraded to values worse than 1.4 mm for oblique incidence due to the depth-of-interaction effect. The prototype curved detector attained spatial resolutions below 280 μm for *all* angles of incidence, demonstrating the elimination of the depth-of-interaction effect. However, a drawback of the prototype curved detector is a degradation of the energy resolution, probably due to scintillation light losses in the optical taper.

One of the advantages of using continuous scintillators is that the choice of scintillator material is no longer restricted to CsI:Tl but many different materials can be used. Furthermore EM-CCDs, in contrast to commonly used PMTs, do not instantaneously read out the detector but integrate the scintillation signal. This property has important consequences for the types of scintillators that can be used in conjunction with EM-CCDs; it enables the use of relatively slow scintillators that have not been considered previously for gamma photon detection. In order to improve the gamma detector performance we compared several high density scintillator materials, such as $CdWO_4$, $(Gd,Lu)_2O_3$:Eu and Lu_2O_3:Eu, to CsI:Tl in **chapter 5**. These denser scintillators can be thinner than CsI:Tl and still have the same interaction probability. The use of these thin and dense scintillators improved the spatial resolution considerably compared to CsI:Tl. However, in all cases the energy resolution was degraded, probably due to a lower light output, the presence of radioactive isotopes in the scintillator or a higher refractive index.

Optimizing gamma camera performance requires a good understanding of the influence of different detector parameters on its performance. For this purpose, Cramer Rao lower bounds can be an aid because they can show what the theoretically best attainable performance is. In **chapter 6** we presented Cramer Rao lower bounds of the energy and spatial resolution as a function of different detector parameters. We found that the predicted

trends of the theoretical lower bounds as a function of the EM gain and depth-of-interaction were reproduced by the measurements. Both measurements and calculations show that the spatial and energy resolution are optimal for moderate EM gain and they predict an almost quadratic degradation of spatial resolution with increasing depth-of-interaction. This suggests that scintillator thickness is one of the main parameters determining the spatial resolution, which was also found empirically in chapter 2, 3 and 5. Furthermore, we learned that the amount of detected photons (determined e.g. by the quantum efficiency (QE), the scintillator light output and light collection efficiency onto the detector) and the noise originating in the image area have a strong influence on the performance. The amount of detected photons cannot be increased significantly by the use of an EM-CCD with a higher QE as it is already at 90 % but could in principle be improved using a scintillator with higher light output. Furthermore, a 10-fold reduction of the noise originating in the image area has been shown to be possible[201] and can lead to an improvement of approximately a factor 1.5 in spatial and energy resolution of the gamma camera.

To increase the number of photons that arrive at the EM-CCD detector, we present the use of retro reflectors in **chapter 7**. These retro reflectors are designed to reflect an optical photon into the direction it originally came from. We showed by simulation that the retro reflector significantly improves the light output, especially for scintillations close to the top of the scintillator. The use of the retro reflector resulted in a significant improvement of the energy resolution and signal to background ratio compared to a setup without reflector. The spatial resolution for scintillations close to the top of the scintillator improved significantly although the overall spatial resolution was not strongly affected.

The effect of binning -the combination of signals from multiple pixels- on the spectral characteristics, spatial and energy resolution was investigated in **chapter 8**. Due to binning before the gain register, pixels become larger and the number of transfers of charge is reduced. Because of the reduced number of charge transfers the noise in the image area is expected to be lower and can also facilitate a higher frame rate. We showed that binning leads to an improvement in energy resolution and a better quality of the ^{125}I energy peaks at low energy (around 30 keV). Nevertheless some degradation in spatial resolution occurs but, with the use of a sub-pixel scintillation detection algorithm, this could be alleviated. For instance, the maximum-likelihood algorithm in chapter 3 uses pixels digitally binned to 64 μm x 64 μm without loss of spatial resolution compared to an algorithm without binning.

A recently devised light detector, the silicon photo multiplier (SiPM)[107] is being more and more applied in scintillation detectors[109,111].We have taken the approach of combining these SiPMs with our EM-CCD-based set-up, by using the SiPMs as side detectors (**chapter 9**). This allowed us to combine the good signal-to-noise ratio of SiPMs with the good spatial resolution of EM-CCD based gamma cameras. We showed that when SiPMs were used to detect the number of scintillations in each EM-CCD frame, the signal to background ratio of the gamma-camera set-up was improved while the excellent spatial resolution was maintained. Furthermore, the use of SiPMs as side detectors even allows for detection of the low-energy ^{125}I scintillations when thick continuous scintillators are used because the scintillations can now be discerned from the background in the EM-CCD.

As a next step into the development of a hybrid SiPM-EM-CCD based gamma camera, we used the information provided by the SiPMs in a more advanced manner than to merely count the number of gamma interactions (**chapter 10**). The SiPMs were read-out individually to also allow for a position estimation of the scintillation event which was subsequently used for pre-locating scintillations in the EM-CCD frames. This improved the signal to background ratio by a factor 4 compared to only using the EM-CCD, albeit resulting in some loss of detected scintillations. The energy resolution was improved significantly compared to only using the EM-CCD with the multi-scale algorithm from 50% to 19%. This good energy resolution was combined with the high spatial resolution (180 μm) of the EM-CCD.

In the research presented in this thesis, we have shown that EM-CCD based gamma cameras can achieve a spatial resolution better than 0.2 mm for detection of ^{99m}Tc gamma photons. This spatial resolution is approximately 20 times better than that of the current photo multiplier based systems. These high resolutions were obtained with continuous CsI:Tl scintillators with thicknesses of up to 3 mm thereby increasing the detection efficiency of the EM-CCD based gamma camera from lower than 30% with micro columnar scintillators up to 66%. We believe that a further increase in thickness is not advisable as the current noise levels would complicate the detection of the scintillations furthest from the detector due to their large light spread.
Compared to other gamma cameras that can determine the gamma energy and have a reasonable detection efficiency the spatial resolution of EM-CCD based gamma cameras is unprecedented, which was already illustrated in the introduction (figure 1.11). However the detector also has some drawbacks such as a mediocre energy resolution and a count rate which is limited by the frame rate of the EM-CCD.
For the application in small animal SPECT this mediocre energy resolution does not necessarily pose a large problem when one isotope is imaged at a time. A very good energy resolution would be necessary to separate the gamma photons that scatter and therefore change their direction from those that do not. However, very few photons scatter in a small animals, due to their small sizes, or in the pinhole[202]. Furthermore, the required count rate in the envisioned EM-CCD based SPECT scanner, consisting of many EM-CCD gamma cameras to image a single animal (figure 1.5), would not exceed the EM-CCD count rate capabilities (see Chapter 9).
All these characteristics taken together make this detector very promising to improve pinhole SPECT imaging, mainly due to the unprecedented spatial resolution increase of a factor 20 compared to the Anger camera.

There are still challenges, beyond the scope of this thesis, that need to be met for practical use of the EM-CCD based gamma camera in SPECT imaging.

The first challenge relates to the large amount of data that is constantly being collected by the detectors. For detection of scintillations this detector data needs to be analyzed real-time in order to prevent unmanageable data accumulation.

Earlier, it has been shown that real time data processing of scintillation flashes is possible with thin micro columnar scintillators[120], which have a very small scintillation light spread. This small light spread results in a small number of pixels that have to be taken into account for scintillation detection, making it feasible to use real time scintillation detection even when using iterative maximum-likelihood algorithms[208]. In our set-up, employing thicker continuous scintillators, light spread is much larger and a large number of pixels is considered, making real time scintillation detection much more challenging. A possible solution is the use of binning to reduce the number of data points and/or using the increasing computational power of Field Programmable Gate Arrays (FPGAs)[283].

A second challenge is related to the cooling required for favourable operation of the EM-CCD based gamma detector. In this thesis, the EM-CCD detector was cooled to -40 °C, which, while feasible for single detector operation[119,203,204], would be troublesome for an array of detectors as envisioned in a multi pinhole SPECT scanner[37]. It is hoped that ongoing research into new low dark current noise EM-CCD designs can reduce its cooling requirements[205].

As already discussed in the introduction (see also figure 1.11), many types of gamma detectors that improve the Anger camera spatial resolution by a large factor while maintaining energy resolution and detection efficiency are under development or have already been constructed. It can therefore be expected that the Anger camera will be replaced by some of these new detectors. Whether the EM-CCD, I-CCD[206,207], the SiPM, the PSAPD, the semiconductor detector or another detector will be used for SPECT imaging will depend on the requirements and budget of a specific application and the result of ongoing detector development.

Chapter 12

Samenvatting en vooruitzicht

Hoge-resolutie EM-CCD scintillatie gamma camera's

De ontwikkeling van hoge resolutie gamma detectoren is een belangrijk stap voor verbetering van SPECT imaging. De huidige SPECT scanners gebruiken nog traditionele Anger camera's die bestaan uit een NaI scintillator, uitgelezen door een reeks photomultiplicator buizen (PMT's). Ter vervanging van de Anger camera worden verschillende gamma detectoren met een hoge spatiële resolutie beschouwd. In dit proefschrift onderzochten we een scintillatie gamma detector gebaseerd op een lichtsensor met hoge gevoeligheid en hoge resolutie -de EM-CCD- die een grote verbetering in resolutie ten opzichte van de Anger camera kan behalen. Zulke EM-CCD gebaseerde gamma camera's kunnen vooral tot nut zijn in preklinische SPECT.

Deze EM-CCD lichtsensor, het eerst aangekondigd een decennium geleden, is een speciale CCD met signaalversterking op de CCD zelf[115,116]. Vanwege deze signaalversterking wordt de uitleesruis, typisch de dominante ruisbron in CCDs, teniet gedaan in EM-CCDs.
In scintillatie gamma detectoren werden EM-CCDs initieel gebruikt in combinatie met CsI:Tl scintillatoren die zijn gestructureerd in micro kolommen, ter vermindering van teveel lichtspreiding[114,120]. In deze configuratie is aangetoond dat, vanwege de lage ruis van de EM-CCD, het mogelijk is individuele gamma photonen te detecteren[123].

Het onderzoek beschreven in dit proefschrift is gericht op het gebruik van EM-CCD gebaseerde gamma detectoren in combinatie met monolithische scintillatoren in plaats van in kolommen gestructureerde scintillatoren. Monolithische scintillatoren kunnen de detectie efficiëntie voor gamma's verbeteren omdat ze beschikbaar zijn in veel grotere diktes dan in micro kolommen gestructureerde scintillatoren. Bovendien zijn in micro kolommen gestructureerde scintillatoren alleen beschikbaar in een paar materialen. Echter, het gebruik van dikkere monolithische scintillatoren resulteert in nieuwe uitdagingen zoals een grotere lichtspreiding van scintillatie photonen voordat ze de EM-CCD bereiken en een grotere variatie van de diepte van interactie in de scintillator. Als gamma photonen onder een hoek op de scintillator invallen resulteert de variatie van de interactiediepte in een variatie van de gedetecteerde positie. Dit resulteert in een degradatie van de spatiële resolutie. Deze degradatie wordt het interactiediepte effect genoemd en komt in de meeste SPECT pinhole camera's voor. Dit effect wordt groter als dikkere scintillatoren worden gebruikt en speelt een grote rol voor de relatief dikke monolithische scintillatoren, gebruikt in dit onderzoek.

Een manier om de problemen ten gevolge van de variabele interactiediepte aan te pakken is een detectie algoritme te gebruiken dat de licht spreiding als functie van diepte modelleert waardoor detectie van de interactie diepte mogelijk wordt. In dit proefschrift werden twee nieuwe detectie algoritmes gepresenteerd en getest. Het eerste detectie algoritme, beschreven in **hoofdstuk 2**, is een snel analytisch scintillatiedetectie algoritme gebaseerd op analyse van een gedetecteerde scintillatie bij verschillende schalen, het multi-scale algoritme.
We lieten zien dat het multi-scale algoritme, voor gamma photonen onder een hoek, de interactiediepte kan detecteren en hierdoor het interactiediepte effect kan worden verminderd. Dit resulteerde in een 5-voudige verbetering van de spatiële resolutie voor gamma photonen onder een hoek van 45 graden vergeleken met een analytisch Gaussisch filter algoritme dat geen interactiediepte informatie gebruikt.

Verder verbeterde het multi-scale algoritme de energie resolutie en de signaal-tot-achtergrond verhouding significant vergeleken met het Gaussische filter algoritme.

Een tweede detectie algoritme onderzocht in dit proefschrift is een statistisch Maximum-Likelihood algoritme dat niet alleen de diepteafhankelijke licht verdeling op de EM-CCD modelleert maar ook de statistiek van de EM-CCD. In **hoofdstuk 3**, onderzochten we de onderzoeksvraag of zo een statistisch scintillatiedetectie algoritme een verbetering is ten opzichte van het multi-scale algoritme. Het statistische Maximum-Likelihood algoritme bleek een substantiële verbetering in energie resolutie van meer dan een factor 1.6, een significante verbetering van de spatiële resolutie voor gamma photonen onder een hoek en van de signaal-tot-achtergrond verhouding te leveren.
Onafhankelijk van het algoritme ontdekten we dat de dikte van de scintillator een sterke invloed heeft op de spatiële resolutie; voor grotere diktes degradeert de spatiële resolutie monotoon van een resolutie van 59 μm voor een 0.6 mm dikke scintillator naar een resolutie van 147 μm voor een 3 mm dikke scintillator.

Een andere benadering om het interactiediepte effect te verhelpen, vanuit een nieuwe detector geometrie, werd gepresenteerd in **hoofdstuk 4**. Deze nieuwe detector geometrie bestaat uit een gekromde scintillator die geplaatst is op een concaaf gevormde optische taper, waarvan alle fiber wijzen naar de pinhole.
Door deze geometrie is het zwaartepunt van de scintillatie licht verdeling ten gevolge van een puntbron onafhankelijk van de interactiediepte. De nieuwe gekromde detector werd vergeleken met een standaard vlakke detector met vergelijkbare taper dikte voor gamma photonen loodrecht invallend en onder een hoek van 30 graden. De standaard detector bereikte een spatiële resolutie onder 280 μm voor loodrecht invallende photonen, maar voor photonen onder hoek degradeerde dit tot waarden boven 1.4 mm vanwege het interactiediepte effect.
Het nieuwe prototype van de gekromde detector behaalde spatiële resoluties onder de 280 mm voor zowel loodrecht invallende als gamma photonen onder een hoek, waarmee de eliminatie van het interactiediepte effect gedemonstreerd werd. Echter een nadeel van het prototype gekromde detector is een degradatie van de energie resolutie, waarschijnlijk ten gevolge van scintillatie licht verliezen in de optische taper.

Een van de voordelen van monolithische scintillatoren is dat de keuze voor het scintillator materiaal niet langer beperkt is tot CsI:Tl maar vele verschillende scintillatie materialen. EM-CCD's, in tegenstelling tot PMT's, lezen niet instantaan de detector uit maar accumuleren het scintillatie signaal over een bepaalde tijd. Deze eigenschap heeft consequenties voor de type scintillatoren die kunnen worden gebruikt in combinatie met EM-CCDs; het maakt het mogelijk relatief langzame scintillatoren te gebruiken die tot nog toe niet beschouwd waren voor gamma photondetectie.
Voor verbetering van de gamma detector prestatie vergeleken we verscheidene scintillator materialen met een hoge dichtheid zoals $CdWO_4$, $(Gd,Lu)_2O_3$:Eu en Lu_2O_3:Eu met CsI:Tl in **hoofdstuk 5**. Deze scintillatoren met een hogere dichtheid kunnen dunner zijn dan CsI:Tl met behoud van dezelfde gamma interactie kans. Deze dunnere scintillatoren met een hogere dichtheid verbeteren de spatiële resolutie significant vergeleken met CsI:Tl. Echter de energie

resolutie degradeerde, waarschijnlijk vanwege de lagere lichtopbrengst, de aanwezigheid van radioactieve isotopen in de scintillator of een hogere brekingsindex.

Optimalisatie van de prestaties van de gamma camera vereist een goed begrip van de invloed van verschillende detector parameters op de prestaties. Daarom kan de Cramer Rao ondergrens nuttig zijn omdat deze de theoretisch best haalbare prestatie kan tonen. In **hoofdstuk 6** laten we Cramer Rao ondergrenzen voor de energie en spatiële resolutie zien als functie van verschillende detector parameters. De voorspelde trends van de theoretische ondergrens als functie van de EM versterkingsfactor en interactiediepte werden bevestigd door metingen. Zowel de metingen als de berekeningen toonden dat de spatiële en energie resolutie optimaal zijn voor een matige EM versterkingsfactor en ze toonden een bijna kwadratische degradatie van de spatiële resolutie bij toenemende interactiediepte. Dit laatste suggereert dat de scintillator dikte een van de belangrijke parameters is die de spatiële resolutie bepaald, wat ook empirisch gevonden is in hoofdstuk 2, 3 en 5. Bovendien vonden we dat de hoeveelheid gedetecteerde photonen (bepaald e.g. door de Quantum Efficiëntie (QE), de scintillator lichtopbrengst en de lichtcollectie efficiëntie naar de detector) en de ruis in het beeldvormende deel van de CCD een sterke invloed op de prestaties hebben.
De hoeveelheid gedetecteerde photonen kan niet significant worden verhoogd door een EM-CCD met een hogere QE te gebruiken omdat deze reeds 90% is maar zou in principe kunnen worden verbeterd door een scintillator met een hogere lichtopbrengst te gebruiken. Bovendien is aangetoond dat een 10 voudige vermindering van de ruis in het beeldvormende deel van de CCD mogelijk is[201] en kan leiden tot een verbetering van de spatiële en energie resolutie van de gamma camera met een factor 1.5.

Ter verhoging van het aantal photonen dat de EM-CCD detector bereikt presenteren we het gebruik van retro-reflectoren in **hoofdstuk 7**. Deze retro reflectoren zijn ontworpen om een optisch photon te reflecteren in de richting waar het vandaan kwam. Door middel van simulaties toonden we aan dat de retro-reflector de lichtopbrengst significant verhoogt, in het bijzonder voor scintillaties nabij de bovenkant van de scintillator. Het gebruik van de retro reflector resulteerde in een significante verbetering van de energie resolutie en de signaal-tot-achtergrond verhouding vergeleken met een opstelling zonder reflector. De spatiële resolutie voor enkel die scintillaties nabij de bovenkant van de scintillator verbeterde significant maar de gehele spatiële resolutie veranderde nauwelijks.

Het effect van binning -de combinatie van het signaal van meerdere pixels- op het energie spectrum, de spatiële en energie resolutie werd onderzocht in **hoofdstuk 8**. Vanwege binning voor het versterkingsregister worden pixels groter en neemt het aantal ladingsoverdrachten af. Vanwege het lagere aantal ladingsoverdrachten is de verwachting dat de ruis in het beeldvormende dele van de CCD lager is en dat een hogere frame frequentie mogelijk is. We lieten zien dat binning leidt tot een verbetering in de energie resolutie en een betere kwaliteit van de ^{125}I energie piek bij lage energie (rond 30 keV). Toch is er sprake van enige degradatie van de spatiële resolutie wat met behulp van sub-pixel scintillatiedetectie algoritmes verminderd zou kunnen worden. Bijvoorbeeld het maximum-likelihood algoritme in hoofdstuk 3 gebruikt pixels die digitaal gebinned zijn tot 64 μm x 64 μm zonder verlies van spatiële resolutie vergeleken met een algoritme zonder binning.

Een recent ontwikkelde lichtsensor, de silicium photomultiplicator (SiPM)[107] wordt meer en meer toegepast in scintillatie detectoren.[109,111] We hebben ervoor gekozen deze SiPM's te combineren met onze EM-CCD gebaseerde opstelling door de SiPMs te gebruiken als zij-detectoren (**hoofdstuk 9**). Dit maakte het ons mogelijk de goede signaal-ruis verhouding van SiPMs met de goede spatiële resolutie van EM-CCD gebaseerde gamma detectoren te combineren. We toonden aan dat als de SiPMs gebruikt werden om het aantal scintillaties gedurende elk EM-CCD frame te tellen, de signaal-tot-achtergrond verhouding van de gamma-camera verbeterde terwijl de excellente spatiële resolutie behouden bleef. Bovendien maakte het gebruik van SiPMs als zij-detectoren detectie van de lage energie ^{125}I scintillaties mogelijk terwijl dikke monolithische scintillatoren werden gebruikt doordat scintillaties van de achtergrond konden worden onderscheiden.

Als volgende stap in het ontwikkelen van een hybride SiPM-EMCCD gebaseerde gamma camera gebruikten we de informatie van de SiPMs geavanceerder dan enkel het aantal scintillaties te tellen (**hoofdstuk 10**). De SiPMs werden individueel uitgelezen om positie bepaling van de scintillaties mogelijk te maken zodat we scintillaties in EM-CCD frames konden pre-lokaliseren. Dit verbeterde die signaal-tot-achtergrond met een factor 4 vergeleken met het gebruik van enkel de EM-CCD ten koste van een klein verlies in het aantal gedetecteerde scintillaties. De energie resolutie verbeterde significant vergeleken met de EM-CCD gamma camera gebruikmakend van het multi-scale algoritme van 50% tot 19%. Deze goede energieresolutie werd gecombineerd met de hoge spatiële resolutie (180 μm) van de EM-CCD.

In het onderzoek beschreven in dit proefschrift hebben we laten zien dat EM-CCD gebaseerde gamma camera's een spatiële resolutie beter dan 0.2 mm kunnen bereiken voor detectie van ^{99m}Tc gamma photonen. De behaalde spatiële resolutie is ongeveer een factor 20 keer beter dan dat van de huidige photomultiplicator gebaseerde systemen. Deze hoge resoluties werden behaald met monolithische CsI:Tl scintillatoren met een dikte tot op 3 mm waardoor de detectie efficiëntie van de EM-CCD gebaseerde gamma camera van minder dan 30%, voor scintillatoren gestructureerd in micro kolommen, tot op 66% werd verhoogd. We geloven dat een verdere vergroting van dikte niet aan te raden is omdat het huidige ruisniveaus detectie van scintillaties bij de bovenkant van de detector zeer moeilijk zal maken vanwege de grote lichtspreiding.
Vergeleken met andere gamma camera's, die de gamma energie kunnen bepalen en een redelijke detectie efficiëntie hebben, is de spatiële resolutie van EM-CCD gebaseerde gamma camera's ongeëvenaard, zoals reeds beschreven in de introductie (figuur 1.11). Deze detector heeft echter wel een aantal tekortkomingen zoals een middelmatige energie resolutie en een maximale telsnelheid die beperkt wordt door de frame frequentie van de EM-CCD.
Voor SPECT scanners voor kleine dieren zoals muizen is deze middelmatige energie resolutie niet noodzakelijkerwijs een groot probleem als 1 isotoop tegelijkertijd wordt gebruikt. Een zeer goede energie resolutie zal noodzakelijk zijn om gamma photonen die scatteren, en daarom van richting veranderen, te onderscheiden van ongescatterde photonen. Echter zeer weinig photonen scatteren in kleine dieren, vanwege hun kleine grootte, of in de pinhole[202].

De vereiste maximale telsnelheid in de voorgestelde EM-CCD gebaseerde SPECT scanner, bestaande uit vele EM-CCD gamma camera's om een dier af te beelden (figuur 1.5), zou niet de EM-CCD telsnelheid mogelijkheden overtreffen (zie hoofdstuk 9).
All deze eigenschappen bij elkaar maken deze detector veelbelovend om pinhole SPECT imaging te verbeteren, voornamelijk vanwege de ongeëvenaarde spatiële resolutie toename met een factor 20 ten opzichte van de Anger camera.

Er zijn uitdagingen, niet behandeld in dit proefschrift, die moeten worden voldaan voor het praktische gebruik van EM-CCD gebaseerde gamma camera's in SPECT imaging.

De eerste uidaging is de grote hoeveelheid data die constant wordt verzameld door de detectoren. Voor scintillatiedetectie moet deze detector data worden geanalyseerd in real time om onhanteerbare data accumulatie te voorkomen.
Eerder is al aangetoond dat real time data verwerking van scintillatie flitsen mogelijk is met dunne scintillatoren gestructureerd in micro kolommen[120], die een kleine scintillatie licht spreiding hebben. Deze kleine lichtspreiding resulteert in een klein aantal pixels die beschouwd moeten worden voor scintillatiedetectie. waardoor het mogelijk is in real time scintillaties te detecteren, zelfs met een iteratief maximum-likelihood algoritme[208].
In onze opstelling, gebruikmakend van dikkere monolithische scintillatoren, is de lichtspreiding veel groter en moet een groter aantal pixels in overweging genomen worden waardoor real time scintillatiedetectie een grotere uitdaging is. Een mogelijke oplossing is het gebruik van binning om het aantal data punten te reduceren en/of het benutten van de toenemende computationele kracht van Field Programmable Gate Array's (FPGA's)[283].

Een tweede uitdaging is de koeling die nodig is voor een optimale werking van de EM-CCD gebaseerde gamma camera. Voor experimenten beschreven in dit proefschrift werd de EM-CCD detector gekoeld tot -40 ℃, wat mogelijk is voor gebruik van een enkele detector[119,203,204] maar moeilijk voor een reeks detectoren zoals gepland in een multi pinhole SPECT scanner[37]. Het is te hopen dat lopend onderzoek naar nieuwe EM-CCD's met een lage donkerstroom ruis de eisen aan de koeling kan verminderen[205].

Velen van de in de introductie (zie figuur 1.11) besproken gamma detectoren, die in ontwikkeling zijn of reeds zijn gebouwd, kunnen een veel betere spatiële resolutie bereiken vergeleken met de Anger camera met behoud van de energie resolutie en detectie efficiëntie. Het is daarom de verwachting dat de Anger camera zal worden vervangen door sommige van deze nieuwe detectoren. Of de EM-CCD, I-CCD[206,207], de SiPM, de PSAPD, de halfgeleider detector of een andere detector gebruikt zal worden voor SPECT imaging zal afhangen van de eisen en het budget van een specifieke applicatie en de toekomstige resultaten van het detector onderzoek.

Chapter 13

References

[1] W.C. Röntgen, "On a new kind of rays", *Science*, 3, pp.227-231, 1896.

[2] B.H. Kevles, *Naked to the Bone: Medical Imaging in the Twentieth Century*, Rutgers University Press, New Brunswick, N.J., pp.21, 1997.

[3] G.N. Hounsfield, "Computerised transverse axial scanning (tomography). I. Description of system". *Br. J. Radiol.*, 46, pp.1016, 1973.

[4] E.M. Haacke, R.W. Brown, M.R. Thompson and R. Venkatesan, *Magnetic resonance imaging: Physical principles and sequence design*, John Wiley & Sons, New York, 1999.

[5] S. Ogawa, T.M. Lee, A.S. Nayak, and P. Glynn, "Oxygenation-sensitive contrast in magnetic resonance image of rodent brain at high magnetic fields", *Magn. Reson. Med.*, 14, 1, pp.68-78, 1990.

[6] N.K. Logothetis, "What we can do and what we cannot do with fMRI" *Nature*, 453, pp. 869-878, 2008.

[7] N.M. Wilke, M. Jerosch-Herold, A. Zenovich, A.E. Stillman, "Magnetic resonance First-pass myocardial perfusion imaging: clinical validation and future", *J. Magn. Reson. Imaging*, 10, pp.676-85, 1999.

[8] D.J. Pennell, U. P. Sechtem, C.B. Higgins, W.J. Manning, G.M. Pohost, F.E. Rademakers, A.C. van Rossum, L.J. Shaw, and E. Kent Yucel, "Clinical indications for cardiovascular magnetic resonance (CMR): Consensus Panel report", *European heart journal*, 25, pp.1940-1965, 2004.

[9] N. Al-Saadi, E. Nagel, M. Gross, A. Bornstedt, B. Schnackenburg, C. Klein, W. Klimek, H. Oswald, and E. Fleck, 2000. "Noninvasive detection of myocardial ischemia from perfusion reserve based on cardiovascular magnetic resonance" *Circulation*, 101, 12, pp.1379-1383, 2000.

[10] R.W. Gill, "Measurement of blood flow by ultrasound: Accuracy and sources of error", *Ultrasound in Medicine & Biology,* 11, 4, pp.625-641, 1985.

[11] P.Bourguet, "Going Nuclear", *Public Service Review: European Science and Technology*, 12, pp.60-61, 2011.

[12] S.R. Cherry, J.A. Sorenson, and M.E. Phelps, *Physics in Nuclear Medicine, third edition*, Elsevier, Philadelphia, 2003.

[13] Nuclear Medicine Barbados Inc., http://nclrmedicine.com/NMBI/WBnormal.jpg.

[14] G. Hevesy and F. Paneth, "Die Loslichkeit des Bleisulfids und Bleichromats", *Z Anorg Chem,* 82: 323, 1913.

[15] G. Hevesy, "The absorption and translocation of lead by plants", *Biochem. J.*, 17, pp.439-445, 1923.

[16] H.L. Blumgarth and O.C. Yens, O.C., "Studies on the velocity of blood flow: I. The method utilized", *J Clin Invest,* 4, 1, pp.1-13, 1926.

[17] S. Hertz, A. Roberts, and R.D. Evans, "Radioactive iodine (^{128}I) – Study of thyroid physiology", *Proc. Soc. Exp. Biol. Med.*, 38, pp. 510, 1938.

[18] B.V.A. Low-Beer, "Surface measurements of radioactive phosphorus in breast tumors as a possible diagnostic method", *Science*, 104, 2704, pp. 399, 1946.

[19] B.V.A. Low-Beer, H.G. Bell, H.J. McCorkle, and R.S. Stone, "Measurement of radioactive phosphorus in breast tumors in situ", *Radiology*, 47, pp.492-493, 1946.

[20] G.E. Moore, "Use of radioactive diiodofluorescein in the diagnosis and localization of brain tumours", *Science*, 107, pp.569-571, 1948.

[21] B. Selverstone and A.K. Solomon, "Radioactive Isotopes in the Study of Intracranial Tumors: Preliminary Report of Methods and Results", *Tr. Am. Neurol. A.*, 115, 1948.

[22] E.J. Hoffman, M.P. Tornai, M. Janecek, B.E. Patt, and J.S. Iwanczyk, "Intraoperative probes and imaging probes" *Eur. J. Nucl. Med.,* 26, 8, pp.913-35, 1999.

[23] B. Cassen, L. Curtis, A. Reed, and R.L. Libby, "Instrumentation for 1-131 use in medical studies", *Nucleonics,* 9, pp.46-49, 1951.

[24] D.E. Kuhl and R.Q. Edwards, "Cylindrical and section radioisotope scanning of the liver and brain", *Radiology*, 83, 5, pp.926-936, 1964.

[25] R.J. Jaszczak, "The early years of single photon emission computed tomography (SPECT): an anthology of selected reminiscences", *Phys. Med. Biol.*, 51, pp.R99-R115, 2006.

[26] F. van der Have, Ph.D. dissertation, *Ultra-high-resolution small-animal SPECT imaging*, University of Utrecht, 2007.

[27] R. Hachamovitch, D.S. Berman, H. Kiat, I. Cohen, J.A. Cabico, J. Friedman, and G.A. Diamond, "Exercise myocardial perfusion SPECT in patients without known coronary artery disease: Incremental prognostic value and use in risk stratification", *Circulation*, 93, 5, pp.905-914, 1996.

[28] D.S. Berman, R. Hachamovitch, H. Kiat, I. Cohen, J.A. Cabico, F.P. Wang, J.D. Friedman, G. Germano, K. Vantrain, and G.A. Diamond, "Incremental value of prognostic testing in patients with known or suspected ischemic-heart-disease – a basis for optimal utilization of exercise Tc-99m sestamibi myocardial perfusion single-photon emission computed-tomography", *journal of the american college of cardiology*, 26, 3, pp.639-647, 1995.

[29] E. Even-Sapir, U. Metser, E. Mishani, G. Lievshitz, H. Lerman, and I. Leibovitch, "The detection of bone metastases in patients with high-risk prostate cancer: Tc-99m-MDP planar bone scintigraphy, single- and multi-field-of-view SPECT, F-18-fluoride PET, and F-18-fluoride PET/CT", *Journal of Nuclear Medicine*, 47, 2, pp.287-297, 2006.

[30] P. Rigo, P. Paulus, B.J. Kaschten, R. Hustinx, T. Bury, G. Jerusalem, T. Benoit, and J. Foidart-Willems, "Oncological applications of positron emission tomography with fluorine-18 fluorodeoxyglucose", *Eur. J. Nucl. Med.*, 23, 12, pp.1641-1674, 1996.

[31] T. Jones, "The role of positron emission tomography within the spectrum of medical imaging", *European journal of nuclear medicine*, 23, 2, pp.207-211, 1996.

[32] K.A. Johnson, K. Jones, B.L. Holman, J.A. Becker, P.A. Spiers, A. Satlin, and M.S. Albert, "Preclinical prediction of Alzheimer's disease using SPECT", *Neurology*, 50, 6, pp.1563-1571, 1998.

[33] D.H.S. Silverman, G.W. Small, C.Y. Chang, C.S. Lu, M.A.K. de Aburto, W. Chen, J. Czernin, S.I. Rapoport, P. Pietrini, G.E. Alexander, M.B. Schapiro, W.J. Jagust, J.M. Hoffman, K.A. Welsh-Bohmer, A. Alavi, C.M. Clark, E. Salmon, M.J. de Leon, R. Mielke, J.L. Cummings, A.P. Kowell, S.S. Gambhir, C.K. Hoh, and M.E. Phelps, "Positron emission tomography in evaluation of dementia - Regional brain metabolism and long-term outcome", *Journal of the American Medical Association*, 286, 17, pp.2120-2127, 2001.

[34] S.K. Das, M.M. Miften, S. Zhou, M. Bell, M.T. Munley, C.S. Whiddon, O. Craciunescu, A.H. Baydush, T. Wong, J.G. Rosenman, M.W. Dewhirst, and L.B. Marks, "Feasibility of optimizing the dose distribution in lung tumors using fluorine-18-fluorodeoxyglucose positron emission tomography and single photon emission computed tomography guided dose prescriptions", *Medical Physics*, 31, 6, pp.1452-1461, 2004.

[35] J.T. Yap, J.P.J. Carney, N.C. Hall, and D.W. Townsend, "Image-guided cancer therapy using PET/CT", *Cancer Journal*, 10, 4, pp.221-233, 2004.

[36] R. Weissleder and U. Mahmood, "Molecular Imaging", *Radiology*, 219, pp.316-333, 2001.

[37] V. Ntziachristos, C.H. Tung, C. Bremer, and R. Weissleder, "Fluorescence molecular tomography resolves protease activity in vivo", *Nat. Med.*, 8, 7, pp.757-760, 2002.

[38] F. Kiessling and B.J. Pichler, eds., *Small Animal Imaging: Basics and Practical Guide*, Springer-Verlag, Berlin Heidelberg, 2011.

[39] R. Weissleder, B.D. Ross, A. Rehemtulla, and S. Gambhir, *Molecular Imaging, principles and practice*, People's Medical Publishing House – USA, Shelton, 2010.

[40] D.J. Rowland and S.R. Cherry, "Small-animal preclinical nuclear medicine instrumentation and methodology", *Semin. Nucl. Med.*, 38, 3, pp.209-222, 2008.

[41] H.O. Anger, "Use of a gamma-ray pinhole camera for in vivo studies", *Nature*, 170, pp.200-201, 1952.

[42] D.E. Copeland and E.W. Benjamin, "Pinhole camera for gamma-ray sources", *Nucleonics*, 5, pp.45-49, 1949.

[43] D.A. Weber, M. Ivanovic, D. Franceschi, S.E. Strand, K. Erlandsson, M. Franceschi, H.L. Atkins, J.A. Coderre, H. Susskind, T. Button, and K. Ljunggren, "Pinhole SPECT – an approach to in-vivo high-resolution SPECT imaging in small laboratory-animals", *Journal of nuclear medicine*, 35, 2, pp.342-348, 1994.

[44] S.R. Meikle, P. Kench, M. Kassiou, and R.B. Banati, "Small animal SPECT and its place in the matrix of molecular imaging technologies", *Phys. Med. Biol.,* 50, pp.R45-61, 2005.

[45] F. Beekman and F. van der Have, "The pinhole: gateway to ultra-high-resolution three-dimensional radionuclide imaging", *Eur. J. Nucl. Med. Mol. Imaging*, 34, 2, pp.151-61, 2007.

[46] R.J. Jaszczak, J.Y. Li, H.L. Wang, M.R. Zalutsky, and R.E. Coleman, R.E., "Pinhole collimation for ultra-high-resolution-small-field-of-view SPECT", *Phys. Med. Biol.*, 39, pp.425-37, 1994.

[47] N. Schramm, A. Wirrwar, F. Sonnenberg, and H. Halling, "Compact high resolution

detector for small animal SPECT", *IEEE Trans. Nucl. Sci.*, 47, pp.1163-7, 2000.

[48] L.R. Furenlid, D.W. Wilson, Y.C. Chen, H. Kim, P.J. Pietraski, M.J. Crawford, and H.H. Barrett, "FastSPECT II: A second-generation high-resolution dynamic SPECT imager", *IEEE Trans. Nucl. Sci.*, 51, 3, pp.631-635, 2004.

[49] F.J. Beekman, F. van der Have, B. Vastenhouw, A.J.A. van der Linden, P.P van Rijk, J.P.H. Burbach, J.P.H., and M.P. Smidt, "U-SPECT-I: a novel system for submillimeter-resolution tomography with radiolabeled molecules in mice", *J. Nucl. Med.*, 46, pp.1194-200, 2005.

[50] B. Vastenhouw, F. van der Have, A.J.A. van der Linden, L. von Oerthel, J. Booij, J.P.H. Burbach, M.P. Smidt, and F.J. Beekman, "Movies of dopamine transporter occupancy with ultra-high resolution focusing pinhole SPECT", *Mol. Psychiatry*, 12, pp.984-7, 2007.

[51] H.O. Anger, "Scintillation camera", *Rev. Sci. Instrum.*, 29, pp. 27-33, 1958.

[52] T.E. Peterson and L.R. Furenlid, "SPECT detectors: the Anger camera and beyond", *Phys. Med. Biol*, 56, pp.145-182, 2011.

[53] M.C. Goorden, M.C.M. Rentmeester, and F.J. Beekman, "Theoretical analysis of full-ring multi-pinhole brain SPECT", *Phys. Med. Biol.*, 54, pp.6593-6610, 2009.

[54] F.J. Beekman and B. Vastenhouw, "Design and simulation of a high resolution stationary SPECT system for small animals", *Phys. Med. Biol.*, 49, 19, pp.4579-4592, 2004.

[55] B. Vastenhouw, Ph.D. dissertation, *Simulation, construction and application of focused pinhole small animal SPECT*, University of Utrecht, 2008.

[56] G.F. Knoll, *Radiation Detection and Measurement*, 3rd Ed., John Wiley & Sons Inc., Hoboken, NJ, 2000.

[57] D.S. McGregor and H. Hermon, "Room-temperature compound semiconductor radiation detectors", *Nucl. Instrum. Methods Phys. Res. A*, 395, pp.101-124, 1997.

[58] L.C. Johnson, D.L. Campbell, E.L. Hull, and T.E. Peterson, "Characterization of a high-purity germanium detector for small-animal SPECT", *Phys. Med. Biol.*, 56, pp.5877-88, 2011.

[59] Y. Yin, S. Komarov, H. Wu, T.Y. Song, Q. Li, A. Garson, K. Lee, G. Simburger, P. Dowkontt, H. Krawczynski, and Y.C. Tai, "Characterization of highly pixelated CZT detectors for sub-millimeter PET", *IEEE Nucl. Sci. Symp. Conf. Record*, pp. 2411-2414, 2009.

[60] B. Mueller, M.K. O'Connor, I. Blevis, D.J. Rhodes, R. Smith, D.A. Collins, and S.W. Phillips, "Evaluation of a small CZT detector for scintimammography", *J. Nucl. Med.*, 44, pp. 602-609, 2003.

[61] A. Zumbiehl, M. Sowinska, M. Friedrich, A. Kazandjian, and C. Scheiber, "Comparison between three gamma cameras based on cadmium telluride and cadmium zinc telluride detector arrays", *Nuclear Science Symposium Conference Record*, 3, pp.1972-75, 2003.

[62] B.E. Patt, M.P. Tornai, J.S. Iwanczyk, C.S. Levin, and E.J. Hoffman, "Development of an intraoperative gamma camera based on a 256-pixel mercuric iodide detector array", *IEEE Trans. Nucl. Sci.*, 44, 3, pp.1242-1248, 1997.

[63] Y. Eisen, I. Mardor, A. Shor, Z. Baum, D. Bar, G. Feldman, H. Cohen, E. Issac, R. Haham-Zada, S. Blitz, Y. Cohen, B. Glick, R. Falk, S. Roudebush, and I. Blevis, "NUCAM3-a gamma camera based on segmented monolithic CdZnTe detectors", *IEEE Trans. Nucl. Sci.*, 49, pp.1728–32, 2002.

[64] S.S. Gambhir, D.S. Berman, J. Ziffer, M. Nagler, M. Sandler, J. Patton, B. Hutton, T. Sharir, S.B. Haim, and S.B. Haim, "A novel high-sensitivity rapid-acquisition single-photon cardiac imaging camera", *J. Nucl. Med.*, 50, pp. 635-43, 2009.

[65] K. Ogawa, N. Ohmura, H. Iida, K. Nakamura, T. Nakahara, and A. Kubo, "Development of an ultra-high resolution SPECT system with a CdTe semiconductor detector", *Ann. Nucl. Med.*, 23, pp.763-770, 2009.

[66] H. Kim, L.R. Furenlid, M.J. Crawford, D.W. Wilson, H.B. Barber, T.E. Peterson, W.C.J. Hunter, Z. Liu, J.M. Woolfenden, and H.H. Barrett, "SemiSPECT: a small-animal single-photon emission computed tomography (SPECT) imager based on eight cadmium zinc telluride (CZT) detector arrays", *Med. Phys.*, 33, pp.465-474, 2006.

[67] E. Rutherford and H. Geiger, "An electrical method of counting the number of α particles from radioactive substances", *Proceedings of the Royal Society of London. Series A, Containing Papers of a Mathematical and Physical Character*, 81, 546, pp.141-161, 1908.

[68] H. Geiger and W. Müller, "Elektronenzählrohr zur Messung schwächster Aktivitäten", *Die Naturwissenschaften*, 16, 31, pp.617-618, 1928.

[69] J.L. Lacy, A.D. LeBlanc, J.W. Babich, M.W. Bungo, L.A. Latson, R.M. Lewis, L.R. Poliner, R.H. Jones, and P.C. Johnson, "A gamma camera for medical applications, using a multiwire proportional counter, *J. Nucl. Med.*, 25, 9, pp.1003-1012, 1984.

[70] J.E. Bateman and J.F. Conolly, "A multiwire proportional gamma camera for imaging ^{99m}Tc Radionuclide Distributions", *Phys. Med. Biol.*, 23, 3, pp.455-470, 1978.

[71] R.E. Zimmerman, B.L. Holman, F.H. Fahey, R.C. Lanza, C. Cheng, and S. Treves, "Cardiac imaging with a high pressure low dead time multiwire proportional chamber", *IEEE Trans. Nucl. Sci.*, 28, 1, pp.55-56, 1981.

[72] M.N. Wernick and J.N. Aarsvold, *Emission Tomography, the fundamentals of PET and SPECT*, Elsevier Academic Press, San Diego, CA, 2004.

[73] A.P. Jeavons, R.A. Chandler, and C.A.R. Dettmar, "A 3D HIDAC-PET Camera with Sub-millimetre Resolution for Imaging Small Animals", *IEEE Trans. Nucl. Sci.*, 46, 3, pp.468-473, 1999.

[74] K.P. Schafers, A.J. Reader, M. Kriens, C. Knoess, O. Schober, and M. Schafers, "Performance evaluation of the 32-Module quadHIDAC Small-Animal PET scanner", *J. Nucl. Med.*, 46, 6, pp.996-1004, 2005.

[75] S.P. Langley, "The Bolometer and Radiant Energy", *Proceedings of the American Academy of Arts and Sciences*, 16, p.343, 1881.

[76] P.L. Richards, "Bolometers for infrared and millimeter waves", *J. Appl. Phys.*, 76, 1, pp.1-24, 1994.

[77] K.D. Irwin and G.C. Hilton, "Transition-Edge Sensors", in *Cryogenic Particle Detection*, edited by C. Enss, Springer, Berlin, pp.81-97, 2005.

[78] H.F.C. Hoevers, A.C. Bento, M.P. Bruijn, L. Gottardi, M.A.N. Korevaar, W.A. Mels, and P.A.J. de Korte., "Thermal fluctuation noise in a voltage biased superconducting transition edge thermometer", *Appl. Phys. Lett.,* 77, 26, pp.4422-4424, 2000.

[78] A.S. Hoover, N. Hoteling, M.W. Rabin, J.M. Ullom, D.A. Bennett, P.J. Karpius, D.T. Vo, W.B. Doriese, G.C. Hilton, R.D. Horansky, K.D. Irwin, V. Kotsubo, D.W. Lee, and L.R. Vale, "Large microcalorimeter arrays for high-resolution X- and gamma-rayspectroscopy", *Nucl. Instrum. Methods Phys. Res. A*, 652, 1, pp.302-305, 2011.

[79] E.N. Harvey, *History of luminescence*, The American philosophical society, Philadelphia, 1957.

[80] R. Hofstadter, "The detection of gamma-rays with thallium-activated sodium iodide crystals", *Phys. Rev.*, 75, pp.796-810, 1949.

[81] C.W.E. van Eijk, "Inorganic scintillators in medical imaging", *Phys. Med. Biol.*, 47, pp.R85-R106, 2002.

[82] F.J. Beekman and G.A. de Vree, "Photon-counting versus an integrating CCD-based gamma camera: important consequences for spatial resolution", *Phys. Med. Biol.*, 50, pp.N109-N119, 2005.

[83] G.A. Morton, "The scintillation counter story part II", *IEEE Trans. Nucl. Sci.*, 22, 1, pp.26-28, 1975.

[84] S.C. Curran and J.D. Craggs, *Counting tubes: theory and application*, Academic Press, New York, 1949.

[85] H. Kallmann, Lesson in a colloquium in Berlin–Dahlem, reported by Bloch, W. "Kann man Elektronen sehen", *Natur und Technik*, 13, 15, 1947.

[86] J.W. Coltman and F.H. Marshall., 1947, "Some Characteristics of the photo-multiplier Radiation Detector", *Phys. Rev.*, 72, p.582, 1947.

[87] H.O. Anger, "A multiple scintillation counter in vivo scanner", *Am. J. Roentgenol. Radium Ther. Nucl. Med.*, 70, 4, pp.605-612, 1953.

[88] L.R. Furenlid, J.Y. Hesterman, and H.H. Barrett, "Real-time data acquisition and maximum-likelihood estimation for gamma cameras", *IEEE-NPSS Real Time Conference*, pp.498-501, 2005.

[89] A. Kuhn, S. Surti, J.S. Karp, P.S. Raby, K.S. Shah, A.E. Perkins, and G. Muehllehner, "Design of a lanthanum bromide detector for time-of-flight PET", *IEEE Trans. Nucl. Sci.,* 51, 5, pp.2550-2557, 2004.

[90] S. Yamamoto and H. Ishibashi, "A GSO depth of interaction detector for PET", *IEEE Trans. Nucl. Sci.*, 45, 3, pp.1078-1082, 1998.

[91] H. Zaklad, S.E. Derenzo, R.A. Muller, G. Smadja, R.G. Smits, and L.W. Alvarez, "A liquid xenon radioisotope camera", *IEEE Trans. Nucl. Sci.*, 19, pp.206-212, 1972.

[92] V.V. Egorov, V.P. Miroshnichenko, B.U. Rodionov, A.I. Bolozdinja, S.D. Kalashnikov, and V.L. Krivoshein, "Electroluminescence emission gamma-camera", *Nucl. Instrum. Methods*, 205, pp.373-374, 1983.

[93] E. Aprille, "Liquid xenon detectors for particle physics and astrophysics", *J. Nucl. Med.*, 46, 6, pp.996-1004, 2010.

[94] H. Kume, S. Muramatsu, and M. Iida, "Position sensitive photomultiplier tubes for scintillation imaging", *IEEE Trans. Nucl. Sci.*, 33, pp.359-63, 1986.

[95] R. Wojcik, S. Majewski, B. Kross, D. Steinback, and A.G. Weisenberger, "High spatial resolution Gamma imaging detector based on a 5" diameter R3292 Hamamatsu PSPMT", *IEEE Trans. Nucl. Sci.*, 45, 3, pp.487-491, 1998.

[96] R.S. Miyaoka, S.G. Kohlmyer, and T.K. Lewellen, 2001. "Performance characteristics of micro crystal element (MiCE) detectors", *IEEE Trans. Nucl. Sci.*, 48, 4, pp.1403-07, 2001.

[97] P.D. Olcott, F. Habte, A.M. Foudray, and C.S. Levin, "Performance Characterization of a Miniature, High Sensitivity Gamma Ray Camera", *IEEE Trans. Nucl. Sci.*, 54(5), pp.1492-1497, 2007.

[98] C.W. Lerche, J.M. Benlloch, F. Sanchez, N. Pavon, B. Escat, E.N. Gimenez, M. Fernandez, I. Torres, M. Gimenez, A. Sebastia, and J. Martinez, "Depth of gamma-ray interaction with continuous crystals from the width of its scintillation light distribution", *IEEE Trans. Nucl. Sci.,* 52, 3, pp.560-572, 2005.

[99] C.J. Hunter, H.H. Barrett, and L.R. Furenlid, L.R., "Calibration method for ML estimation of 3D interaction position in a thick gamma-ray detector", *IEEE Trans. Nucl. Sci.*, 56, 1, pp.189-196, 2009.

[100] R. Pani, A. Soluri, R. Scafe, A. Pergola, R. Pellegrini, G. De Vincentis, G. Trotta, and F. Scopinaro, "Multi-PSPMT scintillation camera", *IEEE Trans. Nucl. Sci.*, 46, pp.702-708, 1999.

[101] G.J. Gruber, W.W. Moses, S.E. Derenzo, N.W. Wang, E. Beuville, and M.H. Ho, "A discrete scintillation camera module using Silicon photodiode readout of CsI(Tl) crystals for breast cancer imaging", *IEEE Trans. Nucl. Sci.*, 45, pp.1063-68, 1998.

[102] B.E. Patt, J.S. Iwanczyk, C.R. Tull, N.W. Wang, M.P. Tornai, E.J. Hoffman, "High resolution CsI(Tl)/Si-PIN detector development for breast imaging", *IEEE Trans. Nucl. Sci.,* 45, pp.2126-31, 1998.

[103] W.S. Choong, G.J. Gruber, W.W. Moses, S.E. Derenzo, S.E. Holland, M. Pedrali-Noy, B. Krieger, E. Mandelli, G. Meddeler, N.W. Wang, and E.K. Witt, "A compact 16-module camera using 64-pixel CsI(Tl)/Si p-i-n photodiode imaging modules", *IEEE Trans. Nucl. Sci.,* 49, pp.2228-35, 2002.

[104] E. Gatti and P. Rehak, 1984, "Semiconductor drift chamber - an application of a novel charge transport scheme", *Nucl.Instrum. Methods Phys. Res. A*, 225, pp.608-14, 1984.

[105] C. Fiorini, A. Longoni, and F. Perotti, "New detectors for gamma-ray spectroscopy and imaging, based on scintillators coupled to silicon drift detectors", *Nucl. Instrum. Methods Phys. Res. A*, 454, pp.241-6, 2000.

[106] C. Fiorini, A. Gola, A. Longoni, M. Zanchi, A. Restelli, F. Perotti, P. Lechner, H. Soltau, and L. Strüder, "A large-area monolithic array of silicon drift detectors for medical imaging", *Nucl. Instrum. Meth. A.*, 568, pp.96-100, 2006.

[107] C. Fiorini, A. Gola, R. Peloso, A. Longoni, P. Lechner, H. Soltau, and L. Struder, "Imaging performances of the DRAGO gamma camera", *Nucl. Instrum. Meth. A.*, 604, pp.101–3, 2009.

[108] K. S. Shah, R. Farrell, R. Grazioso, R. Myers, and L. Cirignano, "Large area APD's and monolithic APD arrays", *IEEE Trans. Nucl. Sci.*, 48, 6, pp.2352-2356, 2001.

[109] K. S. Shah, R. Farrell, R. Grazioso, E.S. Harmon, and E. Karplus, "Position-sensitive avalanche photodiodes for gamma-ray imaging", *IEEE Trans. Nucl. Sci.*, 49, pp.1687-92, 2002.

[110] C. Levin, A. Foudray, P. Olcott, and F. Habte, "Investigation of position sensitive avalanche photodiodes for a new high-resolution PET detector design", *IEEE Trans. Nucl. Sci.*, 51, 3, pp.805–810, 2004.

[111] W. Barber, T. Funk, M. McClish, K. Shah, and B. Hasegawa, "PSAPD gamma camera for SPECT imaging", *IEEE Nucl. Sci. Symp. Conf. Record*, 5, pp.2815–2817, 2004.

[112] T. Funk, P. Despres, W.C. Barber, K.S. Shah, and B.H. Hasegawa, "A multipinhole small animal SPECT system with submillimeter spatial resolution", *Med. Phys.*, 33, pp.1259-1268, 2006.

[113] M.C. Maas, D.R. Schaart, D.J. van der Laan, P. Bruyndonckx, C. Lemaitre, F. Beekman, and C.W.E. van Eijk, "Monolithic scintillator PET detectors with intrinsic depth-of-interaction correction", *Phys. Med. Biol.*, 54, pp.1893-1908, 2009.

[114] S. Kim, M. McClish, F. Alhassen, Y. Seo, K.S. Shah, and R.G. Gould, "Phantom Experiments on a PSAPD-Based Compact Gamma Camera With Submillimeter Spatial Resolution for Small Animal SPECT", *IEEE Trans. Nucl. Sci.*, 57, 5, pp.2518-23, 2010.

[115] G. Bondarenko, B. Dolgoshein, V. Golovin, A. Ilyin, R. Klanner, and E. Popova, "Limited Geiger-mode silicon photodiode with very high gain", *Nucl. Phys. B*, 61B, pp.347-352, 1998.

[116] P. Buzhan, B. Dolgoshein, L. Filatov, A. Ilyin, V. Kantzerov, V. Kaplin, A. Karakash, F. Kayumov, S. Klemin, E. Popova, and S. Smirnov, "Silicon photomultiplier and its possible applications", *Nucl. Instrum. Methods Phys. Res. A*, 504, pp.48-52, 2003.

[117] D. Renker, "Geiger mode avalanche photodiodes, history, properties and problems", *Nucl. Instrum. Methods Phys. Res. A*, 567, 2006.

[118] D.R. Schaart, H.T. van Dam, S. Seifert, R. Vinke, P. Dendooven, H. Löhner, F.J. Beekman, "A novel, SiPM-array-based, monolithic scintillator detector for PET", *Phys. Med. Biol.*, 54, 11, pp.3501-12, 2009.

[119] H.T. van Dam, S. Seifert, R. Vinke, P. Dendooven, H. Löhner, F.J. Beekman and D.R. Schaart, "A comprehensive model of the response of silicon photomulitpliers", *IEEE Trans. Nucl. Sci.*, 57, pp.2254-2266, 2010.

[120] A.T. Tao, *Development of a silicon photomultiplier based gamma camera*, Doctoral Dissertation, McMaster University, Hamilton, Canada, 2011.

[121] S. Yamamoto, H. Watabe, Y. Kanai, M. Imaizumi, T. Watabe, E. Shimosegawa, and J. Hatazawa, "Development of a high-resolution Si-PM-based gamma camera system", *Phys. Med. Biol.*, 56, pp.7555-7567, 2011.

[122] A.J.P. Theuwissen, *Solid-State Imaging with Charge-Coupled Devices*, Kluwer academic publishers, Dordrecht, the Netherlands, 1995.

[123] J.E. Lees, G.W. Fraser, A. Keay, D.J. Bassford, R.J. Ott, and W. Rlyder, "The High Resolution Gamma Imager (HRGI): A CCD based camera for medical imaging", *Nucl. Instrum. Methods Phys. Res. A*, 513, pp.23-26, 2003.

[124] B.W. Miller, H.H. Barrett, L.R. Furenlid, H.B. Barber, and R.J. Hunter, "Recent advances in BazookaSPECT: Real-time data processing and the development of a gamma-ray microscope", *Nucl. Instrum. Methods Phys. Res. A*, 591, 1, pp.272-275, 2008.

[125] P. Jerram, P. Pool, R. Bell, D. Burt, S. Bowring, S. Spencer, M. Hazelwood, I. Moody, N. Catlett, and P. Heyes, "The LLLCCD: low light imaging without the need for an intensifier", *Proc. SPIE*, 4306, pp.178–86, 2001.

[126] J. Hynecek, "Impactron-a new solid state image intensifier", *IEEE Trans. Electron Devices*, 48, pp.2238-41, 2001.

[127] M.S. Robbins and B.J. Hadwen, "The noise performance of electron multiplying charge-coupled devices", *IEEE Trans. Electron Devices*, 50, pp.1227-32, 2003.

[128] S.K. Madan, B. Bhaumik, and J.M. Vasi, "Experimental observation of avalanche multiplication in charge-coupled devices", *IEEE Trans. Electron Devices*, 30, 6, pp.694-699, 1983.

[129] D. Ives, N. Bezawada, V. Dhillon, and T. Marsh, "ULTRASPEC: an electron multiplication CCD camera for very low light level high speed astronomical spectrometry", *SPIE Conference Series*, 7021, 2008.

[130] A. Giltinan, D. Loughnan, A. Collins and N. Smith, "Using EMCCD's to improve the photometric precision of ground-based astronomical observations", *J. Phys.: Conf. Ser.*, 307, pp.1-6, 2011.

[131] K.B.W. Harpsøe, U.G. Jørgensen, M.I. Andersen, and F. Grundahl, "High Frame-rate Imaging Based Photometry, Photometric Reduction of Data from Electron-multiplying Charge Coupled Devices (EMCCDs)", *Arxiv Astronomy and Astrophysics*, arxiv:1202.3814v2, 2012.

[132] S. Tulloch, "Monte Carlo Modeling of L3 Detectors in High Time Resolution Applications", *HIGH TIME RESOLUTION ASTROPHYSICS: The Universe at Sub-Second Timescales. AIP Conference Proceedings*, 984, pp.148-161, 2008.

[133] F. Bestvater, Z. Seghiri, M.S. Kang, N. Gröner, J.Y. Lee, K.-B. Im, and M. Wachsmuth, "EMCCD-based spectrally resolved fluorescence correlation spectroscopy", *Opt. Express*, 18, 23, pp.23818-28, 2010.

[134] Sarkar, R.B. Robertson, and J.M. Fernandez, "Simultaneous atomic force microscope and fluorescence measurements of proteine unfolding using a calibrated evanescant wave", *PNAS*, 101, 35, pp.12882-12886, 2004.

[135] T. Korten, B. Nitzsche, C. Gell, F. Ruhnow, C. Leduc, and S. Diez, "Fluorescence imaging of single Kinesin motors on immobilized microtubules", *Methods Mol. Biol.*, 783, pp.121-137, 2011.

[136] S.C. Thacker, B.C. Stack, V. Lowe, V. Gaysinskiy, S. Cool, V.V. Nagarkar, and G. Entine, "A novel imaging beta probe for radio-guided surgery", *IEEE Nucl. Sci. Symp. Conf. Record*, pp.3875-3878, 2008.

[137] J.L. Meng, "An intensified EMCCD camera for low energy gamma ray imaging applications", *IEEE Trans. Nucl. Sci.*, 53, 4, pp.2376-2384, 2006.

[138] G.A. de Vree, A.H. Westra, I. Moody, F. van der Have, C.M. Ligtvoet, and F.J. Beekman, "Photon-counting gamma camera based on an electron-multiplying CCD", *IEEE Trans. Nucl. Sci.*, 52, 3, pp.580-8, 2005.

[139] V.V. Nagarkar, T.K. Gupta, S.R. Miller, Y. Klugerman, M.R. Squillante, and G. Entine, "Structured CsI(Tl) scintillators for X-ray imaging applications", *IEEE Trans. Nucl. Sci.*, 45, pp.492-6, 1998.

[140] V.V. Nagarkar, I. Shestakova, V. Gaysinskiy, S.V. Tipnis, B. Singh, W. Barber, B. Hasegawa, and G. Entine, "A CCD-based detector for SPECT", *IEEE Trans. Nucl. Sci.*, 53, 1, pp.54-58, 2006.

[141] H.H. Barrett, W.C.J. Hunter, B.W. Miller, S.K. Moore, Y. Chen and L.R. Furenlid, "Maximum-likelihood methods for processing signals from gamma-ray detectors", *IEEE Trans. Nucl. Sci.*, 56, pp.725-35, 2009.

[142] C.W. Lerche, A. Ros, J.M. Monzo, R.J. Aliaga, N. Ferrando, J.D. Martinez, V. Herrero, R. Esteve, R. Gadea, R.J. Colom, J. Toledo, F. Mateo, A. Sebastia, F. Sanchez, and J.M. Benlloch, "Maximum Likelihood positioning for gamma-ray imaging detectors with depth of interaction measurement", *Nucl. Instrum. Methods Phys. Res. A*, 604, pp.359-362, 2009.

[143] H.T. van Dam, S. Seifert, R. Vinke, P. Dendooven, H. Löhner, F. J. Beekman and D. R. Schaart, "Improved Nearest Neighbor Methods for Gamma Photon Interaction Position Determination in Monolithic Scintillator PET Detectors", *IEEE Trans. Nucl. Sci.*, 58, pp.2139-2147, 2011.

[144] M.A.N. Korevaar, J.W.T. Heemskerk, M.C. Goorden, F.J. Beekman, "Multi-scale algorithm for improved scintillation detection in a CCD-based gamma camera", *Phys. Med. Biol.*, 54, 4, pp.831-842, 2009.

[145] M.A.N. Korevaar, M.C. Goorden, J.W.T. Heemskerk, and F.J. Beekman, "Maximum-likelihood scintillation detection for EM-CCD based gamma cameras", *Phys. Med. Biol.*, 56, pp.4785-4801, 2011.

[146] J.W.T. Heemskerk, A.H. Westra, P.M. Linotte, K.M. Ligtvoet, W. Zbijewski and F.J. Beekman, "Front-illuminated versus back-illuminated photon-counting CCD-based gamma camera: important consequences for spatial resolution and energy resolution", *Phys. Med. Biol.*, 52, pp.N149-N162, 2007.

[147] M. Holstensson, M. Partridge, S.E. Buckley and G.D. Flux, "The effect of energy and source location on gamma camera intrinsic and extrinsic spatial resolution: an experimental and Monte Carlo study", *Phys. Med. Biol.*, 55, pp.1735-1751, 2010.

[148] L.J. Meng and G. Fu, "Investigation of the intrinsic spatial resolution of an intensified EMCCD scintillation camera", *IEEE Trans. Nucl. Sci.*, 55, 5, pp.2508-2517, 2008.

[149] L.H. Barone, K. Blazek, D. Bollini, A. Del Guerra, F. de Notaristefani, G. De Vincentis, G. Di Domenico, M. Galli, M. Giganti, P. Maly, R. Pani, R. Pellegrini, A. Pergola, A. Piffanelli, F. Scopinaro, A. Soluri, and F. Vittori, "Towards a nuclear medicine with sub-millimeter spatial resoltuion", *Nucl. Instrum. Methods Phys. Res. A*, 360, pp.302-306, 1995.

[150] G.J. Gruber, W.-S., Choong, W.W. Moses, S.E. Derenzo, S.E. Holland, M. Pedrali-Noy, B. Krieger, E. Mandelli, G. Meddeler, and N.W. Wang, "A Compact 64-Pixel CsI(Tl)/Si PIN Photodiode Imaging Module with IC readout", *IEEE Trans. Nucl. Sci.*, 49, 1, pp.147-152, 2002.

[151] M.K. Bacrania, A.S. Hoover, P.J. Karpius, M.W. Rabin, C.R. Rudy, D.T. Vo, J.A. Beall, D.A. Bennett, W.B. Doriese, G.C. Hilton, R.D. Horansky, K.D. Irwin, N. Jethava, E. Sassi, J.N. Ullom, and L.R. Vale, "Large-Area Microcalorimeter Detectors for Ultra-High-Resolution X-Ray and Gamma-Ray Spectroscopy", *IEEE Trans. Nucl. Sci.*, 56, 4, pp.2299-2302, 2009.

[152] Z.L. Liu, G.D. Stevenson, H.H. Barrett, G.A. Kastis, M. Bettan, L.R. Furenlid, D.W. Wilson, J.M. Woolfenden, and K.Y. Pak, "Tc-99m glucarate high-resolution imaging of drug sensitive and drug resistant human breast cancer xenografts in SCID mice", *Nuclear Medicine Communications*, 25, 7, pp.711-720, 2004.

[153] M.M. Rogulski, H.B. Barber, H.H. Barrett, R.L. Shoemaker, and J.M. Woolfenden, "Ultra-High-Resolution Brain Spect Imaging - Simulation Results", *IEEE Trans. Nucl. Sci.*, 40, 4, pp.1123-1129, 1993.

[154] H.B. Barber, "Applications of semiconductor detectors to nuclear medicine", *Nucl. Instrum. Methods Phys. Res. A*, 436, 1-2, pp.102-110, 1999.

[155] M.C.M. Rentmeester, F. van der Have, and F.J. Beekman, "Optimizing multi-pinhole SPECT geometries using an analytical model", *Phys. Med. Biol.*, 52, 9, pp.2567-2581, 2007.

[156] J.L. Matteson, W. Coburn, F. Duttweiler, W.A. Heindl, G.L. Huszar, P.C. Leblanc, M.R. Pelling, L.E. Peterson, R.E. Rotschild, and R.T. Skelton, "CdZnTe arrays for astrophysics applications", *Proc. SPIE*, 3115, pp.160-175, 1997.

[157] C. Fiorini, A. Longoni, F. Perotti, C. Labanti, E. Rossi, P. Lechner, H. Soltau, and L. Struder, "A monolithic array of silicon drift detectors coupled to a single scintillator for gamma-ray imaging with sub-millimeter position resolution", *Nucl. Instrum. Methods Phys. Res. A*, 512, 1-2, pp.265-271, 2003.

[158] Z. He, W. Li, G.F. Knoll, D.K. Wehe, J. Berry, and C.M. Stahle, "3-D position sensitive CdZnTe gamma-ray spectrometers", *Nucl. Instrum. Methods Phys. Res. A*, 422, 1-3, pp.173-178, 1999.

[159] J. Kataoka, T. Saito, Y. Kuramoto, T. Ikagawa, Y. Yatsu, J. Kotoku, M. Arimoto, N. Kawai, Y. Ishikawa, and N. Kawabata, "Recent progress of avalanche photodiodes in high-resoution X-rays and gamma-rays detection", *Nucl. Instrum. Methods Phys. Res. A*, 541, 1-2, pp.398-404, 2005.

[160] L. Menard, Y. Charon, M. Solal, P. Laniece, R. Mastrippolito, L. Pinot, L. Ploux, M. Ricard, and L. Valentin, "POCI: A compact high resolution gamma camera for intra-operative surgical use", *IEEE Trans. Nucl. Sci.*, 45, 3, pp.1293-1297, 1998.

[161] D. Vavrik, J. Jakubek, J. Visschers, S. Pospisil, C. Ponchut, and J. Zemankova, "First tests of a Medipix-1 pixel detector for X-ray dynamic defectoscopy", *Nucl. Instrum. Methods Phys. Res. A*, 487, 1-2, pp.216-223, 2002.

[162] E. Miyata, M. Miki, N. Tawa, D. Kamiyama, and K. Miyaguchi, "Development of new X-ray imaging device sensitive to 0.1-100 keV", *Nucl. Instrum. Methods Phys. Res. A*, 525, 1-2, pp.122-125, 2004.

[163] V.V. Nagarkar, J.S. Gordon, S. Vasile, P. Gothoskar, and F. Hopkins, "High resolution X-ray sensor for non destructive evaluation", *IEEE Trans. Nucl. Sci.*, 43, 3, pp.1559-1563, 1996.

[164] C. Ponchut, F. Zontone, and H. Graafsma, "Experimental comparison of pixel detector arrays and CCD-based systems for X-ray area detection on synchrotron beamlines", *IEEE Trans. Nucl. Sci.*, 52, 5, pp.1760-1765, 2005.

[165] B.W. Miller, H.B. Barber, and H.H. Barrett, "Single-photon spatial and energy resolution enhancement of a columnar CsI(Tl) / EMCCD gamma-camera using maximum-likelihood estimation", *Proc. SPIE*, 6142, pp.61421T-1-61421T-10, 2006.

[166] J. Hynecek and T. Nishiwaki, "Excess noise and other important characteristics of low light level imaging using charge multiplying CCDs", *IEEE Trans. Nucl. Sci.*, 50, 1, pp.239-245, 2003.

[167] T. Plakhotnik, A. Chennu, and A.V. Zvyagin, "Statistics of single-electron signals in electron-multiplying charge-coupled devices", *IEEE Trans. Nucl. Sci.*, 53, 4, pp.618-622, 2006.

[168] A.B. Hwang, K. Iwata, B.H. Hasegawa, "Simulation of depth of interaction effects for pinhole SPECT", *IEEE Nucl. Sci. Symp. Conf. Record*, 1-4, pp.1293-1297, 2002.

[169] B.M. ter Haar Romeny, ed., *Geometry-Driven Diffusion in Computer Division.* Kluwer Academic Publishers, Dordrecht, the Netherlands, 1994.

[170] J.J. Koenderink, "The Structure of Images", *Biological Cybernetics*, 50, 5, pp.363-370, 1984.

[171] M.J.Berger, J.H.Hubbell, S.M.Seltzer, J.Chang, J.S.Coursey, R.Sukumar, and D.S.Zucker, *XCOM: Photon Cross Section Database*, 1998, http://physics.nist.gov/PhysRefData/Xcom/Text/XCOM.html.

[172] F.H.Attix, *Introduction to radiological physics and radiation dosimetry*, John Wiley and Sons Inc., 1986.

[173] F. van der Have, B. Vastenhouw, R.M. Ramakers, W. Branderhorst, J.O. Krah, C.G. Ji, S.G. Staelens, and F.J. Beekman, "U-SPECT-II: an ultra-high-resolution device for molecular small-animal imaging", *J. Nucl. Med.*, 50, 4, pp.599-605, 2009.

[174] J.W.T. Heemskerk, M.A.N. Korevaar, R. Kreuger, C.M. Ligtvoet, P. Schotanus, and F.J. Beekman, "A micromachined retro-reflector for improving light yield in ultra-high-resolution gamma cameras", *Phys. Med. Biol.*, 54, 10, pp.3003–3014, 2009.

[175] M.A.N. Korevaar, J.W.T. Heemskerk, and F.J. Beekman, "A pinhole gamma camera with optical depth-of-interaction elimination", *Phys. Med. Biol.*, 54**,** 13, pp.N267–N272, 2009.

[176] A.G. Basden, C.A. Haniff, and C.D. Mackay, "Photon counting strategies with low-light-level CCDs", *Monthly Notices of the Royal Astronomical Society*, 345, 3, pp.985-991, 2003.

[177] E. Lantz, J.L. Blanchet, L. Furfaro, and F. Devaux, "Multi-imaging and Bayesian estimation for photon counting with EMCCDs", *Monthly Notices of the Royal Astronomical Society*, 386, 4, pp.2262-2270, 2008.

[178] A. Westra, J. Heemskerk, M. Korevaar, A. Theuwissen, R. Kreuger, C. Ligtvoet, and F. Beekman, "On-chip pixel binning in photon-counting CCD-based gamma camera: powerful tool for the reduction of noise", *IEEE Trans. Nucl. Sci.*, 56, pp.2559-2565, 2009.

[179] P. Dorenbos, J.T.M. Dehaas, and C.W.E. van Eijk, "Nonproportional response of scintillation crystals to X-rays and gamma-rays", *Radiation Measurements*, 24**,** 4, pp.355-358, 1995.

[180] M.A. Kupinski and H.H. Barrett, *Small animal SPECT imaging*, Springer, 2005.

[181] H.H. Barrett and K.J. Myers, *Foundations of image science*, John Wiley & Sons Inc., pp.636-637, 2004.

[182] H.H. Barrett, W.C.J. Hunter, B.W. Miller, S.K. Moore, C. Yichun, and L.R. Furenlid, "Maximum-likelihood methods for processing signals from gamma-ray detectors", *IEEE Trans. Nucl. Sci.*, 56, 3, pp.725–735, 2009.

[183] H.H. Barrett and K.J. Myers, *Foundations of image science*, John Wiley & Sons Inc., pp.637-638, 2004.

[184] H.H. Barrett and K.J. Myers, *Foundations of image science*, John Wiley & Sons Inc., p.1450, 2004.

[185] M.J.D. Powell, "Efficient method for finding minimum of function of several-variables without calculating Derivatives", *Computer Journal*, 7, 2, pp.155-162, 1964.

[186] W.C.J. Hunter, H.H. Barrett, L.R. Furenlid, and S.K. Moore, "Method of calibrating response statistics for ML estimation of 3D interaction position in a thick-detector gamma camera", *IEEE Nucl. Sci. Symp. Conf. Record*, 6, pp.4359-4363, 2007.

[187] J.Y. Hesterman, L. Caucci, M.A. Kupinski, H.H. Barrett, and L.R. Furenlid, "Maximum-likelihood estimation with a contracting-grid search algorithm", *IEEE Trans. Nucl. Sci.*, 57, 3, pp.1077-1084, 2010.

[188] B. Efron, "1977 Rietz lecture - bootstrap methods - another look at the jackknife", *Annals of Statistics*, 7, 1, pp.1-26, 1979.

[189] O. Daigle, C. Carignan, J.L. Gach, C. Guillaume, S. Lessard, C.A. Fortin, and S. Blais-Ouellette, "Extreme Faint Flux Imaging with an EMCCD", *Publications of the Astronomical Society of the Pacific*, 121, 882, pp.866-884, 2009.

[190] J.W.T. Heemskerk, M.A.N. Korevaar, J. Huizenga, R. Kreuger, D.R. Schaart, M.C. Goorden, and F.J. Beekman, "An enhanced high-resolution EMCCD-based gamma camera using SiPM side detection", *Phys. Med. Biol.,* 55, 22, pp.6773-6784, 2010.

[191] Epoxy-Technology, *Optical Products, EPO-TEK 301-2 Technical Data Sheet*, 2010, http://www.epotek.com/sscdocs/datasheets/301-2.PDF.

[192] A.W. Snyder, C. Pask, and D.J. Mitchell, "Light-acceptance property of an optical fiber", *Journal of the Optical Society of America*, 63, 1, pp.59-64, 1973.

[193] R.J. Potter, "Transmission properties of optical fibers", *Journal of the Optical Society of America*, 51, 10, pp.1079-1089, 1961.

[194] Saint-Gobain-Crystals, *CsI(Na) and CsI(Tl) material product data sheet*, 2007, http://www.detectors.saint-gobain.com/CsI(Tl).aspx.

[195] A. Braem, E. Chesi, F. Ciocia, R.D. Leo, C. Joram, L. Lagamba, E. Nappi, J. Sguinot, I. Vilardi, and P. Weilhammer, "Scintillator studies for the hpd-pet concept", *Nucl. Instrum. Methods Phys. Res. A*, 571, 1-2, pp.419-424, 2007.

[196] D.F.R. Mildner and H. Chen, "The Neutron Transmission Through A Cylindrical Guide Tube", *Journal of Applied Crystallography*, 27, pp.316-325, 1994.

[197] E. Hecht, *Optics*, Addison Wesley, 1987.

[198] D.P. McElroy, L.R. MacDonald, F.J. Beekman, Y.C. Wang, B.E. Patt, J.S. Iwanczyk, B.M.W. Tsui, and E.J. Hoffman, "Performance evaluation of A-SPECT: A high resolution desktop pinhole SPECT system for imaging small animals", *IEEE Trans. Nucl. Sci.*, 49, 5, pp.2139-2147, 2002.

[199] Z.L. Liu, G.A. Kastis, G.D. Stevenson, H.H. Barrett, L.R. Furenlid, M.A. Kupinski, D.D. Patton, and D.W. Wilson, "Quantitative analysis of acute myocardial infarct in rat hearts with ischemia-reperfusion using a high-resolution stationary SPECT system", *J. Nucl. Med.*, 43, 7, pp.933-939, 2002.

[200] N.U. Schramm, G. Ebel, U. Engeland, T. Schurrat, M. Behe, and T.M. Behr, "High-resolution SPECT using multipinhole collimation", *IEEE Trans. Nucl. Sci.*, 50, 3, pp.315-320, 2003.

[201] S.D. Metzler, R.J. Jaszczak, N.H. Patil, S. Vemulapalli, G. Akabani, and B.B. Chin, "Molecular imaging of small animals with a triple-head SPECT system using pinhole collimation", *IEEE Trans. Med. Im.*, 24, 7, pp.853-862, 2005.

[202] B. Vastenhouw and F. Beekman, "Submillimeter total-body murine imaging with U-SPECT-I", *J. Nucl. Med.*, 48, 3, pp.487-493, 2007.

[203] H.B. Barber, H.H. Barrett, E.L. Dereniak, N.E. Hartsough, D.L. Perry, P.C.T. Roberts, M.M. Rogulski, J.M. Woolfenden, and E.T. Young, "A gamma-ray imager with multiplexer readout for use in ultra-high-resolution brain SPECT", *IEEE Trans. Nucl. Sci.*, 40, 4, pp.1140-1144, 1993.

[204] B.K. Teo, I. Shestakova, M. Sun, W.C. Barber, V.V. Nagarkar, and B.H. Hasegawa, "Evaluation of a EMCCD Detector for Emission-Transmission Computed Tomography", *IEEE Trans. Nucl. Sci.*, 53, 5, pp.2495-2499, 2006.

[205] F.J. Beekman, *Scintillation camera for producing image, has scintillation material on side facing away from detector provided with antireflective layer transparent to high-energy radiation, and light guides are located in front of detector*, Patent NL1029558(C1), 22 Jan. 2007.

[206] F.J. Beekman, *Radiation Detection Apparatus*, Patent WO 2007/011214A1, 25 Jan. 2007.

[207] F.J. Beekman, *Radiation Detection Apparatus*, Patent EP1915640 (A1), 30 Apr. 2008.

[208] Burle/Photonis, *Fiber Optics: Theory and Application*, Technical Memorandum, 2000, http://www.photonis.com/attachment.php?id_attachment=111 .

[209] H.H. Barrett and W. Swindell, *Radiological Imaging: The Theory of Image Formation, Detection, and Processing*, Academic Press, pp.121-123, 1981.

[210] R. Accorsi and S.D. Metzler, "Analytic determination of the resolution-equivalent effective diameter of a pinhole collimator", *IEEE Trans. Med. Im.*, 23, 6, pp.750-763, 2004.

[211] A. Karellas, H. Liu, C. Reinhardt, L.J. Harris, and A.B. Brill, "Imaging of radionuclide emissions with a low-noise charge-coupled device", *IEEE Trans. Nucl. Sci.*, 40, 4, pp.979-982, 1993.

[212] J.H. MacDonald, K. Wells, A.J. Reader, and R.J. Ott, "A CCD-based tissue imaging system", *Nucl. Instr. and Meth. A*, A392, pp.220-226, 1997.

[213] J. Caballo, A. Baily, I. Kitchen, M. Prydderch, A. Clark, R. Turchetta, and K. Wells, 2007, "Digital autoradiography using room temperature CCD and CMOS imaging technology", *Phys. Med. Biol.*, 52, pp.4993-5011, 2007.

[214] M. Suzuki, M. Yamamoto, T. Kumasaka, K. Sato, H. Toyokawa, I.F. Aries, P.A. Jerram, D. Gullick, and T. Ueki, "A multiple-CCD X-ray detector and its basic characterization", *J. Synchrotron Rad.*, 6, pp.6-18, 1999.

[215] W.C. Phillips, M. Stanton, A. Stewart, H. Qian, C. Ingersoll, and R.M. Sweet, "Multiple CCD detector for macromolecular X-ray crystallography", *J. Appl. Cryst.*, 33, pp.243-251, 2000.

[216] L.J. Meng, N.H. Clinthorne, S. Skinner, R.V. Hay, and M. Gross, "Design and feasibility study of a single photon emission microscope system for small animal I-125 imaging", *IEEE Trans. Nucl. Sci.*, 53, 3, pp.1168-1178, 2006.

[217] S.M. Gruner, M.W. Tate, and E.F. Eikenberry, "Charge-coupled device area X-ray detectors", *Rev. Sci. Instrum.*, 73, 8, pp.2815-2842, 2002.

[218] Saint-Gobain Crystals, *Thallium activated Cesium Iodide*, 2012, http://www.detectors.saint-gobain.com/CsI(Tl).aspx

[219] N.J. Cherepy, S.A. Payne, B.W. Sturm, S.P. O'Neal, Z.M. Seeley, O.B. Drury, L.K. Haselhorst, B.L. Rupert, R.D. Sanner, P.A. Thelin, S.E. Fisher, R. Hawrami, K.S. Shah, A. Burger, J.O. Ramey, and L.A. Boatner, "Performance of europium-doped strontium iodide, transparent ceramics and bismuth-loaded polymer scintillators", *Proc. SPIE*, 8142, pp.81420W-81420W-8, 2011.

[220] Z.M. Seeley, J.D. Kuntz, N.J. Cherepy, and S.A. Payne, "Transparent Lu_2O_3:Eu ceramics by sinter and HIP optimization", *Optical Materials*, 33, pp.1721-1726, 2011.

[221] Saint-Gobain Crystals, *Cadmium Tungstate*, 2012, http://www.detectors.saint-gobain.com/CdWO4.aspx

[222] T.C. Soesbe, M.A. Lewis, N.V. Slavine, E. Richer, F.J. Bonte, and P.P. Antich, "High-Resolution Photon Counting Using a Lens-Coupled EMCCD Gamma Camera", *IEEE Trans. Nucl. Sci.*, 57, 3, pp.958-963, 2010.

[223] F. Alhassen, H. Kudrolli, B. Singh, S. Kim, Y. Seo, R.G. Gould, and V.V.Nagarkar, "Depht-of-Interaction Compensation Using a Focused-Cut Scintillator for a Pinhole Gamma Camera", *IEEE Trans. Nucl. Sci.*, 58, 3, pp.634-638, 2011.

[224] H. Cramer, *Mathematical methods of statistics*, Princeton University Press, 1946.

[225] Y.T. Chan and K.C. Ho, "A simple and efficient estimator for hyperbolic location", *IEEE Trans. Signal Process.*, 42, 8, pp.1905-1915, 1994.

[226] P. Stoica and A. Nehorai, A, "Music, maximum-likelihood, and Cramer-Rao bound", *IEEE T. Acoust. Speech.*, 37, 5, pp.720-741, 1989.

[227] A.R. Pineda, S.B. Reeder, Z.F. Wen, and N.J. Pelc, "Cramer-Rao bounds for three-point decomposition of water and fat", *Magnetic resonance in medicine*, 54, 3, pp.625-635, 2005.

[228] N. Patwari, A.O. Hero, M. Perkins, N.S. Correal, and R.J. O'Dea, "Relative location estimation in wireless sensor networks", *IEEE Trans. Signal Process.*, 52, 8, pp.2137-2148, 2003.

[229] A.N. Dandrea, U. Mengali, and R. Reggiannini, "The modified cramer-rao bound and its application to synchronization problems", *IEEE Trans. Commun.*, 42, 2-4, pp.1391-1399, 1994.

[230] E. Roessl and C. Herrmann, "Cramer-Rao lower bound of basis image noise in multiple-energy X-ray imaging", *Phys. Med. Biol.*, 54, 5, pp.1307-1318, 2009.

[231] L.J. Meng and N.H. Clinthorne, "A modified uniform Cramer-Rao bound for multiple pinhole aperture design", *IEEE Trans. Med. Im.*, 23, 7, pp.896-902, 2004.

[232] D.J.J. van der Laan, M.C. Maas, D.R. Schaart, P. Bruyndonckx, S. Leonard, and C.W.E van Eijk, "Using Cramer-Rao theory combined with Monte Carlo simulations for the optimization of monolithic scintillator PET detectors", *IEEE Trans. Nucl. Sci.*, 53, 3, pp.1063-1070, 2006.

[233] X. Li, W.C.J. Hunter, T.K. Lewellen, and R.S. Miyaoka, "Spatial resolution performance evaluation of a monolithic crystal PET detector with Cramer-Rao lower bound (CRLB)", *IEEE Nucl. Sci. Symp. Conf. Record*, pp.2202-2205, 2010.

[234] A.O. Hero, N.H. Clinthorne, and W.L. Rogers, "A lower bound on PET timing estimation with pulse pileup", *IEEE Trans. Nucl. Sci.*, 38, 2, pp.709-712, 1991.

[235] L.E. Smith, Z. He, D.K. Wehe, G.F. Knoll, and S.J. Wilderman, "Design and modeling of the Hybrid Portable Gamma Camera system", *IEEE Trans. Nucl. Sci.*, 45, 3, pp.963-969, 1998.

[236] J.W. Heemskerk, R. Kreuger, M.C. Goorden, M.A.N. Korevaar, S. Salvador, Z.M. Seeley, N.J. Cherepy, E. van der Kolk, S.A. Payne, P. Dorenbos, and F.J. Beekman, "Experimental comparison of high-density scintillators for EMCCD-based gamma ray imaging", *Phys. Med. Biol.*, 57, 14, pp.4545-4554, 2012.

[237] Nuvucameras, O. Daigle, O. Djazovski, D. Laurin, R Doyon, and E. Artigau, *Characterization results of EMCCDs for extreme low light imaging*, 2012, http://www.nuvucameras.com/wp-content/uploads/2012/07/Characterization-results-of-EMCCDs-for-extreme-low-light-imaging.pdf

[238] C.W. Lerche, A. Ros, V. Herrero, R. Esteve, J.M. Monzo, A. Sebastia, F. Sanchez, A. Munar, and J.M. Benlloch, "Dependency of Energy-, Position- and Depth of Interaction Resolution on Scintillation Crystal Coating and Geometry", *IEEE Trans. Nucl. Sci.*, 55, 3, pp.1344-1351, 2008.

[239] C. Hansell, "Nuclear Medicine's Double Hazard", *The Nonproliferation Review*, 15, 2, pp.185-208, 2008.

[240] M.C. Maas, D.J. van der Laan, C.W.E. van Eijk, D.R. Schaart, F.J. Beekman, P. Bruyndonckx, and C. Lemaitre, "Model of the point spread function of monolithic scintillator PET detectors for perpendicular incidence", *Med. Phys.*, 37, 4, pp.904-913, 2010.

[241] S. Agostinelli et al., "Geant4-a simulation toolkit", *Nucl. Instrum. Meth. A*, 506, 3, pp.250-303, 2003.

[242] H.H. Barrett and K.J. Myers, *Foundations of image science*, John Wiley & Sons Inc., 2004.

[243] M.A. King, P.H. Pretorius, T. Farncombe, and F.J. Beekman, "Introduction to the physics of molecular imaging with radioactive tracers in small animals (review)", *J. Cell. Biochem.*, 39, pp.221-230, 2002.

[244] J.Y. Hesterman, M.A. Kupinski, L.R. Furenlid, D.W. Wilson, and H.H. Barrett, "The multi-module, multi-resolution system (M3R): a novel small-animal SPECT system", *Med. Phys.*, 34, pp.987-993, 2007.

[245] T.C. Soesbe , M.A. Lewis, E. Richer, N.V. Slavine, and P.P. Antich, "Development and evaluation of an EMCCD based gamma camera for preclinical SPECT imaging", *IEEE Trans. Nucl. Sci.*, 54, 5, pp.1516-1524, 2007.

[246] A.A.R. Fremout, R. Chen, R. Bruyndonckx, and S.P.K. Tavernier, "Spatial resolution and depth-of-interaction studies with a PET detector module composed of LSO and an APD array", *IEEE Trans. Nucl. Sci.*, 49, 1, pp.131-138, 2002.

[247] F. van der Have and F.J. Beekman, "Characterization of photon penetration and scatter in micro-pinholes", *Phys. Med. Biol.*, 49, 8, pp.1369-1386, 2004.

[248] H.H. Barrett and W. Swindell, *Radiological Imaging: The Theory of Image Formation, Detection, and Processing*, Academic Press, 1981.

[249] E2V low-light technical note 4, *Dark signal and clock-induced charge in L3Vision CCD sensors*, 2004, http://www.e2v.com/e2v/assets/File/documents/imaging-space-and-scientific-sensors/Papers/low_light_tn4.pdf

[250] E2V technical papers, http://www.e2v.com/products-and-services/high-performance-imaging-solutions/technical-papers/

[251] C.D. Mackay, "High-speed digital CCD Cameras – Principals and applications", *Fluorescent and luminescent probes for biological activity, 2nd edition, Academic Press*, pp.517-524, 1999.

[252] R.K. Rowe, J.N. Aarsvold, H.H. Barrett, J-C. Chen, W.P. Klein, B.C. Moore, I.W. Pang and T.A. White, "A stationary hemispherical SPECT imager for three-dimensional brain imaging", *J. Nucl. Med.*, 34, 3, pp.474-480, 1993.

[253] B. Ostendorf, A. Scherer, A. Wirrwar, J.W. Hoppin, C. Lackas, N.U. Schramm, M. Cohnen, U. Mödder, W.B. van den Berg, H.W. Müller, M. Schneider, and L.A.B. Joosten, "High-resolution multipinhole single-photon-emission computed tomography in experimental and human arthritis", *Arthritis rheum*, 54, 4, pp.1096-1104, 2006.

[254] S. Shokouhi, S.D. Metzler, D.W. Wilson, and T.E. Peterson, "Multi-pinhole collimator design for small-object imaging with SiliSPECT: a high-resolution SPECT", *Phys. Med. Biol.*, 54, 2, pp.207-225, 2009.

[255] L.J. Meng, G. Fu, E.J. Roy, B. Suppe, and C.T. Chen, "An ultrahigh resolution SPECT system for I125 mouse brain imaging studies", *Nucl. Instr. and Meth. A*, 600, pp.498-505, 2009.

[256] F.J. Beekman, *Radiation detection device, scintillation device and detection method, as well as multiple image-forming device*, Patent EP1934634 (B1), WO 2007/043868, 19 Apr. 2007.

[257] G. Bondarenko, P. Buzhan, B. Dolgoshein, V. Golovin, E. Gushin, A. Ilyin, V. Kaplin, A. Karakash, R. Klanner, V. Pokachalov, E. Popova, and K. Smirnov, "Limited Geiger-mode microcell silicon photodiode: new results", *Nucl. Instr. Meth. A*, 442, pp.187-192, 2000.

[258] K. Yamamoto, K. Yamamura, K. Sato, S. Kamakura, T. Ota, H. Suzuki, and S. Ohsuka, "Development of multi-pixel photon counter (MPPC)", *IEEE Nucl. Sci. Symp. Conf. Record*, pp.1511-1515, 2007.

[259] G.A. de Vree, A.H. Westra, I. Moody, F. van der Have, C.M. Ligtvoet, and F.J. Beekman, "Electronics for a photon-counting gamma camera based on an electron-multiplying CCD", *IEEE Nucl. Sci. Symp.Conf. Record*, 1, 7, pp.4159-4163, 2004.

[260] C.L. Kim, G.C. Wang and S. Dolinsky, "Multi-pixel photon counters for TOF PET detector and its challenges", *IEEE Nucl. Sci. Symp. Conf. Record*, pp.3586-3590, 2008.

[261] D.R. Schaart, S. Seifert, R. Vinke, H.T. van Dam, P. Dendooven, H. Löhner, and F.J. Beekman, "$LaBr_3$:Ce and SiPMs for time-of-flight PET: achieving 100 ps coincidence resolving time", *Phys. Med. Biol.*, 55, pp.N179-189, 2010.

[262] S. España, G. Tapias, L.M. Fraile, J.L. Herraiz, E. Vicente, J. Udias, M. Desco, and J.J. Vaquero, "Performance evaluation of SiPM detectors for PET imaging in the presence of magnetic fields", *IEEE Nucl. Sci. Symp. Conf. Record*, pp.3591-3595, 2008.

[263] G. Llosá, N. Belcari, M.G. Bisogni, G. Collazuol, A. Del Guerra, S. Marcatili, P. Barrillon, C. De la Taille, S. Bondil-Blin, N. Dinu, M. Melchiorri, A. Tarolli, and C. Piemonte, "Evaluation of the first silicon photomultiplier matrices for a small animal PET scanner", *IEEE Nucl. Sci. Symp. Conf. Record*, pp.3574-3580, 2008.

[264] S. Seifert, D.R. Schaart, H.T. van Dam, J. Huizenga, R. Vinke, P. Dendooven, H. Löhner, and F.J. Beekman, "A high bandwidth preamplifier for SiPM-based TOF PET scintillation detectors", *IEEE Nucl. Sci. Symp. Conf. Record*, pp.1616-1619, 2008.

[265] L.J. Meng, J.W. Tan, K. Spartiotis, and T. Schulman, "Preliminary evaluation of a novel energy-resolved photon-counting gamma ray detector", *Nucl. Instrum. Methods A*, 604, pp.548-554, 2009.

[266] G. Mettivier, M.C. Montesi, A.S. Curion, A. Lauria, M. Marotta, and P. Russo, "High resolution ^{125}I pinhole SPECT imaging of the mouse thyroid with the MediSPECT small animal CdTe scanner", *IEEE Trans. Nucl. Sci.*, 57, pp.1029-1037, 2010.

[267] R. Accorsi, B. Celentano, P. Lacetti, R.C. Lanza, M. Marotta, G. Mettivier, M.C. Montesi, G. Roberti, and P. Russo, "High-resolution ^{125}I small animal imaging with a coded aperture and a hybrid pixel detector", *IEEE Trans. Nucl. Sci.*, 55, pp.481-490, 2008.

[268] V. Saveliev and V. Golovin, "Silicon avalanche photodiodes on the base of metal-resistor-semiconductor (MRS) structures", *Nucl. Instrum. Methods A*, 442, pp.223-229, 2000.

[269] Z. Sadygov, A. Olshevski, I. Chirikov, I. Zheleznykh, and A. Novikov, "Three advanced designs of micro-pixel avalanche photodiodes: Their present status, maximum possibilities and limitations", *Nucl. Instrum. Methods A*, 567, pp.70-73, 2006.

[270] H.T. van Dam, S. Seifert, R. Vinke, P. Dendooven, H. Löhner, F.J. Beekman, and D.R. Schaart, "Improved Nearest Neighbor Methods for Gamma Photon Interaction Position Determination in Monolithic Scintillator PET Detectors", *IEEE Trans. Nucl. Sci.*, 58, pp.2139-2147, 2011.

[271] X. Li, C. Lockhart, T.K. Lewellen, and R.S. Miyaoka, "Study of PET detector performance with varying SiPM parameters and readout schemes", *IEEE Trans. Nucl. Sci.*, 58, pp.590-596, 2011

[272] T. Ling, T.K. Lewellen and R.S. Miyaoka, "Improving the intrinsic spatial resolution performance of the continuous miniature crystal element (cMiCE) detector", *IEEE Nucl. Sci. Symp. Conf. Record*, 6, pp.4308-4313, 2007.

[273] W.M. Higgins, A. Churilov, E. van Loef, J. Glodo, M. Squillante, and K. Shah, "Crystal growth of large diameter LaBr3:Ce and CeBr3", *J. Crystal Growth*, 310, pp.2085-2089, 2008.

[274] G. Bonanno, P. Finocchiaro, A. Pappalardo, S. Billota, L. Cosentino, M. Belluso, S. Di Mauro, and G. Occhipinti, "Precision measurements of photon detection efficiency for SiPM detectors", *Nucl. Instrum. Methods A*, 610, pp.93–97, 2009.

[275] J. Huizenga, S. Seifert, F. Schreuder, H.T. van Dam, P. Dendooven, H. Löhner, R. Vinke, D.R. Schaart, "A fast preamplifier concept for SiPM-based time-of-flight PET detectors", *Nucl. Instrum. Methods A.,* 695, pp.379-384, 2012.

[276] S. Seifert, H.T. van Dam, R. Vinke, P. Dendooven, H. Löhner, F.J. Beekman, and D.R. Schaart, "Monolithic LaBr3:Ce crystals on silicon photomultiplier arrays for time-of-flight positron emission tomography", *Phys. Med. Biol.*, 57, pp.2219-2233, 2012.

[277] Hamamatsu Solid State Division, *S10931-100P Technical Data Sheet*, 2011, http://sales.hamamatsu.com/assets/pdf/parts_S/s10362-33series_kapd1023e05.pdf .

[278] Scionix, *Scintillation crystals, Mechanical and optical properties*, 2011, http://www.scionix.nl .

[279] R.S. Miyaoka, T. Ling, C. Lockhart, X. Li, and T.K. Lewellen, "Calibration procedure for a continuous miniature crystal element (cMICE) detector", *IEEE Trans. Nucl. Sci.*, 57, pp.1023-1028, 2010.

[280] Y. Du and F. Retière, "After-pulsing and cross-talk in multi-pixel photon counters", *Nucl. Instrum. Methods A*, 596, pp.396-401, 2008.

[281] L. Caucci, L.R. Furenlid, and H.H. Barrett, "Maximum likelihood event estimation and list-mode image reconstruction on GPU hardware", *IEEE Nucl. Sci. Symp. Conf. Record*, pp.4072-4076, 2009.

[282] J.Y. Hwang, S.J. Lee, C.H. Baek, H.K. Kwang, and H.C. Yong, "New design of a gamma camera detector with reduced edge effect for breast imaging", *Nucl. Instrum. Methods A*, 633, pp.S166-S168, 2011.

[283] K. Compton and S. Hauck, "Reconfigurable computing: A survey of systems and software", *Acm Computing Surveys*, 34, 2, pp.171-210, 2002.

[284] M. Bras-Amoròs, J. Domingo-Ferrer and V. Torra, "A bibliometric index based on collabotarion distance between cited and citing authors", *Journal of Informetrics*, 5, 2, pp.248-264, 2011.

[285] E. Carlos, "The decline of natural sciences: confronting diminishing interest, fewer scientists and poorer working conditions in western countries. A comparative analysis between Spain and the United Kingdom*", Papers: revista de sociologia*, 93, pp.69-79, 2009.

[286] I. Stadelmann-Steffen, and A, Vatter, "Does Satisfaction with Democracy Really Increase Happiness? Direct Democracy and Individual Satisfaction in Switzerland*"*, *Political Behavior*, 34, 3, pp.535-559, 2012.

[287] B. Sparrow, J. Liu, and D. Wegner, "Google Effects on Memory: Cognitive Consequences of Having Information at Our Fingertips", *Science*, 2011.

[288] David Schneider, "The microsecond market*"*, *IEEE spectrum*, 2012, http://spectrum.ieee.org/computing/networks/the-microsecond-market/ .

[289] S. Seifert, H. van Dam, and D. Schaart, "The lower bound on the timing resolution of scintillation detectors", *Phys. Med. Biol.*, 57, p.1797, 2012.

[290] O. Daigle, O. Djazovski, D.G. Laurin, E. Artigau, R. Doyon, and H. Lavoie, "Characterization results of EMCCDs for extreme low light imaging", *Proc. SPIE*, 8453, 2012.

Dankwoord

Mijn promotietraject wil ik graag vergelijken met een van de eerste beklimmingen met onze klimgroep in de Alpen.
Als jonge en onervaren alpinisten hadden we de route Fliegerbandl op de Riepenwand in de Oostenrijkse Kalkögel uitgezocht en waren vol goede moed dat we alle problemen op onze weg zouden overwinnen. Het eerste deel van de klimroute, alhoewel moeilijk, verliep vlot totdat we bij een lange traverse kwamen waardoor we niet rechtdoor omhoog konden klimmen. Deze traverse bleek een turnstuk met meer dan 200 meter lucht onder de voeten terwijl stenen langs onze hoofden naar beneden suisden. Hierbij waren we slechts gezekerd aan enkele antieke en roestige haken. Na de traverse werd de rots van steeds mindere kwaliteit en brak geregeld een stuk rots waar een van ons zich aan vast hield af, wat gelukkig steeds net goed afliep. Terwijl we nog bezig waren omhoog te klimmen begon het al donker te worden; we hadden gepland op dit tijdstip al lang klaar te zijn. Na uiteindelijk in het donker en zonder lamp te zijn bovengekomen en weer afgedaald naar de voet van de wand overheerste enkel grote opluchting.

Net als bij het begin van de beklimming was bij het begin van mijn promotietraject in Utrecht goede moed essentieel, had ik geweten welke uitdagingen op me te wachten lagen zou ik wellicht nooit zijn begonnen.
De horizontale verplaatsing van de traverse zou doen denken aan de verhuizing van het promotieonderzoek van Utrecht naar Delft ware het niet dat de laatste vlekkeloos verliep, onder andere vanwege de goede ontvangst in Delft.
Momenten dat het onderzoek niet vlot liep en er moeilijk grip te krijgen was op de onderzoeksmaterie door o.a. experimentele uitdagingen, wil ik graag vergelijken met moeilijke klimterrein met afbrekende rots.
Net als de beklimming heeft het afronden van het proefschrift uiteindelijk langer geduurd dan vantevoren gepland wat de opluchting aan het eind des te groter maakt.

Terugkijkend op de beklimming zie ik de momenten met grote moeilijkheden maar ben ik blij dat we ze hebben doorstaan en is ze een bron van waardevolle ervaring geweest. Op mijn promotietraject, dat momenten van grote moeilijkheden heeft gekend, kijk ik nu het bijna is afgerond tevreden terug en ga ik ervan uit dat het ook nuttige ervaringen voor de rest van mijn leven bevat.

Bij onderzoek, net als klimmen, is de samenwerking met enkelen en de hulp en de morele ondersteuning van velen essentieel. Daarom wil ik, nu het er (bijna) allemaal opzit en de promotie in zicht is iedereen bedanken die heeft bijgedragen in welke vorm dan ook.

Allereerst wil ik mijn promotor, prof. dr. F.J. Beekman bedanken. Beste Freek, ik wil je bedanken voor je gestelde vertrouwen aan het begin van het promotietraject terwijl ik toen al 4 jaar uit de natuurkunde was. Je motiverende woorden en je vele creatieve ideeën zijn van grote waarde voor me geweest. Daarnaast heb ik je snelle feedback als ik je een tekst

stuurde altijd gewaardeerd. Verder wil ik je bedanken voor je inzet voor me op momenten dat het tegenzat.

Daarnaast wil ik mijn co-promotor en dagelijkse begeleider, dr. ir. M. Goorden, bedanken. Beste Marlies, jouw talent voor onderzoek en je tekstuele vaardigheden hebben dit proefschrift tot een hoger niveau weten te tillen. Verder wil ik je danken voor je inzet en steun bij het afronden van het proefschrift.

Zonder de bijdrage van Jan Heemskerk was dit boekje in de huidige vorm er niet gekomen. Naast de hulp in het lab zijn vooral je tekstuele kwaliteiten van onschatbare waarde geweest, hiervoor mijn dank. Thank you Samuel Salvador, for your quick experimental and simulation skills which proved invaluable in the work on SiPMs.

Voor het opbouwen en ontwerpen van de elektronica, het aanbrengen van aanpassingen en het snel en vakkundig verhelpen van storingen wil ik Albert Westra en Jan Huizenga bedanken. Verder wil ik Rob Kreuger bedanken voor het helpen regelen van allerlei praktische zaken in het lab en het helpen verbeteren van de meetopstelling. Ook wil ik Gerralt de Vree hier met name noemen op wiens voorbereidende werk Jan en ik hebben kunnen bouwen tijdens onze promoties.

Graag wil ik de leden van de beoordelingscommissie, prof. dr. R. Boellaard, prof. dr. R. Verdaasdonk, prof. ir. A.J.M. van Tuijl, prof. dr. P. Dorenbos, dr. F.W.B. van Leeuwen en prof. dr. H.T. Wolterbeek, bedanken voor het interesse in het beschreven onderzoek. Daarnaast wil ik mijn afstudeer professor dr. Johan Bleeker bedanken voor zijn interesse in het onderzoek en zijn kundige opmerkingen bij reeds een eerste blik op het proefschrift.

Van de oorspronkelijke onderzoeksgroep uit Utrecht wil ik Frans van der Have danken voor het me wegwijs maken in alle zaken rondom radioactieve straling en zijn vermogen elk onderwerp tot in detail te kunnen uitleggen. Brendan Vastenhouw bedankt voor het snel en bondig beantwoorden van allerhande vragen op IT gebied. Tim de Wit bedankt voor het me bijbrengen van de beginselen van de beeldreconstructie en de fijne samenwerking bij Capita Selecta. Woutjan Branderhorst, bedankt voor de motiverende, leerzame en interessante gesprekken over onderzoek, programmeren en andere zaken en voor de steun als het tegenzat. Woutjan, ik ben vereerd dat jij mijn paranimf wil zijn.

Van de onderzoeksgroep in Delft heb ik profijt gehad van het wetenschappelijk enthousiasme en de talenten van Herman van Dam en Stefan Seifert. Voor de vele interessante gesprekken en de nuttige opmerkingen wil ik hen bedanken. Daarnaast wil ik dr.ir. Dennis Schaart en dr. Bernd Rieger bedanken voor de minder frequente maar niet minder interessante en nuttige gesprekken over het onderzoek en prof. dr. Pieter Dorenbos en dr. Erik van der Kolk voor het delen van hun onschatbare kennis over scintillatoren.

De bijdrage van technici, de instrumentele diensten, Medische Technologie en DEMO waren essentieel bij het opbouwen en uitbreiden van de opstelling of voor het snel maken van een prototype. Hier wil ik speciaal Kees Ligtvoet en Henk te Biesebeek van het UMC, Norbert van Milabs, en Rene den Oudsten van de TU Delft bedanken. Johan en Martijn

bedankt voor de snelle hulp bij vele praktische lab vragen. Gustavo, thanks for saving the day by helping us out with soldering when our electronics broke down.

Paul Schotanus van Scionix bedankt voor het rijkelijk beschikbaar stellen van scintillator samples en je kennis. Voor de samenwerking binnen het IOP photonics project wil ik de penvoerder prof. Albert Theuwisse en Yue Chen van de TU Delft en Inge Peters, Jan Bosiers, Erik Boogaart, Harry van Kuijk en Jan Nooien van Dalsa bedanken.

Experimenten met radioactieve straling worden goed begeleid door mensen die daarvoor zijn opgeleid. Van de Stralings Beschermings Dienst in Delft wil ik met name Aad, Jan, Wingman, Henk, Koos en Christian danken voor het nauwgezet in de gaten houden van de veiligheid. De stralingsdeskundige in het UMC Utrecht, Marina Keiman, wil ik bedanken voor de vakkundige en snelle bijstand bij de puntbron fabricage in Utrecht en het transport naar Delft. Rene Nousse bedankt voor de vele transporten van radioactiviteit en voor de hulp bij het melken van de Technetium koe wil ik Jolanda, Mark, Klazien en Marcel van de onderwijs afdeling van het Nationaal Centrum voor Stralingsveiligheid bedanken.

Zonder de uistekende secretariële ondersteuning zouden vele zaken niet tot stand zijn gekomen, daarom mijn bijzondere dank voor Peggy van den Brink-Brouwer in Utrecht en Jose Buurman en Thea Miedema in Delft. Thea bedankt voor het uit handen nemen van veel praktische zaken bij het einde van het promotietraject.
Het algoritme en simulatie onderzoek zou welhaast onmogelijk zijn geweest zonder toegang tot een snel computercluster; mijn dank hiervoor aan Danny Lathouwers en anderen.
Verder wil ik graag de studenten die ik mede begeleid heb: Jan, Emma, Osman en Leo danken voor de prettige samenwerking en het bieden van de mogelijkheid het onderzoek vanuit een ander gezichtspunt te bekijken.
My PhD colleagues Pieter, Melvin, Ivan and Mikhail thank you for the great skiing vacation to Val Thorens. Candice bedankt voor het organiseren van sociale activiteiten in de groep en de gezellige kopjes koffie. For "gezelligheid" and nice coffees I would also like to thank Ola and Ana Maria. Mark bedankt voor de leuke sportieve uitjes op de fiets of in het water. Leon bedankt voor het organiseren van de vrijdag poker avonden.
I would like to thank my colleagues and ex-colleagues from Milabs and the UMC Utrecht: Carmen, Changuo, Chao, Eelco, Jianbin, Jose, Leonard, Mariette, Mart, Paul, Rudolf, Ruud, Samira and Tobias, and from Delft: Adri, Alice, Andreas, Allastair, Carel, Christina, David, Edith, Enrica, Folkert, Francesco, Giacomo, Jakob, Leila, Lorette, Martijn, Michiel, Patricia, Pieter, Romee, Susan, Valerio, Victor, Wendy, Anca, Bart, Dimitrios, Karoly, Lucas, Jose, Stuart, Susanna and all those I have mistakenly not named here.

Verder wil ik graag alle huisgenoten, vrienden en familieleden die me bewust of onbewust gesteund hebben gedurende het promotietraject danken, ook diegenen hier niet speciaal genoemd:
Mijn huisgenoten in "Villa Tarweboll" bedankt voor de goede tijden en speciaal Maurice, Anna, Noortje, Anneke Winterman, Rens, Birgitta, Danique, Jeroen, Teuntje en Reinier.

Furthermore I would like to thank my housemates Luca, Shalinni, Marco, Paola, Donato and Markus for the nice times in Pijnacker. Jozsef Kophazi, I very much enjoyed the interesting talks over dinner and the rowing on the Rijn-Schiekanaal.
For the many nice parties I would like to thank the people at Lange Nieuwstraat. Voor hulp bij het maken van de omslag wil ik voor advies o.a. Claudia Kisters, Marko Masselink, Daniela Anastasopol en Marieke van Kammen bedanken en Erik Bruis voor de uitgewerkte suggesties en tips. Voor de ontspannende tango lessen wil ik de leraren Birkit en Muzaffer en dansers Iris, Stephanie, Marian, Sacha, Zillah, Sophie, Dodijn, Stefan en Tuna bedanken.

My thanks go out to the people I met at the Evangeliegemeente Utrecht and especially Karen, Wai-ching, Hadassa, Levi, Kim, Maryse, Franciska, Bart, Flora, Jethro, Wim, Niclaa, Allard, Renske, Hans, Rita, Ginette, Matthijs and Erik-Frans. Erik-Frans en Matthijs bedankt voor de goede gesprekken en steun in moeilijke tijden. Matthijs, ik voel me vereerd dat je mijn paranimf wil zijn.
Thank you Thijmen, Anup and Erik for many nice Saturday evenings well spent. Walter en Rink bedankt voor de vele avonturen in binnen en buitenland en de geslaagde verrassing bij het huis van de toekomst. Uri, ik heb genoten van de gezellige en interessante gesprekken tijdens etentjes en wil je bedanken voor je steun toen ik het nodig had. Marko en Hanneke bedankt voor de leuke momenten, goede gesprekken en natuurlijk de wandelingen met Zoey.

To get my mind of my Ph.D. it was very nice to go climbing with friends especially in the Alps, thank you John, Mark Oppe, Jesse, Errit, Mikhail, Alexander, Letty, Rob, Irwin and Andreas. Voor de ontspannende (en soms koude) surf sessies in Scheveningen wil ik Erik en Kim bedanken. Erik bedankt voor je vriendschap en het bieden van een luisterende oor als ik daar behoefte aan had.
I would like to thank my family in the US for their support, especially Wilma, Bob, David, Robin, Erik, Leigh, Nick and Max.
Weiter würde ich gerne meine Schweizer Familie danken für alles, insbesondere Kathrin, Dani, Michi, Hansrudi, Marianne, Katharina und Niklaus.
Van mijn Nederlandse familie wil ik Bert en Lida speciaal danken voor de logeermogelijkheden in Delft en Karina, Emile, Daniel, Jacqueline, Kimball en mijn vader Jaap danken voor de steun tijdens het promoveren.
Often, the best is saved for last, so I would like to conclude these acknowledgements with you, Claudia, for making the end of my PhD so enjoyable and for your love and support.

Marc

Curriculum Vitae

Marc Korevaar (Amsterdam, 1975) graduated from secondary school in 1994 and obtained a MSc degree in Physics at Utrecht University in 2003. His graduation project was at the Space Research Organisation Netherlands where he worked on superconductive micro-calorimeters for X-ray detection in the group of Prof. dr. Johan Bleeker. After obtaining his degree he worked at the IT company 2AT on network administration, network engineering and software implementation. In 2005 he started to work at the ING Trading Risk Management on calculation and management of foreign exchange and interest rate risks. He started his PhD research on gamma detection with CCD based scintillation detectors under supervision of Prof. dr. Freek Beekman in 2007. First at the University Medical Center Utrecht and later in the group Radiation, Detection and Medical Imaging at the Technical University Delft.

Publications

Peer-reviewd international journal articles:

- **M.A.N. Korevaar**, M.C. Goorden, and F.J. Beekman, "Cramer Rao lower bound optimization of an EM-CCD based scintillation gamma camera", *Phys. Med. Biol.*, submitted.
- S. Salvador, **M.A.N. Korevaar**, J.W.T. Heemskerk, R. Kreuger, J. Huizenga, S. Seifert, D.R. Schaart, and F.J. Beekman, "Improved EMCCD gamma camera performance by SiPM pre-localization", *Phys. Med. Biol.*, 57, 22, pp.7709-24, 2012.
- J.W. Heemskerk, R. Kreuger, M.C. Goorden, **M.A.N. Korevaar**, S. Salvador, Z.M. Seeley, N.J. Cherepy, E. van der Kolk, S.A. Payne, P. Dorenbos, and F.J. Beekman, "Experimental comparison of high-density scintillators for EMCCD-based gamma ray imaging", *Phys. Med. Biol.*, 57, 14, pp.4545-4554, 2012.
- **M.A.N. Korevaar**, M.C. Goorden, J.W.T. Heemskerk, and F.J. Beekman, "Maximum-likelihood scintillation detection for EM-CCD based gamma cameras", *Phys. Med. Biol.*, 56, pp.4785-4801, 2011.
- J.W.T. Heemskerk, **M.A.N. Korevaar**, J. Huizenga, R. Kreuger, D.R. Schaart, M.C. Goorden, and F.J. Beekman, "An enhanced high-resolution EMCCD-based gamma camera using SiPM side detection", *Phys. Med. Biol.,* 55, 22, pp.6773-6784, 2010.
- **M.A.N. Korevaar**, J.W.T. Heemskerk, M.C. Goorden, F.J. Beekman, "Multi-scale algorithm for improved scintillation detection in a CCD-based gamma camera", *Phys. Med. Biol.*, 54, 4, pp.831-842, 2009.
- **M.A.N. Korevaar**, J.W.T. Heemskerk, and F.J. Beekman, "A pinhole gamma camera with optical depth-of-interaction elimination", *Phys. Med. Biol.*, 54**,** 13, pp.N267–N272, 2009.
- A. Westra, J. Heemskerk, **M. Korevaar**, A. Theuwissen, R. Kreuger, C. Ligtvoet, and F. Beekman, "On-chip pixel binning in photon-counting CCD-based gamma camera: powerful tool for the reduction of noise", *IEEE Trans. Nucl. Sci.*, 56, pp.2559-2565, 2009.
- J.W.T. Heemskerk, **M.A.N. Korevaar**, R. Kreuger, C.M. Ligtvoet, P. Schotanus, and F.J. Beekman, "A micromachined retro-reflector for improving light yield in ultra-high-resolution gamma cameras", *Phys. Med. Biol.*, 54, 10, pp.3003–3014, 2009.
- H. Hoevers, A. Bento, M. Bruijn, L. Gottardi, **M. Korevaar**, W. Mels, P. de Korte "Performance of a microcalorimeter with a superconducting transition edge thermometer", *Nucl. Instrum. Methods Phys. Res. A*, 444, 1, pp.192-195, 2000.
- H. Hoevers, A. Bento, M. Bruijn, L. Gottardi, **M. Korevaar**, W. Mels, P. de Korte, "Thermal fluctuation noise in a voltage biased superconducting transition edge thermometer", *Appl. Phys. Lett.*, 77, p.4422-24, 2000.

Abstracts and conference papers:

- S. Salvador, **M. Korevaar**, J. Heemskerk, R. Kreuger, J. Huizenga, S. Seifert, D. Schaart and F. Beekman, "SiPM side detectors for performance enhancements of an EMCCD-based gamma camera"*, IEEE NSS-MIC Abstract*, 2011.
- J.W.T. Heemskerk**, M.A.N. Korevaar**, J. Huizenga, R, Kreuger, D.R. Schaart, M.C. Goorden, F.J. Beekman, Enhanced High-Resolution EMCCD-Based Gamma Camera Using SiPM Side Detection"*, IEEE NSS-MIC Abstract*, M14-178, 2010.
- **M.A.N. Korevaar**, M.C. Goorden, J.W.T. Heemskerk, D.R. Schaart, F.J. Beekman "Cramer Rao Lower Bound Optimization of an EM-CCD Based Scintillation Gamma Camera"*, IEEE NSS-MIC Abstract*, M06-3, 2009.
- **M.A.N. Korevaar**, M.C. Goorden, J.W.T. Heemskerk, R. Kreuger, F.J. Beekman, "Statistical versus Analytical Scintillation Detection Algorithms for CCD Based Gamma Cameras", *IEEE NSS-MIC Abstract*, M09-68, 2009.
- J.W.T. Heemskerk, M.C. Goorden, **M.A.N. Korevaar,** E. van der Kolk, R. Kreuger, P. Dorenbos, F.J. Beekman, "Comparison of Scintillators for an EM-CCD-Based Gamma Camera"*, IEEE NSS-MIC Abstract*, M13-264, 2009.
- **M.A.N. Korevaar**, J.W.T. Heemskerk, M.C. Goorden, F.J. Beekman "Depth-of-interaction detection and correction with a multi-scale algorithm in CCD based gamma camera"*, IEEE NSS-MIC Conference Record,* pp. 4544–4549, 2008.
- **M.A.N. Korevaar**, J.W.T. Heemskerk, F.J. Beekman. "Scale-space algorithm for improved optical scintillation photon detection in a CCD based camera", *EOS Topical Meeting on Photonic Devices*, 2008
- F.J. Beekman, **M.A.N. Korevaar**, J.W. Heemskerk, "Pinhole Camera with Light-Spread Suppression and Depth-of-Interaction Elimination Through Optical Cone Beam Ligh Collimation"*, IEEE NSS-MIC Abstract,* M11-1, 2007.
- J.W.T. Heemskerk, **M.A.N. Korevaar**, P. Schotanus, K.M. ligtvoet, F.J. Beekman "Micro-Machined Retroreflector for Improving Light Yield in Ultra-High Resolution Gamma Cameras"*, IEEE NSS-MIC Abstract,* M05-2, 2007.
- J. van der Kuur, W.A. Mels, **M.A.N. Korevaar**, P.A.J. de Korte, M. Kiviranta, Heikki Seppa, "Characteristics of transition-edge microcalorimeters under AC bias" *Low Temperature Detectors 9 abstract*, 2001.